



BEILSTEIN JOURNAL OF ORGANIC CHEMISTRY

# Organic photovoltaics

Edited by David J. Jones and Wallace Wing Ho Wong

## Imprint

Beilstein Journal of Organic Chemistry

[www.bjoc.org](http://www.bjoc.org)

ISSN 1860-5397

Email: [journals-support@beilstein-institut.de](mailto:journals-support@beilstein-institut.de)

The *Beilstein Journal of Organic Chemistry* is published by the Beilstein-Institut zur Förderung der Chemischen Wissenschaften.

Beilstein-Institut zur Förderung der Chemischen Wissenschaften  
Trakehner Straße 7–9  
60487 Frankfurt am Main  
Germany  
[www.beilstein-institut.de](http://www.beilstein-institut.de)

The copyright to this document as a whole, which is published in the *Beilstein Journal of Organic Chemistry*, is held by the Beilstein-Institut zur Förderung der Chemischen Wissenschaften. The copyright to the individual articles in this document is held by the respective authors, subject to a Creative Commons Attribution license.



## Separation and identification of indene–C<sub>70</sub> bisadduct isomers

Bolong Zhang, Jegadesan Subbiah, David J. Jones and Wallace W. H. Wong<sup>\*</sup>

### Full Research Paper

Open Access

Address:  
School of Chemistry, Bio21 Institute, University of Melbourne, 30  
Flemington Rd, Parkville, Victoria, 3010, Australia

Email:  
Wallace W. H. Wong<sup>\*</sup> - [wwhwong@unimelb.edu.au](mailto:wwhwong@unimelb.edu.au)

\* Corresponding author

Keywords:  
chromatographic separation; electron acceptor; fullerene bisadduct;  
organic solar cell; regioisomers

*Beilstein J. Org. Chem.* **2016**, *12*, 903–911.  
doi:10.3762/bjoc.12.88

Received: 15 January 2016  
Accepted: 20 April 2016  
Published: 06 May 2016

This article is part of the Thematic Series "Organic photovoltaics".

Associate Editor: T. P. Yoon

© 2016 Zhang et al; licensee Beilstein-Institut.  
License and terms: see end of document.

### Abstract

Following an initial work on the isolation of a single geometric isomer from an indene–C<sub>70</sub> bisadduct (IC<sub>70</sub>BA) mixture, we report the full fractionation and identification of the bisadduct species in the material. Eleven fractions of IC<sub>70</sub>BA isomers were separated by high-performance liquid chromatography. A number of fractions contained relatively pure isomer species and their configuration were deduced using a variety of analytical techniques including <sup>1</sup>H and <sup>13</sup>C NMR and UV–vis spectroscopy. The electrochemical properties and the organic solar cell device performance were investigated for fractions where a reasonable quantity of sample could be isolated.

### Introduction

Organic solar cells (OSCs) are an emerging renewable energy technology that has achieved remarkable progress over the past two decades. Compared to traditional inorganic semiconductor solar cells, OSCs promise a number of advantages, such as lightweight flexible devices and low-cost fabrication using roll-to-roll printing [1]. Bulk-heterojunction organic solar cells (BHJ OSC) are a specific type of OSCs which contain a blend of organic electron donor and acceptor materials as the photoactive component.

Fullerenes and their derivatives are widely used in BHJ OSC devices as the electron acceptor material. They have several characteristics that make them favorable for this application including good electron transport [2], reversible reduction behavior [3], and easily functionalized structures [4]. Indene fullerene bisadducts, specifically the C<sub>60</sub> (IC<sub>60</sub>BA) and C<sub>70</sub> (IC<sub>70</sub>BA)

analogues (Figure 1), have been used successfully to boost the performance of poly(3-hexylthiophene) (P3HT) based devices. The use of fullerene bisadducts improves the open circuit voltage of the device compared to mono-functionalized derivatives. In recent studies, the solar cell devices achieved power conversion efficiency as high as 7.5% for IC<sub>60</sub>BA [5] and 7.4% for IC<sub>70</sub>BA [6].

The IC<sub>70</sub>BA material used in most reports consisted of a mixture of isomers [7–9]. The synthesis of IC<sub>70</sub>BA involves [2 + 4] Diels–Alder cycloaddition reaction between C<sub>70</sub> and two isoindene molecules generated in situ from indene. The symmetry of the ellipsoidal C<sub>70</sub> molecule means that there are four different bonds between two six membered rings ([6,6]-bonds) that can participate in the Diels–Alder reaction. These are known as  $\alpha$ -,  $\beta$ -,  $\varepsilon$ - and  $\kappa$ -bonds (Figure 2a). The  $\alpha$ -bonds are the most reac-

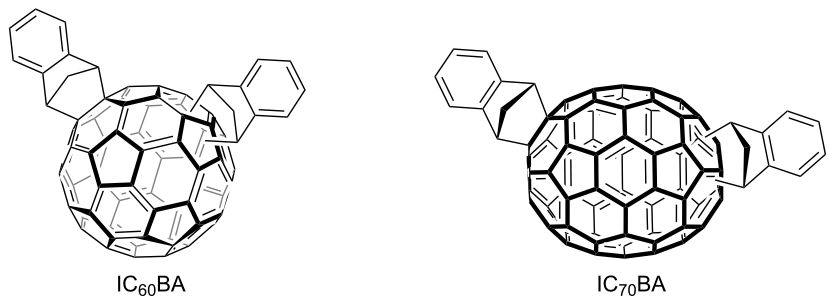


**Figure 1:** Molecular structure of  $\text{IC}_{60}\text{BA}$  and  $\text{IC}_{70}\text{BA}$ .

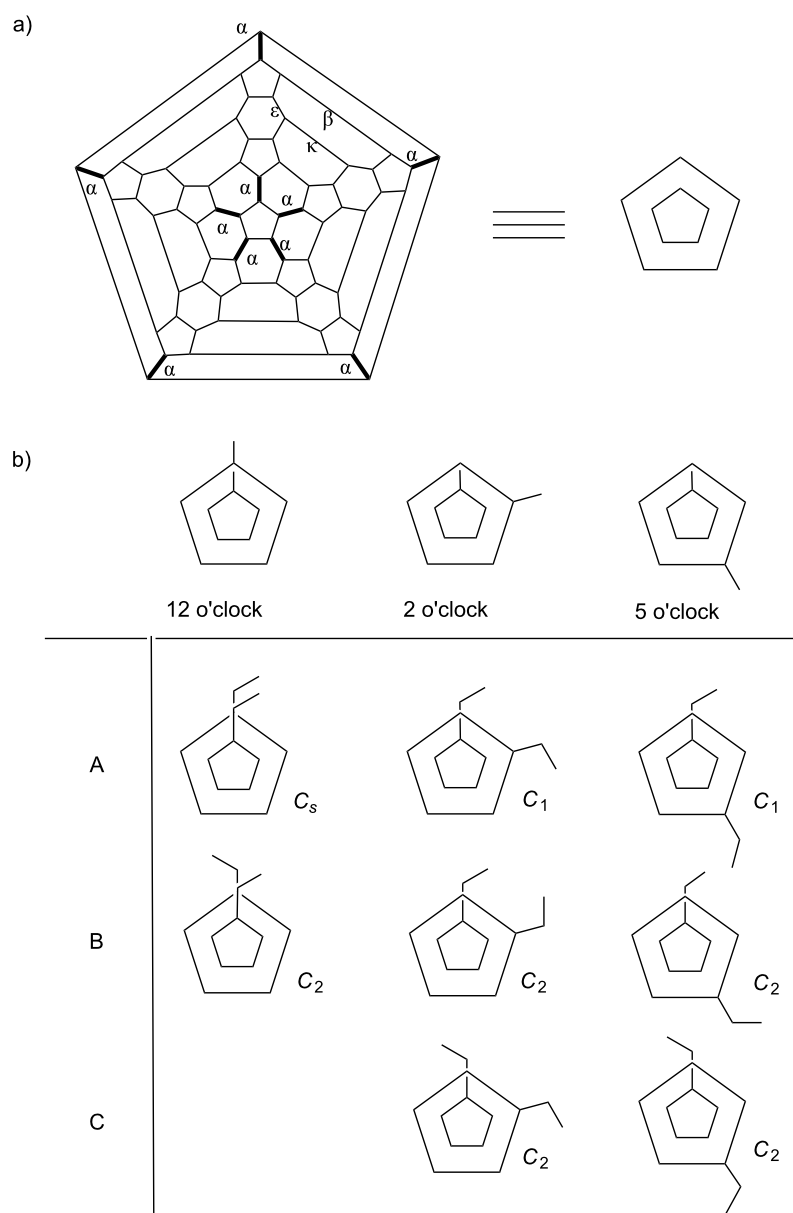


**Figure 2:** a) Schlegel diagram of  $\text{C}_{70}$ ; b) illustrations of three regioisomers of  $\text{IC}_{70}\text{BA}$  and their geometrical isomers.

tive as they situated at the ends of the C<sub>70</sub> molecule and therefore experience higher strain from the curvature of the molecule [10]. While reaction at non-[6,6]-bonds are possible, the thermodynamic products of fullerene adducts are usually located on the [6,6]-bonds [11]. Therefore, bisadducts of C<sub>70</sub> usually consist of three major regioisomers, which have been described as the 12 o'clock, 2 o'clock and 5 o'clock isomers (Figure 2b) [10]. Each of these three regioisomers also includes two or three geometric isomers as a result of the conformation of the substituents.

Given the numerous possible isomers in IC<sub>70</sub>BA, our group took interest in examining the possibility of isolating single isomers from the mixture. It was anticipated that material containing a single isomer would have higher crystallinity compared to the mixture and this would have significant effects on device performance. In a previous communication [9], an isomer of IC<sub>70</sub>BA was obtained by chromatographic separation using both flash chromatography and high pressure liquid chromatography (HPLC). X-ray crystallography revealed that this sample contained the 2 o'clock-B isomer (Figure 2b). This material was used with P3HT in solar cell devices that showed higher performance compared to devices containing the isomer mixture. Analysis of the materials and devices indicated that the single isomer had better charge transport properties probably as a result of higher crystallinity of the material.

It is noteworthy that there are a handful of other studies in the literature that reported on chromatographic separation of fullerene bisadduct isomers [8,12-14]. To the best of our knowledge, this is the first comprehensive analysis of IC<sub>70</sub>BA mixture using HPLC. Eleven fractions were collected and analyzed. Among these fractions, all of the major regioisomers as well as some minor regioisomers of IC<sub>70</sub>BA were identified. The separation process, full characterizations as well as the device performance of these isomers of IC<sub>70</sub>BA are presented in this work.

## Results and Discussion

The synthesis of the isomeric mixture of IC<sub>70</sub>BA was achieved by heating C<sub>70</sub> with indene at 180 °C in 1,2-dichlorobenzene [9]. Following the reaction, flash chromatography (silica gel, toluene: cyclohexane, 1:9) was performed to remove any excess reagents, mono-adducts of C<sub>70</sub> as well as other impurities. In our previous work, the mixture of IC<sub>70</sub>BA was separated into two fractions by means of flash chromatography; however in this case these two fractions were combined and further purified by HPLC using a Cosmosil Buckyprep-D column (4.6 i.d. × 250 mm, toluene, 0.2 mL/min, UV detection 325 nm). More than thirteen peaks were observed in the HPLC chromatogram (Figure 3). From these, eleven fractions were collected by the liquid handler of the HPLC equipment (see details in Support-

ing Information File 1 and Figure S1). The cleanest fractions were 1, 4 and 9 as shown in the chromatograms (Figure 3) and fractions 2, 3, 9 and 11 contained the biggest portions of the original mixture, enough for device testing. Notably, fraction 9 contained two IC<sub>70</sub>BA species and was further separated by flash chromatography (silica gel, toluene/cyclohexane 1:9) into fraction 9-1 and fraction 9-2 which are known to contain the 2 o'clock-B isomer [9].

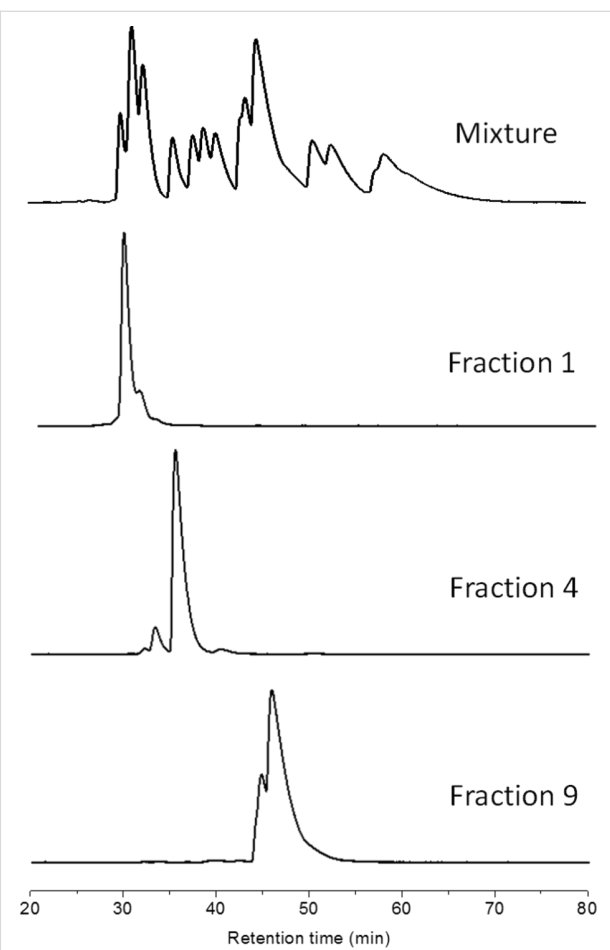


**Figure 3:** Chromatograms of IC<sub>70</sub>BA mixture and fractions 1, 4 and 9 separated by HPLC (Cosmosil Buckyprep-D column, toluene, 0.2 mL/min). Note that fraction 9 was further separated by flash chromatography (silica gel, toluene/cyclohexane 1:9) into fractions 9-1 and 9-2.

According to the <sup>1</sup>H NMR spectra, there are five fractions which show clear identifiable proton resonances. These are fractions 1, 4, 9-1, 9-2 and 11 (Figure 4, see Supporting Information File 1, Figure S2 for comparisons between other fractions). The resonances located in the area of 4 ppm to 5 ppm belonged to CH protons (H<sub>b</sub>) of IC<sub>70</sub>BA, while the resonances between 2 ppm to 3 ppm were attributed to the CH<sub>2</sub> protons (H<sub>a</sub>). Due to the limitations of the separating efficiency of HPLC, other fractions were either too low in yield or mixed

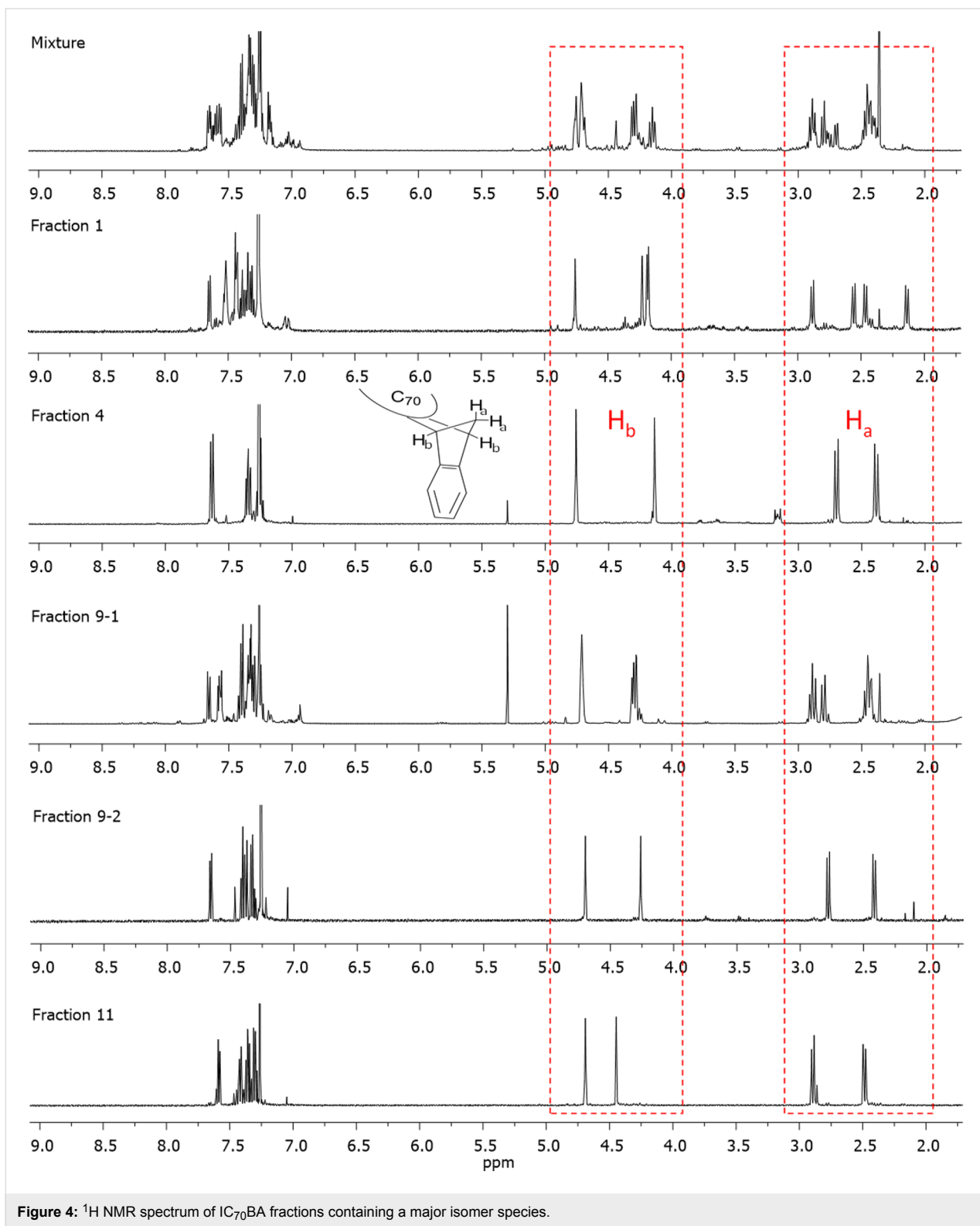


Figure 4:  $^1\text{H}$  NMR spectrum of  $\text{IC}_{70}\text{BA}$  fractions containing a major isomer species.

with neighboring fractions. In those cases, the  $^1\text{H}$  NMR experiments did not provide useful information for identifying the configuration of isomers contained in the samples (see Supporting Information File 1).

As shown in Figure 2, some geometrical isomers of  $\text{IC}_{70}\text{BA}$  belong to the  $C_2$  or  $C_s$  point group while others are in the  $C_1$  point group. For isomers in  $C_2$  or  $C_s$  configurations, each of their two substituents is in the same chemical environment. As a

result, their  $-\text{CH}_2$  resonances should split into two doublet peaks and the  $-\text{CH}$  resonances should also split into two singlet or doublet peaks depending on whether it couples with the protons of the  $-\text{CH}_2$  group. According to the  $^1\text{H}$  NMR spectra, fractions 4, 9-2 and 11 were symmetrical isomers due to their simplified  $^1\text{H}$  resonances, while the compounds in fractions 1 and 9-1 did not have any plane or point of symmetry (Figure 4). Although fraction 3 included approximately 30% impurities of fraction 2, we could still observe clearly two sharp singlet resonances at 4.75 and 4.14 ppm, which suggested that the major compound in fraction 3 had  $C_2$  or  $C_s$  symmetry (Supporting Information File 1, Figure S2). The  $^{13}\text{C}$  NMR spectrum of fractions 4, 9-2 and 11 showed 40 resonances in the 120–165 ppm region where the  $\text{sp}^2$  carbon resonances of the fullerene molecule were commonly observed (see Supporting Information File 1). This was a strong indication that these fractions contained  $C_2$  or  $C_s$  symmetric derivatives. On the other hand, there were more than 70 resonances in that region for fractions 1 and 9-1. This was further evidence that the fullerene derivatives in fractions 1 and 9-1 did not have any plane or point of symmetry.

The separation mechanism of the Cosmosil Buckyprep-D column is based on the electronic  $\pi$ -orbital interactions between fullerene species and the nitrocarbazoyl-functionalized silica stationary phase [15]. As a consequence, it was envisaged that the fullerene derivatives with smaller  $\pi$ -conjugated area would interact less strongly with the stationary phase of the column and therefore elute faster than derivatives with larger  $\pi$ -surface. In addition, the substitution on fullerenes may block the interaction between fullerene and the stationary phase which also shortens the retention time on the Cosmosil Buckyprep-D column. Considering the configurations of the three major regioisomers of  $\text{IC}_{70}\text{BA}$ , the 5 o'clock regioisomers are likely to elute first because the substituent geometry blocks the largest fullerene surface area. In contrast, the 12 o'clock regioisomers are expected to elute last as a result of the smallest angle between the two indene adducts. Applying logical deduction, we would anticipate that the isomers of  $\text{IC}_{70}\text{BA}$  elute from the HPLC in the following order: 5 o'clock, 2 o'clock and then 12 o'clock. This is consistent with our previous isolation and identification of the known single isomer, 2 o'clock-B, which is located in the middle of the HPLC chromatogram (Supporting Information File 1, Figure S1 and Table S1) [9].

The fast HPLC elution time of fractions 1, 2 and 3 meant that these fractions were likely to contain 5 o'clock regioisomers (Supporting Information File 1, Figure S1 and Table S1). With symmetry information from NMR experiments, there is a high probability that fraction 1, assigned to the  $C_1$  point group, contained the 5 o'clock-A isomer (Figure 2b). Fraction 2 has a

slightly shorter retention time relative to fraction 3. This indicates that fraction 2 could be in 5 o'clock-C configuration with its two indene substituents covering a larger conjugated area of  $\text{C}_{70}$  than fraction 3. Meanwhile, fractions 4 and 9-1 are more likely to be in the 2 o'clock-A and 2 o'clock-C configuration, respectively. That is because they are in the center of the HPLC chromatogram while in the  $C_1$  and  $C_2$  point groups, respectively. Fractions 10 and 11 are thought to be the 12 o'clock isomers, because of their locations in the rear of the HPLC stream. These two fractions were analyzed with a silica gel HPLC column (cyclohexane 1.0 mL/min), respectively, to assess their relative polarity. The HPLC chromatogram clearly illustrated that the retention time of fraction 10 was shorter than of fraction 11, which suggested that the configuration of fraction 10 was less polar than fraction 11 (Figure 5). With this information in mind, we are confident that fraction 10 contained the 12 o'clock-B isomer while fraction 11 contained the 12 o'clock-A isomer (Figure 2b).

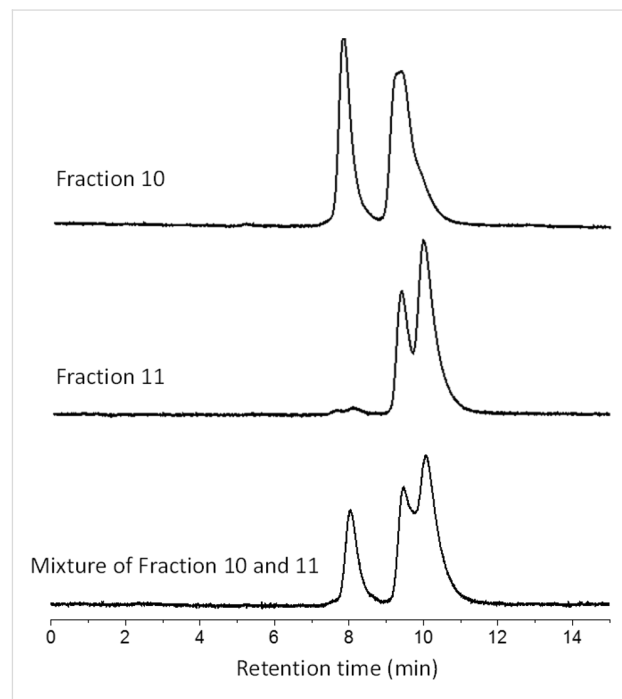


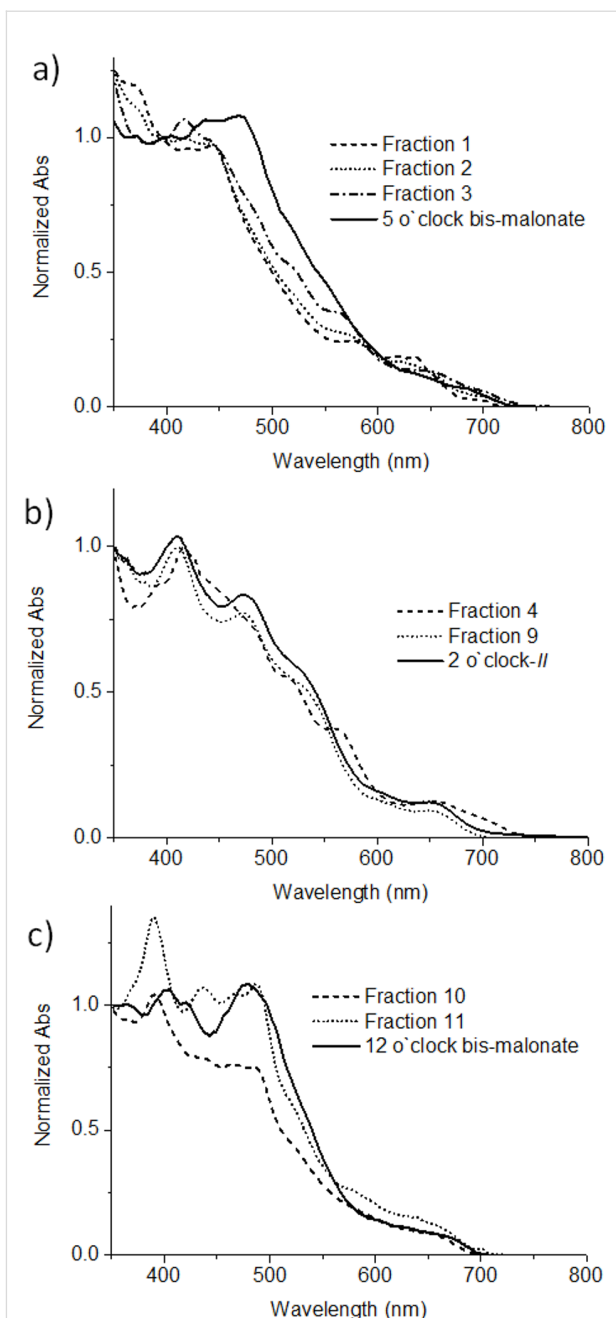
**Figure 5:** The retention time of the first species in fraction 10 is shorter than the species in fraction 11 on silica gel HPLC column (cyclohexane, 1.0 mL/min) providing information on the relative polarity of the compounds under investigation.

The assignments from chromatography and NMR experiments were supported by the analysis of the UV-vis absorption spectrum of the  $\text{IC}_{70}\text{BA}$  fractions. It is widely known that the UV-vis spectrum of fullerene derivatives are highly correlated to their conjugated structures [16]. Therefore, comparison of the UV-vis spectrum of each fraction with known  $\text{C}_{70}$  bisadducts, for example the known 2 o'clock-B isomer of  $\text{IC}_{70}\text{BA}$  [9] and

$C_{70}$  bis-malonate isomers [17], was expected to provide further information on adduct configurations. The UV-vis spectra of fractions 1, 2 and 3 showed very similar spectral features when compared with the spectrum of the 5 o'clock isomer of  $C_{70}$  bis-malonate, suggesting that they are all 5 o'clock isomers (Figure 6a). Similarly, the spectrum of fractions 4 and 9-1 matched that of the previously identified 2 o'clock-B IC<sub>70</sub>BA quite well. They all show an absorption maximum at 410 nm and a shoulder at around 478 nm (Figure 6b). Finally, fractions 10 and 11 showed a very similar UV-vis spectrum profile to the 12 o'clock  $C_{70}$  bis-malonate (Figure 6c). Thus the eight major regioisomers of IC<sub>70</sub>BA were identified. However, the remaining fractions 5–8, were also confirmed to be IC<sub>70</sub>BA isomers by mass spectrometry. Since the UV-vis spectrum of these fractions did not correlate to those of the known  $\alpha$ -bonds  $C_{70}$  bisadducts (Supporting Information File 1, Figure S13), it was reasonable to expect that these fractions contained IC<sub>70</sub>BA compounds with at least one indene substitution located on non- $\alpha$ -bonds of  $C_{70}$ . A summary of the isomer configuration assignments and related characterization data for the various fractions of IC<sub>70</sub>BA is shown in Table 1.

In order to analyze the electrochemical properties of the IC<sub>70</sub>BA fractions, cyclic voltammetry was performed on each fraction. The first reduction potentials of all 11 fractions were found to be in the range of  $-1.13$  to  $-1.25$  eV versus that of ferrocene/ferrocenium (see Supporting Information File 1, Figure S14). Therefore, the LUMO energy level of all single isomer of IC<sub>70</sub>BA and the isomer mixture were close to  $-3.6$  eV. The UV-vis and electrochemical characterization are summarized in Table 1.

The solar cell devices were fabricated in the architecture: ITO/PEDOT:PSS/active layer/Ca/Al (Figure 7a). The active layer consisted of a blend of the listed fractions of IC<sub>70</sub>BA with P3HT (see details in Table 2), in the ratio of 1:1 by weight. The fractions were chosen depending on their abundance and purities (Supporting Information File 1, Table S1). The open circuit voltage ( $V_{oc}$ ) of all devices were at around 0.8 eV which corresponded to the  $E_{LUMO}$  values from electrochemical experiments (Table 1 and Table 2). Figure 7b shows the current density–voltage ( $J$ – $V$ ) curves of the solar cell devices, under the illumination of AM1.5G, 100 mW cm<sup>-2</sup>. The photovoltaic performance data of the devices are summarized in Table 2 for a clear comparison between various ICBA fractions. The device with fraction 9-2 exhibits highest power conversion efficiencies (PCE) of 5.2% which is superior than the ICBA mixture (PCE of 4.5%) based device. The enhanced performance might be due to the favorable molecular packing in the active layer due to crystalline isomer fraction 9-1 as well as nanoscale phase separation morphology (Supporting Information File 1,



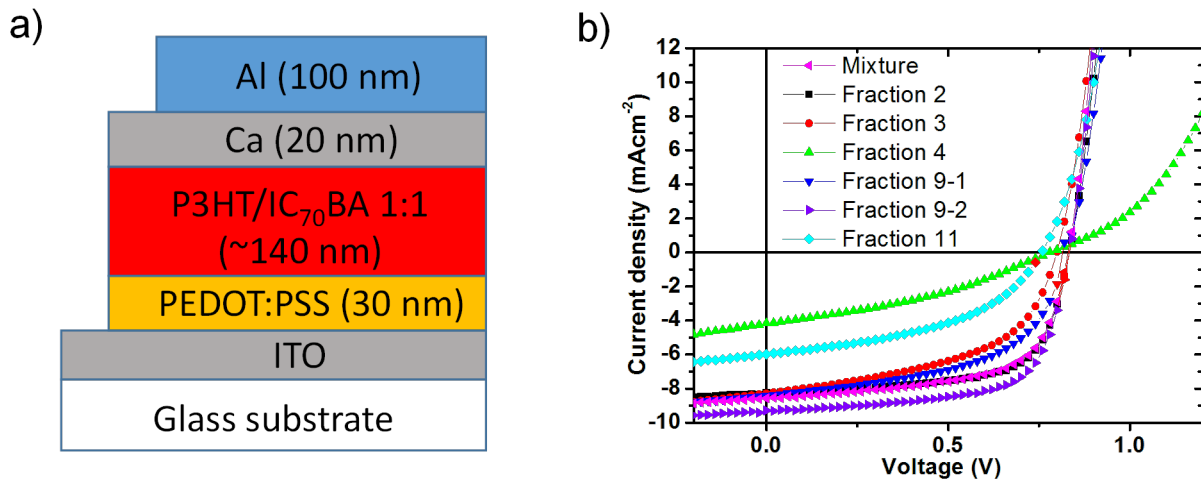
**Figure 6:** The UV-vis spectrum of each fraction of IC<sub>70</sub>BA as well as known  $C_{70}$  bisadducts: a) fraction 1, 2, 3 and 5 o'clock bis-malonate [17]; b) fraction 4, 9-1 and 2 o'clock-B of IC<sub>70</sub>BA [9]; c) fraction 10, 11 and 12 o'clock bis-malonate [17].

Figure S16d) of active layer blend [14]. The other fullerene fractions (2, 3 and 9-1) showed the moderate device performance with short circuit current density ( $J_{sc}$ ) and PCE value in the range of 8.0–8.3 mA/cm<sup>2</sup> and 3.1–4.4%, respectively. However, the  $J_{sc}$  and PCE and of the devices containing fractions 4 and 11 were significantly lower in performance compared (Table 2) to the devices of other fractions.

**Table 1:** Characterization data of various IC<sub>70</sub>BA fractions.

	Configuration of major isomer in the sample <sup>a</sup>	UV-vis $\lambda_{\text{max}}$ (nm) <sup>b</sup>	Reduction $E_{1/2}$ (eV) <sup>c</sup>	$E_{\text{LUMO}}$ (eV) <sup>d</sup>
IC <sub>70</sub> BA mixture	–	–	–1.24	–3.56
Fraction 1	5 o'clock-A	447 (1.1)	–1.13	–3.67
Fraction 2 <sup>e</sup>	5 o'clock-C	446 (2.1)	–1.19	–3.61
Fraction 3	5 o'clock-B	417 (1.8)	–1.19	–3.61
Fraction 4	2 o'clock-C	417 (1.6)	–1.22	–3.58
Fraction 9-1	2 o'clock-A	410 (1.2)	–1.15	–3.65
Fraction 9-2	2 o'clock-B	411 (2.1)	–1.25	–3.55
Fraction 10 <sup>e</sup>	12 o'clock-B	390 (1.2)	–1.20	–3.60
Fraction 11	12 o'clock-A	389 (2.0)	–1.17	–3.63

<sup>a</sup>Assignments made using a combination of NMR, UV-vis and chromatographic experiment data; <sup>b</sup>Solution UV-vis data. Absorption coefficient ( $\times 10^3 \text{ M}^{-1} \text{ cm}^{-1}$ ) in brackets; <sup>c</sup>Half-wave potential of first reduction; <sup>d</sup>Calculated from  $E_{\text{LUMO}} = -4.8 + E_{1/2}$ ; <sup>e</sup>Fractions 2 and 10 contained a substantial quantity of other IC<sub>70</sub>BA isomers.

**Figure 7:** Schematic diagram of the architecture of BHJ solar cell devices (a) and J-V curves of the devices containing P3HT and each IC<sub>70</sub>BA fractions (b).**Table 2:** Performance of BHJ solar cell devices based on a blend of P3HT and each IC<sub>70</sub>BA fractions as the active layer.<sup>a</sup>

Active layer P3HT/IC <sub>70</sub> BA (1:1)	$J_{\text{sc}}$ (mA/cm <sup>2</sup> )	$V_{\text{oc}}$ (V)	FF (%)	PCE (%)
Mixture	$8.6 \pm 0.30$	$0.82 \pm 0.02$	$64 \pm 3$	$4.5 \pm 0.25$
Fraction 2	$8.1 \pm 0.20$	$0.80 \pm 0.02$	$66 \pm 2$	$4.4 \pm 0.20$
Fraction 3	$8.0 \pm 0.30$	$0.76 \pm 0.02$	$50 \pm 3$	$3.1 \pm 0.30$
Fraction 4	$3.9 \pm 0.35$	$0.74 \pm 0.02$	$34 \pm 4$	$0.9 \pm 0.40$
Fraction 9-1	$8.2 \pm 0.25$	$0.78 \pm 0.02$	$55 \pm 2$	$3.6 \pm 0.25$
Fraction 9-2	$9.3 \pm 0.15$	$0.82 \pm 0.02$	$68 \pm 2$	$5.2 \pm 0.15$
Fraction 11	$5.7 \pm 0.30$	$0.72 \pm 0.02$	$44 \pm 3$	$1.8 \pm 0.30$

<sup>a</sup>The data shown are the average values obtained from 10 devices with standard deviation.

It is important to point out that fraction 4 had the highest purity among all the fractions (Supporting Information File 1, Table S1), which demonstrated that the purity is not the only factor influencing the performance of devices. Taking into account both fraction purity and assigned geometric configuration, a surprising trend emerged with apparent decrease in  $J_{sc}$  with increasing fraction purity and crystallinity. The crystallinity of a given fraction can be considered as dependent on the symmetry of the assigned isomer configuration. That is, the degree of symmetry varies in the order  $C_1 < C_2 < C_5$ , which resulted in the order of crystallinity for the five fractions ranked as  $9 < 2 \approx 3 < 4 < 11$ . Considering fraction 4 had the highest purity, the order of crystallinity may be modified to  $9 < 2 \approx 3 < 11 < 4$ , which corresponded to the decreasing  $J_{sc}$  of the devices containing these fractions. One way to rationalise this observation is that increasing crystallinity of IC<sub>70</sub>BA can improve the charge carrier mobility of the bulk material but the miscibility with the P3HT electron donor material can also change. A key feature of efficient BHJ solar cell devices is the nanoscale phase separation of the electron donor and acceptor materials into continuous interpenetrating networks. Some indications on the degree of phase separation can be obtained in tapping mode atomic force microscopy (AFM) experiments (see Supporting Information File 1 for experimental details). Both height and phase AFM images suggested unfavourable phase separation for blend films containing IC<sub>70</sub>BA fractions 4 and 11 with domain sizes in the micrometre range (Supporting Information File 1, Figure S16c and S16e). This larger domain size is usually detrimental for charge separation and this is reflected in the lower  $J_{sc}$  and PCE for the devices containing fractions 4 and 11 as shown in Table 2.

## Conclusion

Herein we report the successful isolation of isomers of IC<sub>70</sub>BA through HPLC. Eleven distinct fractions were collected and analyzed to identify the various geometrical and regioisomers of this fullerene derivative. Furthermore, photophysical and electrochemical characterization was performed to evaluate the properties of these materials. From the eleven fractions, all major ( $\alpha$ -bond) regioisomers of IC<sub>70</sub>BA were identified with the details of their configuration and symmetry factors confirmed. It was found that material purity and crystallinity and their effects on the thin film nanostructure are key factors in determining the performance of these fullerene derivatives in BHJ solar cell devices. With the observations in this study, it can be argued that the success of IC<sub>70</sub>BA (and in extension, IC<sub>60</sub>BA) as the electron acceptor component in BHJ solar cells is serendipitous and surprising given the large number of chemical structures involved. It is noteworthy that there have been several studies on reducing the number of isomers in fullerene bisadduct materials using synthetic strategies and about the suc-

cessful application in solar cell devices [18–22]. While high material purity and composition is generally considered an advantage for organic electronic materials, the material criteria for bulk heterojunction organic solar cell applications is less clear. This is owing to the fact that bulk heterojunctions are a mixture of at least two materials (an electron donor and an electron acceptor) with the film nanostructure being extremely important for the device performance.

## Supporting Information

### Supporting Information File 1

Details on the separation procedure and characterization of the materials as well as device fabrication and testing.

[<http://www.beilstein-journals.org/bjoc/content/supplementary/1860-5397-12-88-S1.pdf>]

## Acknowledgements

This work was made possible by support from the Australian Renewable Energy Agency which funds the project grants within the Australian Centre for Advanced Photovoltaics. WWHW is supported by an Australian Research Council Future Fellowship (FT130100500). Responsibility for the views, information or advice expressed herein is not accepted by the Australian Government.

## References

1. Krebs, F. C. *Polymer Solar Cells - Materials, Design, Manufacture*; DEStech Publications, Inc.: USA, 2010.
2. Bracher, P. J.; Schuster, D. I. In *Fullerenes: From Synthesis to Optoelectronic Properties*; Guldi, D.; Martin, N., Eds.; Springer: Netherlands, 2002; Vol. 4, pp 163 ff. doi:10.1007/978-94-015-9902-3\_6
3. Echegoyen, L.; Echegoyen, L. E. *Acc. Chem. Res.* **1998**, *31*, 593. doi:10.1021/ar970138v
4. Langa, F.; Nierengarten, J.-F. *Fullerenes: principles and applications*; Royal Society of Chemistry, 2007. doi:10.1039/9781847557711
5. Liao, S.-H.; Li, Y.-L.; Jen, T.-H.; Cheng, Y.-S.; Chen, S.-A. *J. Am. Chem. Soc.* **2012**, *134*, 14271. doi:10.1021/ja303813s
6. Guo, X.; Cui, C. H.; Zhang, M. J.; Huo, L. J.; Huang, Y.; Hou, J. H.; Li, Y. *Energy Environ. Sci.* **2012**, *5*, 7943. doi:10.1039/c2ee21481d
7. Fan, X.; Cui, C.; Fang, G.; Wang, J.; Li, S.; Cheng, F.; Long, H.; Li, Y. *Adv. Funct. Mater.* **2012**, *22*, 585. doi:10.1002/adfm.201102054
8. Hu, L.; Cui, R.; Huang, H.; Lin, G.; Guo, X.; Yang, S.; Lian, Y.; Dong, J.; Sun, B. *J. Nanosci. Nanotechnol.* **2015**, *15*, 5285. doi:10.1166/jnn.2015.10022
9. Wong, W. W. H.; Subbiah, J.; White, J. M.; Seyler, H.; Zhang, B.; Jones, D. J.; Holmes, A. B. *Chem. Mater.* **2014**, *26*, 1686. doi:10.1021/cm404054z
10. Herrmann, A.; Rüttimann, M.; Thilgen, C.; Diederich, F. *Helv. Chim. Acta* **1995**, *78*, 1673. doi:10.1002/haca.19950780705
11. Li, Z.; Shevlin, P. B. *J. Am. Chem. Soc.* **1997**, *119*, 1149. doi:10.1021/ja963088i

12. Zhao, F.; Meng, X.; Feng, Y.; Jin, Z.; Zhou, Q.; Li, H.; Jiang, L.; Wang, J.; Li, Y.; Wang, C. *J. Mater. Chem. A* **2015**, *3*, 14991. doi:10.1039/C5TA04040J

13. Matsuo, Y.; Kawai, J.; Inada, H.; Nakagawa, T.; Ota, H.; Otsubo, S.; Nakamura, E. *Adv. Mater.* **2013**, *25*, 6266. doi:10.1002/adma.201302607

14. Meng, X.; Zhao, G.; Xu, Q.; Tan, Z. a.; Zhang, Z.; Jiang, L.; Shu, C.; Wang, C.; Li, Y. *Adv. Funct. Mater.* **2014**, *24*, 158. doi:10.1002/adfm.201301411

15. Information on column specifications can be found at  
[http://www.nacalai.co.jp/global/download/pdf/cosmosil\\_buckyprep-d.pdf](http://www.nacalai.co.jp/global/download/pdf/cosmosil_buckyprep-d.pdf)

16. Wong, W. W. H.; Diederich, F. *Chem. – Eur. J.* **2006**, *12*, 3463. doi:10.1002/chem.200501523

17. van Eis, M. J.; Seiler, P.; Muslinkina, L. A.; Badertscher, M.; Pretsch, E.; Diederich, F.; Alvarado, R. J.; Echegoyen, L.; Núñez, I. P. *Helv. Chim. Acta* **2002**, *85*, 2009. doi:10.1002/1522-2675(200207)85:7<2009::AID-HLCA2009>3.0.CO;2-G

18. Liao, M.-H.; Lai, Y.-Y.; Lai, Y.-Y.; Chen, Y.-T.; Tsai, C.-E.; Liang, W.-W.; Cheng, Y.-J. *ACS Appl. Mater. Interfaces* **2014**, *6*, 996. doi:10.1021/am404485t

19. Tao, R.; Umeyama, T.; Higashino, T.; Koganezawa, T.; Imahori, H. *Chem. Commun.* **2015**, *51*, 8233. doi:10.1039/C5CC01712B

20. Tao, R.; Umeyama, T.; Higashino, T.; Koganezawa, T.; Imahori, H. *ACS Appl. Mater. Interfaces* **2015**, *7*, 16676. doi:10.1021/acsami.5b04351

21. Zhang, B.; Subbiah, J.; Lai, Y.-Y.; White, J. M.; Jones, D. J.; Wong, W. W. H. *Chem. Commun.* **2015**, *51*, 9837. doi:10.1039/C5CC02701B

22. Zhang, B.; White, J. M.; Jones, D. J.; Wong, W. W. H. *Org. Biomol. Chem.* **2015**, *13*, 10505. doi:10.1039/C5OB01630D

## License and Terms

This is an Open Access article under the terms of the Creative Commons Attribution License (<http://creativecommons.org/licenses/by/2.0>), which permits unrestricted use, distribution, and reproduction in any medium, provided the original work is properly cited.

The license is subject to the *Beilstein Journal of Organic Chemistry* terms and conditions:  
(<http://www.beilstein-journals.org/bjoc>)

The definitive version of this article is the electronic one which can be found at:  
doi:10.3762/bjoc.12.88



# 3,6-Carbazole vs 2,7-carbazole: A comparative study of hole-transporting polymeric materials for inorganic–organic hybrid perovskite solar cells

Wei Li<sup>1</sup>, Munechika Otsuka<sup>2</sup>, Takehito Kato<sup>\*2</sup>, Yang Wang<sup>1</sup>, Takehiko Mori<sup>1</sup> and Tsuyoshi Michinobu<sup>\*1</sup>

## Full Research Paper

Open Access

Address:

<sup>1</sup>Department of Materials Science and Engineering, Tokyo Institute of Technology, 2-12-1 Ookayama, Meguro-ku, Tokyo 152-8552, Japan and <sup>2</sup>Department of Mechanical Engineering, National Institute of Technology, Oyama College, 771 Nakakuki, Oyama, Tochigi 323-0806, Japan

Email:

Takehito Kato<sup>\*</sup> - kato\_t@oyama-ct.ac.jp; Tsuyoshi Michinobu<sup>\*</sup> - michinobu.t.aa@m.titech.ac.jp

\* Corresponding author

Keywords:

carbazole polymer; hole transport; perovskite solar cell; polycondensation

*Beilstein J. Org. Chem.* **2016**, *12*, 1401–1409.

doi:10.3762/bjoc.12.134

Received: 27 April 2016

Accepted: 22 June 2016

Published: 07 July 2016

This article is part of the Thematic Series "Organic photovoltaics".

Guest Editor: D. J. Jones

© 2016 Li et al.; licensee Beilstein-Institut.

License and terms: see end of document.

## Abstract

The ever increasing demand for clean energy has encouraged researchers to intensively investigate environmentally friendly photovoltaic devices. Inorganic–organic hybrid perovskite solar cells (PSCs) are very promising due to their potentials of easy fabrication processes and high power conversion efficiencies (PCEs). Designing hole-transporting materials (HTMs) is one of the key factors in achieving the high PCEs of PSCs. We now report the synthesis of two types of carbazole-based polymers, namely 3,6-Cbz-EDOT and 2,7-Cbz-EDOT, by Stille polycondensation. Despite the same chemical composition, 3,6-Cbz-EDOT and 2,7-Cbz-EDOT displayed different optical and electrochemical properties due to the different connectivity mode of the carbazole unit. Therefore, their performances as hole-transporting polymeric materials in the PSCs were also different. The device based on 2,7-Cbz-EDOT showed better photovoltaic properties with the PCE of 4.47% than that based on 3,6-Cbz-EDOT. This could be due to its more suitable highest occupied molecular orbital (HOMO) level and higher hole mobility.

## Introduction

Inorganic–organic hybrid perovskite solar cells (PSCs) have recently received significant attention due to their remarkably high power conversion efficiencies (PCEs). After the seminal study reported by Miyasaka et al. in 2009 with the PCE of 4%

[1], some key improvements have been made in designing device structures and fabrication methods, and the PCE of the PSCs rapidly increased to >20% [2–5]. Compared to the conventional organic photovoltaics and dye-sensitized solar

cells (DSSCs), PSCs benefit from a broad light absorption and high carrier diffusion length as excellent features of the perovskite materials. The development of efficient hole-transporting materials (HTMs), which extract a hole from the perovskite layer and transport it to the anode, is also significant for the further improvement of the PSC performances. So far, 2,2',7,7'-tetrakis(*N,N*-di(*p*-methoxyphenyl)amino)-9,9-spirobi-fluorene (spiro-OMeTAD) is regarded as the most conventional solid state hole transporter for the PSCs [6–10]. Despite the high PCEs conferred by this hole transporting layer, spiro-OMeTAD has several limitations, such as its complicated multistep synthesis, low hole mobility in its pristine form, and expensive fabrication costs of the PSCs due to the sublimable small molecule. Accordingly, solution-processable hole-transporting polymers with simple structures have also been pursued as HTMs in the PSCs. Common p-type semiconducting polymers, such as poly(3-hexylthiophene) (P3HT), and the state-of-the-art narrow band gap polymers, such as poly[2,5-bis(2-decyldodecyl)pyrrolo[3,4-*c*]pyrrole-1,4(2*H,5H*)-dione-(*E*)-1,2-di(2,2'-bithiophen-5-yl)ethane (PDPPDBTE), were successfully applied to the HTM in the PSCs [11,12]. Among them, the poly(triarylamine) derivatives are currently some of the best polymeric hole-transporting materials for the PSCs [13].

Carbazole (Cbz)-based conjugated polymers are widely used as active photo- and semiconducting materials in a variety of organic electronics due to their tunable optical and electrical properties [14–21]. For example, the 3,6-positions of the carbazole readily react with various electrophiles, and accordingly, many types of linear and hyperbranched poly(3,6-carbazole) derivatives have been reported to show potent redox activities and nonlinear optical or photorefractive properties [22–24]. These features were also applied to organic light-emitting diodes (OLEDs) [25]. In contrast, the poly(2,7-carbazole)

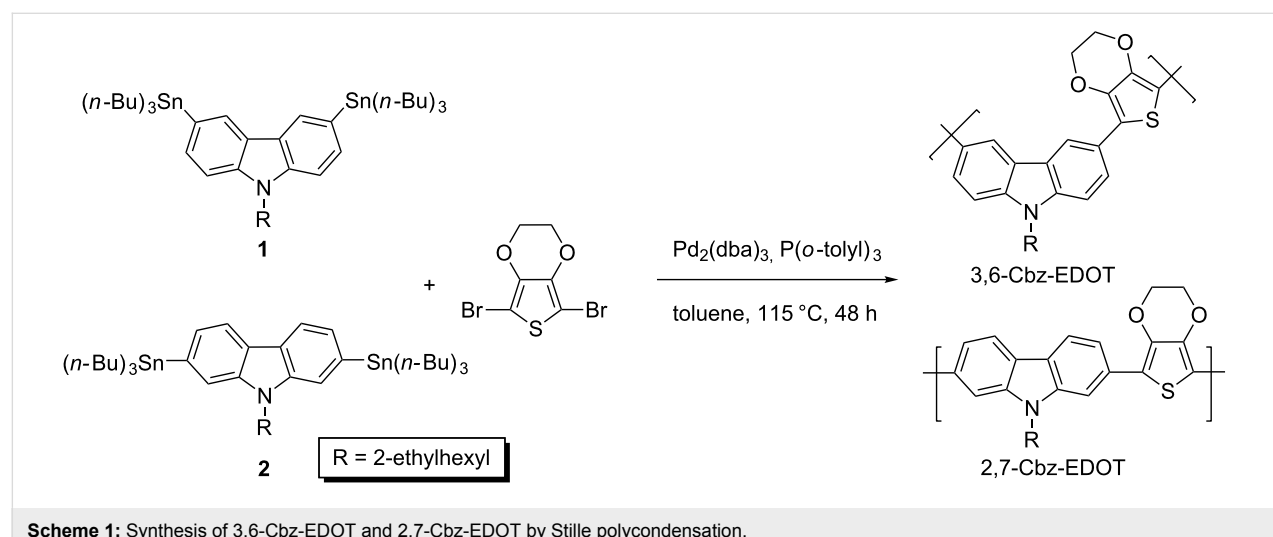
derivatives appeared after the pioneering synthetic studies of the 2,7-dihalogeno-carbazole monomers [26,27]. A series of 2,7-carbazole-based copolymers were synthesized, and most of them showed better semiconducting properties in organic field effect transistors (OFETs), bulk-heterojunction (BHJ) solar cells, thermoelectric and electrical memory devices as compared to the counter 3,6-carbazole-based polymers [28–36]. However, this structural relationship between the 3,6-carbazole and 2,7-carbazole has not yet been elucidated in the PSCs because of the emerging new devices.

In this study, we designed two carbazole-based hole-transporting polymers with different connectivity patterns. In order to enhance the electron-donating properties, the carbazole monomers were copolymerized with the electron-rich 3,4-ethylenedioxythiophene (EDOT) unit by Stille polycondensation. The energy levels and hole mobilities of the resulting carbazole copolymers, namely 3,6-Cbz-EDOT and 2,7-Cbz-EDOT, were estimated from the optical and electrochemical measurements and OFET performances, respectively. Finally, they were applied as the hole-transporting layer of the PSCs, and the photovoltaic properties of both devices were compared. The device based on 2,7-Cbz-EDOT displayed a higher PCE of 4.47% than that based on 3,6-Cbz-EDOT, which could be explained by their energy levels and hole mobilities.

## Results and Discussion

### Polymer synthesis

Carbazole copolymers with different connectivity patterns were synthesized by the Stille polycondensation between the bis(*tri-n*-butylstannyl)carbazole monomers and 2,5-dibromo-EDOT (Scheme 1). We very recently reported the synthesis of the same polymer structures by the microwave-assisted direct arylation polycondensation, but it should be noted that the soluble



**Scheme 1:** Synthesis of 3,6-Cbz-EDOT and 2,7-Cbz-EDOT by Stille polycondensation.

2,7-Cbz-EDOT could not be obtained due to undesired side reactions [37]. In contrast, the conventional Stille polycondensation afforded the desired linear polymers without any side reactions. The number-averaged molecular weight ( $M_n$ ) and polydispersity indices ( $M_w/M_n$ ), determined by GPC using THF as the eluent, were  $2.0 \text{ kg mol}^{-1}$  ( $n \sim 5$ ) and 1.5 for 3,6-Cbz-EDOT and  $3.0 \text{ kg mol}^{-1}$  ( $n \sim 7$ ) and 1.4 for 2,7-Cbz-EDOT, respectively. The polymer structures were characterized by  $^1\text{H}$  NMR and FTIR spectroscopies (Figure S1, Supporting Information File 1). The  $^1\text{H}$  NMR spectra revealed the ethylene groups of EDOT at ca. 4.2 ppm and the methylene group directly attached to the nitrogen atom of the carbazole at ca. 4.4 ppm, respectively, suggesting the successful copolymerization. Both polymers showed an explicit difference in their chemical shift values ascribed to the carbazole units due to the different connectivity patterns. In contrast, the IR spectra of the polymers were almost the same.

### Optical and electrochemical properties

The UV–vis absorption spectra were employed to evaluate the optical properties of 3,6-Cbz-EDOT and 2,7-Cbz-EDOT. The spectra were measured in  $\text{CH}_2\text{Cl}_2$  and in thin films (spin-coated on an ITO glass). The absorption maximum ( $\lambda_{\text{max}}$ ) of 3,6-Cbz-EDOT in  $\text{CH}_2\text{Cl}_2$  was 362 nm, whereas the thin film showed the bathochromically-shifted  $\lambda_{\text{max}}$  at 374 nm (Figure 1a). Compared to 3,6-Cbz-EDOT, 2,7-Cbz-EDOT showed a lower energy absorption in both the solution and thin film states ( $\lambda_{\text{max}} = 435 \text{ nm}$  in  $\text{CH}_2\text{Cl}_2$ ;  $\lambda_{\text{max}} = 443 \text{ nm}$  in the thin film), which is consistent with previous reports [26]. The red shifts in the absorption spectra from the solution to thin film states implied the presence of strong intermolecular interactions between the polymer backbones.

Cyclic voltammetry (CV) of the polymer thin films was measured in  $\text{CH}_3\text{CN}$  with  $0.1 \text{ M}$  ( $n\text{-C}_4\text{H}_9\text{)}_4\text{NPF}_6$  as the supporting electrolyte at  $20^\circ\text{C}$ . Both polymers displayed irreversible oxidation peaks in the measurement range (Figure 1b). 3,6-Cbz-EDOT exhibited the onset oxidation potential ( $E_{\text{ox, onset}}$ ) at 0.38 V (vs  $\text{Ag}/\text{Ag}^+$ ), whereas the  $E_{\text{ox, onset}}$  of 2,7-Cbz-EDOT was slightly higher (0.50 V). This difference can also be explained by the different connectivity pattern between the two polymers. The linkage through the 3,6-positions of the carbazole unit forms a linear conjugation between the nitrogen atoms, which facilitates the electron removal from the conjugated main chain. In contrast, the nitrogen atoms through the 2,7-linked carbazoles are classified as a formal cross-conjugated structure [38].

As an efficient HTM for the PSCs, p-type polymers should have a good energy balance with the perovskite layer [39]. Most importantly, the highest occupied molecular orbital (HOMO) energy level should be close to the valence band of the perovskite. The HOMO levels of 3,6-Cbz-EDOT and 2,7-Cbz-EDOT were calculated according to Equation 1:

$$E_{\text{HOMO}} = -(E_{\text{ox, onset}} + 4.80 - \varphi_{\text{Fc/Fc}^+}) [\text{eV}] \quad (1)$$

where  $\varphi_{\text{Fc/Fc}^+}$  is the redox potential of the ferrocene/ferrocnium ( $\text{Fc}/\text{Fc}^+$ ) couple measured under the same conditions (in this case, 0.09 V vs the  $\text{Ag}/\text{Ag}^+$  electrode). 2,7-Cbz-EDOT has a deeper HOMO level than 3,6-Cbz-EDOT. This was also the case for the lowest unoccupied molecular orbital (LUMO) levels, which were calculated from the HOMO levels and optical band gaps. All the data are listed in Table 1.

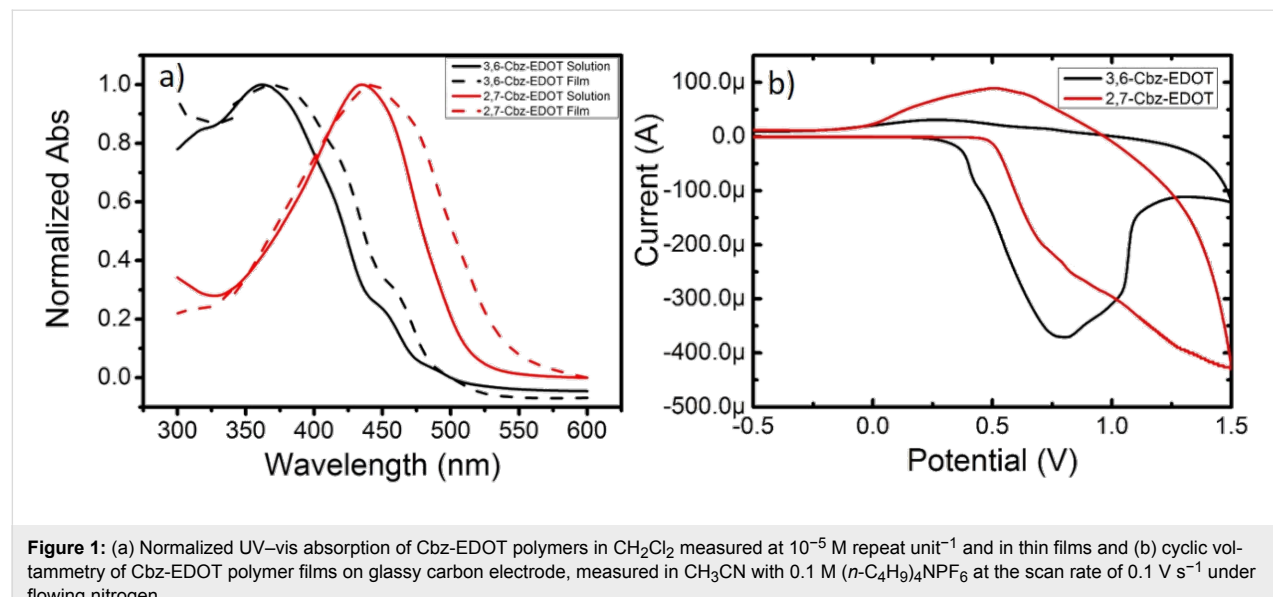


**Figure 1:** (a) Normalized UV–vis absorption of Cbz-EDOT polymers in  $\text{CH}_2\text{Cl}_2$  measured at  $10^{-5} \text{ M}$  repeat unit $^{-1}$  and in thin films and (b) cyclic voltammetry of Cbz-EDOT polymer films on glassy carbon electrode, measured in  $\text{CH}_3\text{CN}$  with  $0.1 \text{ M}$  ( $n\text{-C}_4\text{H}_9\text{)}_4\text{NPF}_6$  at the scan rate of  $0.1 \text{ V s}^{-1}$  under flowing nitrogen.

**Table 1:** Optical, electrochemical, and electrical properties of Cbz-EDOT polymers<sup>a</sup>.

Polymer	$\lambda_{\text{onset}}$ (nm)	Band gap (eV) <sup>b</sup>	$E_{\text{ox, onset}}$ (V) <sup>c</sup>	HOMO (eV) <sup>d</sup>	LUMO (eV) <sup>e</sup>	Hole mobility (cm <sup>2</sup> V <sup>-1</sup> s <sup>-1</sup> ) <sup>f</sup>
3,6-Cbz-EDOT	480	2.58	0.38	-5.09	-2.50	$3.5 \times 10^{-7}$
2,7-Cbz-EDOT	536	2.31	0.50	-5.21	-2.90	$5.1 \times 10^{-6}$

<sup>a</sup>In the thin film states. <sup>b</sup>Calculated from the  $\lambda_{\text{onset}}$  (1240/ $\lambda_{\text{onset}}$ ). <sup>c</sup>vs Ag/Ag<sup>+</sup> <sup>d</sup>Calculated from  $E_{\text{ox, onset}}$  and  $\phi_{\text{Fc/Fc}^+}$ . <sup>e</sup>Calculated from the HOMO levels and optical band gaps. <sup>f</sup>Determined from the OFET performances.

The carrier mobilities of the HTMs are some of the important parameters that determine the PSC performances. In order to elucidate the charge-transporting properties of the Cbz-EDOT polymers, top-contact/bottom-gate type OFET devices were fabricated, and the transistor performances were initially evaluated in air (for details see Supporting Information File 1). Both Cbz-EDOT polymers showed a p-type unipolar behavior during the measurements (Figure S2, Supporting Information File 1). Although the hole mobilities of both polymers were disappointingly low ( $<10^{-5}$  cm<sup>2</sup> V<sup>-1</sup> s<sup>-1</sup>) probably due to the unoptimized annealing conditions, the data clearly suggested that 2,7-Cbz-EDOT has a hole mobility one-order higher than 3,6-Cbz-EDOT (Table 1). This result is also consistent with the reported mobilities of other carbazole-based semiconducting polymers [40,41].

## Photovoltaic performances

It was shown that the HOMO level ( $-5.21$  eV) of 2,7-Cbz-EDOT is deeper than that ( $-5.09$  eV) of 3,6-Cbz-EDOT. The former value is comparable to that ( $-5.20$  eV) of P3HT and closer to the valence band ( $-5.45$  eV) of the perovskite layer employed in this study. Accordingly, this carbazole polymer (2,7-Cbz-EDOT) is expected to be a better HTM in the PSCs as compared to 3,6-Cbz-EDOT. In order to evaluate this theory, PSCs with the Cbz-EDOT hole-transporting layer were fabri-

cated, and the photovoltaic properties were compared. The device based on P3HT was also fabricated as the control sample [42]. The device structure is FTO/TiO<sub>2</sub>/perovskite (CH<sub>3</sub>NH<sub>3</sub>PbI<sub>3</sub>)/Cbz-EDOT (or P3HT)/Au, and the energy level diagram of the materials used in the devices is depicted in Figure 2.

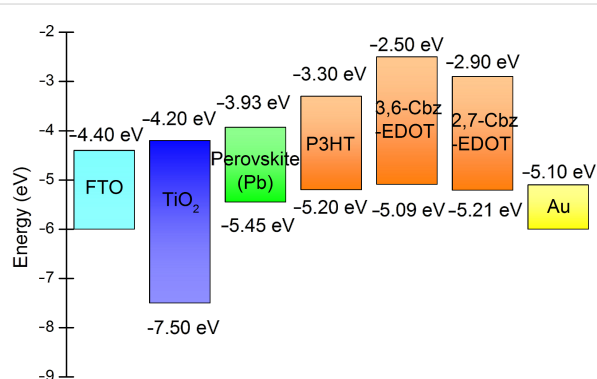


**Figure 2:** Energy level diagram of PSC components including P3HT, 3,6-Cbz-EDOT, and 2,7-Cbz-EDOT.

Figure 3a shows the current density–voltage ( $J$ – $V$ ) curves for the devices based on 3,6-Cbz-EDOT, 2,7-Cbz-EDOT, and P3HT. The device performance parameters are summarized in

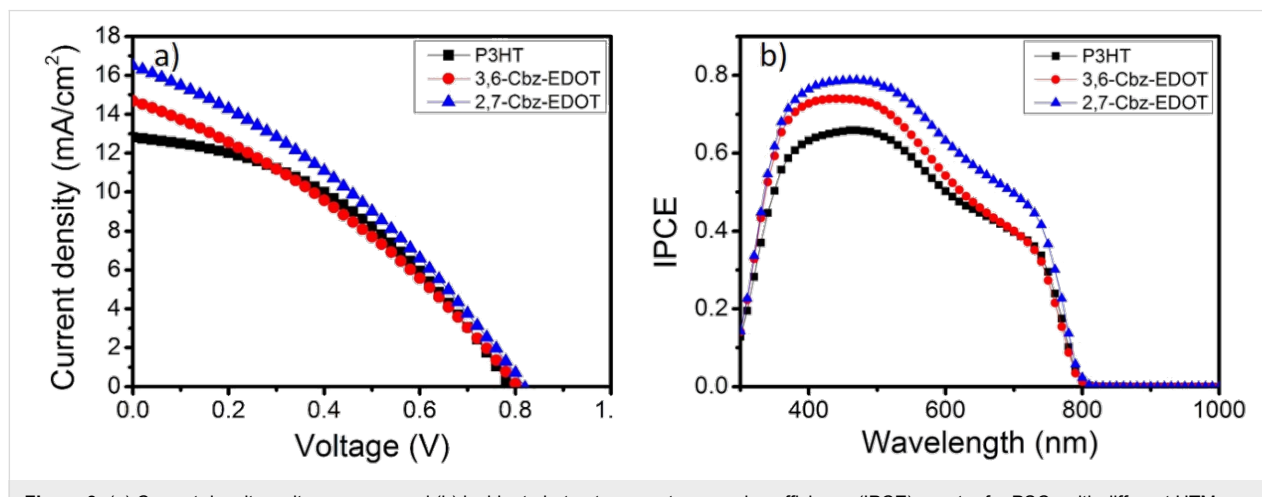


**Figure 3:** (a) Current density–voltage curves and (b) incident photon to current conversion efficiency (IPCE) spectra for PSCs with different HTMs under AM1.5G illumination at 100 mW cm<sup>-2</sup>.

Table 2. Among the three devices, the device based on 2,7-Cbz-EDOT displayed the highest power conversion efficiency (PCE) of 4.47% with a short-circuit current density ( $J_{SC}$ ) of  $16.5 \text{ mA cm}^{-2}$ , open circuit voltage ( $V_{OC}$ ) of 0.81 V, and fill factor (FF) of 0.33. The lower PCE (3.90%) of the device based on 3,6-Cbz-EDOT was mainly due to the lower  $J_{SC}$  ( $14.7 \text{ mA cm}^{-2}$ ), which would be reflected in the absorption range and hole mobility of the HTMs [43]. In addition, it was postulated that the deeper HOMO level of 2,7-Cbz-EDOT facilitated the hole extraction from the valence band of the perovskite layer [44]. Moreover, it should be noted that 2,7-Cbz-EDOT outperforms the benchmark p-type semiconducting polymer, P3HT, despite almost the same HOMO levels.

The incident photon to current conversion efficiency (IPCE) spectra of the three devices were measured (Figure 3b). The perovskite nanocrystals strongly absorbed light over the entire visible range, and accordingly, the IPCE spectral shapes of all the devices were almost identical. This result indicates that light absorption by the hole-transporting polymers does not significantly contribute to the photocurrent generation and the main role of the polymers is hole transport. The peak intensities of the IPCE spectra obtained from the devices based on 3,6-Cbz-EDOT and 2,7-Cbz-EDOT exceeded 0.70 in the wavelength range of 380–510 nm. This value is apparently higher than that of the device based on P3HT with the maximum IPCE peak intensity of 0.66 at 470 nm, as supported by the  $J_{SC}$  values obtained from the  $J$ – $V$  curves. All these results strongly suggest that the Cbz-EDOT polymers are better HTMs in the PSCs as compared to P3HT.

### Dynamic impedance spectroscopy

Dynamic impedance spectroscopy was used to determine the charge-transporting parameters in the PSCs, such as the chemical capacitance, recombination resistance, and charge conductivity [45]. It is known that the performance metrics of the HTMs in the PSCs can be partially explained by these parameters. For example, it was suggested that FF is associated with the series resistance ( $R_s$ ), and a low  $R_s$  is required to construct high performance photovoltaic devices [46]. The dynamic impedance spectra of the PSCs with different HTMs over the

frequency range of 1 Hz to 1 MHz are shown in Figure 4, and the  $R_s$  values are listed in Table 2. It was found that the order of  $R_s$  is  $R_s(\text{P3HT}) < R_s(\text{2,7-Cbz-EDOT}) < R_s(\text{3,6-Cbz-EDOT})$ , which is in good agreement with the inverse order of the FFs of the corresponding PSCs (vide supra).

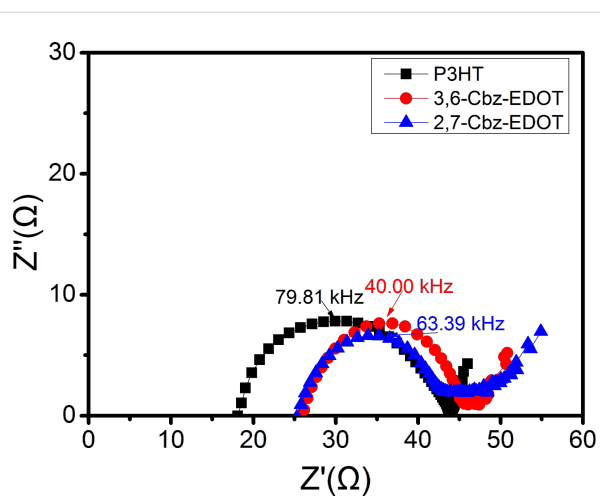


**Figure 4:** Impedance spectroscopy characterization of the PSCs with different HTMs over the frequency range from 1 Hz to 1 MHz at 0 V bias voltage under simulated AM1.5G illumination ( $100 \text{ mW cm}^{-2}$ ).

On the other hand, the effective carrier lifetime or time constant ( $\tau$ ) is related to the recombination of an electron and a hole at the interfaces between the perovskite and  $\text{TiO}_2$  or hole-transporting layers. This parameter can be calculated according to Equation 2 [47]:

$$\tau = 1 / (2\pi f) \quad (2)$$

where  $f$  is the maximum frequency derived from the semicircle of the impedance spectra, also known as the character frequency. The calculated  $\tau$  values are listed in Table 2. The device based on 3,6-Cbz-EDOT displayed the longest lifetime of  $3.98 \mu\text{s}$ , which is almost twice as high as that of the device based on P3HT. This result can be explained by the LUMO levels of the HTMs [48]. Since 3,6-Cbz-EDOT has the highest LUMO level of  $-2.50 \text{ eV}$ , the electron-blocking ability of this

**Table 2:** Photovoltaic parameters of PSCs based on 3,6-Cbz-EDOT, 2,7-Cbz-EDOT, and P3HT.

HTM	$J_{SC}$ ( $\text{mA/cm}^2$ ) <sup>a</sup>	$V_{OC}$ (V) <sup>a</sup>	FF <sup>a</sup>	PCE (%) <sup>a</sup>	$R_s$ ( $\Omega$ ) <sup>b</sup>	$\tau$ ( $\mu\text{s}$ ) <sup>b</sup>
3,6-Cbz-EDOT	14.7	0.80	0.32	3.90	26.51	3.98
2,7-Cbz-EDOT	16.5	0.81	0.33	4.47	25.98	2.51
P3HT	12.8	0.79	0.41	4.14	17.94	1.99

<sup>a</sup>Average values from 10 devices with the sample area of  $0.75 \text{ cm}^2$  under illumination of  $100 \text{ mW cm}^{-2}$ . <sup>b</sup>Average values from 10 devices with the DC potential of 0 V, AC amplitude of 10 mV, and frequency of 1 Hz to 1 MHz under illumination of  $100 \text{ mW cm}^{-2}$ .

hole-transporting layer is more significant than the other two polymer layers. There is indeed a clear correlation between the  $\tau$  values of the devices and the LUMO levels of the HTMs.

## Conclusion

In summary, highly electron-rich donor–donor type polymers with the different carbazole connectivity patterns, i.e., 3,6-Cbz-EDOT and 2,7-Cbz-EDOT, were synthesized by the Pd-catalyzed Stille polycondensation. The HOMO/LUMO energy levels of these polymers were determined from the onset oxidation potentials and optical band gaps. Similar to the reported carbazole-based semiconducting polymers, 3,6-Cbz-EDOT had higher energy levels than 2,7-Cbz-EDOT. These Cbz-EDOT polymers were applied to the hole-transporting layer of PSCs, and the photovoltaic properties were investigated in comparison to that based on P3HT. The 2,7-Cbz-EDOT based device showed the higher PCE of 4.47% as compared to those based on 3,6-Cbz-EDOT and also P3HT. This was due to the deeper HOMO level and higher hole mobility, suggesting the importance of the molecular design regarding the carbazole connectivity. In addition, the IPCE spectra suggested the higher photocurrent generation of the device based on 2,7-Cbz-EDOT, which is associated with the  $J_{SC}$ . Furthermore, the impedance spectroscopy characterization revealed that the carrier recombination of the devices based on the Cbz-EDOT polymers is effectively suppressed due to the prolonged carrier lifetime. It is worth noting that there is still a room for improvement of the carrier mobility and lifetime by the increase in the molecular weights of these polymers. Overall, the Cbz-EDOT polymers, especially 2,7-Cbz-EDOT, are solution-processable promising HTMs of the PSCs.

## Experimental

### Materials

3,6-Dibromo-9-(2-ethylhexyl)carbazole [49] and 2,7-dibromo-9-(2-ethylhexyl)carbazole [27] were prepared according to the reported literature procedure. Commercially available solvents and reagents were used without further purification unless stated otherwise. P3HT (regioregular) was purchased from Aldrich.

## Synthesis

### Synthesis of 9-(2-ethylhexyl)-3,6-bis(*tri-n*-butylstannyly)carbazole (**1**)

To a solution of 3,6-dibromo-9-(2-ethylhexyl)carbazole (0.360 g, 0.800 mmol) in THF (10 mL), *n*-butyllithium (1.6 M, 1.20 mL) in THF was added dropwise at  $-78^{\circ}\text{C}$  under Ar. After stirring for 30 min, 0.88 mL of chlorotributyltin (1.04 g, 2.00 mmol) were injected by a syringe. Then, the mixture was warmed to  $0^{\circ}\text{C}$  and stirred at this temperature for 30 min. After the mixture was further warmed and stirred at room tempera-

ture overnight, water was added and the organic layer was extracted with  $\text{CH}_2\text{Cl}_2$  (3 times). The combined organic layer was dried over  $\text{MgSO}_4$ . After filtration, the solvent was removed under reduced pressure and the crude product was purified by column chromatography ( $\text{SiO}_2$ ,  $\text{CHCl}_3$ ), yielding the desired product **1** (0.338 g, 48%).  $^1\text{H}$  NMR (300 MHz,  $\text{CDCl}_3$ )  $\delta$  8.22 (s, 2H), 7.55 (d,  $J = 7.9$  Hz, 2H), 7.42 (d,  $J = 8.0$  Hz, 2H), 4.17 (dd,  $J = 7.2, 3.8$  Hz, 2H), 2.10 (s, 1H), 1.64 (d,  $J = 7.6$  Hz, 12H), 1.42 (dd,  $J = 14.6, 7.3$  Hz, 21H), 1.26–1.09 (m, 12H), 0.95 ppm (dd,  $J = 8.4, 6.2$  Hz, 25H);  $^{13}\text{C}$  NMR (75 MHz,  $\text{CDCl}_3$ )  $\delta$  140.85, 133.09, 129.25, 128.03, 122.81, 108.78, 47.15, 39.37, 30.86, 29.07, 28.74, 27.71, 27.32, 26.96, 26.73, 24.27, 22.96, 17.37, 13.94, 13.58, 13.48, 10.75, 9.59 ppm; FTIR (neat) v: 2955, 2923, 2852, 2361, 1798, 1652, 1614, 1581, 1462, 1419, 1376, 1342, 1276, 1258, 1218, 1143, 1063, 1014, 961, 867, 794, 749, 698, 679, 654, 624, 607  $\text{cm}^{-1}$ ; MALDI–TOF MS ( $M_w = 859.4$ ):  $m/z = 860.7$  ( $[\text{M} + \text{H}]^+$ ).

### Synthesis of 9-(2-ethylhexyl)-2,7-bis(*tri-n*-butylstannyly)carbazole (**2**)

To a solution of 2,7-dibromo-9-(2-ethylhexyl)carbazole (0.437 g, 1.00 mmol) in THF (10 mL), *n*-butyllithium (1.6 M, 1.50 mL) in THF was added dropwise at  $-78^{\circ}\text{C}$  under Ar. After stirring for 30 min, 1.10 mL of chlorotributyltin (1.30 g, 2.50 mmol) was injected by a syringe. Then, the mixture was warmed to  $0^{\circ}\text{C}$  and stirred at this temperature for 30 min. After the mixture was further warmed and stirred at room temperature overnight, water was added and the organic layer was extracted with  $\text{CH}_2\text{Cl}_2$  (3 times). The combined organic layer was dried over  $\text{MgSO}_4$ . After filtration, the solvent was removed under reduced pressure and the crude product was purified by column chromatography ( $\text{SiO}_2$ ,  $\text{CHCl}_3$ ), yielding the desired product **2** (0.407 g, 46%).  $^1\text{H}$  NMR (300 MHz,  $\text{CDCl}_3$ )  $\delta$  8.05 (d,  $J = 7.5$  Hz, 2H), 7.48 (s, 2H), 7.28 (d,  $J = 7.6$  Hz, 2H), 4.18 (d,  $J = 6.5$  Hz, 2H), 2.05 (s, 1H), 1.76–1.49 (m, 12H), 1.36 (dd,  $J = 14.7, 7.3$  Hz, 21H), 1.12 (dd,  $J = 9.6, 6.7$  Hz, 12H), 0.89 ppm (dd,  $J = 9.2, 5.3$  Hz, 25H);  $^{13}\text{C}$  NMR (75 MHz,  $\text{CDCl}_3$ )  $\delta$  140.90, 139.17, 126.57, 123.19, 119.98, 117.02, 47.31, 40.02, 31.53, 29.49, 27.73, 24.82, 23.38, 14.34, 14.00, 11.21, 10.08, 7.84 ppm; FTIR (neat) v: 2955, 2923, 2870, 2852, 1485, 1458, 1441, 1415, 1376, 1339, 1319, 1250, 1200, 1146, 1071, 996, 962, 911, 860, 826, 814, 794, 741, 723, 710, 695, 653, 633, 616  $\text{cm}^{-1}$ ; MALDI–TOF MS ( $M_w = 859.4$ ):  $m/z = 860.5$  ( $[\text{M} + \text{H}]^+$ ).

### Synthesis of 3,6-Cbz-EDOT

Analogously to the description in [50], a solution of **1** (0.337 g, 0.400 mmol) and 2,5-dibromo-3,4-ethylenedioxythiophene (0.117 g, 0.400 mmol) in toluene (5 mL) was degassed with nitrogen for 15 min.  $\text{Pd}_2(\text{dba})_3$  (0.010 g, 0.011 mmol) and  $\text{P}(o\text{-tolyl})_3$  (0.015 g, 0.049 mmol) were added. The reaction

mixture was further degassed and then heated to 110 °C for 48 h. After cooling to room temperature, the mixture was poured into methanol. The precipitate was collected and washed with methanol and hexane. The precipitate was subsequently subjected to Soxhlet extraction with chloroform. The solvent was removed under reduced pressure, yielding 3,6-Cbz-EDOT (0.10 g, 60%). GPC (THF):  $M_n = 2.0 \text{ kg mol}^{-1}$ ,  $M_w/M_n = 1.5$ ;  $^1\text{H}$  NMR (300 MHz,  $\text{CDCl}_3$ )  $\delta$  8.50–8.37 (br, Ar-H), 8.00–7.73 (br, Ar-H), 7.54–7.07 (br, Ar-H), 4.64–4.24 (br,  $\text{CH}_2$ ), 4.24–3.85 (br,  $\text{OCH}_2$ ), 2.04 (br, CH), 1.50–1.16 (br,  $\text{CH}_2$ ), 1.01–0.70 ppm (br,  $\text{CH}_3$ ); FTIR (neat) v: 2955, 2921, 2852, 1581, 1463, 1419, 1375, 1341, 1276, 1258, 1219, 1142, 1063, 1015, 961, 868, 795, 749, 699, 653, 625, 607  $\text{cm}^{-1}$ .

### Synthesis of 2,7-Cbz-EDOT

Analogously to the description in [50], a solution of **2** (0.392 g, 0.450 mmol) and 2,5-dibromo-3,4-ethylenedioxythiophene (0.136 g, 0.450 mmol) in toluene (5 mL) was degassed with nitrogen for 15 min.  $\text{Pd}_2(\text{dba})_3$  (0.010 g, 0.011 mmol) and  $\text{P}(o\text{-tolyl})_3$  (0.015 g, 0.049 mmol) were added. The reaction mixture was further degassed and then heated to 110 °C for 48 h. After cooling to room temperature, the mixture was poured into methanol. The precipitate was collected and washed with methanol and hexane. The precipitate was subsequently subjected to Soxhlet extraction with chloroform. The solvent was removed under reduced pressure, yielding 2,7-Cbz-EDOT (0.13 g, 78%). GPC (THF):  $M_n = 3.0 \text{ kg mol}^{-1}$ ,  $M_w/M_n = 1.4$ ;  $^1\text{H}$  NMR (300 MHz,  $\text{CDCl}_3$ )  $\delta$  8.22–7.97 (br, Ar-H), 7.97–7.79 (br, Ar-H), 7.74–7.47 (br, Ar-H), 4.47 (br,  $\text{CH}_2$ ), 4.35–3.92 (br,  $\text{OCH}_2$ ), 2.14 (br, CH), 1.62–1.17 (br,  $\text{CH}_2$ ), 1.12–0.67 ppm (br,  $\text{CH}_3$ ); FTIR (neat) v: 2955, 2925, 2870, 1599, 1558, 1482, 1455, 1428, 1361, 1332, 1252, 1216, 1196, 1168, 1120, 1088, 997, 935, 906, 860, 801, 727, 720, 700, 675, 649, 633, 625, 618  $\text{cm}^{-1}$ .

### General measurements

$^1\text{H}$  NMR and  $^{13}\text{C}$  NMR spectra were measured on a JEOL model AL300 spectrometer at 20 °C. Chemical shifts are reported in ppm downfield from  $\text{SiMe}_4$ , using the solvent's residual signal as an internal reference. Fourier transform infrared (FTIR) spectra were recorded on a JASCO FT/IR-4100 spectrometer in the range from 4000 to 600  $\text{cm}^{-1}$ . MALDI-TOF mass spectra were measured on a Shimadzu/Kratos AXIMA-CFR mass spectrometer equipped with nitrogen laser ( $\lambda = 337 \text{ nm}$ ) and pulsed ion extraction, which was operated in a linear-positive ion mode at an accelerating potential of 20 kV. Dichloromethane solutions containing 1 g  $\text{L}^{-1}$  of a sample, 10 g  $\text{L}^{-1}$  of dithranol, and 1 g  $\text{L}^{-1}$  of sodium trifluoroacetate were mixed at the ratio of 1:1:1, and 1 mL aliquot of this mixture was deposited onto a sample target plate. Gel permeation chromatography (GPC) was measured on a JASCO

GULLIVER 1500 equipped with a pump (PU-2080 Plus), an absorbance detector (RI-2031 Plus), and two Shodex GPC KF-803 columns (8.0 mm I.D.  $\times$  300 mm L) based on a conventional calibration curve using polystyrene standards. Tetrahydrofuran (40 °C) was used as a carrier solvent at the flow rate of 1.0  $\text{mL min}^{-1}$ . UV-vis absorption spectra were measured on a JASCO V-670 spectrophotometer. Polymer thin films were prepared on an ITO glass (about  $0.8 \times 2.5 \text{ cm}^2$ ) by spray-coating of polymer solutions (5.0 g  $\text{L}^{-1}$  in  $\text{CH}_2\text{Cl}_2$ ). Electrochemistry measurements were carried out on a BAS electrochemical analyzer model 612C at 25 °C in dehydrated  $\text{CH}_3\text{CN}$  containing 0.1 M  $(n\text{-C}_4\text{H}_9)_4\text{NPF}_6$  in the three electrode cell. The working, reference, and auxiliary electrodes were a glassy carbon electrode,  $\text{Ag}/\text{Ag}^+/\text{CH}_3\text{CN}/(n\text{-C}_4\text{H}_9)_4\text{NPF}_6$ , and a Pt wire, respectively.

### Fabrication and measurements of perovskite solar cells

Fluorine-doped tin oxide (FTO)-coated glass substrates ( $20 \Omega$  per square) were patterned to fabricate the solar cells. These substrates were successively washed by ultrasonication in water, acetone, and isopropyl alcohol for 10 min each, and then dried in a stream of dry air. The washed substrates were further treated with a UV- $\text{O}_3$  cleaner (Filgen, Model UV253E) for 20 min. The electron-accepting  $\text{TiO}_2$  compact layer was spin-coated (1500 rpm for 30 s) from a mildly acidic (after addition of 12  $\mu\text{M}$  HCl) solution of titanium(IV) isopropoxide in anhydrous ethanol and sintered at 120 °C for 10 s. The mesoporous  $\text{TiO}_2$  layer composed of 20 nm-sized particles was deposited by spin-coating at 4000 rpm for 30 s using a commercial  $\text{TiO}_2$  paste (PST-18NR, JGC Catalysts and Chemicals Ltd.) diluted in ethanol (2:7, weight ratio). After drying at 120 °C, the  $\text{TiO}_2$  films were gradually heated to 500 °C, baked at this temperature for 20 min, and cooled to room temperature. The mesoporous  $\text{TiO}_2$  films were infiltrated with  $\text{PbI}_2$  by spin-coating a  $\text{PbI}_2$  solution in DMF (465 g  $\text{L}^{-1}$ ) at 80 °C. After drying, the films were dipped in a solution of  $\text{CH}_3\text{NH}_3\text{I}$  in 2-propanol (10 g  $\text{L}^{-1}$ ) for 20 s and rinsed with 2-propanol. After drying, the hole transporting materials were deposited by spin-coating a solution of P3HT, 3,6-Cbz-EDOT, or 2,7-Cbz-EDOT in chlorobenzene (7.82 g  $\text{L}^{-1}$ ). All hole-transporting layers were dried in the dark. The thickness of the hole-transporting layers was about 30 nm. Finally, gold (80 nm) was thermally evaporated on the top of the device to form the back contact.

The current density–voltage ( $J$ – $V$ ) characteristics, incident photon current efficiency (IPCE), and dynamic impedance spectroscopy of the fabricated perovskite solar cells were evaluated. The active area of the devices was  $0.75 \text{ cm}^2$ . The  $J$ – $V$  curves were measured on a CEP-2000RS (Bunko-Keiki Co., Ltd.) under illumination of a solar simulator with a light intensity of

100 mW cm<sup>-2</sup> (AM1.5). IPCE measurements were carried out using a Xenon lamp attached to a monochromator. Two focusing lenses were used to focus the monochromatic light to the active area of solar cells. Dynamic impedance spectroscopy was measured on an SI1260 Impedance/Gain-Phase Analyzer and SI1286 Electrochemical Interface (Solartron) at 0 V bias voltage and a frequency range from 1 Hz and 1 MHz with an AC amplitude of 10 mA under illumination of simulated solar AM1.5 global light at 100 mW cm<sup>-2</sup>. A Z-View Analyst software was used to model the Nyquist plots obtained from the impedance measurements.

## Supporting Information

### Supporting Information File 1

Synthesis of carbazole derivatives, <sup>1</sup>H NMR and IR spectra of the polymers, and OFET performances.

[<http://www.beilstein-journals.org/bjoc/content/supplementary/1860-5397-12-134-S1.pdf>]

## Acknowledgements

This work was supported by JSPS KAKENHI (Grant Number 26620173), Kurata Memorial Hitachi Science and Technology Foundation, Tokuyama Science Foundation, and the Support for Toyotech Advanced Researchers (T.M.) and the Tochigi Industrial Promotion Center (T.K.).

## References

- Kojima, A.; Teshima, K.; Shirai, Y.; Miyasaka, T. *J. Am. Chem. Soc.* **2009**, *131*, 6050–6051. doi:10.1021/ja809598r
- Liu, M.; Johnston, M. B.; Snaith, H. J. *Nature* **2013**, *501*, 395–398. doi:10.1038/nature12509
- Zhou, H.; Chen, Q.; Li, G.; Luo, S.; Song, T.-b.; Duan, H.-S.; Hong, Z.; You, J.; Liu, Y.; Yang, Y. *Science* **2014**, *345*, 542–546. doi:10.1126/science.1254050
- Rakstys, K.; Abate, A.; Dar, M. I.; Gao, P.; Jankauskas, V.; Jacopin, G.; Kamarauskas, E.; Kazim, S.; Ahmad, S.; Grätzel, M.; Nazeeruddin, M. K. *J. Am. Chem. Soc.* **2015**, *137*, 16172–16178. doi:10.1021/jacs.5b11076
- Huang, C.; Fu, W.; Li, C.-Z.; Zhang, Z.; Qiu, W.; Shi, M.; Heremans, P.; Jen, A. K.-Y.; Chen, H. *J. Am. Chem. Soc.* **2016**, *138*, 2528–2531. doi:10.1021/jacs.6b00039
- Jeon, N. J.; Lee, J.; Noh, J. H.; Nazeeruddin, M. K.; Grätzel, M.; Seok, S. I. *J. Am. Chem. Soc.* **2013**, *135*, 19087–19090. doi:10.1021/ja410659k
- Bi, D.; Yang, L.; Boschloo, G.; Hagfeldt, A.; Johansson, E. M. J. *J. Phys. Chem. Lett.* **2013**, *4*, 1532–1536. doi:10.1021/jz400638x
- Margulis, G. Y.; Christoforo, M. G.; Lam, D.; Bailey, Z. M.; Bowring, A. R.; Bailie, C. D.; Salleo, A.; McGehee, M. D. *Adv. Energy Mater.* **2013**, *3*, 1657–1663. doi:10.1002/aenm.201300660
- Jeon, N. J.; Lee, H. G.; Kim, Y. C.; Seo, J.; Noh, J. H.; Lee, J.; Seok, S. I. *J. Am. Chem. Soc.* **2014**, *136*, 7837–7840. doi:10.1021/ja502824c
- Liu, J.; Pathak, S.; Stergiopoulos, T.; Leijtens, T.; Wojciechowski, K.; Schumann, S.; Kausch-Busies, N.; Snaith, H. J. *J. Phys. Chem. Lett.* **2015**, *6*, 1666–1673. doi:10.1021/acs.jpclett.5b00545
- Di Giacomo, F.; Razza, S.; Matteocci, F.; D'Epifanio, A.; Licoccia, S.; Brown, T. M.; Di Carlo, A. *J. Power Sources* **2014**, *251*, 152–156. doi:10.1016/j.jpowsour.2013.11.053
- Kwon, Y. S.; Lim, J.; Yun, H.-J.; Kim, Y.-H.; Park, T. *Energy Environ. Sci.* **2014**, *7*, 1454–1460. doi:10.1039/c3ee44174a
- Ryu, S.; Noh, J. H.; Jeon, N. J.; Kim, Y. C.; Yang, W. S.; Seo, J.; Seok, S. I. *Energy Environ. Sci.* **2014**, *7*, 2614–2618. doi:10.1039/C4EE00762J
- Grazulevicius, J. V.; Strohriegel, P.; Pielichowski, J.; Pielichowski, K. *Prog. Polym. Sci.* **2003**, *28*, 1297–1353. doi:10.1016/S0079-6700(03)00036-4
- Morin, J.-F.; Leclerc, M.; Adès, D.; Siove, A. *Macromol. Rapid Commun.* **2005**, *26*, 761–778. doi:10.1002/marc.200500096
- Blouin, N.; Leclerc, M. *Acc. Chem. Res.* **2008**, *41*, 1110–1119. doi:10.1021/ar800057k
- Li, J.; Grimsdale, A. C. *Chem. Soc. Rev.* **2010**, *39*, 2399–2410. doi:10.1039/b915995a
- Beaupré, S.; Boudreault, P.-L. T.; Leclerc, M. *Adv. Mater.* **2010**, *22*, E6–E27. doi:10.1002/adma.200903484
- Boudreault, P.-L. T.; Beaupré, S.; Leclerc, M. *Polym. Chem.* **2010**, *1*, 127–136. doi:10.1039/B9PY00236G
- Wong, W.-Y.; Harvey, R. D. *Macromol. Rapid Commun.* **2010**, *31*, 671–713. doi:10.1002/marc.200900690
- Beaupré, S.; Leclerc, M. *J. Mater. Chem. A* **2013**, *1*, 11097–11105. doi:10.1039/c3ta12420g
- Tao, X.-T.; Zhang, Y.-D.; Wada, T.; Sasabe, H.; Suzuki, H.; Watanabe, T.; Miyata, S. *Adv. Mater.* **1998**, *10*, 226–230. doi:10.1002/(SICI)1521-4095(199802)10:3<226::AID-ADMA226>3.0.C0;2-E
- Michinobu, T.; Okoshi, K.; Osako, H.; Kumazawa, H.; Shigehara, K. *Polymer* **2008**, *49*, 192–199. doi:10.1016/j.polymer.2007.11.022
- Cai, B.; Xing, Y.; Yang, Z.; Zhang, W.-H.; Qiu, J. *Energy Environ. Sci.* **2013**, *6*, 1480–1485. doi:10.1039/c3ee40343b
- Dumur, F. *Org. Electron.* **2015**, *25*, 345–361. doi:10.1016/j.orgel.2015.07.007
- Morin, J.-F.; Leclerc, M. *Macromolecules* **2001**, *34*, 4680–4682. doi:10.1021/ma010152u
- Dierschke, F.; Grimsdale, A. C.; Müllen, K. *Synthesis* **2003**, 2470–2472. doi:10.1055/s-2003-42418
- Blouin, N.; Michaud, A.; Wakim, S.; Boudreault, P.-L. T.; Leclerc, M.; Vercelli, B.; Zecchin, S.; Zotti, G. *Macromol. Chem. Phys.* **2006**, *207*, 166–174. doi:10.1002/macp.200500423
- Leclerc, N.; Michaud, A.; Sirois, K.; Morin, J.-F.; Leclerc, M. *Adv. Funct. Mater.* **2006**, *16*, 1694–1704. doi:10.1002/adfm.200600171
- Blouin, N.; Michaud, A.; Gendron, D.; Wakim, S.; Blair, E.; Neagu-Plesu, R.; Belletête, M.; Durocher, G.; Tao, Y.; Leclerc, M. *J. Am. Chem. Soc.* **2008**, *130*, 732–742. doi:10.1021/ja0771989
- Aïch, R. B.; Blouin, N.; Bouchard, A.; Leclerc, M. *Chem. Mater.* **2009**, *21*, 751–757. doi:10.1021/cm8031175
- Michinobu, T.; Kumazawa, H.; Otsuki, E.; Usui, H.; Shigehara, K. *J. Polym. Sci., Part A: Polym. Chem.* **2009**, *47*, 3880–3891. doi:10.1002/pola.23454
- Ma, Z.; Chen, L.; Ding, J.; Wang, L.; Jing, X.; Wang, F. *Adv. Mater.* **2011**, *23*, 3726–3729. doi:10.1002/adma.201102140

34. Hahm, S. G.; Lee, T. J.; Kim, D. M.; Kwon, W.; Ko, Y.-G.; Michinobu, T.; Ree, M. *J. Phys. Chem. C* **2011**, *115*, 21954–21962. doi:10.1021/jp207211e

35. Lombeck, F.; Komber, H.; Sepe, A.; Friend, R. H.; Sommer, M. *Macromolecules* **2015**, *48*, 7851–7860. doi:10.1021/acs.macromol.5b01845

36. Berns, B.; Tieke, B. *Polym. Chem.* **2015**, *6*, 4887–4901. doi:10.1039/C5PY00713E

37. Li, W.; Michinobu, T. *Polym. Chem.* **2016**, *7*, 3165–3171. doi:10.1039/C6PY00381H  
Note that 3, 6-Cbz-EDOT was previously synthesized by direct arylation polycondensation.

38. Bucinskas, A.; Bagdziunas, G.; Tomkeviciene, A.; Volynuk, D.; Kostiv, N.; Gudeika, D.; Jankauskas, V.; Rutkis, M.; Grazulevicius, J. V. *RSC Adv.* **2015**, *5*, 49577–49589. doi:10.1039/C5RA09161F

39. Zhu, Z.; Bai, Y.; Lee, H. K. H.; Mu, C.; Zhang, T.; Zhang, L.; Wang, J.; Yan, H.; So, S. K.; Yang, S. *Adv. Funct. Mater.* **2014**, *24*, 7357–7365. doi:10.1002/adfm.201401557

40. Cho, S.; Seo, J. H.; Park, S. H.; Beaupré, S.; Leclerc, M.; Heeger, A. J. *Adv. Mater.* **2010**, *22*, 1253–1257. doi:10.1002/adma.200903420

41. Huang, C.; Sartin, M. M.; Cozzuol, M.; Siegel, N.; Barlow, S.; Perry, J. W.; Marder, S. R. *J. Phys. Chem. A* **2012**, *116*, 4305–4317. doi:10.1021/jp3006712

42. Kim, J. Y.; Kim, S. H.; Lee, H.-H.; Lee, K.; Ma, W.; Gong, X.; Heeger, A. J. *Adv. Mater.* **2006**, *18*, 572–576. doi:10.1002/adma.200501825

43. Dubey, A.; Adhikari, N.; Venkatesan, S.; Gu, S.; Khatiwada, D.; Wang, Q.; Mohammad, L.; Kumar, M.; Qiao, Q. *Sol. Energy Mater. Sol. Cells* **2016**, *145*, 193–199. doi:10.1016/j.solmat.2015.10.008

44. Chen, W.; Bao, X.; Zhu, Q.; Zhu, D.; Qiu, M.; Sun, M.; Yang, R. *J. Mater. Chem. C* **2015**, *3*, 10070–10073. doi:10.1039/C5TC01856K

45. Bisquert, J.; Bertoluzzi, L.; Mora-Sero, I.; Garcia-Belmonte, G. *J. Phys. Chem. C* **2014**, *118*, 18983–18991. doi:10.1021/jp5062144

46. Juarez-Perez, E. J.; Wußler, M.; Fabregat-Santiago, F.; Lakus-Wollny, K.; Mankel, E.; Mayer, T.; Jaegermann, W.; Mora-Sero, I. *J. Phys. Chem. Lett.* **2014**, *5*, 680–685. doi:10.1021/jz500059v

47. Zhang, J.; Hu, Z.; Huang, L.; Yue, G.; Liu, J.; Lu, X.; Hu, Z.; Shang, M.; Han, L.; Zhu, Y. *Chem. Commun.* **2015**, *51*, 7047–7050. doi:10.1039/C5CC00128E

48. Xiao, Y.; Han, G.; Wu, J.; Lin, J.-Y. *J. Power Sources* **2016**, *306*, 171–177. doi:10.1016/j.jpowsour.2015.12.003

49. Jung, S.-H.; Kim, H. K.; Kim, S.-H.; Kim, Y. H.; Jeoung, S. C.; Kim, D. *Macromolecules* **2000**, *33*, 9277–9288. doi:10.1021/ma0003248

50. Li, W.; Michinobu, T. *Macromol. Chem. Phys.* **2016**, *217*, 863–870. doi:10.1002/macp.201500494

## License and Terms

This is an Open Access article under the terms of the Creative Commons Attribution License (<http://creativecommons.org/licenses/by/2.0>), which permits unrestricted use, distribution, and reproduction in any medium, provided the original work is properly cited.

The license is subject to the *Beilstein Journal of Organic Chemistry* terms and conditions: (<http://www.beilstein-journals.org/bjoc>)

The definitive version of this article is the electronic one which can be found at:  
doi:10.3762/bjoc.12.134



# Star-shaped and linear $\pi$ -conjugated oligomers consisting of a tetrathienoanthracene core and multiple diketopyrrolopyrrole arms for organic solar cells

Hideaki Komiya<sup>\*1,2</sup>, Chihaya Adachi<sup>1,3</sup> and Takuma Yasuda<sup>\*2</sup>

## Full Research Paper

Open Access

Address:

<sup>1</sup>International Institute for Carbon Neutral Energy Research (WPI-I2CNER), Kyushu University, 744 Motooka, Nishi-ku, Fukuoka 819-0395, Japan, <sup>2</sup>INAMORI Frontier Research Center (IFRC), Kyushu University and <sup>3</sup>Center for Organic Photonics and Electronics Research (OPERA), Kyushu University

*Beilstein J. Org. Chem.* **2016**, *12*, 1459–1466.

doi:10.3762/bjoc.12.142

Received: 18 April 2016

Accepted: 01 July 2016

Published: 14 July 2016

Email:

Hideaki Komiya<sup>\*</sup> - komiyama@ifrc.kyushu-u.ac.jp;  
Takuma Yasuda<sup>\*</sup> - yasuda@ifrc.kyushu-u.ac.jp

This article is part of the Thematic Series "Organic photovoltaics".

Guest Editor: D. J. Jones

\* Corresponding author

© 2016 Komiya et al.; licensee Beilstein-Institut.

License and terms: see end of document.

Keywords:

bulk heterojunction; diketopyrrolopyrrole; organic solar cells; star-shaped oligomers; tetrathienoanthracene

## Abstract

Solution-processable star-shaped and linear  $\pi$ -conjugated oligomers consisting of an electron-donating tetrathienoanthracene (TTA) core and electron-accepting diketopyrrolopyrrole (DPP) arms, namely, TTA-DPP4 and TTA-DPP2, were designed and synthesized. Based on density functional theory calculations, the star-shaped TTA-DPP4 has a larger oscillator strength than the linear TTA-DPP2, and consequently, better photoabsorption property over a wide range of visible wavelengths. The photovoltaic properties of organic solar cells based on TTA-DPP4 and TTA-DPP2 with a fullerene derivative were evaluated by varying the thickness of the bulk heterojunction active layer. As a result of the enhanced visible absorption properties of the star-shaped  $\pi$ -conjugated structure, better photovoltaic performances were obtained with relatively thin active layers (40–60 nm).

## Introduction

Solution-processable organic semiconductors have been intensively studied as key materials for low-cost, flexible, and large-area optoelectronic devices, including organic solar cells (OSCs) [1–4]. OSCs have drawn much attention as promising next-generation renewable energy sources because abundant sun-light energy can be directly converted into electricity. Recently, the power conversion efficiencies (PCEs) of OSCs based on small molecules with bulk heterojunction (BHJ) archi-

tures have rapidly increased to approximately 10% [5], approaching those of state-of-the-art polymer-based OSCs [6,7]. To produce high-performance OSCs, the donor materials are required to possess suitable frontier orbital energy levels, high carrier mobility, excellent film-forming ability, and good miscibility with a fullerene derivative as an acceptor. Moreover, strong visible light photoabsorption ability for visible light is vital for the donor materials.

Star-shaped molecules tethering multiple  $\pi$ -conjugated arms are capable of harvesting incident light effectively owing to their extended dimensionality, in comparison to their linear analogues. Star-shaped  $\pi$ -conjugated molecules consisting of hexa-*peri*-hexabenzocoronene [8–14], pyrene [15–17], and triphenylamine [18–23] central cores have been developed as donor materials for BHJ-OSCs. The design of star-shaped  $\pi$ -conjugated molecules offers possibilities for not only further enhancement of the photoabsorption ability but also for the improvement of molecular packing, solubility, and film-forming ability. However, the impact of star-shaped molecular structures on optoelectronic functionality has not been fully characterized because of the small variation in the central core units researched so far. Herein, we report the design and synthesis of a new star-shaped  $\pi$ -conjugated oligomer composed of an electron-donating tetraphienoanthracene (TTA) core coupled with multiple electron-accepting diketopyrrolopyrrole (DPP) arms, and its linear ana-

logue, TTA-DPP4 and TTA-DPP2 (Figure 1). TTA can be regarded as a promising central core unit for star-shaped  $\pi$ -conjugated oligomers, and has previously been utilized as a building block of semiconducting polymers for OSCs [24] and organic field-effect transistors [25–27]. To the best of our knowledge, however, there has been no precedent on TTA-based star-shaped and linear  $\pi$ -conjugated oligomers that can be applied to OSCs.

## Results and Discussion

### Molecular design and synthesis

To develop star-shaped and linear  $\pi$ -conjugated oligomers with acceptor–donor–acceptor electronic structures, an electron-donating TTA unit was coupled with electron-accepting diketopyrrolopyrrole (DPP)-based chromophoric units, which are well-known building blocks used in OSCs [28–31]. Such molecular structures facilitate intramolecular charge transfer,

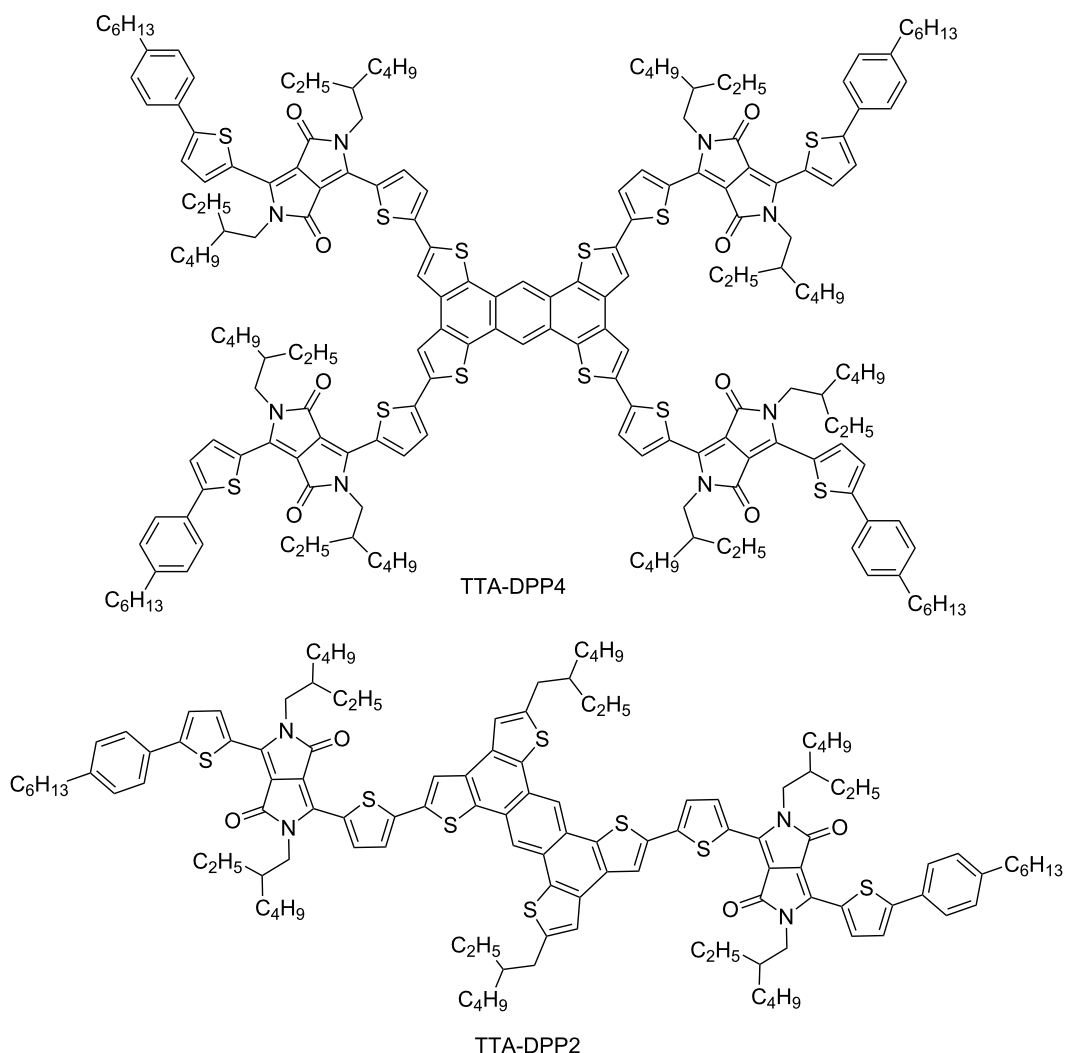


**Figure 1:** Chemical structures of TTA-DPP4 and TTA-DPP2.

rendering the molecules with narrower bandgaps, and broad and strong light absorptions. To gain insight into the geometric and electronic structures of TTA-DPP4 and TTA-DPP2, density functional theory (DFT) calculations were performed at the B3LYP/6-31G(d,p) level. The calculated energy levels and the respective frontier orbital distributions for these molecules are displayed in Figure 2. The HOMOs and LUMOs of TTA-DPP4 and TTA-DPP2 are well-expanded across the entire  $\pi$ -conjugated structure. Both molecules possess similar HOMO and LUMO energy levels of approximately  $-4.7$  and  $-2.7$  eV, respectively. The star-shaped structure has an apparent effect on its oscillator strength ( $f$ ) such that a larger  $f$  value leads to a larger absorption coefficient. Therefore, the four-armed TTA-DPP4 ( $f = 3.02$ ) is expected to show better photoabsorption ability than the two-armed TTA-DPP2 ( $f = 2.60$ ) because of the two-dimensionally extended  $\pi$ -conjugated structure.

The synthetic routes to TTA-DPP4 and TTA-DPP2 are outlined in Scheme 1 (see also Experimental section and Supporting Information File 1 for details). TTA-DPP4 and TTA-DPP2 were synthesized in 44% and 49% yields, respectively, via the palladium-catalyzed Stille cross-coupling reaction. Both TTA-DPP4 and TTA-DPP2 were soluble in common organic solvents, such as chloroform, toluene, and chlorobenzene. The thermal stability of these compounds was analyzed by thermo-

gravimetric analysis (TGA). As shown in Figure 3, the 5% weight-loss temperature of TTA-DPP4 and TTA-DPP2, under  $N_2$  atmosphere, was determined to be 378 and 380 °C, respectively, suggesting the high thermal stability for these compounds as donor materials.

## Optical properties

The UV-vis absorption spectra of TTA-DPP4 and TTA-DPP2 in chloroform solutions and as-spun thin films are depicted in Figure 4, and the corresponding photophysical data are summarized in Table 1. In chloroform solution, TTA-DPP4 and TTA-DPP2 exhibit strong and broad absorptions with two characteristic bands: a shorter-wavelength absorption (300–400 nm) arising from  $\pi$ – $\pi^*$  transitions and a longer-wavelength absorption (500–700 nm) originating from intramolecular charge transfer (ICT) transitions between the electron-donating TTA and the electron-accepting DPP units. Evidently, the maximum absorption coefficient ( $\epsilon$ ) of TTA-DPP4 ( $22.3 \times 10^4 \text{ M}^{-1} \text{ cm}^{-1}$ ) is more than twice that of TTA-DPP2 ( $9.6 \times 10^4 \text{ M}^{-1} \text{ cm}^{-1}$ ), which is consistent with the increment in the oscillator strength revealed by the DFT calculation results. The ICT absorption peaks are slightly red-shifted and broadened in the solid thin films as compared to those in the chloroform solutions, which can be ascribed to molecular aggregation in the condensed solid state. The optical band gaps of TTA-DPP4 and TTA-DPP2 are

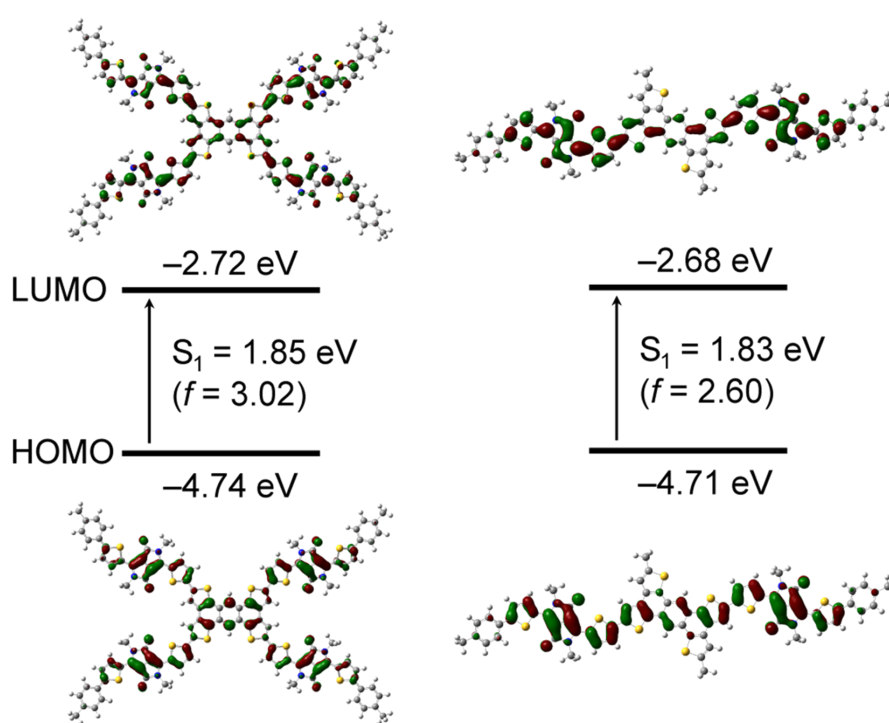
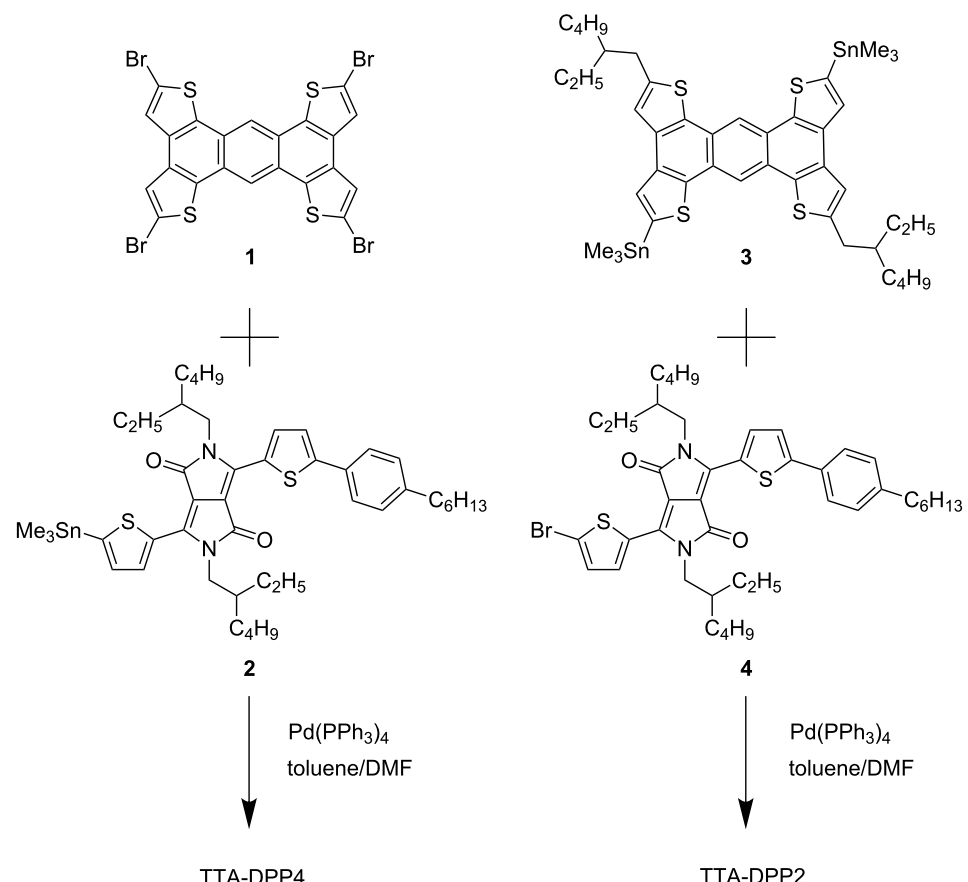


**Figure 2:** HOMO and LUMO distributions, calculated energy levels, and associated oscillator strengths ( $f$ ) for TTA-DPP4 and TTA-DPP2 calculated at the B3LYP/6-31G(d,p) level. The arrows indicate the first singlet–excited state ( $S_1$ ) transition. The alkyl chains are modified to methyl groups to simplify the calculations.



**Scheme 1:** Synthesis of TTA-DPP4 and TTA-DPP2.

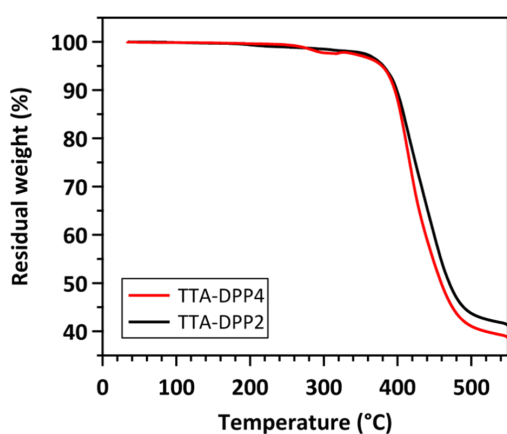


**Figure 3:** TGA curves of TTA-DPP4 and TTA-DPP2 at a heating rate of  $10\text{ }^{\circ}\text{C min}^{-1}$  under  $\text{N}_2$ .

estimated to be 1.64 and 1.65 eV, respectively, from the onset positions of their absorption bands. The absorption coefficient ( $\alpha$ ) of TTA-DPP4 ( $16.7 \times 10^4 \text{ cm}^{-1}$ ) in the thin film is still considerably larger than that of TTA-DPP2 ( $11.5 \times 10^4 \text{ cm}^{-1}$ ), indicating the enhanced photoabsorption property of the four-

armed TTA-DPP4 in the visible region. The HOMO energy levels of TTA-DPP4 and TTA-DPP2 in the thin films were determined to be  $-5.36$  and  $-5.40$  eV, respectively, via photoelectron yield spectroscopy (Figure S1 in Supporting Information File 1). The LUMO energy levels were calculated to be  $-3.72$  and  $-3.75$  eV for TTA-DPP4 and TTA-DPP2, respectively. Because of their deep-lying HOMO levels and sufficient LUMO offsets ( $>0.5$  eV), both TTA-DPP4 and TTA-DPP2 can serve as electron-donor materials in combination with [6,6]-phenyl-C<sub>71</sub>-butyric acid methyl ester (PC<sub>71</sub>BM) as an acceptor materials, which has a LUMO level of  $-4.3$  eV.

## Photovoltaic properties

The photovoltaic properties of TTA-DPP4 and TTA-DPP2 were also evaluated. BHJ-OSCs were fabricated using TTA-DPP4 and TTA-DPP2 as electron-donor materials and PC<sub>71</sub>BM as an electron-acceptor material, with an inverted device configuration of glass/ITO/ZnO/donor:PC<sub>71</sub>BM(1:1.5, w/w)/MoO<sub>3</sub>/Ag. A 30 nm thick ZnO layer was deposited on the ITO-coated glass via the sol-gel method (see Experimental section). The active layer was then spin-coated from a solution of the donor material and PC<sub>71</sub>BM in a mixed solvent of chloroform/1,8-

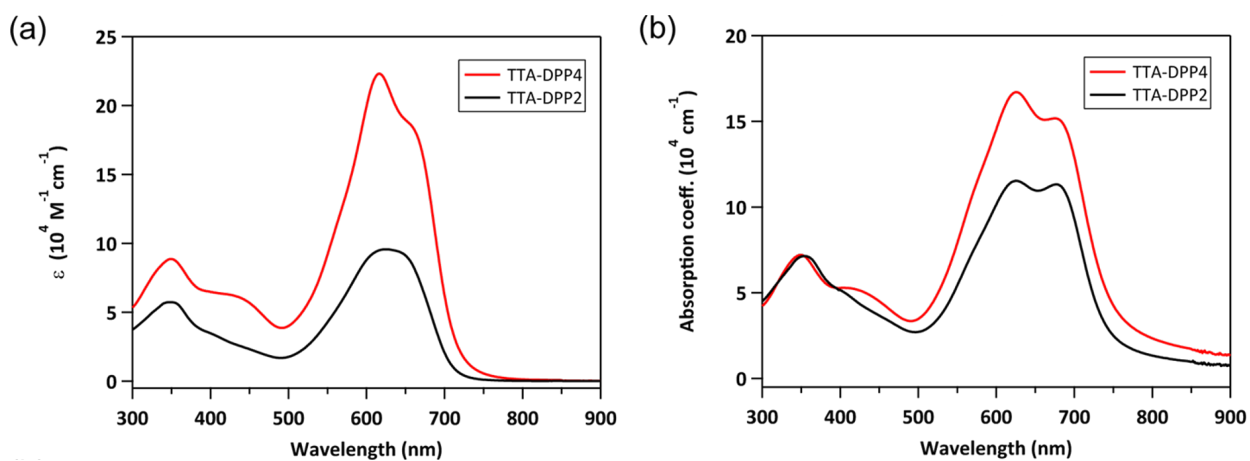


Figure 4: UV-vis absorption spectra of TTA-DPP4 (red) and TTA-DPP2 (black) in (a) chloroform solutions and (b) thin films.

Table 1: Photophysical data of TTA-based molecules.

	Solution <sup>a</sup>		Thin film <sup>b</sup>		HOMO <sup>c</sup> [eV]	LUMO <sup>d</sup> [eV]	$E_g^e$ [eV]
	$\lambda_{\text{max}}$ [nm]	$\epsilon$ [ $10^4 \text{ M}^{-1} \text{ cm}^{-1}$ ]	$\lambda_{\text{max}}$ [nm]	$\alpha$ [ $10^4 \text{ cm}^{-1}$ ]			
TTA-DPP4	616	22.3	625, 676	16.7	-5.36	-3.72	1.64
TTA-DPP2	623	9.6	626, 677	11.5	-5.40	-3.75	1.65

<sup>a</sup>Measured in chloroform solutions ( $10^{-5}$  M); <sup>b</sup>thin films spin-coated from chloroform solution onto quartz substrate; <sup>c</sup>determined by photoelectron yield spectroscopy in spin-coated thin films; <sup>d</sup>determined from the HOMO and optical energy gap ( $E_g$ ): LUMO = HOMO +  $E_g$ ; <sup>e</sup>derived from the absorption onset of the thin films.

diiodooctane (DIO) (98:2, v/v). The thickness of the active layer was controlled within the range of ca. 40–90 nm by varying the rotation speed during spin-coating. A 6 nm thick  $\text{MoO}_3$  layer as a hole extraction layer and a 100 nm thick Ag anode were vacuum-deposited on the active layer. The photovoltaic properties of the fabricated BHJ-OSCs were evaluated under simulated AM 1.5G illumination at an intensity of 100 mW  $\text{cm}^{-2}$  (1 sun).

Figure 5 shows the current density–voltage ( $J$ – $V$ ) characteristics of the BHJ-OSCs based on TTA-DPP4 and TTA-DPP2 with different active layer thicknesses. The dependence of the

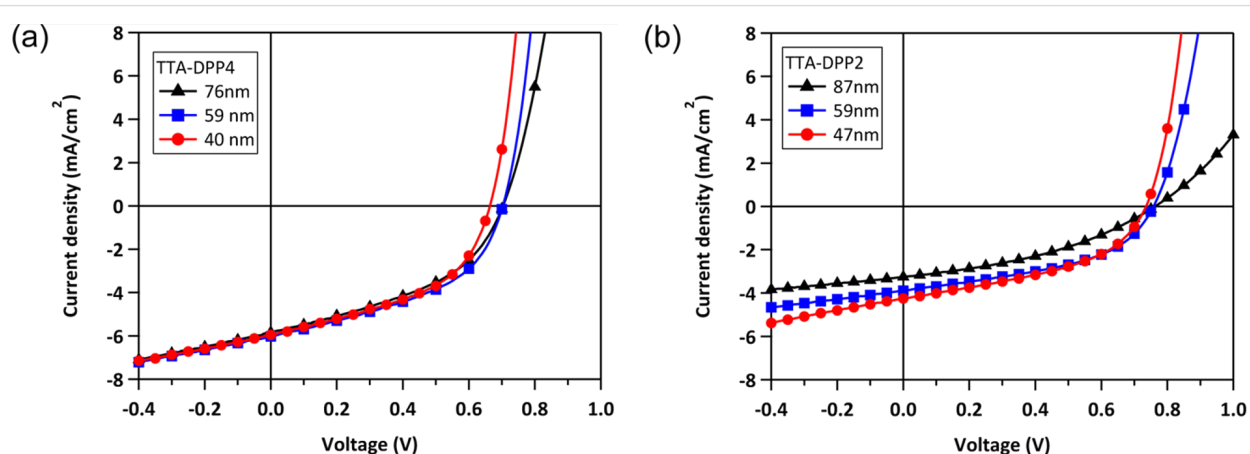


Figure 5:  $J$ – $V$  characteristics of BHJ-OSCs based on (a) TTA-DPP4:PC<sub>71</sub>BM (1:1.5, w/w) and (b) TTA-DPP2:PC<sub>71</sub>BM (1:1.5, w/w) with different active layer thicknesses, measured under simulated AM 1.5G, 100 mW  $\text{cm}^{-2}$  illumination.

active layer thickness on PCE is presented in Figure 6, and the representative photovoltaic parameters are listed in Table 2. For the TTA-DPP4-based devices, the photovoltaic properties were not influenced much when changing the thickness of the active layer in the range of ca. 40–90 nm, providing PCEs of 1.7–2.0%. Apparently, the TTA-DPP4-based OSCs showed better photovoltaic performance with a thinner active layer (40–80 nm), as compared to conventional poly(3-hexylthiophene) (P3HT)-based devices. A similar effect of active layer thickness on PCE was also observed in TTA-DPP2-based devices, where a PCE of 1.4% was obtained with an active layer thickness of 47 nm. In contrast, as presented in Figure 6 and Table 2, the PCEs of P3HT-based devices steeply decreased with decreasing active layer thickness in the range of 40–80 nm, agreeing with the previously reported results [32]. For most of the donor materials, including polymers and small molecules re-

ported, the best photovoltaic performances were generally achieved with an active layer thickness of around 100 nm. However, TTA-DPP4 and TTA-DPP2 presented the highest PCEs with much thinner active layers of approximately 40–60 nm. Moreover, the PCEs of TTA-DPP4-based devices were higher than those of TTA-DPP2, presumably because of its larger absorption coefficient resulting from its star-shaped molecular structure with a two-dimensionally expanded  $\pi$ -conjugated backbone.

## Conclusion

In this study, the first attempt to introduce a TTA unit as central electron-donating core into star-shaped and linear  $\pi$ -conjugated oligomers was demonstrated. Multiple electron-accepting DPP arms were attached to the electron-donating TTA core to form star-shaped TTA-DPP4 and linear TTA-DPP2 that have acceptor–donor–acceptor electronic structures. TTA-DPP4 showed a better photoabsorption property than TTA-DPP2 because of its larger oscillator strength, as expected from the DFT calculations. The BHJ-OSCs based on TTA-DPP4 and TTA-DPP2 showed good photovoltaic properties even with thin active layers of 40–60 nm. This behavior was highly different from that of the reported general polymer- and small-molecule-based OSCs. A star-shaped molecular structure containing a two-dimensionally extended  $\pi$ -conjugated system is a promising electronic system for designing photovoltaic organic materials, as a result of its excellent photoabsorption properties.

## Experimental

### General methods

Matrix-assisted laser desorption ionization time-of-flight (MALDI–TOF) mass spectra were collected on a Bruker Daltonics Autoflex III spectrometer using dithranol as the matrix. Elemental analysis was carried out using a YANACO CHN coder MT-6. Thermogravimetric analysis (TGA) was performed using a Hitachi High-Tech Science TG/DTA7300 with a

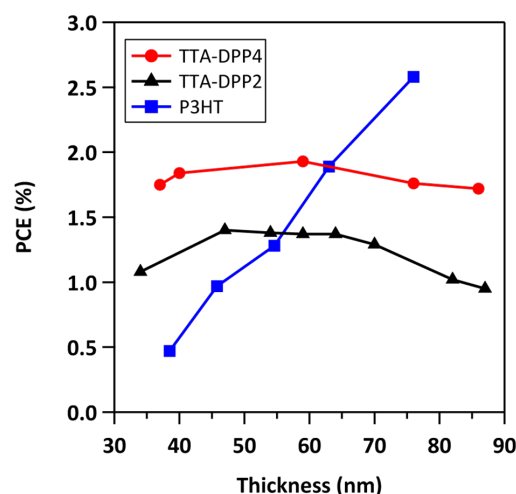


**Figure 6:** Relationship between active layer thickness and power conversion efficiency (PCE) for TTA-DPP4, TTA-DPP2, and P3HT-based BHJ-OSCs (see also Figures S2–S4 in the Supporting Information File 1 for detailed photovoltaic data).

**Table 2:** Photovoltaic parameters for inverted BHJ-OSCs based on TTA-DPP4 or TTA-DPP2:PC<sub>71</sub>BM and P3HT:PC<sub>61</sub>BM under simulated AM 1.5 G, 100 mW cm<sup>-2</sup> illumination.

Donor	Thickness [nm]	J <sub>SC</sub> [mA/cm <sup>2</sup> ]	V <sub>OC</sub> [V]	FF [%]	PCE [%]
TTA-DPP4	76 ± 3	5.84	0.70	42.9	1.76
TTA-DPP4	59 ± 1	6.02	0.70	45.6	1.93
TTA-DPP4	40 ± 2	5.95	0.66	46.7	1.84
TTA-DPP2	87 ± 1	3.26	0.76	44.9	0.95
TTA-DPP2	59 ± 1	3.89	0.76	46.4	1.37
TTA-DPP2	47 ± 2	4.25	0.74	44.7	1.40
P3HT	76 ± 1	7.32	0.56	62.8	2.58
P3HT	55 ± 1	5.60	0.43	52.4	1.28
P3HT	39 ± 1	2.97	0.32	50.0	0.47

heating rate of 10 °C min<sup>-1</sup> under N<sub>2</sub> atmosphere. UV–vis absorption spectra were recorded on a JASCO V-670Y spectrometer. Photoelectron yield spectra were recorded on a Riken-Keiki AC-2 ultraviolet photoelectron spectrometer. The thickness of photoactive layers was measured using a Bruker DektakXT system.

## Synthesis

All reactions were carried out under N<sub>2</sub> atmosphere using standard Schlenk techniques. All starting materials, unless otherwise specified, were purchased from commercial suppliers and used without further purification. 2,5,9,12-Tetrabromoanthra[1,2-*b*:4,3-*b*':5,6-*b*":8,7-*b*"]tetrathiophene (**1**) [25], 2,5-bis(2-ethylhexyl)-3-(5-(4-hexylphenyl)thiophen-2-yl)-6-(5-(trimethylstannylyl)thiophen-2-yl)-2,5-dihydropyrrolo[3,4-*c*]pyrrole-1,4-dione (**2**) [30,33], (5,12-bis(2-ethylhexyl)anthra[1,2-*b*:4,3-*b*':5,6-*b*":8,7-*b*"]tetrathiophene-2,9-diyl)bis(trimethylstannane) (**3**) [24,27], and 3-(5-bromothiophen-2-yl)-2,5-bis(2-ethylhexyl)-6-(5-(4-hexylphenyl)thiophen-2-yl)-2,5-dihydropyrrolo[3,4-*c*]pyrrole-1,4-dione (**4**) [30] were synthesized according to the reported procedures. Detailed synthetic schemes for these compounds are provided in the Supporting Information File 1.

**Synthesis of TTA-DPP4:** To a mixture of **1** (0.19 g, 0.27 mmol) and **2** (2.29 g, 2.70 mmol) in a mixture of dry DMF (10 mL) and dry toluene (20 mL) was added Pd(PPh<sub>3</sub>)<sub>4</sub> (0.016 g, 0.014 mmol). The mixture was stirred for 38 h at 120 °C. After cooling to room temperature, the reaction mixture was poured into water and then extracted with chloroform. The combined organic layers were washed with water and dried over anhydrous Na<sub>2</sub>SO<sub>4</sub>. After filtration and evaporation, the product was purified by silica gel column chromatography (eluent: chloroform/hexane 4:1, v/v) to provide TTA-DPP4 as a dark purple solid. This compound was further purified by recycling preparative gel permeation chromatography (GPC; eluent: chloroform) prior to use (yield = 0.36 g, 44%). MS (MALDI-TOF) *m/z*: [M]<sup>+</sup> calcd for 3133.42; found 3133.51; anal. calcd (%) for C<sub>190</sub>H<sub>226</sub>N<sub>8</sub>O<sub>8</sub>S<sub>12</sub>: C, 72.80; H, 7.27; N, 3.57; found: C, 71.29; H, 7.15; N, 3.53. Well-resolved NMR signals could not be obtained for both TTA-DPP4 and TTA-DPP2 in CDCl<sub>3</sub> or DMSO-*d*<sub>6</sub> even at elevated temperatures due to the macromolecular nature of the compounds (Figure S5 in Supporting Information File 1). The experimental results of isotope pattern deconvolution in mass spectra of TTA-DPP4 and TTA-DPP2 showed good agreements with the theoretical isotope patterns, supporting their chemical structures.

**Synthesis of TTA-DPP2:** This compound was prepared in a similar fashion to TTA-DPP4, using **3** (0.31 g, 0.33 mmol) and **4** (0.53 g, 0.69 mmol), and Pd(PPh<sub>3</sub>)<sub>4</sub> (0.015 g, 0.013 mmol).

The product was purified by silica gel column chromatography (eluent: chloroform/hexane 1:1, v/v) and GPC to give TTA-DPP2 as a dark purple solid (yield = 0.32 g, 49%). MS (MALDI-TOF) *m/z*: [M]<sup>+</sup> calcd for 1991.95; found 1991.67; anal. calcd (%) for C<sub>122</sub>H<sub>150</sub>N<sub>4</sub>O<sub>4</sub>S<sub>8</sub>: C, 73.52; H, 7.59; N, 2.81; found: C, 73.33; H, 7.53; N, 2.84.

## Fabrication and evaluation of organic solar cells

The OSC devices were fabricated and tested by using similar procedures described in reference [30]. Pre-patterned ITO-coated glass substrates were cleansed sequentially by sonicating in detergent solution, deionized water, acetone, and isopropanol for 15 min each, and then subjected to UV/ozone treatment for 30 min. A thin layer (~30 nm) of ZnO was prepared by spin-coating (at 5000 rpm) a precursor solution of zinc acetate (0.50 g) and ethanolamine (0.14 g) in 2-methoxyethanol (5 mL), followed by baking at 200 °C for 10 min under air. The photoactive layer was then prepared by spin-coating from a chloroform solution containing the donor material and PC<sub>71</sub>BM, after passing through a 0.45 μm PTFE membrane filter. Finally, a 6 nm thick MoO<sub>3</sub> layer and a 100 nm-thick Ag layer were thermally evaporated on top of the active layer under high vacuum through a shadow mask, defining an active area of 0.04 cm<sup>2</sup> for each device. Current density–voltage (*J*–*V*) measurements for the fabricated OSCs were conducted on a computer-controlled Keithley 2400 source measure unit in air, under simulated AM 1.5G solar illumination at 100 mW cm<sup>-2</sup> (1 sun), using a Xe lamp-based Bunko-Keiki SRO-25 GD solar simulator. The light intensity was calibrated using a standard silicon photovoltaic reference cell.

## Supporting Information

### Supporting Information File 1

Synthesis of compounds **1**–**13**, evaluation of HOMO levels for TTA-DPP4 and TTA-DPP2, photovoltaic properties of TTA-DPP4, TTA-DPP2, and P3HT-based OSCs and <sup>1</sup>H NMR spectra of TTA-DPP4 and TTA-DPP2.  
[\[http://www.beilstein-journals.org/bjoc/content/supplementary/1860-5397-12-142-S1.pdf\]](http://www.beilstein-journals.org/bjoc/content/supplementary/1860-5397-12-142-S1.pdf)

## Acknowledgements

This work was partially supported by the ACCEL project from Japan Science and Technology Agency (JST), and Grants-in-Aid for Scientific Research (Nos. 16K21218 (H.K.) and 15H01049 (T.Y.)) from JSPS, the Cooperative Research Program of “Network Joint Research Center for Materials and Devices”, the Yoshida Education and Foundation (H.K.), the Yashima Environment Technology Foundation (T.Y.), and the

KDDI Foundation Research Grant (T.Y.). H.K. and C.A. acknowledge the support of WPI-I2CNER, sponsored by MEXT, Japan.

## References

1. Yu, G.; Gao, J.; Hummelen, J. C.; Wudi, F.; Heeger, A. J. *Science* **1995**, *270*, 1789–1791. doi:10.1126/science.270.5243.1789
2. Li, G.; Shrotriya, V.; Huang, J.; Yao, Y.; Moriarty, T.; Emery, K.; Yang, Y. *Nat. Mater.* **2005**, *4*, 864–868. doi:10.1038/nmat1500
3. Sun, Y.; Welch, G. C.; Leong, W. L.; Takacs, C. J.; Bazan, G. C.; Heeger, A. J. *Nat. Mater.* **2012**, *11*, 44–48. doi:10.1038/nmat3160
4. Zhang, Q.; Kan, B.; Liu, F.; Long, G.; Wan, X.; Chen, X.; Zuo, Y.; Ni, W.; Zhang, H.; Li, M.; Hu, Z.; Huang, F.; Cao, Y.; Liang, Z.; Zhang, M.; Russell, T. P.; Chen, Y. *Nat. Photonics* **2015**, *9*, 35–41. doi:10.1038/nphoton.2014.269
5. Kan, B.; Li, M.; Zhang, Q.; Liu, F.; Wan, X.; Wang, Y.; Ni, W.; Long, G.; Yang, X.; Feng, H.; Zuo, Y.; Zhang, M.; Huang, F.; Cao, Y.; Russell, T. P.; Chen, Y. *J. Am. Chem. Soc.* **2015**, *137*, 3886–3893. doi:10.1021/jacs.5b00305
6. Liu, C.; Yi, C.; Wang, K.; Yang, Y.; Bhatta, R. S.; Tsige, M.; Xiao, S.; Gong, X. *ACS Appl. Mater. Interfaces* **2015**, *7*, 4928–4935. doi:10.1021/am509047g
7. Vohra, V.; Kawashima, K.; Kakara, T.; Koganezawa, T.; Osaka, I.; Takimiya, K.; Murata, H. *Nat. Photonics* **2015**, *9*, 403–408. doi:10.1038/nphoton.2015.84
8. Schmidt-Mende, L.; Fechtenkötter, A.; Müllen, K.; Moons, E.; Friend, R. H.; MacKenzie, J. D. *Science* **2001**, *293*, 1119–1122. doi:10.1126/science.293.5532.1119
9. Wong, W. W. H.; Jones, D. J.; Yan, C.; Watkins, S. E.; King, S.; Haque, S. A.; Wen, X.; Ghiggino, K. P.; Holmes, A. B. *Org. Lett.* **2009**, *11*, 975–978. doi:10.1021/ol8029164
10. Wong, W. W. H.; Khouri, T.; Vak, D.; Yan, C.; Jones, D. J.; Crossley, M. J.; Holmes, A. B. *J. Mater. Chem.* **2010**, *20*, 7005–7014. doi:10.1039/c0jm00311e
11. Wong, W. W. H.; Ma, C.-Q.; Pisula, W.; Yan, C.; Feng, X.; Jones, D. J.; Müllen, K.; Janssen, R. A. J.; Bäuerle, P.; Holmes, A. B. *Chem. Mater.* **2010**, *22*, 457–466. doi:10.1021/cm903272y
12. Ren, S.; Yan, C.; Vak, D.; Jones, D. J.; Holmes, A. B.; Wong, W. W. H. *Adv. Funct. Mater.* **2012**, *22*, 2015–2026. doi:10.1002/adfm.201102141
13. Wong, W. W. H.; Subbiah, J.; Puniredd, S. R.; Purushothaman, B.; Pisula, W.; Kirby, N.; Müllen, K.; Jones, D. J.; Holmes, A. B. *J. Mater. Chem.* **2012**, *22*, 21131–21137. doi:10.1039/c2jm34394k
14. Hu, N.; Shao, R.; Shen, Y.; Chen, D.; Clark, N. A.; Walba, D. M. *Adv. Mater.* **2014**, *26*, 2066–2071. doi:10.1002/adma.201304371
15. Takemoto, K.; Karasawa, M.; Kimura, M. *ACS Appl. Mater. Interfaces* **2012**, *4*, 6289–6294. doi:10.1021/am301905m
16. Liu, S.-Y.; Liu, W.-Q.; Xu, J.-Q.; Fan, C.-C.; Fu, W.-F.; Ling, J.; Wu, J.-Y.; Shi, M.-M.; Jen, A. K.-Y.; Chen, H.-Z. *ACS Appl. Mater. Interfaces* **2014**, *6*, 6765–6775. doi:10.1021/am500522x
17. Takemoto, K.; Kimura, M. *RSC Adv.* **2014**, *4*, 64589–64595. doi:10.1039/C4RA10347E
18. Roquet, S.; Cravino, A.; Leriche, P.; Alévêque, O.; Frère, P.; Roncali, J. *J. Am. Chem. Soc.* **2006**, *128*, 3459–3466. doi:10.1021/ja058178e
19. Zhang, J.; Deng, D.; He, C.; He, Y.; Zhang, M.; Zhang, Z.-G.; Zhang, Z.; Li, Y. *Chem. Mater.* **2011**, *23*, 817–822. doi:10.1021/cm102077j
20. Lin, Y.; Zhang, Z.-G.; Li, Y.; Zhu, D.; Zhan, X. *J. Mater. Chem. A* **2013**, *1*, 5128–5135. doi:10.1039/c3ta10205j
21. Paek, S.; Cho, N.; Cho, S.; Lee, J. K.; Ko, J. *Org. Lett.* **2012**, *14*, 6326–6329. doi:10.1021/o1303045p
22. Paek, S.; Choi, H.; Sim, J.; Song, K.; Lee, J. K.; Ko, J. *J. Phys. Chem. C* **2014**, *118*, 27193–27200. doi:10.1021/jp5071709
23. Shang, H.; Fan, H.; Liu, Y.; Hu, W.; Li, Y.; Zhan, X. *Adv. Mater.* **2011**, *23*, 1554–1557. doi:10.1002/adma.201004445
24. He, F.; Wang, W.; Chen, W.; Xu, T.; Darling, S. B.; Strzalka, J.; Liu, Y.; Yu, L. *J. Am. Chem. Soc.* **2011**, *133*, 3284–3287. doi:10.1021/ja1110915
25. Brusso, J. L.; Hirst, O. D.; Dadvand, A.; Ganesan, S.; Ciciora, F.; Robertson, C. M.; Oakley, R. T.; Rosei, F.; Perepichka, D. F. *Chem. Mater.* **2008**, *20*, 2484–2494. doi:10.1021/cm7030653
26. Leitch, A. A.; Stobo, K. A.; Hussain, B.; Ghoussoub, M.; Ebrahimi-Takalloo, S.; Servati, P.; Korobkov, I.; Brusso, J. L. *Eur. J. Org. Chem.* **2013**, *26*, 5854–5863. doi:10.1002/ejoc.201300731
27. Li, C.; Zheng, N.; Chen, H.; Huang, J.; Mao, Z.; Zheng, L.; Weng, C.; Tan, S.; Yu, G. *Polym. Chem.* **2015**, *6*, 5393–5404. doi:10.1039/C5PY00605H
28. Wienk, M. M.; Turbiez, M.; Gilot, J.; Janssen, R. A. J. *Adv. Mater.* **2008**, *20*, 2556–2560. doi:10.1002/adma.200800456
29. Shin, W.; Yasuda, T.; Watanabe, G.; Yang, Y. S.; Adachi, C. *Chem. Mater.* **2013**, *25*, 2549–2556. doi:10.1021/cm401244x
30. Shin, W.; Yasuda, T.; Hidaka, Y.; Watanabe, G.; Arai, R.; Nasu, K.; Yamaguchi, T.; Murakami, W.; Makita, K.; Adachi, C. *Adv. Energy Mater.* **2014**, *4*, 1400879. doi:10.1002/aenm.201400879
31. Huang, J.; Zhan, C.; Zhang, X.; Zhao, Y.; Lu, Z.; Jia, H.; Jiang, B.; Ye, J.; Zhang, S.; Tang, A.; Liu, Y.; Pei, Q.; Yao, J. *ACS Appl. Mater. Interfaces* **2013**, *5*, 2033–2039. doi:10.1021/am302896u
32. Dang, M. T.; Hirsch, L.; Wantz, G. *Adv. Mater.* **2011**, *23*, 3597–3602. doi:10.1002/adma.201100792
33. Fu, L.; Fu, W.; Cheng, P.; Xie, Z.; Fan, C.; Sh, M.; Ling, J.; Hou, J.; Zhanc, X.; Chen, H. *J. Mater. Chem. A* **2014**, *2*, 6589–6597. doi:10.1039/c3ta13534a

## License and Terms

This is an Open Access article under the terms of the Creative Commons Attribution License (<http://creativecommons.org/licenses/by/2.0/>), which permits unrestricted use, distribution, and reproduction in any medium, provided the original work is properly cited.

The license is subject to the *Beilstein Journal of Organic Chemistry* terms and conditions: (<http://www.beilstein-journals.org/bjoc>)

The definitive version of this article is the electronic one which can be found at: [doi:10.3762/bjoc.12.142](http://doi:10.3762/bjoc.12.142)



## Synthesis and characterization of benzodithiophene and benzotriazole-based polymers for photovoltaic applications

Desta Gedefaw<sup>1,2</sup>, Marta Tessarolo<sup>3</sup>, Margherita Bolognesi<sup>4</sup>, Mario Prosa<sup>3</sup>,  
Renee Kroon<sup>2</sup>, Wenliu Zhuang<sup>2</sup>, Patrik Henriksson<sup>2</sup>, Kim Bini<sup>2</sup>, Ergang Wang<sup>2</sup>,  
Michele Muccini<sup>3</sup>, Mirko Seri<sup>\*5</sup> and Mats R. Andersson<sup>\*1,2</sup>

### Full Research Paper

Open Access

Address:

<sup>1</sup>Future Industries Institute, University of South Australia, Mawson Lakes, South Australia 5095, Australia, <sup>2</sup>Department of Chemistry and Chemical Engineering, Polymer Technology, Chalmers University of Technology, Göteborg SE-412 96, Sweden, <sup>3</sup>National Research Council (CNR) – Institute of Nanostructured Materials (ISMN), Via P. Gobetti, 101, 40129 Bologna, Italy, <sup>4</sup>Laboratory MIST E-R, Via P. Gobetti, 101, 40129 Bologna, Italy and <sup>5</sup>National Research Council (CNR) – Institute of Organic Synthesis and Photoreactivity (ISOF), Via P. Gobetti, 101, 40129 Bologna, Italy

*Beilstein J. Org. Chem.* **2016**, *12*, 1629–1637.

doi:10.3762/bjoc.12.160

Received: 10 May 2016

Accepted: 15 July 2016

Published: 01 August 2016

This article is part of the Thematic Series "Organic photovoltaics".

Guest Editor: D. J. Jones

© 2016 Gedefaw et al.; licensee Beilstein-Institut.

License and terms: see end of document.

Email:

Mirko Seri<sup>\*</sup> - [mirko.seri@isof.cnr.it](mailto:mirko.seri@isof.cnr.it); Mats R. Andersson<sup>\*</sup> - [mats.andersson@unisa.edu.au](mailto:mats.andersson@unisa.edu.au)

\* Corresponding author

Keywords:

alkyl side chains; benzodithiophene; bulk heterojunction solar cells; 2D conjugated polymers; fluorinated benzotriazole

### Abstract

Two high bandgap benzodithiophene–benzotriazole-based polymers were synthesized via palladium-catalysed Stille coupling reaction. In order to compare the effect of the side chains on the opto-electronic and photovoltaic properties of the resulting polymers, the benzodithiophene monomers were substituted with either octylthienyl (PTzBDT-1) or dihexylthienyl (PTzBDT-2) as side groups, while the benzotriazole unit was maintained unaltered. The optical characterization, both in solution and thin-film, indicated that PTzBDT-1 has a red-shifted optical absorption compared to PTzBDT-2, likely due to a more planar conformation of the polymer backbone promoted by the lower content of alkyl side chains. The different aggregation in the solid state also affects the energetic properties of the polymers, resulting in a lower highest occupied molecular orbital (HOMO) for PTzBDT-1 with respect to PTzBDT-2. However, an unexpected behaviour is observed when the two polymers are used as a donor material, in combination with PC<sub>61</sub>BM as acceptor, in bulk heterojunction solar cells. Even though PTzBDT-1 showed favourable optical and electrochemical properties, the devices based on this polymer present a power conversion efficiency of 3.3%, considerably lower than the efficiency of 4.7% obtained for the analogous solar cells based on PTzBDT-2. The lower performance is presumably attributed to the limited solubility of the PTzBDT-1 in organic solvents resulting in enhanced aggregation and poor intermixing with the acceptor material in the active layer.

## Introduction

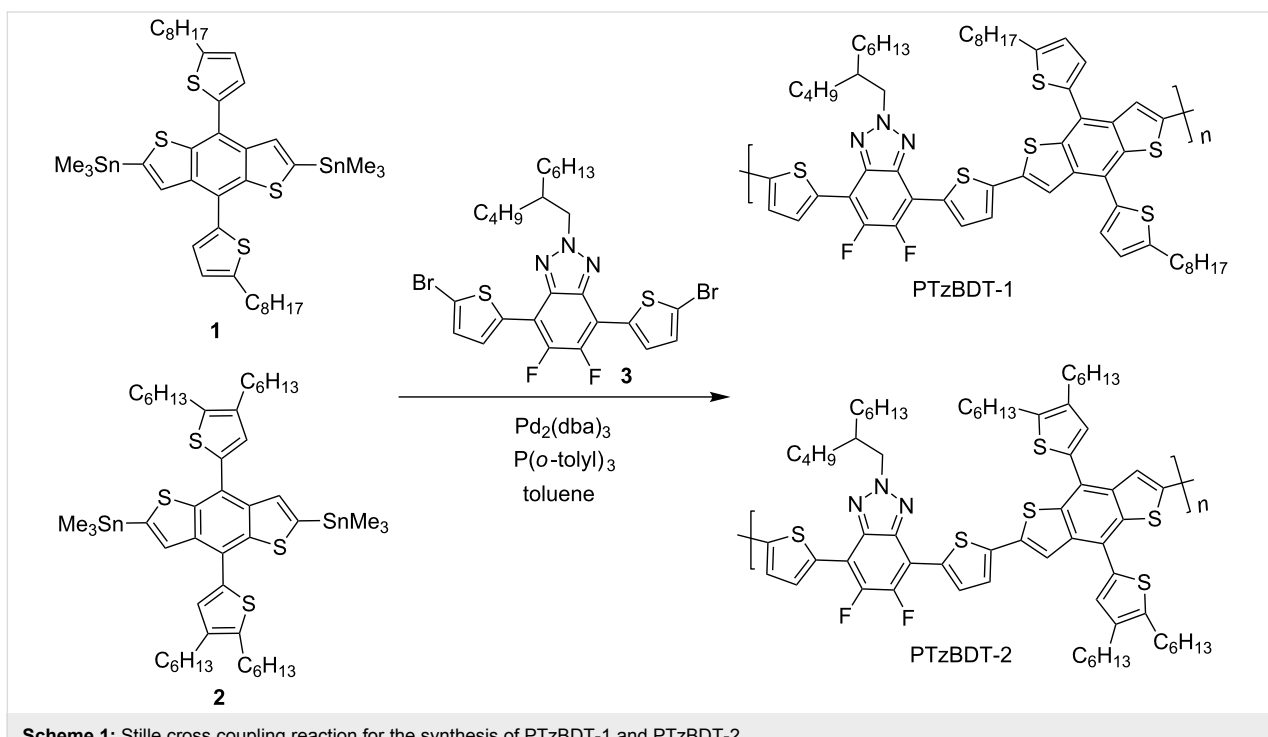
Over the past decades the research on bulk heterojunction (BHJ) polymer solar cells (PSCs) has been intensified due to the attractive perspectives of producing lightweight and flexible devices via a scalable printing technology at low-cost. The active layer consists of a blend of  $\pi$ -conjugated polymer (electron donor) and fullerene derivative (electron acceptor) sandwiched between two electrodes (anode and cathode) [1-4]. Noticeable achievements have been recorded in terms of the power conversion efficiency (PCE) of lab-scale single junction BHJ PSCs surpassing the 10% milestone. It has also been possible to achieve improved PCE by using multi-junction structures (e.g., tandem) [5-8]. The continued development of new active materials with desired properties, understanding of nanoscale morphology and device architecture is expected to push the PCE to even higher value, offering promising perspectives for this technology [9-12].

Despite the different aspects, the properties of the donor polymers remain one of the most important factors on the overall performance of a BHJ device. Specifically, an ideal donor polymer is usually designed to have sufficient solubility in common organic solvents, good stability in air, a suitable bandgap for an effective light harvesting, proper charge transport properties, suitable HOMO and LUMO energy levels compatible with the acceptor material [13] and an excellent film-forming capability. In search of materials endowed with these properties, a huge number of new polymer structures have been

designed, synthesized and used in fabricating efficient BHJ solar cells.

Among these donor polymers, copolymers based on widely known structural units such as benzo[1,2-*b*:4,5-*b'*]dithiophene (BDT) and 5,6-difluoro-2*H*-benzo[*d*][1,2,3]triazole (Tz) have attracted much attention and effectively employed in BHJ PSCs due to their intrinsic advantages, potentials and versatility [14,15]. Thanks to the desirable properties such as structural rigidity, planarity, extended  $\pi$ -conjugation length and favorable interchain  $\pi$ - $\pi$  stacking, BDT is a widely used electron-rich monomer. Moreover, alkyl or aryl groups can easily be introduced to BDT basic units as side groups to finely tune the properties of the resulting polymers, not only in terms of solubility but also contributing, for example, to extend the  $\pi$ -conjugation from the backbone to the lateral substituent (2D  $\pi$ -conjugated systems), thus leading to a bandgap reduction and higher charge carrier mobilities [15-18]. On the other hand, the Tz moiety, usually sandwiched between adjacent thiophene spacers to limit the inter-monomers steric hindrance, is a moderately weak electron-deficient unit that can be easily synthesized and its properties can be finely modulated by attaching groups on the reactive nitrogen atom of the triazole ring [15,19,20].

Here we report the synthesis and characterization of two novel donor polymers, PTzBDT-1 and PTzBDT-2 (Scheme 1), based on Tz and BDT moieties. The Tz ring was substituted



**Scheme 1:** Stille cross coupling reaction for the synthesis of PTzBDT-1 and PTzBDT-2.

with an asymmetrically branched alkyl side chain and sandwiched between two thiophene rings. The chemical structure of the Tz based monomer was made to be the same in both polymers for the comparative study. On the other hand, the BDT monomers used for the synthesis of PTzBDT-1 and PTzBDT-2 were substituted with either 2-octylthienyl (BDT-1) or 2,3-dihexylthienyl (BDT-2) as side groups, respectively. As a consequence of this fine structural modification on the BDT moiety, useful information on the effect of the different alkylthiophene side chains on the properties of the resulting pristine and blended films are collected and discussed.

Solution-processed BHJ PSCs using PTzBDT-1 or PTzBDT-2 as electron-donor materials and PC<sub>61</sub>BM as electron-acceptor counterpart were fabricated, optimized, and fully characterized. PCEs of 3.3% and 4.7% were achieved for PTzBDT-1 and PTzBDT-2 based devices, respectively, likely suggesting a different BHJ self-organization as a consequence of the different material properties induced by the alkyl substitution on the aromatic side groups.

## Results and Discussion

### Synthesis of the polymers

Scheme 1 shows the synthesis of the two polymers. The BDT (**1** and **2**) and Tz (**3**) based monomers were synthesized following literature procedures [21,22]. Thus, Stille cross-coupling reaction between the BDT and Tz based monomers gave the desired polymers in excellent yield. The molecular weights of the polymers were determined using size exclusion chromatography and the results are summarized in Table 1. PTzBDT-2 showed a higher molecular weight ( $M_n = 41.7$  kDa) due to the two *n*-hexyl solubilizing alkyl side chains per thiophene attached to the BDT core unit. On the contrary, PTzBDT-1 with a relatively lower content of alkyl side chain (an *n*-octyl side chain per thiophene attached on the BDT) showed a relatively limited solubility resulting in a slightly lower molecular weight ( $M_n = 20.2$  kDa). In fact, due to the limited solubility of PTzBDT-1, chlorobenzene was used as an extraction solvent to collect it from the extraction thimble at the polymer purification stage while PTzBDT-2, was extracted with chloroform thanks to its better solubility.

### Optical and electrochemical properties

The UV–visible absorption spectra of the pristine PTzBDT-1 and PTzBDT-2 polymers in dilute solution (in chlorobenzene and in chloroform, respectively) and thin films are reported in Figure 1. The detailed absorption data are summarized in Table 1.

Both polymers show a modest peak at 360 nm, likely due to the thiophene side groups linked to the BDT unit [17]. The two evident bands between 500 and 650 nm are likely ascribed to intramolecular charge-transfer-like interactions between the monomers and interchain interactions [23,24], respectively. However, despite the similar molecular structures, the different absorption spectra of PTzBDT-1 and PTzBDT-2 confirm the crucial role of the aryl side groups on the aggregation, in solution and solid state, of the polymer chains.

The solution absorption spectra of the polymers (Figure 1A) exhibit an evident red-shift (~20 nm) of the  $\lambda_{\text{max}}$  of PTzBDT-1 compared to PTzBDT-2 (550/598 nm and 530/574 nm, respectively). Moreover, PTzBDT-1 shows a broader spectrum in comparison to PTzBDT-2 (Figure 1A), as also confirmed by the corresponding absorption onset values ( $\lambda_{\text{onset}}$ ) of 633 nm and 605 nm, respectively. Analogously to our previous work [21], it is reasonable to assume that for PTzBDT-2 (Scheme 1), the two *n*-hexyl side chains placed on the thiophene side groups could sterically interact with the Tz unit, probably leading to a partial twisting of the polymer backbone responsible for the observed trend.

This hypothesis is further confirmed if we consider the absorption onset values ( $\lambda_{\text{onset}}$ ) of the corresponding films (Table 1 and Figure 1B). Interestingly, the red shift magnitude ( $\Delta\lambda_{\text{onset}} = \lambda_{\text{onset}}^{\text{film}} - \lambda_{\text{onset}}^{\text{solution}}$ ) for PTzBDT-1 and PTzBDT-2 is 13 nm and 31 nm, respectively, indicating different intra- and intermolecular interactions likely induced by the alkyl side chain substitution [25,26]. As expected, the twisting of

**Table 1:** Summary of the optical and electrochemical properties of PTzBDT-1 and PTzBDT-2.

Polymer	$M_n^a$ [kDa]	PDI	Solution				Thin-film			$E_{\text{HOMO}}$ [eV]	$E_{\text{LUMO}}$ [eV]
			$\lambda_{\text{max}}$ [nm]	$\lambda_{\text{onset}}$ [nm]	$E_{\text{gap}}^{\text{opt} b}$ [eV]	$\lambda_{\text{max}}$ [nm]	$\lambda_{\text{onset}}$ [nm]	$E_{\text{gap}}^{\text{opt} b}$ [eV]			
PTzBDT-1	20.2	4.40	550, 598	633	1.96	553, 598	646	1.92	-5.94	-3.25	
PTzBDT-2	41.7	2.53	530, 574	605	2.05	536, 580	636	1.95	-5.86	-3.21	

<sup>a</sup>Determined by GPC relative to polystyrene standards using 1,2,4-trichlorobenzene as eluent. <sup>b</sup> $E_{\text{gap}}^{\text{opt}} = 1240/\lambda_{\text{onset}}$ .

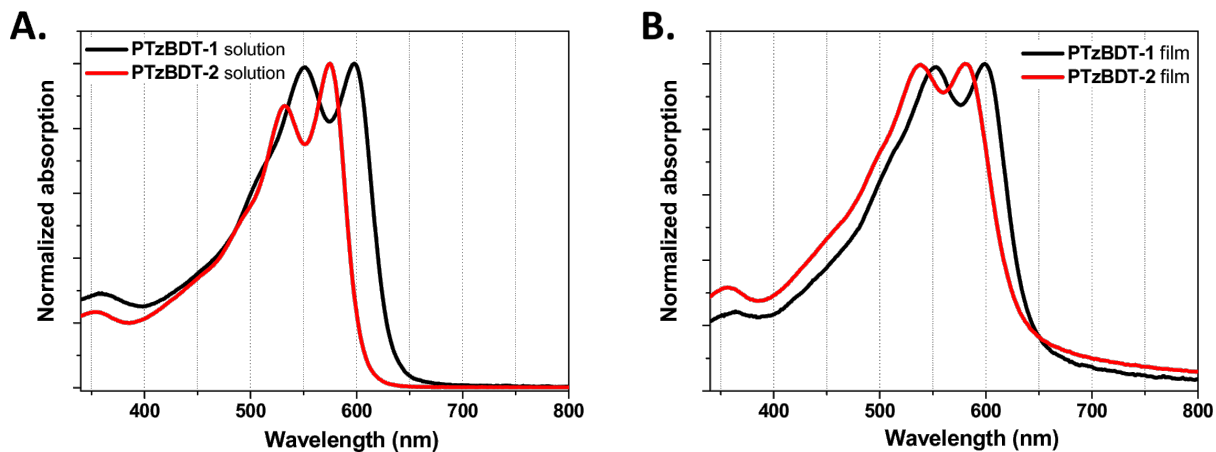


**Figure 1:** UV-visible absorption spectra of the pristine PTzBDT-1 and PTzBDT-2 (A) in chlorobenzene and chloroform, respectively and thin film processed from chlorobenzene (PTzBDT-1) and chloroform (PTzBDT-2) (B).

PTzBDT-2 is favored in dilute solution, while in film, where stronger intermolecular interactions take place, the polymer chains are likely forced to adopt a more planar conformation, in perfect agreement with the significantly red-shifted onset ( $\Delta\lambda_{\text{onset}} = 31 \text{ nm}$ ).

Diversely, PTzBDT-1 (Scheme 1) has a single *n*-octyl side chain linked to the thiophene ring, which should promote the solubility of the polymer without interacting with the adjacent Tz unit. As a result, a more planar conformation is expected for PTzBDT-1, thus allowing a partial pre-aggregation of the polymer chains in solution as confirmed by the relatively small  $\Delta\lambda_{\text{onset}}$  for PTzBDT-1 (13 nm). These findings combined with the still different film absorption spectra, suggest a different self-organization of the polymer chains, as supported by additional optical, electrical and morphological investigations of PTzBDT-1 and PTzBDT-2 based blends (vide infra).

The HOMO and LUMO energy levels of the polymer films were estimated by square wave voltammetry (SWV, Figure 2) using the oxidation and reduction peak values, respectively. As shown by the square wave voltammograms, the electrochemical oxidation shoulder peaks of PTzBDT-1 and PTzBDT-2 are located at 0.81 V and 0.73 V, respectively. As a result the estimated HOMO energy levels, calculated using the relation  $E_{\text{HOMO}} = -(E_{\text{ox}} + 5.13)$  [27], are -5.94 eV and -5.86 eV for PTzBDT-1 and PTzBDT-2, respectively. Similarly, the reduction peak potentials of PTzBDT-1 and PTzBDT-2 are located at -1.88 V and -1.92 V, respectively, resulting in LUMO energies of -3.25 and -3.21 eV, ( $E_{\text{LUMO}} = -(E_{\text{red}} + 5.13)$ ) [27]. Note that the number of alkyl chains linked to the aromatic side groups of the polymers are not expected to significantly affect the  $\pi$ -electron density distribution and thus the energetic proper-

ties of the two polymers [21], however the subsequent different organization in the solid state might be the main factor responsible for the observed variation of the HOMO and LUMO energy levels, which is in perfect agreement with the different optical properties. Interestingly, the deep HOMO energies of both polymers would result in devices with a high open circuit voltage ( $V_{\text{OC}}$ ), according to the difference  $\text{LUMO}_{\text{ACCEPTOR}} - \text{HOMO}_{\text{DONOR}}$  [28]. Good air stability is also expected from these polymers as their HOMO energies are in an ideal range [29]. On the other hand, the slightly raised LUMO observed in both polymers is expected due to the moderately weak electron withdrawing nature of benzotriazole.

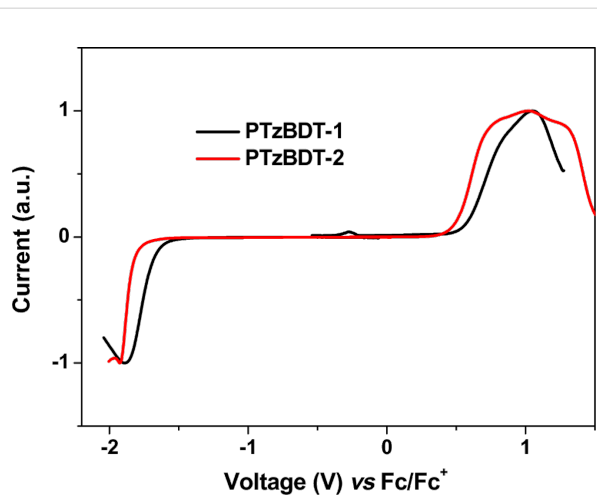


**Figure 2:** Square wave voltammogramme of PTzBDT-1 and PTzBDT-2.

It should be noted that there is a discrepancy between the bandgaps derived from electrochemical and optical measure-

ments of PTzBDT-1 and PTzBDT-2. This incongruence can be ascribed to the different method employed for the measurements. Indeed, in the first case ionized states are generated, while after light absorption the excited state is based on electrons and holes electrostatically bound [30]. Moreover, an energetic barrier between the electrode surface and the polymer film can further contribute to increase the electrochemically derived energies [31]. Finally, the resulting thin-film quality, and subsequent polymer self-organization, prepared over the electrode or over a flat substrate might be different, reflecting possible variations.

### Photovoltaic properties

A set of BHJ solar cells, using PTzBDT-1 and PTzBDT-2 as donors and PC<sub>61</sub>BM as an acceptor counterpart, were fabricated and characterized in order to evaluate the impact of the alkyl substitution on the resulting photovoltaic performance. Devices with standard configuration, glass/ITO/PEDOT:PSS/active layer/LiF/Al, were used. The PTzBDT-1 and PTzBDT-2 based active layers were spin-coated respectively from 1,2,4-trichlorobenzene (TCB) and 1,2-dichlorobenzene (ODCB) solutions (best solvents in terms of solubility and thin-film quality for each polymer) without the need of additional processing solvent additives. All the details for the fabrication and characterization of the devices are reported in the experimental section. The photovoltaic responses including  $V_{OC}$ , short circuit current density ( $J_{SC}$ ), fill factor (FF), and PCE of optimized devices

are summarized in Table 2. The corresponding current density–voltage ( $J$ – $V$ ) plots of the most efficient devices, measured under standard illumination (AM1.5G, 100 mW/cm<sup>2</sup>), are shown in Figure 3.

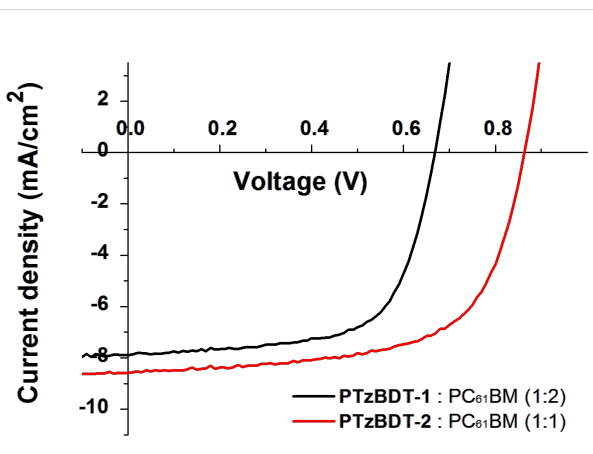


**Figure 3:**  $J$ – $V$  plots, measured under standard illumination (AM1.5G, 100 mW/cm<sup>2</sup>), of PTzBDT-1:PC<sub>61</sub>BM and PTzBDT-2:PC<sub>61</sub>BM BHJ based devices.

The optimal polymer:fullerene ratio was 1:2 and 1:1 (wt/wt) for PTzBDT-1 and PTzBDT-2 based blends, respectively. By varying the amount of the donor content in the BHJ blends, a reduction of the PCEs was observed (Table 3).

**Table 2:** PV characteristics of optimized PTzBDT-1:PC<sub>61</sub>BM and PTzBDT-2:PC<sub>61</sub>BM BHJ devices. The reported results are averaged over 4 solar cells.

Donor:acceptor ratio [wt/wt]	Solvent	Thickness [nm]	Annealing [°C]	$J_{SC}$ [mA/cm <sup>2</sup> ]	$V_{OC}$ [V]	FF [%]	PCE [%]
PTzBDT-1:PC <sub>61</sub> BM (1:2)	TCB	100	110 <sup>a</sup>	7.6	0.67	64	3.3
PTzBDT-2:PC <sub>61</sub> BM (1:1)	ODCB	90	–	8.6	0.86	64	4.7

<sup>a</sup>Annealing time: 10 min.

**Table 3:** PV characteristics of optimized PTzBDT-1:PC<sub>61</sub>BM and PTzBDT-2:PC<sub>61</sub>BM BHJ devices using different donor:acceptor ratios and processing conditions.

Active blend	D:A ratio [wt/wt]	Solvent <sup>a</sup>	Annealing [°C]	$J_{SC}$ [mA/cm <sup>2</sup> ]	$V_{OC}$ [V]	FF [%]	PCE [%]
PTzBDT-1:PC <sub>61</sub> BM	1:1	TCB	No ann.	8.0	0.63	42	2.1
	1:2	TCB	110 <sup>b</sup>	7.4	0.66	62	3.0
PTzBDT-2:PC <sub>61</sub> BM	1:1	ODCB	110 <sup>b</sup>	8.3	0.84	60	4.2
	1:2	ODCB	No ann.	6.6	0.87	65	3.7
	1:2	ODCB	110 <sup>b</sup>	4.7	0.85	60	2.4

<sup>a</sup>Additional solvents have been also tested for each polymer, however the resulting films were unhomogeneous with a poor morphology. For this reason BHJ Devices were not fabricated; <sup>b</sup>annealing time: 10 min.

Additional experiments to further enhance the device performance, for example by testing different processing solvents, thicknesses, annealing temperatures and annealing times (relevant examples are reported in Table 3), were unsuccessfully carried out.

The optimized BHJ solar cells exhibit PCEs of 3.3% and 4.7%, respectively for 1:2 (wt/wt) PTzBDT-1:PC<sub>61</sub>BM and 1:1 (wt/wt) PTzBDT-2:PC<sub>61</sub>BM films. The PTzBDT-1 based device shows relatively low performance with a  $V_{OC} = 0.67$  V,  $J_{SC} = 7.6$  mA/cm<sup>2</sup> and FF = 64%, while the device based on PTzBDT-2 exhibits a  $V_{OC} = 0.86$  V,  $J_{SC} = 8.6$  mA/cm<sup>2</sup> and FF = 64%. The  $V_{OC}$  and  $J_{SC}$  values, which simultaneously increase from PTzBDT-1 to PTzBDT-2, are the main parameters responsible for the different photovoltaic responses. Interestingly, the FF is identical for both films (64%), indicating suitable charge transport properties within the blends. By comparing the  $V_{OC}$  values an increase of 0.19 V is observed passing from PTzBDT-1 to PTzBDT-2. This difference, despite the deeper electrochemically derived HOMO energy levels of PTzBDT-1 (Table 1), could be ascribed to the impact of the alkyl substitution of the thiophene ring (side group) on the chemico-physical (e.g., solubility) and film-forming properties of the corresponding polymer based blend, likely influencing the donor:acceptor phase segregation, molecular aggregation/distances and interfacial energetics, all factors strongly related to the resulting  $V_{OC}$  [21]. The improved  $J_{SC}$  (~15%) of the PTzBDT-2:PC<sub>61</sub>BM device in comparison to that based on PTzBDT-1 might be ascribed to the different optical property of the blends (Figure 4A). In particular, despite a comparable shape, the intensity of the absorption profiles, related to the donor content in the blend and responsible for the light harvesting and exciton generation, are significantly different reflecting the trend of the generated photocurrents. Interest-

ingly, the absorption spectra of the optimized active blends present similar features observed for pristine materials. Indeed, despite the presence of PC<sub>61</sub>BM, the relative maxima of PTzBDT-2 are slightly blue-shifted in comparison to PTzBDT-1 likely reflecting the different conformation and/or twisting of the polymer backbone as previously discussed.

These results suggest that, beside structural factors, other fundamental aspects such as the slightly better solubility of PTzBDT-2 (double alkyl substitution on the thiophene ring) in comparison to PTzBDT-1, not only allows a higher donor content in the blend (enhanced light absorption) but also seems to be crucial in terms of precipitation/segregation kinetics during the deposition/drying process of the active blend, strongly influencing the self-organization, the quality and thus the morphological features of the resulting BHJ film (see below).

The external quantum efficiency (EQE) spectra of optimized PTzBDT-1 and PTzBDT-2 based devices (the same thickness as the best devices), shown in Figure 4B, are consistent with the absorption spectra of the corresponding blends (Figure 4A). Specifically, the EQE responses of PTzBDT-1:PC<sub>61</sub>BM and PTzBDT-2:PC<sub>61</sub>BM based devices reach the maxima of 55% (at 546 nm) and 64% (at 536 nm), respectively, in perfect agreement with the first relative absorption maxima of the corresponding films. The integrated currents from the EQE plots are in good agreement, within a ~10% experimental error, with the experimental values obtained from  $J$ - $V$  measurements.

In order to further investigate the impact of the side chain architecture of PTzBDT-1 and PTzBDT-2 on the solar cell output parameters, we compare the morphological differences of the corresponding optimized blends by tapping-mode atomic force microscope (AFM) (Figure 5).

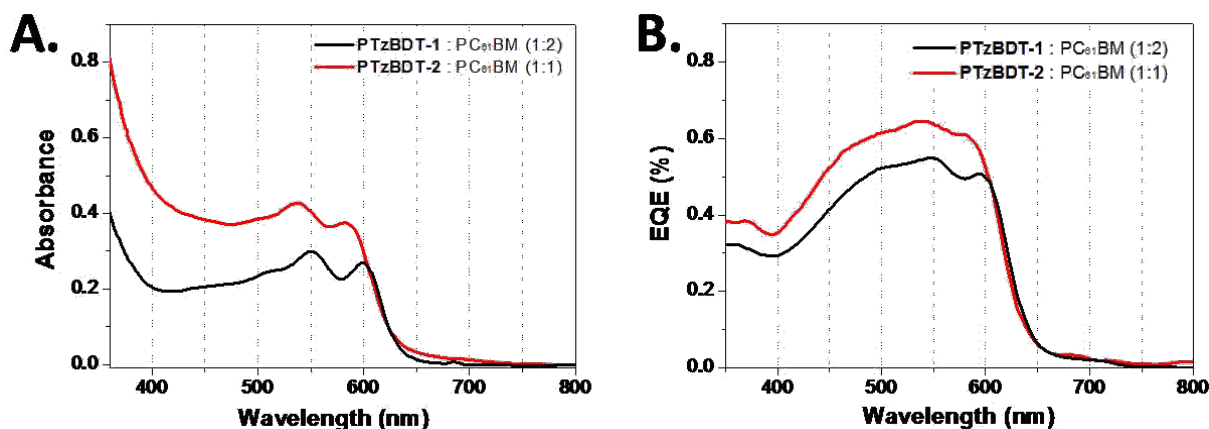
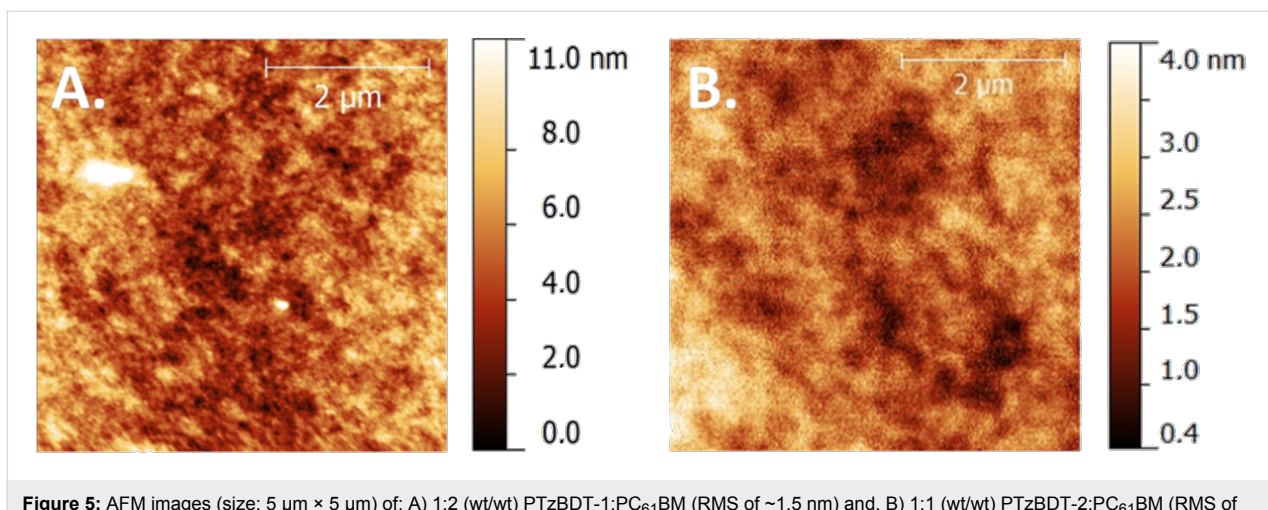


Figure 4: A) UV-vis absorption spectra and, B) EQE plots of optimized PTzBDT-1/PTzBDT-2:PC<sub>61</sub>BM based devices.



**Figure 5:** AFM images (size: 5  $\mu\text{m} \times 5 \mu\text{m}$ ) of: A) 1:2 (wt/wt) PTzBDT-1:PC<sub>61</sub>BM (RMS of  $\sim 1.5 \text{ nm}$ ) and, B) 1:1 (wt/wt) PTzBDT-2:PC<sub>61</sub>BM (RMS of  $\sim 0.5 \text{ nm}$ ) blends.

The surface morphology of the films is quite different, reflecting the trend of the photovoltaic responses. In particular, the topographic image of the 1:2 (wt/wt) PTzBDT-1:PC<sub>61</sub>BM film (Figure 5A) is characterized by an almost featureless surface with randomly oriented and poorly defined domains suggesting a suboptimal phase segregation of the donor:acceptor blend. Diversely, the AFM image of 1:1 (wt/wt) PTzBDT-2:PC<sub>61</sub>BM blend (Figure 5B) seems to be based on more structured and defined domains indicating a higher donor:acceptor intermixing combined with finely ordered and aggregated polymeric domains, in perfect agreement with the improved photovoltaic performance. This better self-organization of the PTzBDT-2:PC<sub>61</sub>BM blend seems in contrast with the intrinsic structural features of the polymer, where the double alkyl substitution is likely responsible for the partial twisting of the polymer backbone, however its enhanced solubility should promote the quality of the resulting thin films, highlighting the key role of the side chains to reach the best compromise between solubility and molecular packing in the solid state for this class of polymers.

## Conclusion

In conclusion, we reported the synthesis and characterization of two high bandgap polymers based on BDT and Tz units. We showed that the aryl substitution pattern on BDT is an important factor for the reorganization of the polymer in the solid state, affecting the optical and electrochemical properties of the pristine polymer thin films as well as the photovoltaic performance of the corresponding solar cells. Indeed, the polymer with dihexylthiophene substituted BDT (PTzBDT-2) showed better solubility and hence formed a well-developed nanomorphology when mixed with PC<sub>61</sub>BM in comparison to the analogous octylthiophene substituted polymer (PTzBDT-1). As the result, PTzBDT-2 gave a PCE of 4.7% when combined with

PC<sub>61</sub>BM. On the other hand, the polymer with octylthiophene substituted BDT (PTzBDT-1) showed a PCE of 3.3% likely due to the slightly lower solubility responsible for the generation of a suboptimal BHJ morphology.

## Experimental

### General

Size exclusion chromatography was performed on Waters Alliance GPCV2000 with a refractive index detector, with columns: Waters Styragel® HT 6E $\times$ 1, Waters Styragel® HMW 6E $\times$ 2. The eluent was 1,2,4-trichlorobenzene and the measurement was performed at 135 °C. The concentration of the samples was 0.5 mg/mL, which was filtered (filter: 0.45  $\mu\text{m}$ ) prior to the analysis. The relative molecular masses were calculated by calibration relative to polystyrene standards.

Square-wave voltammetric measurements were carried out on a CH-Instruments 650A Electrochemical Workstation. As described in [27], a three-electrode setup consisting of platinum wires, both as working electrode and counter electrode, and a Ag/Ag<sup>+</sup> quasi reference electrode were used. A 0.1 M solution of tetrabutylammonium hexafluorophosphate (Bu<sub>4</sub>NPF<sub>6</sub>) in anhydrous acetonitrile was used as supporting electrolyte. The polymers were deposited onto the working electrodes from chloroform solutions. The electrolyte was bubbled with nitrogen gas prior to each experiment. During the scans, nitrogen gas was flushed over the electrolyte surface. After each experiment, the system was calibrated by measuring the ferrocene/ferroceinium (Fc/Fc<sup>+</sup>) redox peak. The HOMO and LUMO energy levels of the polymers and electron acceptors were calculated from the peak values of the third scans by setting the oxidative peak potential of Fc/Fc<sup>+</sup> vs the normal-hydrogen electrode (NHE) to 0.630 V and the NHE vs the vacuum level to 4.5 V [27].

## Synthesis of the polymers

As described in [17], the polymers were synthesized according to the following synthetic procedures.

### Synthesis of PTzBDT-1

(4,8-Bis(5-octylthiophen-2-yl)benzo[1,2-*b*:4,5-*b*']dithiophene-2,6-diyl)bis(trimethylstannane) (**1**, 0.208 g, 0.23 mmol) and 4,7-bis(5-bromothiophen-2-yl)-2-(2-butyloctyl)-5,6-difluoro-2*H*-benzo[*d*][1,2,3]triazole (**3**, 0.15 g, 0.23 mmol) were dissolved in toluene (10 mL) and degassed with N<sub>2</sub> gas for 10 minutes. Pd<sub>2</sub>(dba)<sub>3</sub> (4.2 mg, 2 mol %) and P(*o*-tolyl)<sub>3</sub> (6.3 mg, 9 mol %) were added and purged with nitrogen gas for 25 minutes. The reaction mixture was heated at 90 °C for 40 min. The polymer solution was then added to methanol and the solid formed was collected by filtration. The polymer was re-dissolved in chlorobenzene by heating at 60 °C for 1 hour and 10% aqueous solution of sodium diethyldithiocarbamate trihydrate (100 mL) was added and stirred at room temperature overnight. The chlorobenzene soluble portion was separated and washed with distilled water three times. The chlorobenzene solution was reduced to small volume and then added to methanol. The solid was collected and then purified by soxhlet extraction using methanol, hexane, diethyl ether, dichloromethane and chloroform. Finally, the polymer that goes into chlorobenzene was collected and the volume was reduced and precipitated by adding on methanol. The polymer was collected by filtration, dried in a vacuum oven at 40 °C overnight to give a black solid (149 mg).

### Synthesis of PTzBDT-2

(4,8-Bis(4,5-dihexylthiophen-2-yl)benzo[1,2-*b*:4,5-*b*']dithiophene-2,6-diyl)bis(trimethylstannane) (**2**, 0.095 g, 0.147 mmol) and 4,7-bis(5-bromothiophen-2-yl)-2-(4-((2-butyloctyl)oxy)butyl)-5,6-difluoro-2*H*-benzo[*d*][1,2,3]triazole (**3**, 0.15 g, 0.147 mmol) were dissolved in toluene (8 mL) and degassed with N<sub>2</sub> gas for 10 minutes. Pd<sub>2</sub>(dba)<sub>3</sub> (3.4 mg, 2 mol %) and P(*o*-tolyl)<sub>3</sub> (8 mg, 9 mol %) were added and purged with nitrogen gas for 25 minutes. The reaction mixture was heated at 90 °C for 30 min. The polymer solution was then added to methanol and the solid formed was collected by filtration. The polymer was re-dissolved in chloroform by heating at 60 °C for 1 h and 10% aqueous solution of sodium diethyldithiocarbamate trihydrate (100 mL) was added and stirred at room temperature overnight. The chloroform soluble portion was separated and washed with distilled water three times. The chloroform solution was reduced to small volume and then added to methanol. The solid was collected and then purified by soxhlet extraction using methanol, hexane, acetone and diethyl ether. Finally, the polymer that goes into chloroform was collected and the volume was reduced and precipitated by adding on methanol. The polymer was collected by filtra-

tion, dried in vacuum oven at 40 °C overnight to give a brown solid (167 mg).

## Device fabrication and characterization

All materials, PEDOT:PSS (poly(3,4-ethylenedioxythiophene):poly(4-styrenesulfonate), Clevios P VP A1 4083, H.C. Starck), PC<sub>61</sub>BM ([6,6]-phenyl-C61-butyric acid methyl ester, Solenne BV), anhydrous 1,2,4-trichlorobenzene (TCB) and 1,2-dichlorobenzene (ODCB) were purchased from commercial sources (Sigma-Aldrich) and used without further purification.

Analogously to the description in [21] we report the main steps for the preparation and characterization of the devices. Patterned ITO-coated glasses ( $R_s \sim 10 \Omega \text{ sq}^{-1}$ ) were cleaned in sequential sonicating baths (for 15 min) in deionized water, acetone and isopropanol. After the final sonication step, substrates were dried with a stream of Ar gas and then placed in an oxygen plasma chamber for 5 min. Next, a thin layer (~30 nm) of PEDOT:PSS was spun-cast on the ITO surface and subsequently annealed at 150 °C for 15 min. The active layer blend solutions were formulated inside the glove box and stirred overnight at 80 °C. The active layers were prepared from solutions of PTzBDT-1:PC<sub>61</sub>BM and PTzBDT-2:PC<sub>61</sub>BM, dissolved in ODCB or TCB with a total concentration of 36 mg/mL. The resulting solutions were deposited in a glove-box by spin-coating on top of the ITO/PEDOT:PSS surface. Before cathode deposition, always in a glove-box, the substrates were then either thermally annealed or left as-cast. To complete the device fabrication, LiF and Al (0.6 and 100 nm) were deposited sequentially without breaking vacuum ( $\sim 1 \times 10^{-6}$  Torr) using a thermal evaporator directly connected to the glove box. The current–voltage (*J*–*V*) characteristics of all devices were recorded by a Keithley 236 source-measure unit under AM1.5G simulated solar irradiation, 100 mW/cm<sup>2</sup> (Abet Technologies Sun 2000 Solar Simulator). The light intensity was determined by a calibrated silicon solar cell fitted with a KG5 color glass filter to bring spectral mismatch to unity. The active area of the solar cell was exactly 6 mm<sup>2</sup>. During testing, each cell was carefully masked, by calibrated mask, to prevent an excess photocurrent generated from the parasitic device regions outside the overlapped electrodes area. All solar cells were tested, without encapsulation, inside the glove box in oxygen and moisture free environment.

## Thin-film characterization

All thin-film characterizations were performed in air. Film optical absorption spectra were recorded on a JASCO V-550 spectrophotometer. The thickness of the various active layers was measured by a profilometer (KLA Tencor, P-6). Atomic force microscopy (AFM) images, recorded directly on tested

devices, were taken with a Solver Pro (NT-934 MDT) scanning probe microscope in tapping mode.

## Acknowledgements

We acknowledge Laboratory MISTE-R, the Swedish Energy Agency and *South Australian Research Fellowship program*, Premier's Research and Industry Fund for financial support. The authors wish to thank Vincenzo Ragona and Federico Prescimone for the technical support and Anders Mårtensson for GPC measurement.

## References

- Kroon, R.; Diaz de Zerio Mendaza, A.; Himmelberger, S.; Bergqvist, J.; Bäcke, O.; Faria, G. C.; Gao, F.; Obaid, A.; Zhuang, W.; Gedefaw, D.; Olsson, E.; Inganäs, O.; Salleo, A.; Müller, C.; Andersson, M. R. *J. Am. Chem. Soc.* **2014**, *136*, 11578. doi:10.1021/ja5051692
- Boudreault, P.-L. T.; Najari, A.; Leclerc, M. *Chem. Mater.* **2011**, *23*, 456. doi:10.1021/cm1021855
- Lv, M.; Lei, M.; Zhu, J.; Hirai, T.; Chen, X. *ACS Appl. Mater. Interfaces* **2014**, *6*, 5844. doi:10.1021/am5007047
- Matsidik, R.; Komber, H.; Luzio, A.; Caironi, M.; Sommer, M. *J. Am. Chem. Soc.* **2015**, *137*, 6705. doi:10.1021/jacs.5b03355
- Li, X.; Choy, W. C. H.; Huo, L.; Xie, F.; Sha, W. E. I.; Ding, B.; Guo, X.; Li, Y.; Hou, J.; You, J.; Yang, Y. *Adv. Mater.* **2012**, *24*, 3046. doi:10.1002/adma.201200120
- He, Z.; Zhong, C.; Su, S.; Xu, M.; Wu, H.; Cao, Y. *Nat. Photonics* **2012**, *6*, 591. doi:10.1038/nphoton.2012.190
- Dou, L.; You, J.; Yang, J.; Chen, C.-C.; He, Y.; Murase, S.; Moriarty, T.; Emery, K.; Li, G.; Yang, Y. *Nat. Photonics* **2012**, *6*, 180. doi:10.1038/nphoton.2011.356
- You, J.; Dou, L.; Yoshimura, K.; Kato, T.; Ohya, K.; Moriarty, T.; Emery, K.; Chen, C.-C.; Gao, J.; Li, G.; Yang, Y. *Nat. Commun.* **2013**, *4*, No. 1446. doi:10.1038/ncomms2411
- Espinosa, N.; Hösel, M.; Jørgensen, M.; Krebs, F. C. *Energy Environ. Sci.* **2014**, *7*, 855. doi:10.1039/c3ee43212b
- Urbina, A.; Emmott, C. J. M.; Röhr, J. A.; Campoy-Quiles, M.; Kirchartz, T.; Ekins-Daukes, N. J.; Nelson, J. *Energy Environ. Sci.* **2015**, *8*, 1317. doi:10.1039/C4EE03132F
- Berny, S.; Blouin, N.; Distler, A.; Egelhaaf, H.-J.; Krompiec, M.; Lohr, A.; Lozman, O. R.; Morse, G. E.; Nanson, L.; Pron, A.; Sauermann, T.; Seidler, N.; Tierney, S.; Tiwana, P.; Wagner, M.; Wilson, H. *Adv. Sci.* **2016**, *3*. doi:10.1002/advs.201500342
- Roth, B.; dos Reis Benatto, G. A.; Corazza, M.; Carlé, J. E.; Helgesen, M.; Gevorgyan, S. A.; Jørgensen, M.; Søndergaard, R. R.; Krebs, F. C. *Adv. Eng. Mater.* **2016**, *18*, 511. doi:10.1002/adem.201500361
- Li, Y. *Acc. Chem. Res.* **2012**, *45*, 723. doi:10.1021/ar002446
- Kim, J.-H.; Song, C. E.; Shin, N.; Kang, H.; Wood, S.; Kang, I.-N.; Kim, B. J.; Kim, B.; Kim, J.-S.; Shin, W. S.; Hwang, D.-H. *ACS Appl. Mater. Interfaces* **2013**, *5*, 12820. doi:10.1021/am401926h
- Price, S. C.; Stuart, A. C.; Yang, L.; Zhou, H.; You, W. *J. Am. Chem. Soc.* **2011**, *133*, 8057. doi:10.1021/ja202672c
- Kim, J.-H.; Kim, H. U.; Song, C. E.; Kang, I.-N.; Lee, J.-K.; Shin, W. S.; Hwang, D.-H. *Sol. Energy Mater. Sol. Cells* **2013**, *108*, 113. doi:10.1016/j.solmat.2012.09.019
- Bolognesi, M.; Gedefaw, D.; Dang, D.; Henriksson, P.; Zhuang, W.; Tessarolo, M.; Wang, E.; Muccini, M.; Seri, M.; Andersson, M. R. *RSC Adv.* **2013**, *3*, 24543. doi:10.1039/c3ra44238a
- Gedefaw, D.; Tessarolo, M.; Zhuang, W.; Kroon, R.; Wang, E.; Bolognesi, M.; Seri, M.; Muccini, M.; Andersson, M. R. *Polym. Chem.* **2014**, *5*, 2083. doi:10.1039/c3py01519j
- Unay, H.; Unlu, N. A.; Hizalan, G.; Hacioglu, S. O.; Yildiz, D. E.; Toppare, L.; Cirpan, A. *J. Polym. Sci., Part A: Polym. Chem.* **2015**, *53*, 528. doi:10.1002/pola.27467
- Wong, W. W. H.; Subbiah, J.; Puniredd, S. R.; Pisula, W.; Jones, D. J.; Holmes, A. B. *Polym. Chem.* **2014**, *5*, 1258. doi:10.1039/C3PY01142A
- Tessarolo, M.; Gedefaw, D.; Bolognesi, M.; Liscio, F.; Henriksson, P.; Zhuang, W.; Milita, S.; Muccini, M.; Wang, E.; Seri, M.; Andersson, M. R. *J. Mater. Chem. A* **2014**, *2*, 11162. doi:10.1039/c4ta01479k
- Tregnago, G.; Steckler, T. T.; Fenwick, O.; Andersson, M. R.; Cacialli, F. *J. Mater. Chem. C* **2015**, *3*, 2792. doi:10.1039/C5TC00118H
- Li, Z.; Lin, H.; Jiang, K.; Carpenter, J.; Li, Y.; Liu, Y.; Hu, H.; Zhao, J.; Ma, W.; Ade, H.; Yan, H. *Nano Energy* **2015**, *15*, 607. doi:10.1016/j.nanoen.2015.05.016
- Yuan, M.-C.; Chiu, M.-Y.; Chiang, C.-M.; Wei, K.-H. *Macromolecules* **2010**, *43*, 6270. doi:10.1021/ma100522a
- Wang, B.; Zhang, J.; Tam, H. L.; Wu, B.; Zhang, W.; Chan, M. S.; Pan, F.; Yu, G.; Zhu, F.; Wong, M. S. *Polym. Chem.* **2014**, *5*, 836. doi:10.1039/C3PY00961K
- Osaka, I.; Saito, M.; Koganezawa, T.; Takimiya, K. *Adv. Mater.* **2014**, *26*, 331. doi:10.1002/adma.201303059
- Hellström, S.; Zhang, F.; Inganäs, O.; Andersson, M. R. *Dalton Trans.* **2009**, *10032*. doi:10.1039/b913769f
- Brabec, C. J.; Cravino, A.; Meissner, D.; Sariciftci, N. S.; Fromherz, T.; Rispens, M. T.; Sanchez, L.; Hummelen, J. C. *Adv. Funct. Mater.* **2001**, *11*, 374. doi:10.1002/1616-3028(200110)11:5<374::AID-ADFM374>3.0.CO;2-W
- Huo, L.; Hou, J.; Zhang, S.; Chen, H.-Y.; Yang, Y. *Angew. Chem., Int. Ed.* **2010**, *49*, 1500. doi:10.1002/anie.200906934
- Bredas, J.-L. *Mater. Horiz.* **2014**, *1*, 17. doi:10.1039/C3MH00098B
- Chen, Z.-K.; Huang, W.; Wang, L.-H.; Kang, E.-T.; Chen, B. J.; Lee, C. S.; Lee, S. T. *Macromolecules* **2000**, *33*, 9015. doi:10.1021/ma0005670

## License and Terms

This is an Open Access article under the terms of the Creative Commons Attribution License (<http://creativecommons.org/licenses/by/2.0/>), which permits unrestricted use, distribution, and reproduction in any medium, provided the original work is properly cited.

The license is subject to the *Beilstein Journal of Organic Chemistry* terms and conditions: (<http://www.beilstein-journals.org/bjoc>)

The definitive version of this article is the electronic one which can be found at: doi:10.3762/bjoc.12.160



# Effect of the $\pi$ -conjugation length on the properties and photovoltaic performance of A- $\pi$ -D- $\pi$ -A type oligothiophenes with a 4,8-bis(thienyl)benzo[1,2-*b*:4,5-*b'*]dithiophene core

Ni Yin<sup>1,2</sup>, Lilei Wang<sup>1,3</sup>, Yi Lin<sup>4</sup>, Jinduo Yi<sup>1</sup>, Lingpeng Yan<sup>1</sup>, Junyan Dou<sup>1</sup>, Hai-Bo Yang<sup>3</sup>, Xin Zhao<sup>\*2</sup> and Chang-Qi Ma<sup>\*1</sup>

## Full Research Paper

Open Access

Address:

<sup>1</sup>Printable Electronics Research Center, Suzhou Institute of Nano-Tech and Nano-Bionics (SINANO), Chinese Academy of Sciences, 398 Ruo Shui Road, SEID SIP, Suzhou, Jiangsu, 215123, P. R. China, <sup>2</sup>College of Chemistry, Biology and Material Engineering, Suzhou University of Science and Technology, 1 Ke Rui Road, Suzhou, Jiangsu, 215009, P. R. China, <sup>3</sup>Department of Chemistry, Shanghai Key Laboratory of Green Chemistry and Chemical, East China Normal University, 3663 North Zhongshan Road, Shanghai 200062, P. R. China and <sup>4</sup>Department of Chemistry, Xi'an Jiaotong Liverpool University, 111 Ren Ai Road, Dushu Lake Higher Education Town, Suzhou, Jiangsu, 215123, P. R. China

Email:

Xin Zhao<sup>\*</sup> - zhaoxinsz@126.com; Chang-Qi Ma<sup>\*</sup> - cqma2011@sinano.ac.cn

\* Corresponding author

Keywords:

A- $\pi$ -D- $\pi$ -A-type conjugated molecules; benzodithiophene;  $\pi$ -bridge; chain length effect; organic solar cell

*Beilstein J. Org. Chem.* **2016**, *12*, 1788–1797.

doi:10.3762/bjoc.12.169

Received: 25 April 2016

Accepted: 20 July 2016

Published: 10 August 2016

This article is part of the Thematic Series "Organic photovoltaics".

Guest Editor: D. J. Jones

© 2016 Yin et al.; licensee Beilstein-Institut.

License and terms: see end of document.

## Abstract

Benzo[1,2-*b*:4,5-*b'*]dithiophene (BDT) is an excellent building block for constructing  $\pi$ -conjugated molecules for the use in organic solar cells. In this paper, four 4,8-bis(5-alkyl-2-thienyl)benzo[1,2-*b*:4,5-*b'*]dithiophene (TBDT)-containing A- $\pi$ -D- $\pi$ -A-type small molecules (COOP-*n*HT-TBDT, *n* = 1, 2, 3, 4), having 2-cyano-3-octyloxy-3-oxo-1-propenyl (COOP) as terminal group and regioregular oligo(3-hexylthiophene) (nHT) as the  $\pi$ -conjugated bridge unit were synthesized. The optical and electrochemical properties of these compounds were systematically investigated. All these four compounds displayed broad absorption bands over 350–600 nm. The optical band gap becomes narrower (from 1.94 to 1.82 eV) and the HOMO energy levels increased (from −5.68 to −5.34 eV) with the increase of the length of the  $\pi$ -conjugated bridge. Organic solar cells using the synthesized compounds as the electron donor and PC<sub>61</sub>BM as the electron acceptor were fabricated and tested. Results showed that compounds with longer oligothiophene  $\pi$ -bridges have better power conversion efficiency and higher device stability. The device based on the quaterthiophene-bridged compound **4** gave a highest power conversion efficiency of 5.62% with a *V*<sub>OC</sub> of 0.93 V, *J*<sub>SC</sub> of 9.60 mA·cm<sup>−2</sup>, and a FF of 0.63.

## Introduction

Solution-processed organic solar cells (OSCs) are considered to be one of the most promising renewable energy technologies because of the advantages of low cost, lightweight, flexibility, and great potentials in large-scale production [1,2]. In the past few years, OSCs based on polymers have achieved power conversion efficiencies (PCEs) of over 11% [3,4]. Meanwhile, OSCs based on conjugated small molecules attracted also enormous attentions due to their ease of synthesis, defined chemical structure, low batch-to-batch variation, and good reproducibility in photovoltaic performance [5–7]. To date, PCEs of more than 9% for small molecule OSCs (SMOSCs) have been reported [8–12].

Among various electron-donating moieties, benzo[1,2-*b*:4,5-*b'*]dithiophene (BDT) has been widely used as the central building block for constructing high-performance A– $\pi$ –D– $\pi$ –A-type organic semiconductors for organic solar cells, where A represents the terminal electron acceptor unit, D represents the core electron donor unit, and  $\pi$  represents the conjugated  $\pi$ -bridge [13,14], and a maximum PCE of 9.95% was reported for a terthiophene-bridged small molecule with a BDT core [8]. Currently, there are three main structure modifications of A– $\pi$ –D– $\pi$ –A-type molecules with a BDT core. One is the substitution on the 4,8-positions of the BDT core with aromatic units, including alkyl/alkoxyl/alkylthiol-substituted phenyl groups [15], thiienyl group [16–18], and thienothiophene [17,19]. Structure modifications of the BDT core with aromatic units extend the  $\pi$ -conjugation of BDT unit to a two-dimensional structure, which increases intermolecular interactions, and consequently improves the device performance. The other one is to attach different electron acceptor units at the terminal of the molecules, including: dicyanovinyl [20,21], cyanoacetate [20–23], rhodanine [8,14,17,19,23], 1,3-indandione [16], and diketopyrrolopyrrol (DPP) moieties [24,25]. Changing the electron-withdrawing strength of the terminal electron acceptor unit, on the other hand, will change the intramolecular charge transfer state and tune the light absorption ability, which will consequently change the photovoltaic performance of the materials as well.

The third possible structure modification of BDT derivatives is to tune the conjugation length of the  $\pi$ -bridges. In this respect, oligothiophenes, including monothiophene [16,20], bithiophene [16], terthiophene [8,14,15,17–19,21–23,26], quaterthiophene and quinquethiophene [27], and cyclopentadithiophene [28] have been utilized as the  $\pi$ -bridge in constructing conjugated molecules with a BDT core. Among these 3,3"-dihexyl-2,2':5":2"-terthiophene (3T) is the most widely used  $\pi$ -bridge. It is worth to mention that 3-alkylthiophen can be coupled in different ways at the 2- and 5-positions, yielding oligo(3-alkylthio-

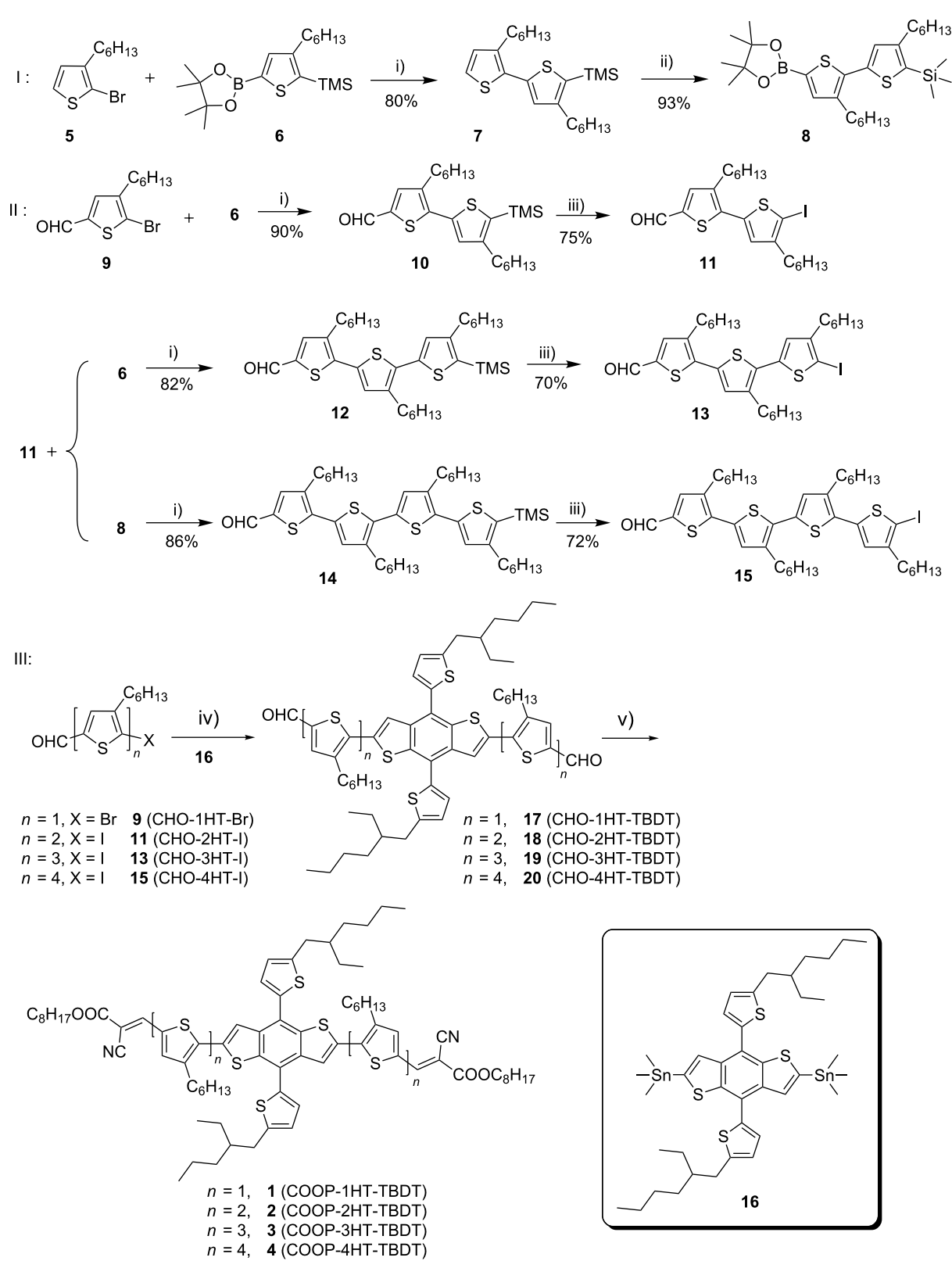
phene)s with different isomeric structures. In order to minimize the synthesis efforts, structurally symmetric oligothiophene units are mostly used for constructing A– $\pi$ –D– $\pi$ –A-type molecules with a BDT core. Interestingly, although various terthiophene-based derivatives with a BDT core have been reported, there is only one paper that reported the synthesis and characterization of BDT derivatives based on oligothiophene  $\pi$ -bridges with more than three thiophene units [27], where symmetric quater- and quinquethiophenes were used as the  $\pi$ -conjugation bridge. Surprisingly, the quaterthiophene-bridged compound showed the worst photovoltaic performance when blending with a fullerene derivative as the photoactive layer. This was ascribed to the influence of the orientation of the alkyl side chains. Although regioregular oligo(3-alkylthiophene)s are better building blocks for studying the effect of the  $\pi$ -conjugation length, only regioregular terthiophene (rr-3T) was reported to be used as the  $\pi$ -bridge unit in BDT derivatives [21,22]. BDT derivatives based on regioregular bi- or quaterthiophene have not been reported, and there is no systematically investigation on the effect of the  $\pi$ -conjugation length yet.

To better understand the effect of the conjugation length on the molecular structure and properties of the conjugated molecules with BDT core, we report here a series of A– $\pi$ –D– $\pi$ –A-type conjugated molecules with a regioregular oligo(3-hexylthiophene) chain as the  $\pi$ -bridge unit. The optical and electrochemical properties of these compounds were systematically investigated. Organic solar cells based these conjugated small molecules as the electron donor were fabricated and tested. In addition, long-term stability of these solar cells was also studied, and a general structure–property–performance relationship of these type of molecules is evaluated, which could serve as a useful guideline for further molecular design and synthesis for organic solar cells.

## Results and Discussion

### Synthesis and structure characterization of COOP-*n*HT-TBDT

The synthetic routes to compounds **1–4** (COOP-*n*HT-TBDT, *n* = 1–4; COOP = 2-cyano-3-octyloxy-3-oxo-1-propenyl, *n*HT = oligo(3-hexylthiophene), TBDT = 4,8-bis(5-alkyl-2-thienyl)benzo[1,2-*b*:4,5-*b'*]dithiophene) is shown in Scheme 1. The bithiophene building block, 3,4'-dihexyl-5'-ido-2,2'-bithiophene-5-carbaldehyde (**11**) was synthesized by an ipso-substitution of **10**, which was synthesized by a Suzuki coupling of **9** with **6**, with ICl. The regioregular terthiophene and quaterthiophene building blocks were synthesized according to a similar synthetic route starting in high yields. The aldehyde precursors with BDT core CHO-*n*HT-TBDTs **17–20** were synthesized through a Pd-catalyzed Stille coupling reaction of **9**, **11**, **13** and



**Scheme 1:** Synthetic route to compounds **1–4** with BDT core. Reagents and conditions: i)  $[\text{Pd}_2(\text{dba})_3 \cdot \text{CHCl}_3, \text{HP}(t\text{-Bu})_3\text{BF}_4, \text{K}_2\text{CO}_3, \text{THF}$ ; ii)  $n\text{-BuLi/THF}$ , 2-isopropoxy-4,4,5,5-tetramethyl-1,3,2-dioxaborolane; iii)  $\text{ICl/THF}$ ; iv)  $\text{Pd}(\text{PPh}_3)_4, \text{DMF}, 80^\circ\text{C}$ ; v) octyl cyanoacetate, piperidine,  $\text{CHCl}_3$ , reflux.

**15** with **16**, respectively (reaction iv), and the final compounds, COOP-*n*HT-TBDTs **1–4**, were obtained by Knoevenagel condensations of CHO-*n*HT-TBDTs **17–20** with octylcyanoacetate (reaction v). Since all these compounds have multiple alkyl chains, they are soluble in common organic solvents, so that the final compounds can be processed well in solution. Complete characterization of both the intermediate and the final compounds was performed by  $^1\text{H}$  NMR,  $^{13}\text{C}$  NMR and mass spectrometry (see details in Supporting Information File 1).

## Optical properties

Figure 1 presents the UV–vis absorption spectra of COOP-*n*HT-TBDTs **1–4** in solution and in thin solid films. The spectroscopic data were collected and listed in Table 1. In dilute chloroform solution, all these compounds show intensive absorption bands from 350 to 600 nm with a gradual increase of the molar extinction coefficient. Interestingly, the three molecules **2**, **3**,

and **4** display one broad absorption band peaking at 494, 491, and 485 nm, respectively, while two absorption bands peaking at 440 and 498 nm were found for **1**. Elongation of the  $\pi$ -conjugated bridge leads to a slight hypochromic shift of the absorption band, presumably ascribed to a disorder of the complex structures of the  $\pi$ -conjugation chain, or due to the steric hindrance effects of the alkyl side chains for the bigger molecules [29,30]. The absorption onset wavelength increases slightly with the increase of the  $\pi$ -bridge chain length, suggesting an extended  $\pi$ -conjugation system for the compounds with longer oligothiophene chains.

In the solid state, absorption spectra of these compounds (see Figure 1b) are remarkably broadened and red-shifted relative to those in solutions, which is attributable to strong  $\pi$ – $\pi$  stacking interaction between the molecular backbones in the solid films [31,32]. It is noticeable that compound **1** in the film shows two

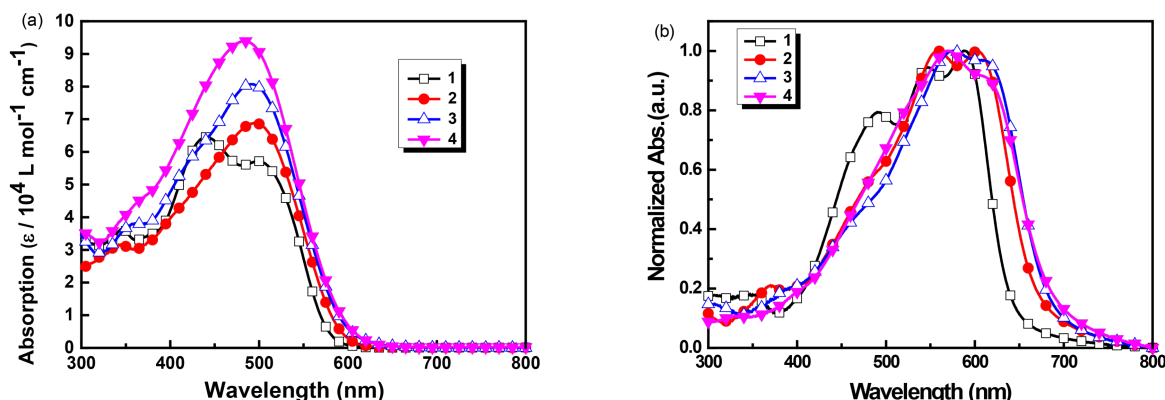


Figure 1: UV–vis absorption spectra of COOP-*n*HT-TBDTs **1–4** (a) in chloroform solution ( $5.0 \times 10^{-5} \text{ mol} \cdot \text{L}^{-1}$ ) and (b) in solid films.

**Table 1:** Optical and electrochemical properties of **1–4** in comparison to other compounds in the literature.

compound	$\lambda_{\max}^{\text{sol}}$ [nm] <sup>a</sup>	$\varepsilon_{\max}^{\text{sol}}$ [mol <sup>-1</sup> ·L <sup>-1</sup> ·cm <sup>-1</sup> ] <sup>b</sup>	$\lambda_{\max}^{\text{film}}$ [nm]	$E_g^{\text{opt}}$ [eV] <sup>c</sup>	$E_{\text{ox}}^0$ [V] <sup>d</sup>	$E_{\text{red}}^0$ [V] <sup>d,e</sup>	$E_{\text{HOMO}}$ [eV] <sup>f</sup>	$E_{\text{LUMO}}$ [eV] <sup>f</sup>	$E_g^{\text{CV}}$ [eV] <sup>g</sup>	ref.
<b>1</b>	440 (498) <sup>h</sup>	64,500	580 (547) <sup>h</sup>	1.94	0.66	-1.53	-5.68 (-5.38) <sup>i</sup>	-3.65 (-3.35) <sup>i</sup>	2.03	[20]
<b>2</b>	494	68,800	558 (602) <sup>h</sup>	1.86	0.50	-1.62	-5.52 (-5.22) <sup>i</sup>	-3.56 (-3.26) <sup>i</sup>	1.96	this work
<b>3</b>	491	80,700	576 (625) <sup>h</sup>	1.82	0.42	-1.63	-5.43 (-5.13) <sup>i</sup>	-3.55 (-3.25) <sup>i</sup>	1.88	this work
<b>4</b>	485	93,900	570 (614) <sup>h</sup>	1.82	0.32	-1.64	-5.35 (-5.05) <sup>i</sup>	-3.53 (-3.23) <sup>i</sup>	1.82	this work
DCAO3TBDT	494	72,000	560	1.84	—	—	-5.04 <sup>i</sup>	-3.24 <sup>i</sup>	1.80	[23]
TBDTCNR	488	—	578	1.75	—	—	-5.40 <sup>i</sup>	-3.63 <sup>i</sup>	1.77	[21]

<sup>a</sup>In  $\text{CHCl}_3$  ( $5.0 \times 10^{-5} \text{ mol} \cdot \text{L}^{-1}$ ); <sup>b</sup>extinction coefficient was obtained by linearly fitting the absorbance as a function of the concentration; <sup>c</sup>optical band gap, calculated from the absorption onset wavelength ( $\lambda_{\text{onset}}$ ) in solid films according to the equation  $E_g^{\text{opt}}$  (eV) =  $1240/\lambda_{\text{onset}}$  (nm); <sup>d</sup>measured in  $\text{CHCl}_3$  solution ( $1.0 \times 10^{-3} \text{ mol} \cdot \text{L}^{-1}$ ); <sup>e</sup>irreversible wave:  $E_{\text{red}}^0$  was estimated as the potential where  $i_{\text{pc}} = 0.855 \times i_{\text{pc}}^{\text{max}}$ ; <sup>f</sup>calculated from the cyclic voltammograms,  $E_{\text{HOMO}} = -[E_{\text{ox}}^{\text{onset}} + 5.1]$  (eV),  $E_{\text{LUMO}} = -[E_{\text{red}}^{\text{onset}} + 5.1]$  (eV); <sup>g</sup>electrochemical band gap  $E_g^{\text{CV}} = E_{\text{HOMO}} - E_{\text{LUMO}} = -[E_{\text{ox}}^{\text{onset}} - E_{\text{red}}^{\text{onset}}]$  (eV); <sup>h</sup>shoulder peak; <sup>i</sup>calculated from the cyclic voltammograms,  $E_{\text{HOMO}} = -[E_{\text{ox}}^{\text{onset}} + 4.8]$  (eV),  $E_{\text{LUMO}} = -[E_{\text{red}}^{\text{onset}} + 4.8]$  (eV).

shoulder peaks in the long wavelength range, while compounds **2**, **3**, and **4** have only one shoulder peak. The optical band gaps calculated from the onsets of absorption edge of the four molecules are 1.94, 1.86, 1.82 and 1.82 eV, respectively, in agreement with the BDT derivatives reported in the literatures [21,23].

### Electrochemical properties

Cyclic voltammetry (CV) was applied to investigate the energy levels of **1–4**. The cyclic voltammograms of these four compounds are presented in Figure 2 and the electrochemical data are listed in Table 1. As can be seen from Figure 2, compounds **1** and **2** exhibited two reversible oxidation processes in the positive range, while **3** and **4** showed multiple oxidation processes, suggesting more oxidation processes of the  $\pi$ -conjugation bridge units for the larger molecules. The first oxidation potentials ( $E_{\text{ox}}^0$  vs  $\text{Fc}^+/\text{Fc}$ ) for COOP-*n*HT-TBDTs were measured to be 0.66, 0.50, 0.42, and 0.32 V, for  $n = 1, 2, 3$ , and 4, respectively, indicating a decreasing trend with the increase of the  $\pi$ -bridge chain length. Meanwhile, one irreversible reduction process was found for all these four compounds in the negative potential range. Except for **1**, which showed a reduction potential ( $E_{\text{red}}^0$ ) of -1.53 eV, the other three compounds showed almost identical  $E_{\text{red}}^0$  of -1.60 V, indicating that the reduction process is mainly due to the reduction of the terminal COOP group. The onset oxidation potentials ( $E_{\text{ox}}^{\text{onset}}$ ) and onset reduction potentials ( $E_{\text{red}}^{\text{onset}}$ ) determined from the CV results are also listed in Table 1. The frontier molecular orbital energy levels (HOMO/LUMO) and also the energy band gaps of these compounds were calculated according to the method reported in our previous paper [20], where the ferrocene/ferrocenium couple ( $\text{Fc}^+/\text{Fc}$ ) was used as the standard, and the vacuum

energy level of  $\text{Fc}^+/\text{Fc}$  was taken as -5.1 eV [33]. As can be seen from this table, the HOMO energy levels of COOP-*n*HT-TBDTs increased slightly from -5.68 to -5.34 V with increasing  $\pi$ -conjugation bridge length. Except for **1**, which has a LUMO level of -3.65 eV, the other three compounds possess similar LUMO level at -3.55 eV, attributed to the same electron-withdrawing terminal units. The LUMO energy levels of COOP-*n*HT-TBDTs are more than 0.3 eV higher than that of  $\text{PC}_{61}\text{BM}$  [34], which provides a sufficient driving force for electron transfer from COOP-*n*HT-TBDTs to  $\text{PC}_{61}\text{BM}$  (Figure 2b). On the other hand, the low-lying HOMO energy level of COOP-*n*HT-TBDTs would be beneficial for achieving a high open circuit voltage ( $V_{\text{OC}}$ ), since  $V_{\text{OC}}$  of organic solar cells is directly related to the difference of the HOMO energy of the donor material and the LUMO energy of the acceptor.

### Photovoltaic performance

Bulk heterojunction (BHJ) solar cells with a device structure of ITO/PEDOT:PSS (30 nm)/photoactive layer/LiF (1.5 nm)/Al (100 nm) were fabricated and tested, where the blended solid film of the synthesized small molecules as donor and  $\text{PC}_{61}\text{BM}$  as acceptor was used as the photoactive layer. The photovoltaic performances of **1** has been reported in our previous paper [20], and the PV performance data of the best cell are listed in Table 2 for comparison. The photovoltaic performance of cells based on compounds **2**, **3**, and **4** were carefully optimized by varying the D/A blend ratio. Figure S4 and S5 (Supporting Information File 1) depict the current density–voltage ( $J$ – $V$ ) curves and the external quantum efficiency (EQE) spectra of cells based on **2**, **3**, and **4**, and the photovoltaic performance data are listed in Table 2. As can be seen from Table 2, the optimal D/A blend ratio for **2**: $\text{PC}_{61}\text{BM}$  based cells was found to

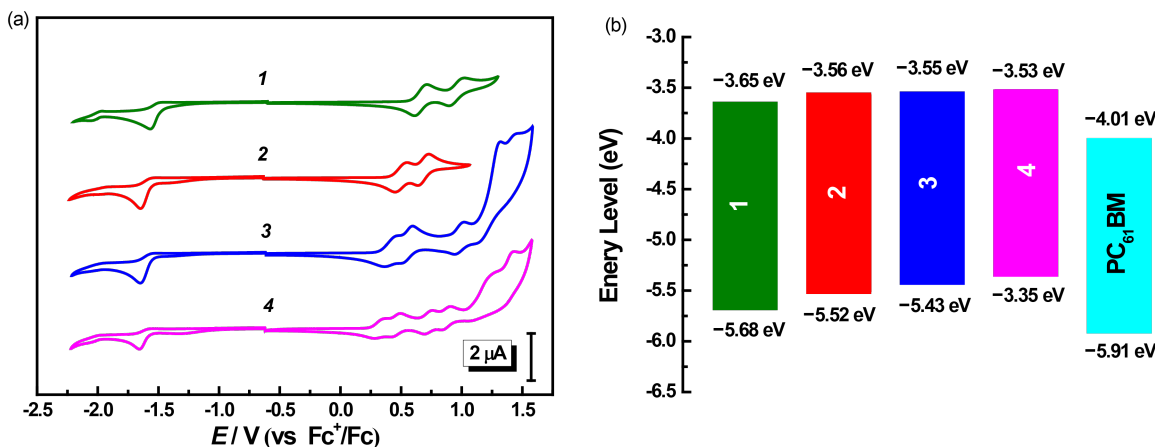


**Figure 2:** (a) Cyclic voltammograms of **1–4** measured in  $\text{CH}_2\text{Cl}_2$  solution ( $1.0 \times 10^{-3}$  mol·L $^{-1}$ ) with  $0.1 \text{ mol}\cdot\text{L}^{-1}$   $\text{Bu}_4\text{NPF}_6$  at a scan rate of  $100 \text{ mV}\cdot\text{s}^{-1}$ ; (b) HOMO and LUMO energy levels of these compounds.

**Table 2:** Photovoltaic properties of COOP-*n*HT-TBDT:PC<sub>61</sub>BM-based devices.

entry	donor	D/A ratio [w/w]	V <sub>OC</sub> [V]	J <sub>SC</sub> [mA·cm <sup>-2</sup> ] <sup>a</sup>	FF [%]	PCE [%]	average PCE [%] ( $\pm$ std. dev.) <sup>b</sup>
1	<b>1<sup>c</sup></b>	1:0.6	1.04	2.28	29	0.69	0.61 ( $\pm$ 0.072)
2		1:0.4	1.04	5.30	36	2.01	1.89 ( $\pm$ 0.24)
3	<b>2</b>	1:0.6	1.07	6.36	37	2.52	2.35 ( $\pm$ 0.10)
4		1:0.8	1.06	5.20	36	1.98	1.78 ( $\pm$ 0.17)
5		1:0.2	0.97	5.99	47	2.73	2.64 ( $\pm$ 0.08)
6	<b>3</b>	1:0.4	0.97	9.38	52	4.73	4.58 ( $\pm$ 0.16)
7		1:0.6	0.97	8.94	47	4.07	3.79 ( $\pm$ 0.18)
8		1:0.8	0.95	6.35	37	2.23	1.97 ( $\pm$ 0.21)
9		1:0.2	0.93	6.07	59	3.33	3.14 ( $\pm$ 0.15)
10	<b>4</b>	1:0.4	0.93	9.60	63	5.62	5.27 ( $\pm$ 0.21)
11		1:0.6	0.91	7.73	44	3.07	2.75 ( $\pm$ 0.27)
12		1:0.8	0.91	5.72	40	2.08	1.93 ( $\pm$ 0.21)

<sup>a</sup>determined by convoluting the spectral response with the AM 1.5G spectrum (100 mW·cm<sup>-2</sup>); <sup>b</sup>standard deviation was calculated over eight individual devices; <sup>c</sup>data from [20].

be 1:0.6, which showed a maximum PCE of 2.52% (and an average PCE of 2.35%) with a high V<sub>OC</sub> of 1.07 V, J<sub>SC</sub> of 6.36 mA·cm<sup>-2</sup>, and FF of 37% for the best cell. The optimal D/A blend ratio was found to be 1:0.4 for cells based on **3** and **4** (Table 2, entry 6 and 10), which is different to that of cells based on **1** and **2**. High PCEs of 4.73% and 5.62% were achieved for cells with **3** and **4**, respectively, which are much higher than that of the devices based on smaller molecules. Obviously, with the extension of conjugation  $\pi$ -bridges, the PV performance of the COOP-*n*HT-TBDTs enhanced gradually. Since V<sub>OC</sub> decreases slightly with the increase of the conjugation length of the  $\pi$ -bridge, such a device performance enhancement was mainly ascribed to the increase of J<sub>SC</sub> and FF (Table 2). EQE spectra comparison clearly confirmed the higher

photon-to-electron conversion efficiency for the bigger molecules (Figure 3b). In addition, the photo responses of devices based on **3** and **4** cover a wavelength range from 380 to 700 nm, which is wider than that of devices based on **1** and **2** (Figure 3b, insert), agreeing with the absorption spectra of the corresponding thin solid films (Figure 1b). Solar cells based on a 4:PC<sub>71</sub>BM photoactive layer were also fabricated and tested. However, the PC<sub>71</sub>BM-based devices showed a slightly decreased performance compared to the PC<sub>61</sub>BM-based devices (Figure S5, Supporting Information File 1). Using additives or post-thermal annealing did not improve device performance. We speculate that impurities in PC<sub>71</sub>BM or the non-ideal interface between PEDOT:PSS and the photoactive layer could be the reason for the lower device performance. However, further

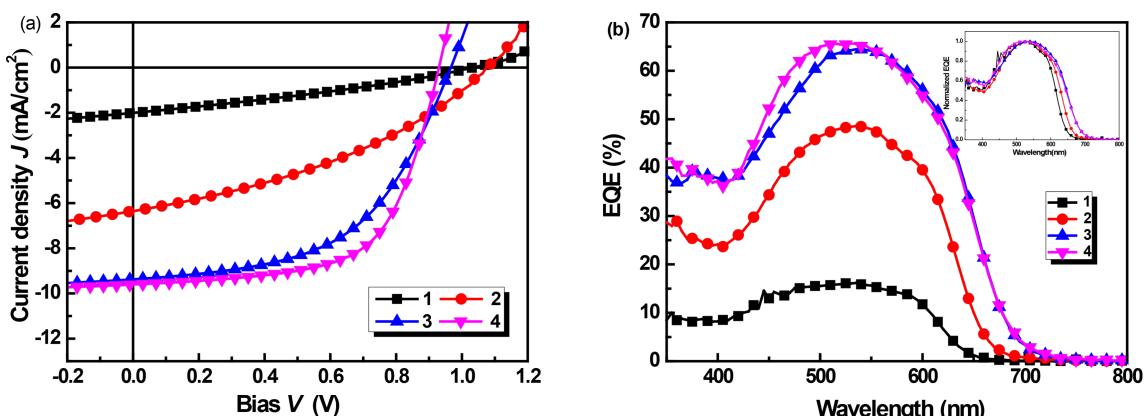


**Figure 3:** (a) J–V curves of the best COOP-*n*HT-TBDT:PC<sub>61</sub>BM solar cells; (b) EQE spectra of the corresponding cells, Inset: normalized EQE spectra of four best devices, showing the difference in spectrum response wavelength range.

experiments are still need to fully understand the detailed reasons. Nevertheless, the PCE of 5.62% for the **4**:PC<sub>61</sub>BM cells is among the best performance for cells based on COOP-capped BDT derivatives [21–23,35–37].

### Surface morphology of the blended films

The surface morphology of the COOP-*n*HT-TBDT:PC<sub>61</sub>BM films was scrutinized with atomic force microscopy (AFM). Figure 4 depicts the topological images of the blended films prepared under the optimized conditions. The surface roughness for the COOP-*n*HT-TBDT:PC<sub>61</sub>BM blended films was measured to be 1.23, 2.14, 0.96 and 2.84 nm for films based on **1**, **2**, **3**, and **4**, respectively, demonstrating a reasonable surface smoothness for these films. Obviously, crystalline domains can be seen in these films, among which, the **2**:PC<sub>61</sub>BM and **4**:PC<sub>61</sub>BM blended films showed larger crystalline domains compared to the films based on **3** and **4**. Such a nanomorphology difference could be ascribed to the chemical structure difference of the  $\pi$ -conjugation bridges, demonstrating a possible odd–even effect. Nevertheless, the large crystalline domains of the **4**-based film lead to a better charge carrier mobility (vide infra), which is beneficial for device performance.

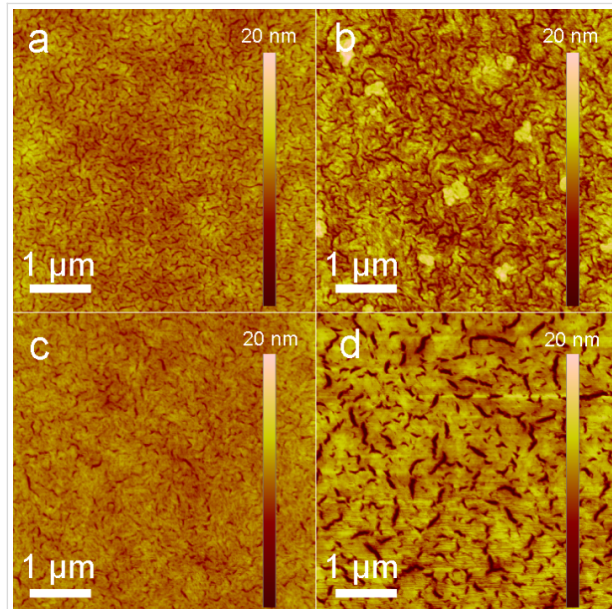


**Figure 4:** AFM height images of COOP-*n*HT-TBDT:PC<sub>61</sub>BM blended films: (a) **1**, 1:0.6 (w/w); (b) **2**, 1:0.6 (w/w); (c) **3**, 1:0.4 (w/w); (d) **4**, 1:0.4 (w/w).

### Charge-carrier mobility of the blended films

To further understand the influence of the chemical structure on the device performance, the hole mobility of these compounds in blended films was measured using the space-charge-limited current method (SCLC). The device structure studied here was

ITO/PEDOT:PSS/COOP-*n*HT-TBDT:PC<sub>61</sub>BM/MoO<sub>3</sub>/Al, and the thin film deposition method is similar to that for solar cell fabrication. The analysis method was described in detail in our previous paper [34]. The hole transport mobilities of COOP-*n*HT-TBDT were measured to be  $2.01 \times 10^{-6}$ ,  $1.81 \times 10^{-6}$ ,  $4.60 \times 10^{-4}$  and  $8.22 \times 10^{-4}$  cm<sup>2</sup>·V<sup>-1</sup>·s<sup>-1</sup> for **1**, **2**, **3**, and **4**, respectively. Obviously, the largest molecule **4** displays the highest hole mobility, which could be owing to the formation of large crystalline domains in **4**:PC<sub>61</sub>BM blended film, as shown in Figure 5. The high hole mobility for the larger molecules could be one of the reasons for the higher power conversion efficiency for devices based on COOP-*n*HT-TBDT:PC<sub>61</sub>BM (Table 2).

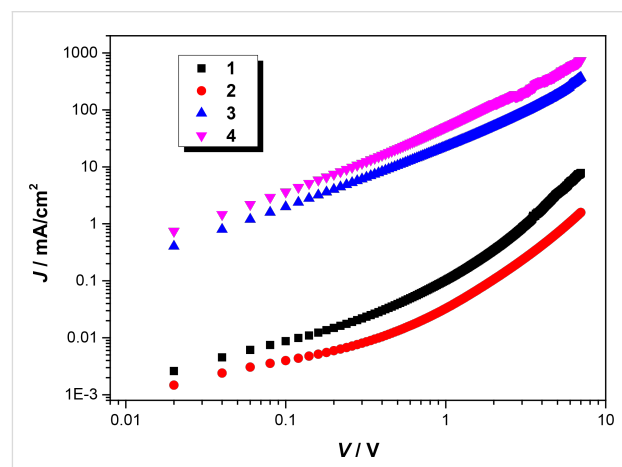


**Figure 5:** J–V curves of COOP-*n*HT-TBDT:PC<sub>61</sub>BM-based hole-only devices.

### Long-term stability

Finally, the long-term stability of these COOP-*n*HT-TBDT-based solar cells was tested. Devices for stability test were fabricated according to the optimized conditions described above, and these devices showed an initial performance similar to the best PCE as listed in Table 2 for each compound. Figure 6 presents the evolution of  $V_{OC}$ ,  $J_{SC}$ , FF and PCE of un-encapsulated COOP-*n*HT-TBDT:PC<sub>61</sub>BM cells tested in N<sub>2</sub> atmosphere under continuous illumination. To fully simulate the degradation behaviour of solar cells under working conditions, an external load to match the maximum power output point (mpp) was attached to each device, which was described in our previous report [38]. Similar to the previous report, the  $V_{OC}$  of the devices decreased only slightly during light illumination. However, the  $J_{SC}$  decreased to 42%, 12%, 10% and 4% of their initial value for cells based on **1**, **2**, **3** and **4**, respectively (Figure 6b). In addition, the FF of these four devices decreased very slowly (Figure 6c) during aging. Overall, the **4**-based devices showed the highest device stability with only 10% decay of its initial device performance, whereas the **1**

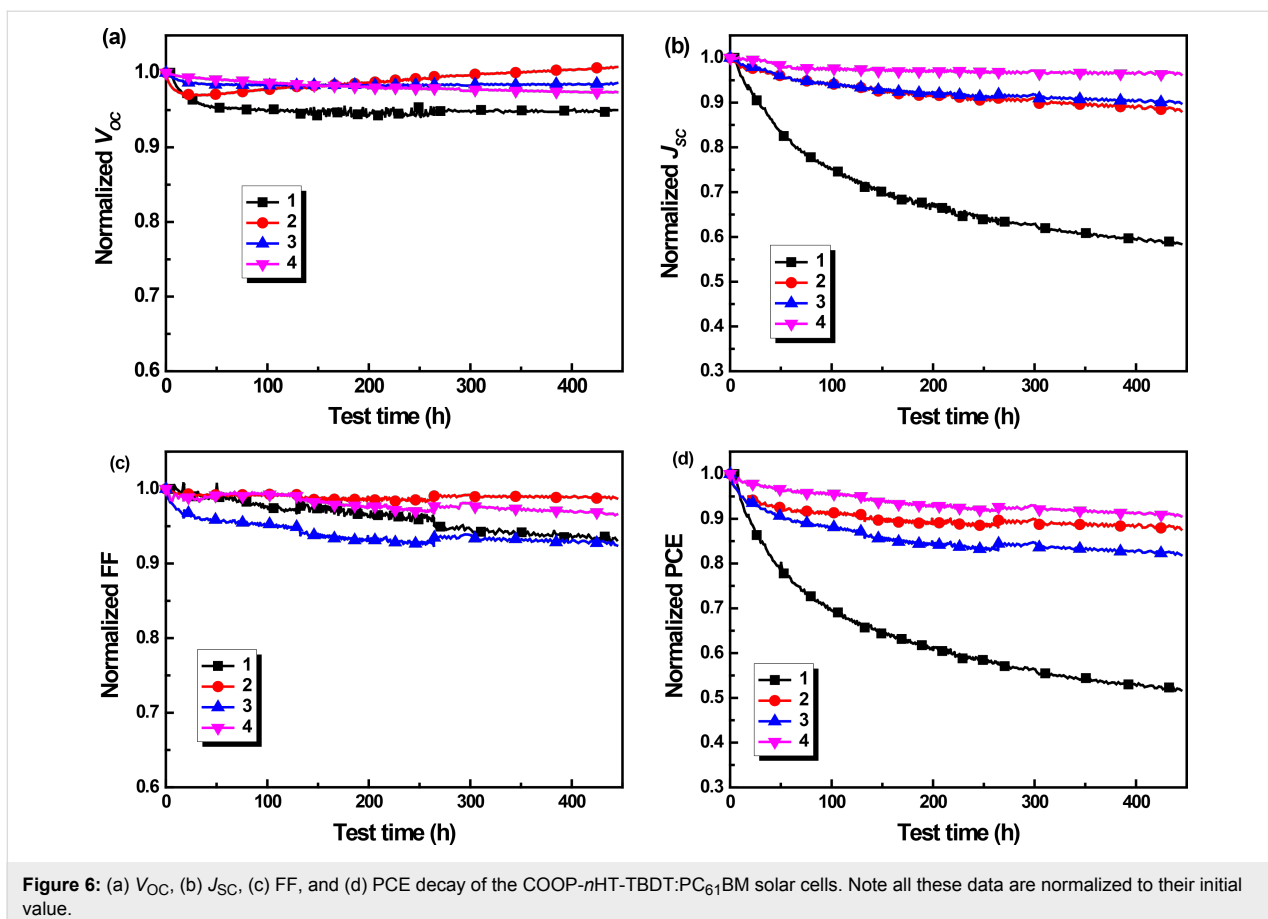


**Figure 6:** (a)  $V_{OC}$ , (b)  $J_{SC}$ , (c) FF, and (d) PCE decay of the COOP-*n*HT-TBDT:PC<sub>61</sub>BM solar cells. Note all these data are normalized to their initial value.

showed the worst device stability, in which a decrease of 48% was measured. Surprisingly, **2** showed also higher device stability when compared to **3**, which was mainly due to a more stable FF. More nanomorphology stability was supposed to be main reason for the higher stability of the larger molecules, since larger molecules have a higher energy barrier for diffusion. However, more experiments are still needed to further understand the stability improvement of the larger molecules.

## Conclusion

Four small A- $\pi$ -D- $\pi$ -A molecules with BDT core (COOP-*n*HT-TBDT, *n* = 1, 2, 3, 4) with regioregular oligo(3-hexylthiophene)  $\pi$ -bridges were synthesized and characterized. The length of the  $\pi$ -conjugation bridges has a significant impact on the optical, electrochemical properties and, in consequence, the device performance. With the elongation of the conjugated chain, broader absorption bands and narrower optical band gaps were observed for this type of compound, which would be beneficial for increasing  $J_{SC}$  in solar cell applications. A high  $V_{OC}$  of 0.9–1.0 V was achieved for the COOP-*n*HT-TBDT:PC<sub>61</sub>BM cells, owing to the low-lying HOMO levels of these compounds. The lengthening of the conjugated  $\pi$ -bridges improves the performance of the COOP-*n*HT-TBDT:PC<sub>61</sub>BM

cells, and a maximum PCE of 5.62% with a  $V_{OC}$  of 0.93 V,  $J_{SC}$  of 9.60 mA·cm<sup>-2</sup>, and FF of 0.63 was achieved for the 4:PC<sub>61</sub>BM-based device. In addition, improved device stability was also found for the larger molecules, which could be ascribed to the higher stability of the nanomorphology.

## Supporting Information

Supporting Information features experimental details about the synthesis of COOP-*n*HT-TBDT, the determination of molecular molar extinction coefficient of COOP-*n*HT-TBDT, the  $J$ - $V$  curves and EQE spectra of organic solar cells based on COOP-*n*HT-TBDT at different blend ratios, a  $J$ - $V$  comparison of devices based on 4:PC<sub>61</sub>BM and 4:PC<sub>71</sub>BM, UV-vis absorption spectra of COOP-*n*HT-TBDT:PC<sub>61</sub>BM blended films, as well as the NMR and MALDI-TOF MS spectra of COOP-*n*HT-TBDT.

### Supporting Information File 1

Additional experimental data.

[<http://www.beilstein-journals.org/bjoc/content/supplementary/1860-5397-12-169-S1.pdf>]

## Acknowledgements

The work is financially supported by the National Natural Science Foundation of China (21274163), Strategic Priority Research Program of the Chinese Academy of Sciences (Grant No. XDA09020201), and the "Hundred Talents Project" (Initialization Support) of the Chinese Academy of Sciences.

## References

1. Lu, L.; Zheng, T.; Wu, Q.; Schneider, A. M.; Zhao, D.; Yu, L. *Chem. Rev.* **2015**, *115*, 12666–12731. doi:10.1021/acs.chemrev.5b00098
2. Nielsen, T. D.; Cruickshank, C.; Foged, S.; Thorsen, J.; Krebs, F. C. *Sol. Energy Mater. Sol. Cells* **2010**, *94*, 1553–1571. doi:10.1016/j.solmat.2010.04.074
3. Yusoff, A. R. b. M.; Kim, D.; Kim, H. P.; Shneider, F. K.; da Silva, W. J.; Jang, J. *Energy Environ. Sci.* **2015**, *8*, 303–316. doi:10.1039/C4EE03048F
4. Zhao, J.; Li, Y.; Yang, G.; Jiang, K.; Lin, H.; Ade, H.; Ma, W.; Yan, H. *Nat. Energy* **2016**, *1*, 15027. doi:10.1038/nenergy.2015.27
5. Roncali, J.; Leriche, P.; Blanchard, P. *Adv. Mater.* **2014**, *26*, 3821–3838. doi:10.1002/adma.201305999
6. Ni, W.; Wan, X.; Li, M.; Wang, Y.; Chen, Y. *Chem. Commun.* **2015**, *51*, 4936–4950. doi:10.1039/C4CC09758K
7. Long, G.; Wan, X.; Chen, Y. *Acc. Chem. Res.* **2013**, *46*, 2645–2655. doi:10.1021/ar400088c
8. Kan, B.; Zhang, Q.; Li, M.; Wan, X.; Ni, W.; Long, G.; Wang, Y.; Yang, X.; Feng, H.; Chen, Y. *J. Am. Chem. Soc.* **2014**, *136*, 15529–15532. doi:10.1021/ja509703k
9. Zhang, Q.; Kan, B.; Liu, F.; Long, G.; Wan, X.; Chen, X.; Zuo, Y.; Ni, W.; Zhang, H.; Li, M.; Hu, Z.; Huang, F.; Cao, Y.; Liang, Z.; Zhang, M.; Russell, T. P.; Chen, Y. *Nat. Photonics* **2015**, *9*, 35–41. doi:10.1038/nphoton.2014.269
10. Kan, B.; Li, M.; Zhang, Q.; Liu, F.; Wan, X.; Wang, Y.; Ni, W.; Long, G.; Yang, X.; Feng, H.; Zuo, Y.; Zhang, M.; Huang, F.; Cao, Y.; Russell, T. P.; Chen, Y. *J. Am. Chem. Soc.* **2015**, *137*, 3886–3893. doi:10.1021/jacs.5b00305
11. Sun, K.; Xiao, Z.; Lu, S.; Zajaczkowski, W.; Pisula, W.; Hanssen, E.; White, J. M.; Williamson, R. M.; Subbiah, J.; Ouyang, J.; Holmes, A. B.; Wong, W. W. H.; Jones, D. J. *Nat. Commun.* **2015**, *6*, 6013. doi:10.1038/ncomms7013
12. Liu, Y.; Chen, C.-C.; Hong, Z.; Gao, J.; Yang, Y.; Zhou, H.; Dou, L.; Li, G.; Yang, Y. *Sci. Rep.* **2013**, *3*, 3356. doi:10.1038/srep03356
13. Li, M.; Ni, W.; Wan, X.; Zhang, Q.; Kan, B.; Chen, Y. *J. Mater. Chem. A* **2015**, *3*, 4765–4776. doi:10.1039/C4TA06452F
14. Cui, C.; Guo, X.; Min, J.; Guo, B.; Cheng, X.; Zhang, M.; Brabec, C. J.; Li, Y. *Adv. Mater.* **2015**, *27*, 7469–7475. doi:10.1002/adma.201503815
15. Qiu, B.; Yuan, J.; Xiao, X.; He, D.; Qiu, L.; Zou, Y.; Zhang, Z.-g.; Li, Y. *ACS Appl. Mater. Interfaces* **2015**, *7*, 25237–25246. doi:10.1021/acsami.5b07066
16. Shen, S.; Jiang, P.; He, C.; Zhang, J.; Shen, P.; Zhang, Y.; Yi, Y.; Zhang, Z.; Li, Z.; Li, Y. *Chem. Mater.* **2013**, *25*, 2274–2281. doi:10.1021/cm400782q
17. Zhou, J.; Zuo, Y.; Wan, X.; Long, G.; Zhang, Q.; Ni, W.; Liu, Y.; Li, Z.; He, G.; Li, C.; Kan, B.; Li, M.; Chen, Y. *J. Am. Chem. Soc.* **2013**, *135*, 8484–8487. doi:10.1021/ja403318y
18. Du, Z.; Chen, W.; Qiu, M.; Chen, Y.; Wang, N.; Wang, T.; Sun, M.; Yu, D.; Yang, R. *Phys. Chem. Chem. Phys.* **2015**, *17*, 17391–17398. doi:10.1039/C5CP02632F
19. Kan, B.; Zhang, Q.; Liu, F.; Wan, X.; Wang, Y.; Ni, W.; Yang, X.; Zhang, M.; Zhang, H.; Russell, T. P.; Chen, Y. *Chem. Mater.* **2015**, *27*, 8414–8423. doi:10.1021/acs.chemmater.5b03889
20. Yin, N.; Wang, L.; Ma, Y.; Lin, Y.; Wu, J.; Luo, Q.; Yang, H.-B.; Ma, C.-Q.; Zhao, X. *Dyes Pigm.* **2015**, *120*, 299–306. doi:10.1016/j.dyepig.2015.04.030
21. Patra, D.; Huang, T.-Y.; Chiang, C.-C.; Maturana, R. O. V.; Pao, C.-W.; Ho, K.-C.; Wei, K.-H.; Chu, C.-W. *ACS Appl. Mater. Interfaces* **2013**, *5*, 9494–9500. doi:10.1021/am4021928
22. Liu, Y.; Wan, X.; Wang, F.; Zhou, J.; Long, G.; Tian, J.; Chen, Y. *Adv. Mater.* **2011**, *23*, 5387–5391. doi:10.1002/adma.201102790
23. Zhou, J.; Wan, X.; Liu, Y.; Zuo, Y.; Li, Z.; He, G.; Long, G.; Ni, W.; Li, C.; Su, X.; Chen, Y. *J. Am. Chem. Soc.* **2012**, *134*, 16345–16351. doi:10.1021/ja306865z
24. Lin, Y.; Ma, L.; Li, Y.; Liu, Y.; Zhu, D.; Zhan, X. *Adv. Energy Mater.* **2013**, *3*, 1166–1170. doi:10.1002/aenm.201300181
25. Huang, J.; Zhan, C.; Zhang, X.; Zhao, Y.; Lu, Z.; Jia, H.; Jiang, B.; Ye, J.; Zhang, S.; Tang, A.; Liu, Y.; Pei, Q.; Yao, J. *ACS Appl. Mater. Interfaces* **2013**, *5*, 2033–2039. doi:10.1021/am302896u
26. Lin, Y.; Ma, L.; Li, Y.; Liu, Y.; Zhu, D.; Zhan, X. *Adv. Energy Mater.* **2014**, *4*, 1300626. doi:10.1002/aenm.201300626
27. Tang, A.; Zhan, C.; Yao, J. *Chem. Mater.* **2015**, *27*, 4719–4730. doi:10.1021/acs.chemmater.5b01350
28. Kumar, C. V.; Cabau, L.; Viterisi, A.; Biswas, S.; Sharma, G. D.; Palomares, E. *J. Phys. Chem. C* **2015**, *119*, 20871–20879. doi:10.1021/acs.jpcc.5b07130
29. Patra, D.; Chiang, C.-C.; Chen, W.-A.; Wei, K.-H.; Wu, M.-C.; Chu, C.-W. *J. Mater. Chem. A* **2013**, *1*, 7767–7774. doi:10.1039/c3ta11544e
30. Chu, H.-C.; Sahu, D.; Hsu, Y.-C.; Padhy, H.; Patra, D.; Lin, J.-T.; Bhattacharya, D.; Lu, K.-L.; Wei, K.-H.; Lin, H.-C. *Dyes Pigm.* **2012**, *93*, 1488–1497. doi:10.1016/j.dyepig.2011.09.012
31. Li, Z.; He, G.; Wan, X.; Liu, Y.; Zhou, J.; Long, G.; Zuo, Y.; Zhang, M.; Chen, Y. *Adv. Energy Mater.* **2012**, *2*, 74–77. doi:10.1002/aenm.201100572
32. Long, G.; Wan, X.; Kan, B.; Liu, Y.; He, G.; Li, Z.; Zhang, Y.; Zhang, Y.; Zhang, Q.; Zhang, M.; Chen, Y. *Adv. Energy Mater.* **2013**, *3*, 639–646. doi:10.1002/aenm.201300046
33. Cardona, C. M.; Li, W.; Kaifer, A. E.; Stockdale, D.; Bazan, G. C. *Adv. Mater.* **2011**, *23*, 2367–2371. doi:10.1002/adma.201004554
34. Wu, J.; Ma, Y.; Wu, N.; Lin, Y.; Lin, J.; Wang, L.; Ma, C.-Q. *Org. Electron.* **2015**, *23*, 28–38. doi:10.1016/j.orgel.2015.04.003
35. Lim, N.; Cho, N.; Paek, S.; Kim, C.; Lee, J. K.; Ko, J. *Chem. Mater.* **2014**, *26*, 2283–2288. doi:10.1021/cm5004092
36. Deng, D.; Zhang, Y.; Yuan, L.; He, C.; Lu, K.; Wei, Z. *Adv. Energy Mater.* **2014**, *4*, 1400538. doi:10.1002/aenm.201400538
37. Du, Z.; Chen, W.; Chen, Y.; Qiao, S.; Bao, X.; Wen, S.; Sun, M.; Han, L.; Yang, R. *J. Mater. Chem. A* **2014**, *2*, 15904–15911. doi:10.1039/C4TA03314K
38. Wu, N.; Luo, Q.; Bao, Z.; Lin, J.; Li, Y.-Q.; Ma, C.-Q. *Sol. Energy Mater. Sol. Cells* **2015**, *141*, 248–259. doi:10.1016/j.solmat.2015.05.039

## License and Terms

This is an Open Access article under the terms of the Creative Commons Attribution License (<http://creativecommons.org/licenses/by/2.0>), which permits unrestricted use, distribution, and reproduction in any medium, provided the original work is properly cited.

The license is subject to the *Beilstein Journal of Organic Chemistry* terms and conditions: (<http://www.beilstein-journals.org/bjoc>)

The definitive version of this article is the electronic one which can be found at:  
[doi:10.3762/bjoc.12.169](https://doi.org/10.3762/bjoc.12.169)



# Synthesis and characterization of fluorinated azadipyrromethene complexes as acceptors for organic photovoltaics

Forrest S. Etheridge<sup>1</sup>, Roshan J. Fernando<sup>1</sup>, Sandra Pejić<sup>1</sup>, Matthias Zeller<sup>2</sup>  
and Geneviève Sauvé<sup>\*1</sup>

## Full Research Paper

Open Access

Address:

<sup>1</sup>Department of Chemistry, Case Western Reserve University, Cleveland, Ohio 44106, United States and <sup>2</sup>Department of Chemistry, Purdue University, West Lafayette, Indiana 47907, United States

Email:

Geneviève Sauvé<sup>\*</sup> - genevieve.sauve@case.edu

\* Corresponding author

Keywords:

dye; fluorine; near-IR absorber; non-fullerene acceptor; zinc(II) complex

*Beilstein J. Org. Chem.* **2016**, *12*, 1925–1938.

doi:10.3762/bjoc.12.182

Received: 04 June 2016

Accepted: 11 August 2016

Published: 29 August 2016

This article is part of the Thematic Series "Organic photovoltaics".

Guest Editor: D. J. Jones

© 2016 Etheridge et al.; licensee Beilstein-Institut.

License and terms: see end of document.

## Abstract

Homoleptic zinc(II) complexes of di(phenylacetylene)azadipyrromethene (e.g., Zn(WS3)<sub>2</sub>) are potential non-fullerene electron acceptors for organic photovoltaics. To tune their properties, fluorination of Zn(WS3)<sub>2</sub> at various positions was investigated. Three fluorinated azadipyrromethene-based ligands were synthesized with fluorine at the *para*-position of the proximal and distal phenyl groups, and at the pyrrolic phenylacetylene moieties. Additionally, a CF<sub>3</sub> moiety was added to the pyrrolic phenyl positions to study the effects of a stronger electron withdrawing unit at that position. The four ligands were chelated with zinc(II) and BF<sub>2</sub><sup>+</sup> and the optical and electrochemical properties were studied. Fluorination had little effect on the optical properties of both the zinc(II) and BF<sub>2</sub><sup>+</sup> complexes, with  $\lambda_{\text{max}}$  in solution around 755 nm and 785 nm, and high molar absorptivities of  $100 \times 10^3 \text{ M}^{-1}\text{cm}^{-1}$  and  $50 \times 10^3 \text{ M}^{-1}\text{cm}^{-1}$ , respectively. Fluorination of Zn(WS3)<sub>2</sub> raised the oxidation potentials by 0.04 V to 0.10 V, and the reduction potentials by 0.01 V to 0.10 V, depending on the position and type of substitution. The largest change was observed for fluorine substitution at the proximal phenyl groups and CF<sub>3</sub> substitution at the pyrrolic phenylacetylene moieties. The later complexes are expected to be stronger electron acceptors than Zn(WS3)<sub>2</sub>, and may enable charge transfer from other conjugated polymer donors that have lower energy levels than poly(3-hexylthiophene) (P3HT).

## Introduction

Azadipyrromethenes (ADPs) (Figure 1a) are a class of monoanionic bidentate ligands with strong absorption in the visible and near IR range. Their absorbance and emission properties can be readily tuned through structural modifications and chelation [1-4]. BF<sub>2</sub><sup>+</sup>-chelated ADP derivatives (Figure 1b) in particular

have drawn interest for photodynamic therapy, bio-imaging and light harvesting applications [5-8].

We have shown that derivatives of Zn(ADP)<sub>2</sub> are promising electron acceptors for organic photovoltaics (OPVs) [9,10].

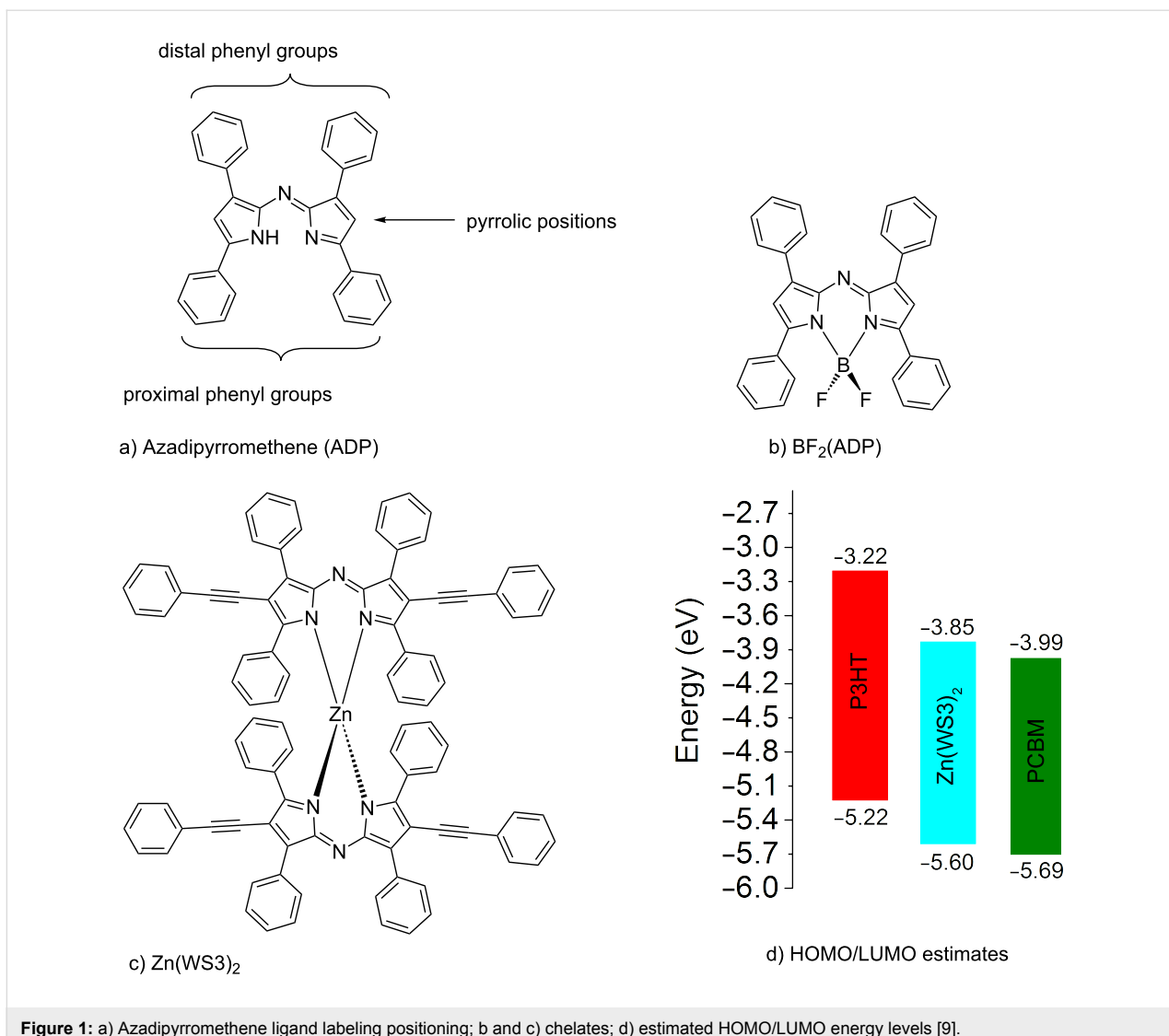


Figure 1: a) Azadipyrromethene ligand labeling positioning; b and c) chelates; d) estimated HOMO/LUMO energy levels [9].

A series of zinc(II) derivatives with various pyrrolic substitutions showed power conversion efficiencies (PCEs) ranging from 2.2–4.1% when blended with poly(3-hexylthiophene) (P3HT), and the highest PCE was obtained with Zn(WS3)<sub>2</sub>, shown in Figure 1c [9,10]. In comparison, free ligands and BF<sub>2</sub><sup>+</sup> chelates showed negligible power conversion efficiencies, and Zn(ADP)<sub>2</sub> gave a maximum efficiency of 1.4% [11]. Free ligands and BF<sub>2</sub><sup>+</sup> chelates tend to self-aggregate too much, leading to large scale phase separation with P3HT and low PCEs. Chelation with zinc(II) lowers the tendency to self-aggregate, but Zn(ADP)<sub>2</sub> still shows some large aggregates in blend films [10]. The addition of pyrrolic phenylacetylene substituents further helped to break the aggregation and to create a favorable nanoscale phase separation in blend films, leading to higher PCEs [9,10]. DFT calculations show that Zn(WS3)<sub>2</sub> is a very large and non-planar molecule with low electron transfer reorganization energy, further supporting its potential to replace

fullerenes in OPVs [12]. However, the HOMO and LUMO energy levels of Zn(WS3)<sub>2</sub> in solution are higher than that of the most popular electron acceptor phenyl-C<sub>61</sub>-butyric acid methyl ester (PCBM, Figure 1d). Decreasing the energy levels of the parent Zn(WS3)<sub>2</sub> would enable this new class of acceptors to be paired with other polymer donors that have lower HOMO and LUMO energy levels than P3HT.

One substituent used to modify the properties of molecules without drastically altering the structure is fluorine, which is a unique element due to its small size and high electronegativity, with many applications in pharmaceuticals and materials [13–15]. Its use as a hydrogen replacement has garnered wide use in industrial applications for high thermal stability and surface effects, most notably with polytetrafluoroethylene (PTFE) [16]. The small size and strong electron-withdrawing properties of fluorine make it ideally suited to tune the molecular orbital

(MO) energy levels of polymer donors in OPVs without major influence on the structure [17–22]. In several cases, the addition of fluorine decreases the energy of the highest occupied molecular orbitals (HOMO), thereby enhancing the open-circuit voltages ( $V_{oc}$ ) and PCEs [17,23–26]. A 2014 investigation by Luscombe and co-workers showed that a fluorine substitution lowered the charge transfer exciton (CTE) binding energy, in turn creating more free carriers and higher PCEs [19]. Additionally, enhancements to the short-circuit current density ( $J_{sc}$ ),  $V_{oc}$ , and fill-factor (FF) in OPVs have been attributed to the addition of fluorine substituents [17,18,20,21,27–29].

While fluorinated polymer donors are well known, fluorinated n-type materials are less common [13,30,31]. Nevertheless, fluorinated n-type materials have been shown to exhibit promising characteristics in devices. For instance, the addition of fluorinated groups to naphthalene diimide (NDI) and perylene diimide (PDI) derivatives increased the reduction potentials (more positive), allowed for air-stable fabrication of organic field effect transistors (OFETs), and showed promise in solar cells [13,32]. Some homoleptic metal complexes, such as Ir(III) phenylpyridine-based complexes, are favored for their use in

light-emitting devices and the fluorinated derivatives allow access to triplet state blue light-emitters [13].

This work further investigates the effects of fluorination in n-type materials for OPVs. A series of selectively fluorinated ADP derivatives based on WS3 were synthesized (Figure 2). To understand the effect of the fluorination position, a single fluorine atom was added at three places: at the proximal phenyl position (L1), at the distal phenyl group (L2), and at the pyrrolic phenylacetylene moiety (L3). At the latter position, the degree of fluorination was further explored with the addition of  $CF_3$  (L4). These four fluorinated derivatives were then chelated with both  $BF_2^+$  and zinc(II) (Scheme 2, see below), and their optical and electrochemical properties were studied. The  $BF_2^+$  chelates were included in this study because they may be useful near-IR absorbers for other light-harvesting applications. The fluorine substitutions had little effect on the optical properties of the  $BF_2^+$  and zinc(II) chelates, and only had a small effect on the electrochemical properties, with the largest increase in oxidation and reduction potentials of 0.1 V observed for L1 and L4 chelates compared to WS3 chelates. Zinc(II) chelates of L1 and L4 are expected to be stronger electron acceptors than

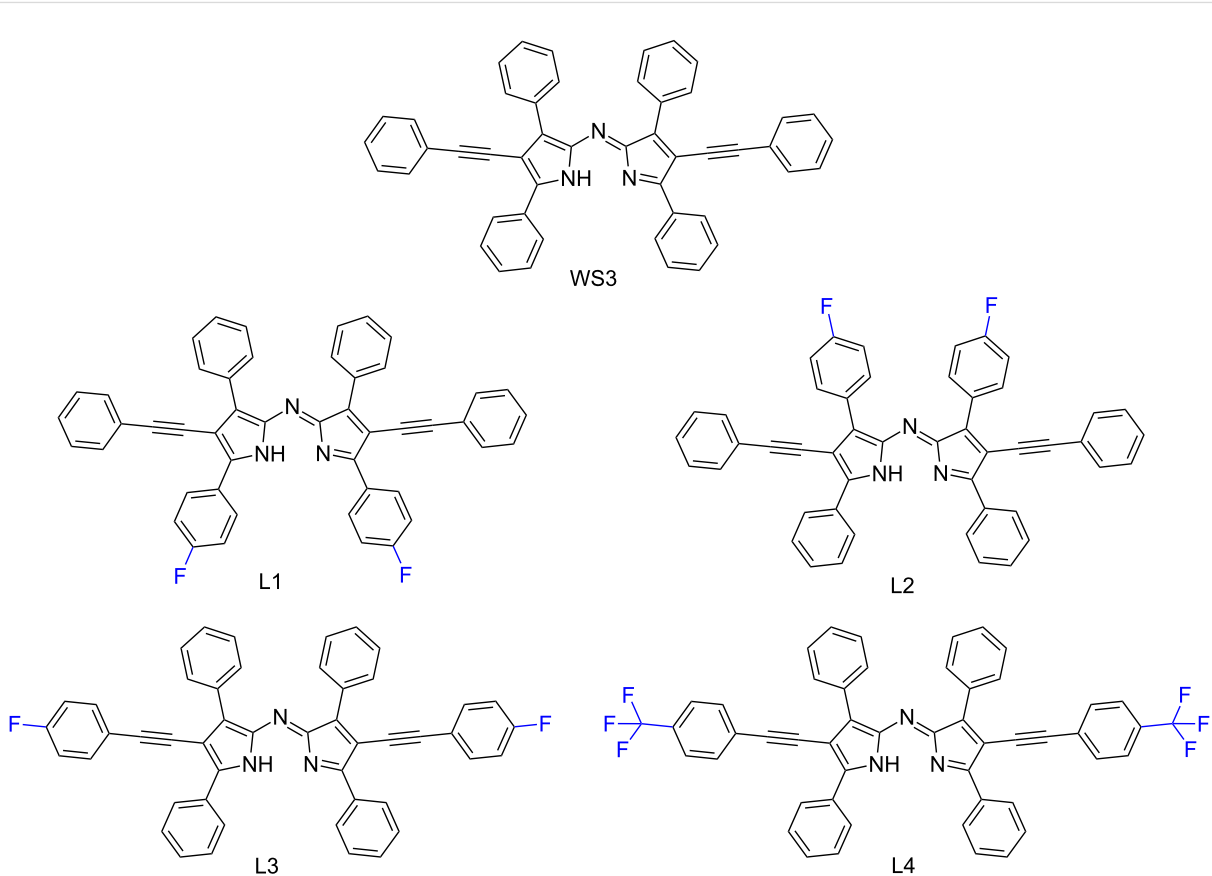


**Figure 2:** Chemical structures of the fluorinated ADP derivatives of WS3 explored in the study.

Zn(WS<sub>3</sub>)<sub>2</sub>, and may enable charge transfer from other conjugated polymer donor that have lower energy levels than P3HT.

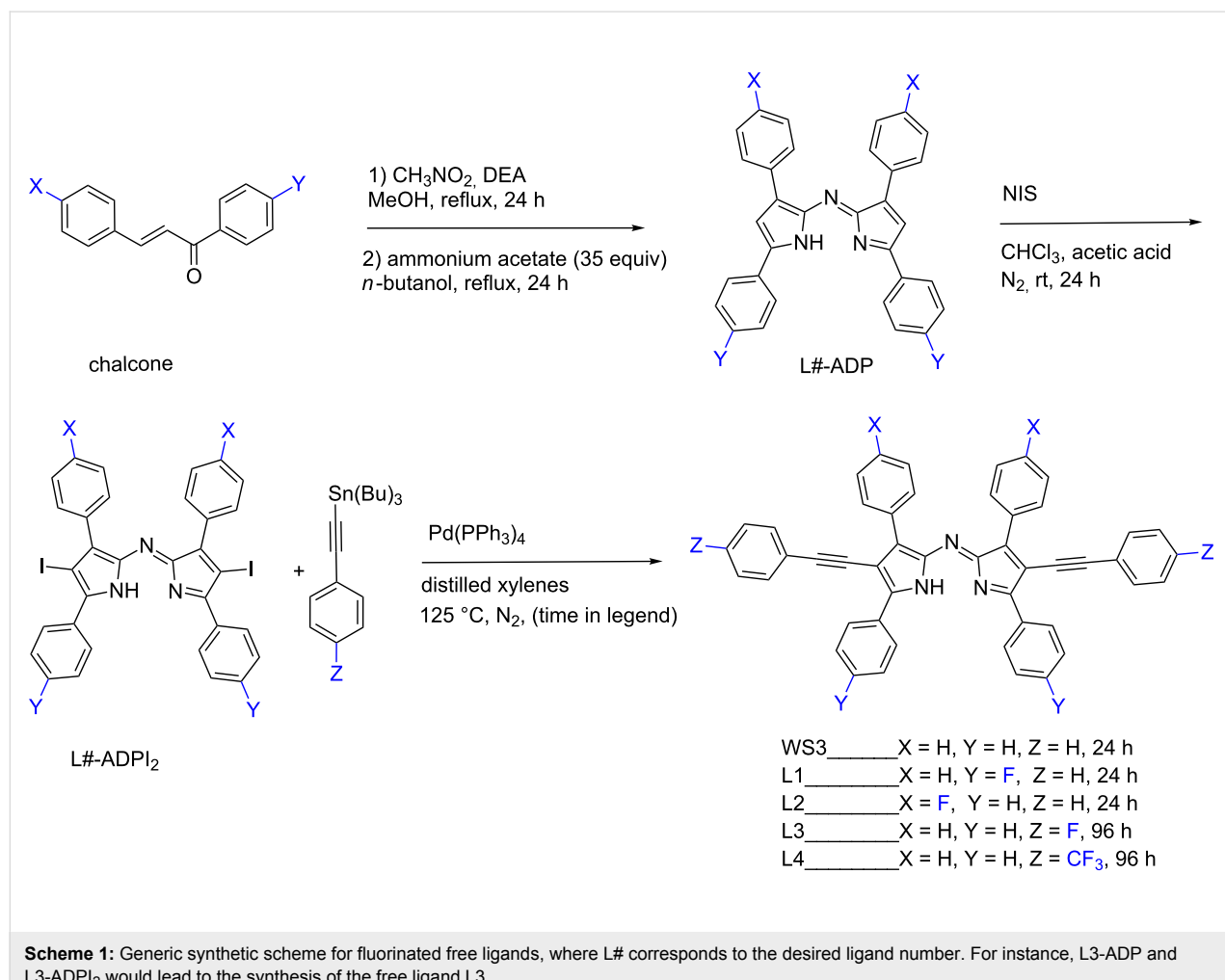
## Results and Discussion

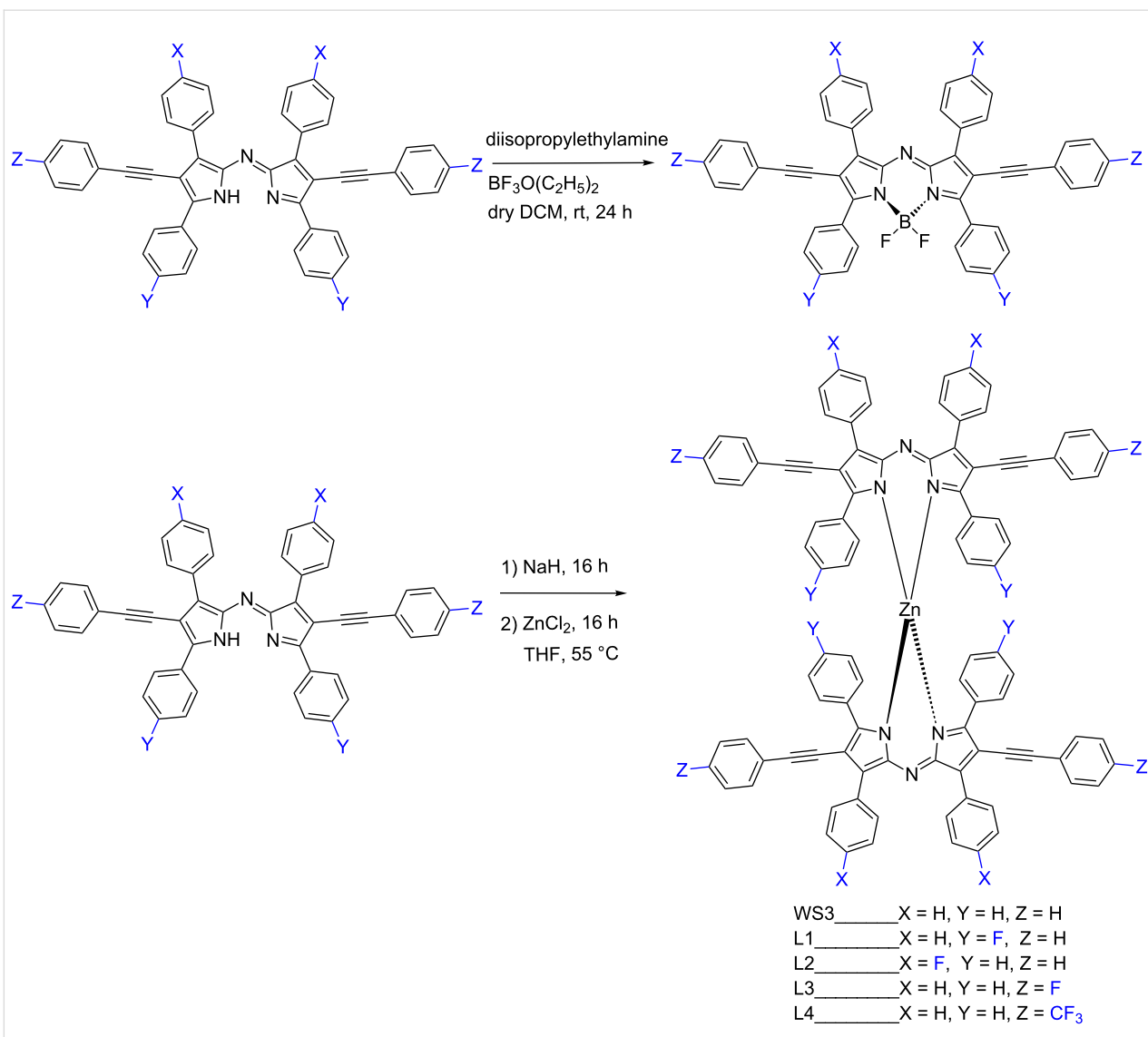
### Synthesis

The synthesis of ADP was carried out according to literature procedures [9,33]. The ADP-analogs with fluorine at the proximal or distal phenyl positions (L1-ADP and L2-ADP) were synthesized in a similar fashion with the respective fluorinated chalcones (Scheme 1). In this case, the nitro intermediates of the fluorinated chalcones could not be isolated as a solid powder, so the synthesis was carried forward assuming complete conversion from the first reaction.

To install phenylacetylene groups, iodination of the ADP derivatives was done according to literature procedures and purified by washing with chloroform in good yield [5,33,34]. Stille cross-coupling with the appropriate tributyltin-phenylacetylene analogs afforded the WS<sub>3</sub> derivatives in good yield (Scheme 1). We chose to utilize Stille coupling instead of Sonogashira cou-

pling because we had previously found that this method gives higher yields for installing phenylethynyl pyrrolic substituents [9]. The fluorinated tributyltinphenylacetylene analogs for the synthesis of L3 and L4 were synthesized according to literature procedures and used without purification [35,36]. The Stille cross coupling reactions for the synthesis of L3 and L4 were monitored by MALDI-TOF-MS and were found to not be complete after increasing the reaction time to 48 h, so the reaction time was increased to 96 h with the addition of more catalyst and tributyltin reactant after 48 h. These modifications were deemed necessary to push the reaction towards completion and aid in purification of the free ligand. The free ligands were isolated from the crude mixture by rotary evaporation and purified by trituration with cold methanol and the remaining solid was washed with cold ether. Due to the lowered solubility of the iodinated ADP derivatives and the free ligands in organic solvents, the identity of these compounds was confirmed only by MADLI-TOF-MS. These modifications allowed for the synthesis of all fluorinated WS<sub>3</sub> derivatives in good yield with sufficient purity for chelation.





The  $\text{BF}_2^+$  chelation was carried out according to the literature procedures in moderate yields (Scheme 2) [2,5]. For the zinc(II) chelation, the reaction was changed from a reaction using  $\text{Zn}(\text{OAc})_2$  to a 2-step, one pot reaction with sodium hydride in tetrahydrofuran, followed by the addition of zinc(II) chloride. Zinc(II) and  $\text{BF}_2^+$  chelates were purified by silica gel column chromatography to isolate the chelates as blue solids and the identity and purity was confirmed by NMR spectroscopy, MALDI-TOF-MS and elemental analysis. In the case of L2, the pure  $\text{BF}_2^+$  chelate could not be isolated by column chromatography, and will therefore be omitted from further analysis.

The thermal stability of the zinc(II) complexes was examined by thermal gravity analysis and the results are shown in Figure 3. The fluorinated complexes had weight loss profiles

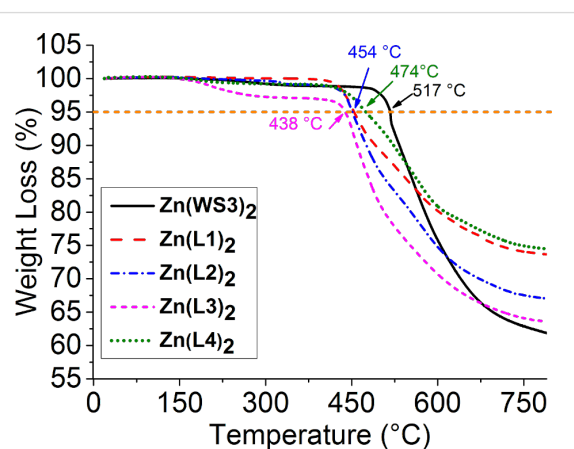


**Figure 3:** TGA spectra for the zinc(II) complexes.

similar to each other with a 5% loss between 438 °C and 474 °C, all lower than that of the unfluorinated  $\text{Zn}(\text{WS3})_2$  at 517 °C.

## Optical properties

Optical studies for the zinc(II) and  $\text{BF}_2^+$  complexes were performed in chloroform solutions and with spun-cast films on microscope slides. Like the solid powders, all of the solutions and films were dark blue. Solution and film optical properties for zinc(II) and  $\text{BF}_2^+$  chelates are summarized in Table 1. The molar absorptivity spectra in chloroform solutions for zinc(II) and  $\text{BF}_2^+$  chelates are reported in Figure 4a and Figure 4b, respectively.

The absorption spectra of the zinc(II) chelates are all similar. In most cases, the  $\lambda_{\text{max}}$  and  $\lambda_{\text{onset}}$  values remain consistent with  $\text{Zn}(\text{WS3})_2$  around 670 nm and 755 nm, respectively. An exception is  $\text{Zn}(\text{L4})_2$ , with  $\lambda_{\text{max}}$  and  $\lambda_{\text{onset}}$  blue-shifted by 10 nm compared to  $\text{Zn}(\text{WS3})_2$ . This hypsochromic shift is consistent with other cases where a highly polarized  $\text{CF}_3$  group is added *para* to the conjugated structure [13,37]. Regardless of fluorination, the extinction coefficients are all near  $100 \times 10^3 \text{ M}^{-1}\text{cm}^{-1}$ , showing the strong absorption properties of the WS3-core.

Solutions of  $\text{BF}_2^+$  chelates show a consistent trend compared with the solutions of zinc(II) chelates. The  $\lambda_{\text{max}}$  and  $\lambda_{\text{onset}}$  values of  $\text{BF}_2(\text{WS3})$ ,  $\text{BF}_2(\text{L1})$ , and  $\text{BF}_2(\text{L3})$  are  $\approx 730$  nm and  $\approx 780$  nm, respectively. Consistent with that of the zinc(II) chelate solutions,  $\lambda_{\text{max}}$  of  $\text{BF}_2(\text{L4})$  is 15 nm blue shifted compared to  $\text{BF}_2(\text{WS3})$ , showing a slightly greater effect from  $\text{CF}_3$  in the  $\text{BF}_2^+$  chelate. Molar absorptivities of the compounds vary from  $49 \times 10^3 \text{ M}^{-1}\text{cm}^{-1}$  for  $\text{BF}_2(\text{WS3})$  to  $66 \times 10^3 \text{ M}^{-1}\text{cm}^{-1}$  for  $\text{BF}_2(\text{L4})$ .

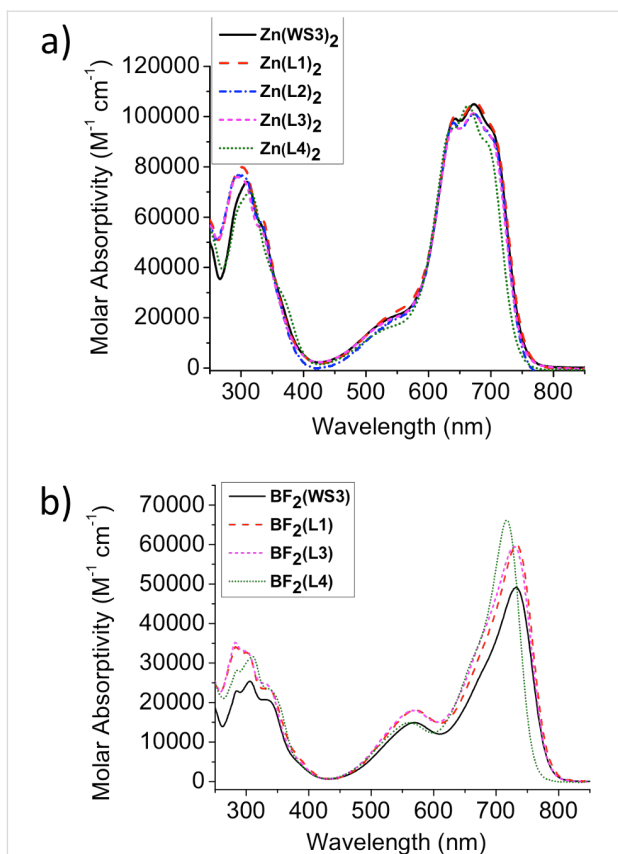


**Figure 4:** Molar absorptivities in chloroform solutions of a) zinc(II) chelates b)  $\text{BF}_2^+$  chelates.

Films of the zinc(II) and  $\text{BF}_2^+$  chelates were made in order to better understand the optical properties of the materials in devices, and the properties are summarized in Table 1. Normalized absorption spectra of zinc(II) and  $\text{BF}_2^+$  chelate films are reported in Figure 5a and Figure 5b, respectively. Following the same trend as the zinc(II) chelate solutions, the zinc(II) chelate

**Table 1:** Summary of optical properties of zinc(II) and  $\text{BF}_2^+$  chelates in solution and film.

	Solution		Film	
	$\lambda_{\text{max}}$ (nm) ( $\epsilon \times 10^3 \text{ M}^{-1}\text{cm}^{-1}$ )	$\lambda_{\text{onset}}$ (nm)	$\lambda_{\text{max}}$ (nm)	$\lambda_{\text{onset}}$ (nm)
$\text{Zn}(\text{WS3})_2$	310(74), 664(99), 674(105)	757	696	791
$\text{BF}_2(\text{WS3})$	732(49)	782	759	835
$\text{Zn}(\text{L1})_2$	302(80), 643(100), 674(106)	759	695	785
$\text{BF}_2(\text{L1})$	732(60)	783	755	829
$\text{Zn}(\text{L2})_2$	302(77), 640(98), 672(101)	757	697	780
$\text{BF}_2(\text{L2})$	–	–	–	–
$\text{Zn}(\text{L3})_2$	294(76), 642(96), 672(101)	755	692	778
$\text{BF}_2(\text{L3})$	729(59)	783	770	868
$\text{Zn}(\text{L4})_2$	314(70), 663(104)	746	676	769
$\text{BF}_2(\text{L4})$	717(66)	763	669	800

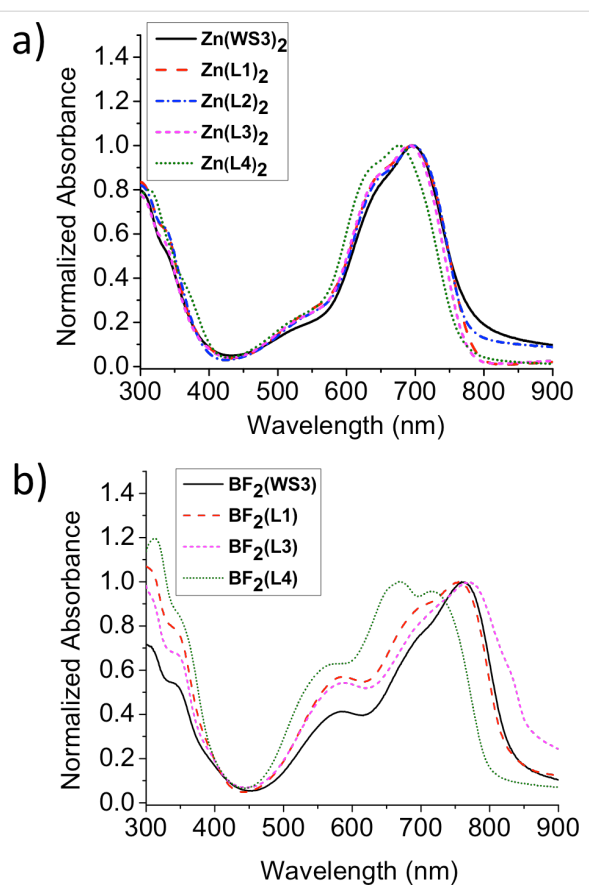


**Figure 5:** Normalized absorbance from spun-coat chloroform solution on microscope glass of a) zinc(II) chelates b)  $\text{BF}_2^+$  chelates.

films exhibited consistent  $\lambda_{\text{max}}$  values of  $\approx 695$  nm, excluding  $\text{Zn(L4)}_2$  at 676 nm. The  $\lambda_{\text{onset}}$  values for films of  $\text{Zn(L1)}_2$ ,  $\text{Zn(L2)}_2$ ,  $\text{Zn(L3)}_2$ , and  $\text{Zn(L4)}_2$  are 785, 780, 778, and 769 nm, respectively, all blue shifted compared to  $\lambda_{\text{onset}}$  of  $\text{Zn(WS3)}_2$  at 791 nm. The shapes of all the curves remain consistent with a broad absorption from 500 to 800 nm, good for OPV applications.

All  $\text{BF}_2^+$  chelate films exhibit broadening compared to solutions, with an absorbance ranging from 450 to 900 nm. The  $\lambda_{\text{max}}$  values for  $\text{BF}_2(\text{WS3})$  and  $\text{BF}_2(\text{L1})$  are similar at 759 and 755 nm, respectively. The onset values for the two films are also similar at 835 and 829 nm, respectively. Films of  $\text{BF}_2(\text{L3})$  and  $\text{BF}_2(\text{L4})$  show marked differences from two different fluorine modifications at the same position. In  $\text{BF}_2(\text{L3})$ , the  $\lambda_{\text{max}}$  and  $\lambda_{\text{onset}}$  are recorded at 770 and 868 nm, respectively. Compared to  $\text{BF}_2(\text{WS3})$ , there is a small 11 nm bathochromic shift of  $\lambda_{\text{max}}$ . For  $\text{BF}_2(\text{L4})$ ,  $\lambda_{\text{max}}$  and  $\lambda_{\text{onset}}$  are observed at 669 and 800 nm, respectively. Compared to  $\lambda_{\text{max}}$  of  $\text{BF}_2(\text{WS3})$ ,  $\text{BF}_2(\text{L4})$  exhibits a large hypsochromic shift of 33 nm.

## Electrochemistry

Cyclic voltammetry of the zinc(II) and  $\text{BF}_2^+$  chelates was studied in dichloromethane solutions using ferrocene/ferri-cinium ( $\text{Fc}/\text{Fc}^+$ ) as an internal reference. The electrochemical properties of the complexes are summarized in Table 2 with the voltammograms of the zinc(II) and  $\text{BF}_2^+$  chelates shown in Figure 6 and Figure 7, respectively. For all zinc(II) complexes, cyclic voltammograms reveal two reversible oxidations, while an irreversible oxidation occurs for all  $\text{BF}_2^+$  chelates. The first oxidation potentials ( $E_{1/2 \text{ ox.}}$ ) of the fluorinated zinc(II) chelates were higher than that of  $\text{Zn(WS3)}_2$  (0.50 V) by at least 0.04 V, with the highest value being 0.61 V. The increased  $E_{1/2 \text{ ox.}}$  values are consistent with the increased oxidative stability afforded by the addition of fluorine [13]. The second oxidation potential for all zinc(II) chelates, 0.77–0.79 V, showed little change except in two cases:  $\text{Zn(L4)}_2$  and  $\text{Zn(L2)}_2$  had second oxidation potentials of 0.84 V and 0.73 V, respectively. The differences between the first and second oxidation potential was 0.27 V for  $\text{Zn(WS3)}_2$ , while it was 0.18 V and 0.19 V for  $\text{Zn(L1)}_2$  and  $\text{Zn(L2)}_2$ , respectively. For both  $\text{Zn(L3)}_2$  and  $\text{Zn(L4)}_2$  the difference between oxidation potentials was 0.23 V, a slight decrease from  $\text{Zn(WS3)}_2$  at 0.27 V. All of the fluorinated zinc(II) complexes exhibit a rise of the first oxida-

**Table 2:** Electrochemical properties of zinc(II) and  $\text{BF}_2^+$  chelates in dichloromethane. All values reported are in V vs  $\text{Fc}/\text{Fc}^+$ .

	$E_{1/2 \text{ ox.}}$	$E_{(\text{p},\text{a})}$	$E_{1/2 \text{ red.}}$	$E_{(\text{p},\text{c})}$
$\text{Zn(WS3)}_2$	0.50, 0.77	0.58, 0.86	-1.25, -1.47	-1.33, -1.55
$\text{BF}_2(\text{WS3})$	-	1.08	-0.79, -1.59	-0.95, -1.75
$\text{Zn(L1)}_2$	0.60, 0.78	0.66, 0.87	-1.16, -1.39	-1.11, -1.33
$\text{BF}_2(\text{L1})$	-	0.96	-0.71, -1.48	-0.67, -1.44
$\text{Zn(L2)}_2$	0.54, 0.73	0.58, 0.81	-1.24, -1.45	-1.19, -1.41
$\text{BF}_2(\text{L2})$	-	-	-	-
$\text{Zn(L3)}_2$	0.56, 0.79	0.61, 0.86	-1.23, -1.44	-1.18, -1.39
$\text{BF}_2(\text{L3})$	-	0.97	-0.72, -1.49	-0.66, -1.44
$\text{Zn(L4)}_2$	0.61, 0.84	0.66, 0.88	-1.15, -1.36	-1.11, -1.32
$\text{BF}_2(\text{L4})$	-	1.06	-0.69, -1.46	-0.65, -1.42

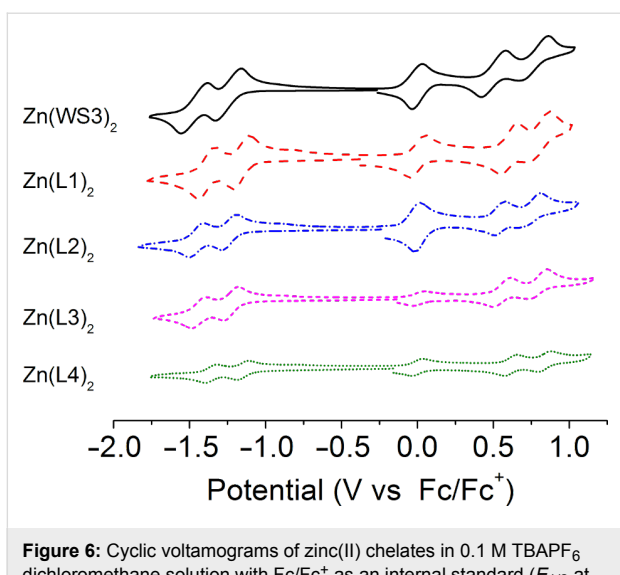


**Figure 6:** Cyclic voltamograms of zinc(II) chelates in 0.1 M TBAPF<sub>6</sub> dichloromethane solution with Fc/Fc<sup>+</sup> as an internal standard ( $E_{1/2}$  at 0.0 V).

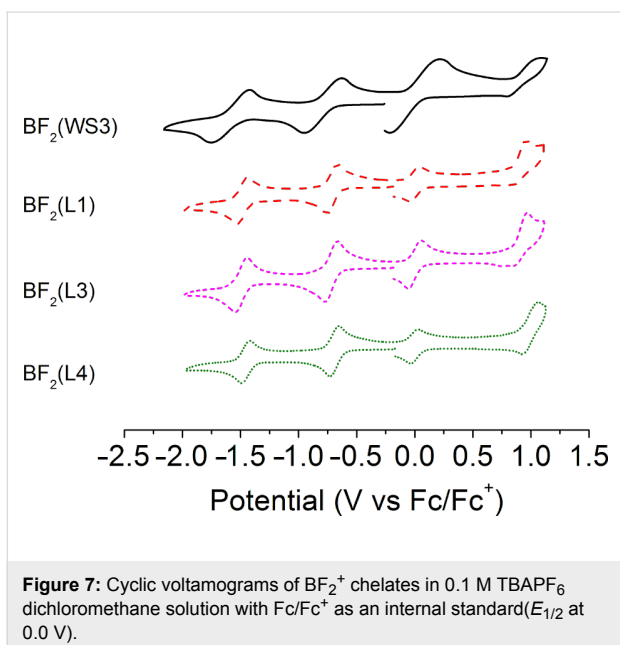


**Figure 7:** Cyclic voltamograms of  $\text{BF}_2^+$  chelates in 0.1 M TBAPF<sub>6</sub> dichloromethane solution with Fc/Fc<sup>+</sup> as an internal standard ( $E_{1/2}$  at 0.0 V).

tion potential as well as a decrease between the first and second oxidation potentials, compared to  $\text{Zn}(\text{WS3})_2$ .

Cyclic voltammograms of both the zinc(II) and  $\text{BF}_2^+$  complexes showed two reversible reduction potentials. The reduction potentials ( $E_{1/2}$  red.) of  $\text{Zn}(\text{L2})_2$  and  $\text{Zn}(\text{L3})_2$  were similar to that of  $\text{Zn}(\text{WS3})_2$ , suggesting that the addition of one fluorine atom at the pyrrolic phenylacetylene or distal phenyl position does not stabilize the anion. On the other hand, there is significant increase of the reduction potentials going from -1.25 V to -1.16 V and -1.15 V for  $\text{Zn}(\text{WS3})_2$ ,  $\text{Zn}(\text{L1})_2$  and  $\text{Zn}(\text{L4})_2$ , respectively. This suggests that fluorine stabilizes the anion when

at the proximal position or when a CF<sub>3</sub> group is installed at the pyrrolic phenylacetylene moiety. The difference between the first oxidation and first reduction potentials of all the zinc(II) complexes are similar, 1.75 V to 1.79 V. This means that in the cases of  $\text{Zn}(\text{L1})_2$  and  $\text{Zn}(\text{L4})_2$ , fluorine has a similar stabilizing effect on both the cation and anion.

The differences between the first and second reduction potentials of each compound were similar, indicating that fluorine influences both reductions equally. For the fluorinated  $\text{BF}_2^+$  complexes, the first and second reduction potentials were slightly more positive than those of  $\text{BF}_2(\text{WS3})$ . The  $E_{1/2}$  red. values ranged from -0.79 V for  $\text{BF}_2(\text{WS3})$  to -0.69 V for  $\text{BF}_2(\text{L4})$ . All the first reduction potentials of the fluorinated  $\text{BF}_2^+$  complexes were -0.70 V with the difference between first and second  $E_{1/2}$  values being 0.77 V. Collectively, the fluorine-modified WS3 chelates showed higher oxidation potentials than those of unmodified chelates. The interpretation of electrochemical data shows that the addition of fluorine had the greatest effect on L1 and L4 chelates, while having minimal effects on the L2 and L3 chelates. The estimated HOMO and LUMO energy levels obtained from cyclic voltammetry are shown in Figure 8. The HOMO and LUMO of  $\text{Zn}(\text{L1})_2$  and  $\text{Zn}(\text{L4})_2$  approach those of PCBM.

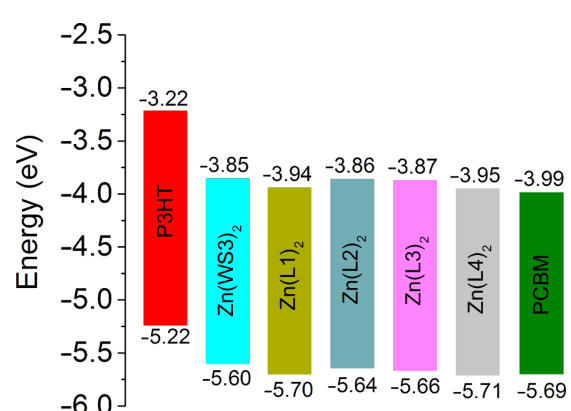
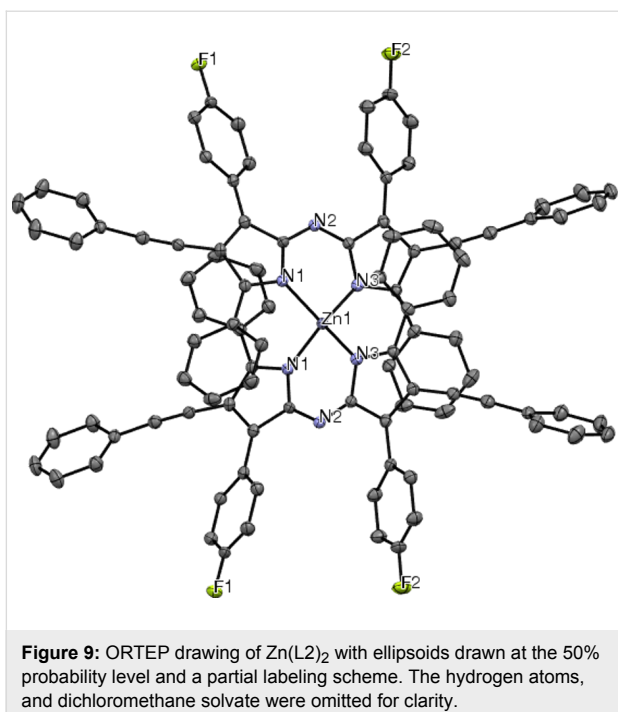


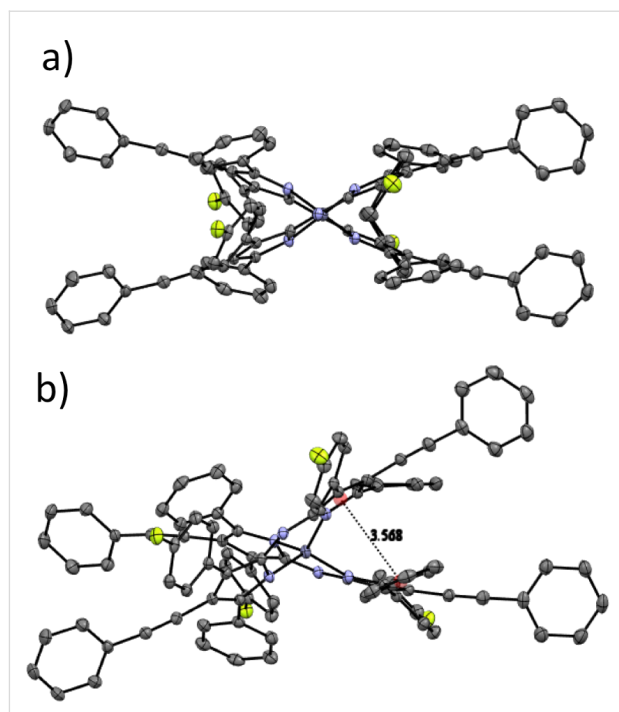
**Figure 8:** Estimated HOMO and LUMO energy levels obtained by cyclic voltammetry from the  $E_{1/2}$  values in dichloromethane solution, using the value of -5.1 eV for Fc/Fc<sup>+</sup>. The included HOMO and LUMO levels of P3HT films were estimated in our laboratory from the oxidation onset and the optical gap.

## Crystallography

Single crystals of the zinc(II) chelates were grown in order to better understand the structure of the materials. Only  $\text{Zn}(\text{L2})_2$  produced crystals suitable for analysis. Figure 9 shows the ORTEP drawing of  $\text{Zn}(\text{L2})_2$  with 50% ellipsoids and a partial labeling scheme for clarity. The crystal structure confirms the identity of the complex and gives an idea of the interactions in



the complex. Like  $\text{Zn}(\text{ADP})_2$ , the structure is distorted tetrahedral with favorable  $\pi$ – $\pi$  stacking distances between the proximal phenyl and pyrrole rings of the two separate ligands (Figure 10a and 10b). The distance between centroids is 3.56 Å for  $\text{Zn}(\text{L2})_2$ , compared to 3.63 Å for  $\text{Zn}(\text{ADP})_2$  [38]. The shorter distance found for  $\text{Zn}(\text{L2})_2$  suggests a stronger interaction between the proximal phenyl and pyrrole rings than in  $\text{Zn}(\text{ADP})_2$ . Unfortunately, it cannot be determined whether the addition of fluorine or phenylacetylene contributed to the shorter  $\pi$ – $\pi$  stacking distances without a crystal structure for  $\text{Zn}(\text{WS3})_2$ . Intermolecular favorable  $\pi$ – $\pi$  stacking distances are observed between the pyrrolic phenylacetylene arms of two chelates seen on the outside of the unit cell, as well as between the distal phenyl rings of two chelates. Due to the crowded packing and difficulty in obtaining a clear image to convey these observations, the authors invite the reader to observe the intermolecular packing on their own using the cif file provided as Supporting Information File 2.



### Preliminary results in OPVs

To test the potential of the new fluorinated zinc(II) complexes as electron acceptor, we fabricated bulk heterojunction OPVs in the inverted configuration using P3HT as the electron donor. The best results obtained so far are reported in Table 3. For comparison, we also included results for a typical P3HT:PCBM solar cell. First, we note that best PCEs for  $\text{Zn}(\text{WS3})_2$  are lower than in our previous publication, 2.36% instead of 4.10% [10]. The main difference is that we now get lower  $J_{\text{sc}}$ , 5.2 mA/cm<sup>2</sup> instead of 9.1 mA/cm<sup>2</sup>. While our previously reported results were reproducible at the time, we are no longer able to reproduce them with the new  $\text{Zn}(\text{WS3})_2$  batches, even after extensive purification. We have therefore decided to report the results

**Table 3:** Preliminary results for OPVs using P3HT as the donor.

Acceptor	Donor:acceptor ratio	$V_{\text{OC}}$ [V]	$J_{\text{sc}}$ [mA/cm <sup>2</sup> ]	FF [%]	PCE [%]
$\text{Zn}(\text{WS3})_2$	1:0.7	0.80	5.16	57	2.36
$\text{Zn}(\text{L1})_2$	1:1	0.68	5.08	47	1.55
$\text{Zn}(\text{L2})_2$	1:0.7	0.73	8.31	59	3.04
$\text{Zn}(\text{L3})_2$	1:0.5	0.73	8.54	60	3.74
$\text{Zn}(\text{L4})_2$	1:0.7	0.59	9.29	66	3.26
PCBM	1:0.8	0.59	11.06	61	3.97

we now routinely obtain because they are obtained under similar conditions as the new results with the fluorinated compounds.

$\text{Zn(L2-L4)}_2$  showed an increase in PCE compared to  $\text{Zn(WS3)}_2$ , due to an increase in  $J_{\text{SC}}$ . This points to a generally positive effect of fluorination on device performance. The current best performance of 3.74% was obtained with  $\text{Zn(L3)}_2$  with an open circuit voltage ( $V_{\text{oc}}$ ) of 0.73V, a short-circuit current density ( $J_{\text{sc}}$ ) of 8.54 mA/cm<sup>2</sup> and a fill factor (FF) of 60%. While maintaining similar  $V_{\text{oc}}$  and FF values,  $\text{Zn(L2)}_2$  had a lower PCE of 3.04% due to a decrease in  $J_{\text{sc}}$ . With a PCE of 3.26%,  $\text{Zn(L4)}_2$  showed the largest  $J_{\text{SC}}$  and FF but a lower  $V_{\text{oc}}$ , consistent with its lower LUMO energy level than the other complexes.  $\text{Zn(L4)}_2$  shows the best potential to be paired with other electron donors of lower HOMO energy levels than P3HT. Compared to the P3HT:PCBM cell, the P3HT: $\text{Zn(L4)}_2$  cell had a similar  $V_{\text{oc}}$ , a higher FF, and a lower  $J_{\text{sc}}$ . The lower  $J_{\text{sc}}$  may be due to several factors, including purity, film thickness, morphology and charge recombination differences. Further studies are underway to better understand these results and will be reported separately.

## Conclusion

In conclusion, four fluorinated WS3 derivatives were synthesized and the optical and electrochemical properties of their respective zinc(II) and  $\text{BF}_2^+$  chelates studied. It was found that the addition of fluorine into the  $\text{Zn(L1)}_2$  and  $\text{Zn(L4)}_2$  complexes raised the oxidation and reduction potentials. Fluorination was found to have little effect on the absorption spectra, both in solution and film. Preliminary results in OPVs suggest that fluorination is generally beneficial for device performance of zinc(II) azadipyrromethene-based acceptors. In particular,  $\text{Zn(L4)}_2$  is the best candidate to directly replace PCBM due to similar energy levels and good performance. More work is underway to better understand the mechanism for the enhancement, and will be published separately.

## Experimental

### Materials

Chalcone (Acros), 4-fluorochalcone (TCI America), 4'-fluorochalcone (TCI America), 4,4'-difluorochalcone (TCI America), 1-ethynyl-4-fluorobenzene (Aldrich), 4-ethynyl- $\alpha,\alpha,\alpha$ -trifluorotoluene (Aldrich), *n*-butyllithium solution (Aldrich), tributyltin chloride (Fisher), tributyl(phenylethynyl)tin (Aldrich), tetrakis(triphenylphosphine)palladium(0) (Aldrich), *n*-iodosuccinimide (abbreviated NIS, Aldrich) were used as received. All other reagents and solvents were used as received unless otherwise specified. Xylenes and tetrahydrofuran were distilled over sodium and benzophenone, degassed and stored under nitrogen. ADP, ADPI<sub>2</sub>,

WS3,  $\text{BF}_2(\text{WS3})$ , and  $\text{Zn}(\text{WS3})_2$  were synthesized and purified according to literature procedures with minor modifications [2,5,9,33,34]. (4-Fluorophenylethynyl)tributyltin (for the synthesis of L3), and [4-(trifluoromethyl)phenyl](tributyltin)acetylene (for the synthesis of L4) were synthesized according to literature procedures with minor modifications and used without purification [35,36].

## Methods

<sup>1</sup>H, <sup>19</sup>F, and <sup>13</sup>C NMR spectra were recorded using a 500 MHz Bruker Ascend Avance III HDTM equipped with ProdigyTM ultra-high sensitivity Multinuclear Broadband CryoProbe or a Varian 400 MHz spectrometer in parts-per-million with respect to tetramethylsilane. MALDI-TOF-MS samples were prepared from chloroform solutions in a terthiophene matrix and run on a Bruker Autoflex III MALDI-TOF-TOF-MS. UV-visible absorption and emission spectra were collected in HPLC grade chloroform on a UV-Cary 50 spectrometer and a Cary Eclipse fluorescence spectrometer, respectively. Solutions for films were prepared at 10 mg/mL concentration in HPLC grade chloroform. The solutions were filtered through a 0.45  $\mu\text{m}$  PTFE filter, then spun-cast at 400 rpm for 60 s. Elemental analyses (C, H, and N) were performed under optimum combustion conditions by Robertson Microlit Laboratories. Thermal gravimetric analysis (TGA) was performed on a TA instrument Q500 thermogravimetric analyzer.

Cyclic voltammetry was performed at room temperature using an Auto-Lab-PGSTAT 302N, Exo Chemie potentiostat. Dichloromethane (DCM) was dried over calcium hydride and stored in a nitrogen glove box prior to use. The samples were prepared in a degassed 0.1 M solution of tetra-*n*-butylammonium hexafluorophosphate (TBAPF<sub>6</sub>) in DCM. Ferrocene/ferrocenium was used as an internal standard and was purified prior to use by sublimation. A typical three-electrode configuration was used, with a glassy carbon electrode as the working electrode and two platinum wires used as the counter and pseudoreference electrodes.

Crystals suitable for X-ray diffraction analysis were obtained by the slow diffusion of methanol into a dichloromethane solution. The crystals obtained were dark blue-black in appearance. Single-crystal X-ray diffraction studies were carried out using a Rigaku Rapid II diffractometer using Cu K $\alpha$  ( $\lambda = 1.54178 \text{ \AA}$ ) radiation monochromated using laterally graded multilayer (Goebel) mirror focusing optics. A single crystal was mounted on a Mitegen loop and cooled to 100 K for data collection. Unit cell parameters were measured and data were collected using the Rigaku CrystalClear software [39]. Data were reindexed and integrated using HKL3000, scaled, and corrected for absorption using Scalepack [40]. The space group was assigned and the

structure was solved by direct methods using the SHELXTL suite of programs [41,42] and refined by full matrix least squares against  $F^2$  with all reflections using Shelxl 2014 [43] using the graphical interface Shelxle [44]. H atoms attached to carbon atoms were positioned geometrically and constrained to ride on their parent atoms, with carbon hydrogen bond distances of 0.95 Å for aromatic C–H and 0.99 Å for CH<sub>2</sub> moieties, respectively.  $U_{\text{iso}}(\text{H})$  values were set to 1.2 times  $U_{\text{eq}}(\text{C})$ . A dichloromethane molecule is disordered around a twofold axis.

## Synthesis

**L1-ADP:** 4'-Fluorochalcone (2.01 g, 8.84 mmol) was dissolved in methanol (25 mL) in a round-bottom flask (100 mL) connected with a reflux condenser. Then nitromethane (2.70 g, 44.2 mmol) and diethylamine (3.23 g, 44.2 mmol) were added and refluxed for 24 h. The mixture was cooled to room temperature and then chilled in an ice bath before adding a 1 M HCl solution dropwise (100 mL). The mixture was then extracted 3× with dichloromethane, dried with anhydrous magnesium sulfate, filtered and rotary evaporated to obtain a yellow oil. This oil was then dissolved in butanol (100 mL) in a 500 mL round-bottom flask. Ammonium acetate (24 g) was added to the solution, stirred and heated to reflux. The solution became blue in about 30 min. After continued refluxing for 24 h, about 75% of the butanol was removed by rotary evaporation and the resulting dark blue slurry was filtered to collect the purplish blue solid product after washing with ethanol (200 mL) and vacuum dried overnight (0.484 g, 22.5%). <sup>1</sup>H NMR (400 MHz, CDCl<sub>3</sub>) δ 8.04–8.02 (d,  $J$  = 8 Hz, 4H), 7.91–7.88 (t,  $J$  = 8 Hz, 4H), 7.44–7.41 (t,  $J$  = 8 Hz, 4H), 7.38–7.35 (t,  $J$  = 8 Hz, 2H), 7.24–7.20 (t,  $J$  = 8 Hz, 4H), 7.13 (s, 2H); <sup>19</sup>F NMR (470 MHz, CDCl<sub>3</sub>) δ –92.35.

**L2-ADP:** 4-Fluorochalcone (3.29 g, 13.26 mmol) was dissolved in methanol (100 mL) in a round-bottom flask (100 mL) connected with a reflux condenser. Then nitromethane (4.32 g, 70.8 mmol) and diethylamine (5.66 g, 77.4 mmol) were added and heated to reflux for 24 h. The mixture was cooled to room temperature and then chilled on an ice bath before adding 1 M HCl solution drop-wise (100 mL). The mixture was then extracted 3× with dichloromethane, dried with anhydrous magnesium sulfate, filtered and rotary evaporated to obtain a yellow oil. This oil was then dissolved in 1-butanol (200 mL) in a 500 mL round-bottom flask. Ammonium acetate (37.6 g) was added to the solution and stirred and heated to reflux. After continued refluxing for 24 h, the 1-butanol was removed by rotary evaporation and the resulting solid was suspended in ethanol, filtered, and washed with ethanol (100 mL), and hexanes (50 mL). The solid was collected and vacuum dried overnight (0.919 g, 26%). <sup>1</sup>H NMR (500 MHz, CDCl<sub>3</sub>) δ 8.00

(dd,  $J$  = 8 Hz, 2H), 7.96 (d,  $J$  = 8 Hz, 2H), 7.55 (t,  $J$  = 7.5 Hz, 4H), 7.48 (t,  $J$  = 7.5 Hz, 2H), 7.16 (s, 2H), 7.12 (t,  $J$  = 7 Hz, 4H); <sup>19</sup>F NMR (470 MHz, CDCl<sub>3</sub>) δ –113.37.

**L1-ADPI<sub>2</sub>:** A similar procedure was used as for ADPI<sub>2</sub> (0.550 g, 75%) [33]. <sup>19</sup>F NMR (470 MHz, CDCl<sub>3</sub>) δ –92.35.

**L2-ADPI<sub>2</sub>:** A similar procedure was used as for ADPI<sub>2</sub> (0.998 g, 82%) [33]. MALDI–TOF–MS *m/z*: calcd for C<sub>32</sub>H<sub>19</sub>F<sub>2</sub>I<sub>2</sub>N<sub>3</sub>, 736.96; found, 735.85.

**L1:** Tributyl(phenylethynyl)tin (318 mg, 0.813 mmol) and L1-ADPI<sub>2</sub> (200 mg, 0.271 mmol) was taken into a Schlenk flask (50 mL) which was evacuated and refilled with N<sub>2</sub> three times. Dry chlorobenzene (15 mL) was added to the flask using a syringe and stirred and N<sub>2</sub> was bubbled through for 10 min. Then Pd(PPh<sub>3</sub>)<sub>4</sub> (0.094 g, 10 mmol %) was added inside a glove box. The mixture was heated at 90 °C for 48 h under N<sub>2</sub>. After cooling to room temperature, the mixture was dissolved in dichloromethane (500 mL) and passed through a Celite plug. The filtrate was concentrated using rotary evaporation of dichloromethane and poured into methanol (300 mL) to precipitate. The precipitate was filtered and washed with methanol and ether. After drying under vacuum overnight, the product was obtained as a dark blue solid (0.145 g, 78%). <sup>19</sup>F NMR (470 MHz, CDCl<sub>3</sub>, δ) –92.35.

**L2:** Tributyl(phenylethynyl)tin (0.928 g, 2.373 mmol) and L2-ADPI<sub>2</sub> (0.500 g, 0.678 mmol) was taken into a Schlenk flask (100 mL), which was evacuated and refilled with N<sub>2</sub> three times. Distilled xylenes (50 mL) were added to the flask using a syringe and placed under slight vacuum. Then Pd(PPh<sub>3</sub>)<sub>4</sub> (0.110 g, 14 mmol %) was added inside a glove box. The mixture was heated at 125 °C for 24 h under N<sub>2</sub>. After cooling to room temperature, the mixture was concentrated to a solid using rotary evaporation. The mixture was then cooled on dry ice and triturated with cold methanol (125 mL), filtered, and then washed with cold diethyl ether (125 mL). After drying under vacuum overnight, the product was obtained as a dark blue solid (0.441 g, 94%). MALDI–TOF–MS *m/z*: calcd. for C<sub>48</sub>H<sub>29</sub>F<sub>2</sub>N<sub>3</sub>, 685.23; found, 684.06.

**L3:** (4-Fluorophenylethynyl)tributyltin (0.612 g, 1.495 mmol) and ADPI<sub>2</sub> (0.300 g, 0.427 mmol) was taken into a Schlenk flask (100 mL), which was evacuated and refilled with N<sub>2</sub> three times. Distilled xylenes (50 mL) were added to the flask using a syringe and placed under slight vacuum. Then Pd(PPh<sub>3</sub>)<sub>4</sub> (0.049 g, 10 mmol %) was added inside a glove box. The mixture was heated at 125 °C for 48 h under N<sub>2</sub>. After 48 h, additional (4-fluorophenylethynyl)tributyltin (0.612 g, 1.495 mmol) and Pd(PPh<sub>3</sub>)<sub>4</sub> (0.049 g, 10 mmol %) were added in one shot.

The reaction mixture was allowed to react an additional 48 h at 125 °C under N<sub>2</sub>. After cooling to room temperature, the mixture was concentrated using rotary evaporation. The mixture was then cooled on dry ice and triturated with cold methanol (125 mL), filtered, and then washed with cold diethyl ether (125 mL). After drying under vacuum overnight, the product was obtained as a dark blue solid (0.206 g, 70%). MALDI–TOF–MS *m/z*: calcd. for C<sub>48</sub>H<sub>28</sub>BF<sub>4</sub>N<sub>3</sub>, 733.23; found, 731.94; anal. calcd for: C, 78.59; H, 3.85; N, 5.73; found: C, 78.41; H, 3.62; N, 5.98.

**L4:** [4-(Trifluoromethyl)phenyl](tributyltin)acetylene (0.686 g, 1.495 mmol) and ADPI<sub>2</sub> (0.313 g, 0.445 mmol) was taken into a Schlenk flask (100 mL), which was evacuated and refilled with N<sub>2</sub> three times. Distilled xylenes (50 mL) were added to the flask using a syringe and placed under slight vacuum. Then Pd(PPh<sub>3</sub>)<sub>4</sub> (0.049 g, 10 mmol %) was added inside a glove box. The mixture was heated at 125 °C for 48 h under N<sub>2</sub>. After 48 h, additional [4-(trifluoromethyl)phenyl](tributyltin)acetylene (0.686 g, 1.495 mmol) and Pd(PPh<sub>3</sub>)<sub>4</sub> (0.049 g, 10 mmol %) were added in one shot. The reaction mixture was allowed to react an additional 48 h at 125 °C under N<sub>2</sub>. After cooling to room temperature, the mixture was concentrated using rotary evaporation. The mixture was then cooled on dry ice and triturated with cold methanol (125 mL), filtered, and then washed with cold diethyl ether (125 mL). After drying under vacuum overnight, the product was obtained as a dark blue solid (0.301 g, 89%). MALDI–TOF–MS *m/z*: calcd. for C<sub>50</sub>H<sub>29</sub>F<sub>6</sub>N<sub>3</sub>, 785.79; found, 783.94

**BF<sub>2</sub>(L1):** It was synthesized using a similar procedure as for BF<sub>2</sub>(WS3)[34]. L1 (0.042 g, 0.1 mmol) was added to a dry round bottom flask (100 mL), sealed, flushed with nitrogen and charged with anhydrous DCM (25 mL). Diisopropylethylamine (0.2 mL) was added via syringe followed immediately by the addition of trifluoroboron etherate (0.4 mL) by syringe. The reaction mixture was stirred for 16 h at room temperature under N<sub>2</sub>. The solution was washed with distilled water ( $\approx$ 50 mL  $\times$  3) and dried over anhydrous MgSO<sub>4</sub> prior to concentration by rotary evaporation. The crude solid was further purified by column chromatography on silica gel using a 1:1 ratio of DCM/hexanes (v/v). The final pure product was obtained as a dark blue solid after removal of solvents (0.047 g, 74%) <sup>1</sup>H NMR (500 MHz, CD<sub>2</sub>Cl<sub>2</sub>,  $\delta$ ) 8.26–8.24 (d, *J* = 10 Hz, 4H), 8.08–8.05 (t, *J* = 10 Hz, 4H), 7.56–7.49 (m, 6H), 7.34 (s, 10H), 7.28–7.24 (t, *J* = 10 Hz, 5H); <sup>19</sup>F NMR (470 MHz, CDCl<sub>3</sub>,  $\delta$ ) –108.30–108.40 (m), –131–131.5 (dd); MALDI–TOF–MS *m/z*: calcd. for C<sub>48</sub>H<sub>28</sub>BF<sub>4</sub>N<sub>3</sub>, 733.23; found, 731.86; anal. calcd for: C, 78.59; H, 3.85; N, 5.73; found: C, 78.56; H, 4.00; N, 5.45.

**BF<sub>2</sub>(L3):** It was synthesized using a similar procedure as for BF<sub>2</sub>(L1) (0.039 g, 73%). <sup>1</sup>H NMR (500 MHz, CDCl<sub>3</sub>)  $\delta$  8.23

(m, 4H), 8.01 (m, 4H), 7.51 (m, 13H), 7.28 (m, 5H), 7.00 (t, *J* = 7 Hz, 4H); <sup>19</sup>F NMR (470 MHz, CDCl<sub>3</sub>)  $\delta$  –109.30–110.40 (m), –131–131.1 (dd); MALDI–TOF–MS *m/z*: calcd. for C<sub>48</sub>H<sub>28</sub>BF<sub>4</sub>N<sub>3</sub>, 733.23; found, 731.94; anal. calcd for: C, 78.59; H, 3.85; N, 5.73; found: C, 78.41; H, 3.62; N, 5.98.

**BF<sub>2</sub>(L4):** It was synthesized using a similar procedure than that of BF<sub>2</sub>(L1) (0.064 g, 59%). <sup>1</sup>H NMR (500 MHz, CDCl<sub>3</sub>)  $\delta$  8.22 (m, 4H), 8.03 (m, 4H), 7.54 (m, 14H), 7.4 (m, 4H); <sup>19</sup>F NMR (470 MHz, CDCl<sub>3</sub>,  $\delta$ ) –62.9 (s), –130–131.1 (dd); MALDI–TOF–MS *m/z*: calcd. for C<sub>50</sub>H<sub>28</sub>BF<sub>8</sub>N<sub>3</sub>, 833.22; found, 831.90; anal. calcd for: C, 72.04; H, 3.39; N, 5.04; found: C, 74.24; H, 3.25; N, 5.30.

**Zn(L1)<sub>2</sub>:** In a 100 mL three-necked flask equipped with a reflux condenser, L1 (100 mg, 0.146 mmol) was dissolved in anhydrous tetrahydrofuran (10 mL) under N<sub>2</sub>. To this dark blue solution, anhydrous NaH (4.00 mg, 0.161 mmol) was added and the mixture was heated to 60 °C. The solution turned to bright blue. After 24 h of heating, anhydrous ZnCl<sub>2</sub> (11.5 mg, 0.084 mmol) was added and heating was continued for another 24 h. The mixture turned back to dark blue. Then the mixture was cooled to room temperature and dissolved in dichloromethane (200 mL). This solution was then passed through a Celite plug and the filtrate was collected. The crude product was obtained by rotary evaporation of dichloromethane, and purified by flash chromatography using a dichloromethane/hexane mixture as the eluent (starting with 80% hexane and gradually decreasing the amount to 60%). The final pure product was obtained as a dark blue solid after removal of solvents (0.091 g, 87%). <sup>1</sup>H NMR (400 MHz, CD<sub>2</sub>Cl<sub>2</sub>)  $\delta$  7.98–7.97 (d, *J* = 4 Hz, 8H), 7.84–7.81 (dd, *J* = 8 Hz, *J* = 4 Hz, 8H), 7.54–7.46 (m, 12H), 7.39–7.36 (m, 8H), 7.35–7.32 (m, 12H), 7.04–7.00 (t, *J* = 8 Hz, 8H); <sup>19</sup>F NMR (470 MHz, CDCl<sub>3</sub>)  $\delta$  –110.36 (s); MALDI–TOF–MS *m/z*: calcd for C<sub>96</sub>H<sub>56</sub>F<sub>4</sub>N<sub>6</sub>Zn, 1433.38; found, 1431.36. anal. calcd for: C, 80.36; H, 3.93; N, 5.86; found: C, 80.58; H, 4.08; N, 5.89.

**Zn(L2)<sub>2</sub>:** In a 100 mL three-necked flask L2 (0.229 g, 0.334 mmol) was dissolved in anhydrous tetrahydrofuran (20 mL) under N<sub>2</sub>. To this dark blue solution, anhydrous NaH (0.008 g, 0.401 mmol) was added and the mixture was heated to 60 °C. The solution turned bright blue. After 16 h of heating, anhydrous ZnCl<sub>2</sub> (0.023 g, 0.168 mmol) was added and heating was continued for another 16 h. The crude product was obtained by rotary evaporation of dichloromethane and purified by flash chromatography using a dichloromethane/hexane mixture as the eluent (started with 80% hexane and gradually decreasing to 60%). The final pure product was obtained as a dark blue solid after removal of solvents (0.167 g, 70%). <sup>1</sup>H NMR (400 MHz, CD<sub>2</sub>Cl<sub>2</sub>,  $\delta$ ) 7.94 (dd, *J* = 8 Hz, 8H), 7.78 (m, 8H),

7.36 (m, 8H), 7.30 (m, 12H), 7.22 (m, 12H), 7.17 (t,  $J$  = 7 Hz, 8H);  $^{19}\text{F}$  NMR (470 MHz,  $\text{CDCl}_3$ )  $\delta$  -112.77 (s). MALDI-TOF-MS  $m/z$ : calcd for  $\text{C}_{96}\text{H}_{56}\text{F}_4\text{N}_6\text{Zn}$ , 1433.38; found, 1432.46; anal. calcd for: C, 80.36; H, 3.93; N, 5.86; found: C, 80.19; H, 4.04; N, 5.78.

**Zn(L3)<sub>2</sub>:** In a 100 mL three-necked flask L3 (0.166 g, 0.242 mmol) was dissolved in anhydrous tetrahydrofuran (15 mL) under  $\text{N}_2$ . To this dark blue solution, anhydrous NaH (0.006 g, 0.266 mmol) was added and the mixture was heated to 60 °C. The solution became bright blue. After 16 h of heating, anhydrous  $\text{ZnCl}_2$  (0.016 g, 0.121 mmol) was added and heating was continued for another 16 h. The crude product was obtained by rotary evaporation of dichloromethane and purified by flash chromatography using a dichloromethane/hexane mixture as the eluent (starting with 80% hexane and gradually decreasing to 60%). The final pure product was obtained as a dark blue solid after removal of solvents (0.119 g, 69%).  $^1\text{H}$  NMR (400 MHz,  $\text{CD}_2\text{Cl}_2$ ,  $\delta$ ) 7.94 (d,  $J$  = 8 Hz, 8H), 7.78 (d,  $J$  = 8 Hz, 8H), 7.48 (m, 12H), 7.34 (m, 8H), 7.01 (t,  $J$  = 7 Hz, 8H);  $^{19}\text{F}$  NMR (470 MHz,  $\text{CDCl}_3$ )  $\delta$  -111.77 (s). MALDI-TOF-MS  $m/z$ : calcd for  $\text{C}_{96}\text{H}_{56}\text{F}_4\text{N}_6\text{Zn}$ , 1433.38; found, 1432.80; anal. calcd for: C, 80.36; H, 3.93; N, 5.86; found: C, 80.13; H, 4.09; N, 5.69.

**Zn(L4)<sub>2</sub>:** In a 100 mL three-necked flask L4 (0.346 g, 0.440 mmol) was dissolved in anhydrous tetrahydrofuran (20 mL) under  $\text{N}_2$ . To this dark blue solution, anhydrous NaH (0.012 g, 0.484 mmol) was added and the mixture was heated to 60 °C. The solution turned into a bright blue solution. After 16 h of heating, anhydrous  $\text{ZnCl}_2$  (0.030 g, 0.220 mmol) was added and heating was continued for another 16 h. The crude product was obtained by rotary evaporation of dichloromethane and purified by flash chromatography using dichloromethane/hexane mixture as the eluent (started with 80% hexane and gradually decreasing to 60%). The final pure product was obtained as a dark blue solid after removal of solvents (0.195 g, 54%).  $^1\text{H}$  NMR (400 MHz,  $\text{CD}_2\text{Cl}_2$ )  $\delta$  7.90 (d,  $J$  = 8 Hz, 8H), 7.76 (m, 8H), 7.63 (d,  $J$  = 7 Hz, 8H), 7.46–7.44 (dd,  $J$  = 8 Hz, 20H);  $^{19}\text{F}$  NMR (470 MHz,  $\text{CDCl}_3$ )  $\delta$  -63.07 (s). MALDI-TOF-MS  $m/z$ : calcd for  $\text{C}_{96}\text{H}_{56}\text{F}_4\text{N}_6\text{Zn}$ , 1633.37; found, 1629.75; anal. calcd for: C, 73.46; H, 3.45; N, 5.14; found: C, 73.42; H, 3.69; N, 5.06.

## Organic solar cells

Photovoltaic properties were studied using the inverted configuration: ITO/ZnO/P3HT:Acceptor/MoO<sub>3</sub>/Ag. ITO-coated glass ( $R = 15 \Omega/\text{sq}$ ) substrates were cleaned stepwise in each of the following under ultra-sonication for 15 minutes: detergent, deionized water, acetone, and isopropanol. From a 0.25 M ZnO precursor solution, the ZnO layer was spun coat. For all of the

devices fabricated, the total concentration of the active layer was 20 mg/mL with varying donor-to-acceptor ratios (see Table 3). While in an oxygen and moisture-free environment, the photoactive layer was spun coat at 1000 rpm for 40 s and 2000 rpm for 2 s. The substrates were annealed at 120 °C for 30 min prior to top electrode deposition. The P3HT:PCBM devices had a total concentration of 40 mg/mL, 1:0.8 donor-to-acceptor ratio, were spun coat at 800 rpm for 40 s and 2000 rpm for 2 s and annealed at 120 °C for 15 min. Molybdenum oxide (10 nm) and silver (80 nm) were thermally evaporated in sequence under a vacuum pressure of  $\approx 3 \times 10^{-6}$  Torr using an Angstrom Engineering Evovac thermal evaporator. The devices were characterized using a Oriel Sol2A solar simulator and a Keithley 2400 SourceMeter. The active area of each solar cell is 0.20  $\text{cm}^2$ .

## Supporting Information

### Supporting Information File 1

NMR and MS data.

[<http://www.beilstein-journals.org/bjoc/content/supplementary/1860-5397-12-182-S1.pdf>]

### Supporting Information File 2

Crystal structure of Zn(L2)<sub>2</sub>.

[<http://www.beilstein-journals.org/bjoc/content/supplementary/1860-5397-12-182-S2.cif>]

## Acknowledgements

We gratefully acknowledge the National Science Foundation (CHEM 1148652) for funding this project. We thank Dr. Ina Martin and the Materials for Opto/Electronic Research and Education (MORE) Center at CWRU for help related to devices. This material is based upon work supported by the National Science Foundation under Grant MRI-28.5 0821515 (for the purchase of the MALDI-TOF-TOF).

## References

1. Loudet, A.; Burgess, K. *Chem. Rev.* **2007**, *107*, 4891–4932. doi:10.1021/cr078381n
2. Palma, A.; Gallagher, J. F.; Müller-Bunz, H.; Wolowska, J.; McInnes, E. J. L.; O'Shea, D. F. *Dalton Trans.* **2009**, 273–279. doi:10.1039/B811764K
3. Partyka, D. V.; Deligonul, N.; Washington, M. P.; Gray, T. G. *Organometallics* **2009**, *28*, 5837–5840. doi:10.1021/om900552e
4. Ge, Y.; O'Shea, D. F. *Chem. Soc. Rev.* **2016**, *45*, 3846–3864. doi:10.1039/C6CS00200E
5. Gorman, A.; Killoran, J.; O'Shea, C.; Kenna, T.; Gallagher, W. M.; O'Shea, D. F. *J. Am. Chem. Soc.* **2004**, *126*, 10619–10631. doi:10.1021/ja047649e

6. Byrne, A. T.; O'Connor, A. E.; Hall, M.; Murtagh, J.; O'Neill, K.; Curran, K. M.; Mongrain, K.; Rousseau, J. A.; Lecomte, R.; McGee, S.; Callanan, J. J.; O'Shea, D. F.; Gallagher, W. M. *Br. J. Cancer* **2009**, *101*, 1565–1573. doi:10.1038/sj.bjc.6605247
7. Killoran, J.; Allen, L.; Gallagher, J. F.; Gallagher, W. M.; O'Shea, D. F. *Chem. Commun.* **2002**, 1862–1863. doi:10.1039/B204317C
8. O'Connor, A. E.; McGee, M. M.; Likar, Y.; Ponomarev, V.; Callanan, J. J.; O'Shea, D. F.; Byrne, A. T.; Gallagher, W. M. *Int. J. Cancer* **2012**, *130*, 705–715. doi:10.1002/ijc.26073
9. Senevirathna, W.; Liao, J.-y.; Mao, Z.; Gu, J.; Porter, M.; Wang, C.; Fernando, R.; Sauvé, G. *J. Mater. Chem. A* **2015**, *3*, 4203–4214. doi:10.1039/C4TA05765A
10. Mao, Z.; Senevirathna, W.; Liao, J.-Y.; Gu, J.; Kesava, S. V.; Guo, C.; Gomez, E. D.; Sauvé, G. *Adv. Mater.* **2014**, *26*, 6290–6294. doi:10.1002/adma.201400647
11. Sauvé, G.; Fernando, R. *J. Phys. Chem. Lett.* **2015**, *6*, 3770–3780. doi:10.1021/acs.jpclett.5b01471
12. Senevirathna, W.; Daddario, C. M.; Sauvé, G. *J. Phys. Chem. Lett.* **2014**, *5*, 935–941. doi:10.1021/jz402735c
13. Babudri, F.; Farinola, G. M.; Naso, F.; Ragni, R. *Chem. Commun.* **2007**, 1003–1022. doi:10.1039/B611336B
14. Leroux, F.; Jeschke, P.; Schlosser, M. *Chem. Rev.* **2005**, *105*, 827–856. doi:10.1021/cr040075b
15. Pagliaro, M.; Ciriminna, R. *J. Mater. Chem.* **2005**, *15*, 4981–4991. doi:10.1039/b507583c
16. Chambers, R. D. *Fluorine in Organic Chemistry*; CRC Press: Boca Raton, FL, U.S.A., 2004; p 406. doi:10.1002/9781444305371
17. Price, S. C.; Stuart, A. C.; Yang, L.; Zhou, H.; You, W. *J. Am. Chem. Soc.* **2011**, *133*, 4625–4631. doi:10.1021/ja1112595
18. Stuart, A. C.; Tumbleston, J. R.; Zhou, H.; Li, W.; Liu, S.; Ade, H.; You, W. *J. Am. Chem. Soc.* **2013**, *135*, 1806–1815. doi:10.1021/ja309289u
19. Yang, P.; Yuan, M.; Zeigler, D. F.; Watkins, S. E.; Lee, J. A.; Luscombe, C. K. *J. Mater. Chem. C* **2014**, *2*, 3278–3284. doi:10.1039/C3TC32087A
20. Liang, Y.; Xu, Z.; Xia, J.; Tsai, S.-T.; Wu, Y.; Li, G.; Ray, C.; Yu, L. *Adv. Mater.* **2010**, *22*, E135–E138. doi:10.1002/adma.200903528
21. Zhou, H.; Yang, L.; Stuart, A. C.; Price, S. C.; Liu, S.; You, W. *Angew. Chem., Int. Ed.* **2011**, *50*, 2995–2998. doi:10.1002/anie.201005451
22. Reichenbächer, K.; Süss, H. I.; Hulliger, J. *Chem. Soc. Rev.* **2005**, *34*, 22–30.
23. Günes, S.; Neugebauer, H.; Sariciftci, N. S. *Chem. Rev.* **2007**, *107*, 1324–1338. doi:10.1021/cr050149z
24. Heremans, P.; Cheyns, D.; Rand, B. P. *Acc. Chem. Res.* **2009**, *42*, 1740–1747. doi:10.1021/ar0000923
25. Love, J. A.; Nagao, I.; Huang, Y.; Kuik, M.; Gupta, V.; Takacs, C. J.; Coughlin, J. E.; Qi, L.; van der Poll, T. S.; Kramer, E. J.; Heeger, A. J.; Nguyen, T.-Q.; Bazan, G. C. *J. Am. Chem. Soc.* **2014**, *136*, 3597–3606. doi:10.1021/ja412473p
26. Liu, Y.; Zhao, J.; Li, Z.; Mu, C.; Ma, W.; Hu, H.; Jiang, K.; Lin, H.; Ade, H.; Yan, H. *Nat. Commun.* **2014**, *5*, 5293. doi:10.1038/ncomms6293
27. Albrecht, S.; Janietz, S.; Schindler, W.; Frisch, J.; Kurpiers, J.; Kniepert, J.; Inal, S.; Pingel, P.; Fostopoulos, K.; Koch, N.; Neher, D. *J. Am. Chem. Soc.* **2012**, *134*, 14932–14944. doi:10.1021/ja305039j
28. Carsten, B.; Szarko, J. M.; Son, H. J.; Wang, W.; Lu, L.; He, F.; Rolczynski, B. S.; Lou, S. J.; Chen, L. X.; Yu, L. *J. Am. Chem. Soc.* **2011**, *133*, 20468–20475. doi:10.1021/ja208642b
29. Yang, L.; Tumbleston, J. R.; Zhou, H.; Ade, H.; You, W. *Energy Environ. Sci.* **2013**, *6*, 316–326. doi:10.1039/C2EE23235A
30. Katz, H. E.; Lovinger, A. J.; Johnson, J.; Kloc, C.; Siegrist, T.; Li, W.; Lin, Y.-Y.; Dodabalapur, A. *Nature* **2000**, *404*, 478–481. doi:10.1038/35006603
31. Sonar, P.; Ng, G.-M.; Lin, T. T.; Dodabalapur, A.; Chen, Z.-K. *J. Mater. Chem.* **2010**, *20*, 3626–3636. doi:10.1039/b924404b
32. Shi, M.-M.; Chen, H.-Z.; Sun, J.-Z.; Ye, J.; Wang, M. *Chem. Commun.* **2003**, 1710–1711. doi:10.1039/b304141g
33. Gao, L.; Senevirathna, W.; Sauvé, G. *Org. Lett.* **2011**, *13*, 5354–5357. doi:10.1021/o1202211t
34. Senevirathna, W.; Sauvé, G. *J. Mater. Chem. C* **2013**, *1*, 6684–6694. doi:10.1039/c3tc31377h
35. delPozo, J.; Carrasco, D.; Pérez-Temprano, M. H.; García-Melchor, M.; Álvarez, R.; Casares, J. A.; Espinet, P. *Angew. Chem., Int. Ed.* **2013**, *52*, 2189–2193. doi:10.1002/anie.201209262
36. Meana, I.; Albéniz, A. C.; Espinet, P. *Adv. Synth. Catal.* **2010**, *352*, 2887–2891. doi:10.1002/adsc.201000430
37. Pavia, D. L.; Lampman, G. M.; Kriz, G. S.; Vyvyan, J. R. *Introduction to Spectroscopy*; Brooks: Belmont, CA, U.S.A., 2009.
38. Teets, T. S.; Partyka, D. V.; Updegraff, J. B.; Gray, T. G. *Inorg. Chem.* **2008**, *47*, 2338–2346. doi:10.1021/ic701190g
39. Rigaku Corp. (2001). CrystalClear, T. W., Texas, USA.
40. Otwinowski, Z.; Minor, W. In *Macromolecular Crystallography, Pt A*; Carter, C. W., Jr.; Sweet, R. M., Eds.; Methods in Enzymology, Vol. 276; 1997; pp 307–326.
41. Sheldrick, G. M. *Acta Crystallogr., Sect. A: Found. Crystallogr.* **2008**, *64*, 112–122. doi:10.1107/S0108767307043930
42. *SHELXTL, Bruker Advanced X-ray Solutions*, Version 6.14; Madison, WI, U.S.A., 2000.
43. Sheldrick, G. M. U. o. G.: Germany, <http://shelx.uni-ac.gwdg.de/SHELX/>.
44. Hübschle, C. B.; Sheldrick, G. M.; Dittrich, B. *J. Appl. Crystallogr.* **2011**, *44*, 1281–1284. doi:10.1107/S0021889811043202

## License and Terms

This is an Open Access article under the terms of the Creative Commons Attribution License (<http://creativecommons.org/licenses/by/4.0/>), which permits unrestricted use, distribution, and reproduction in any medium, provided the original work is properly cited.

The license is subject to the *Beilstein Journal of Organic Chemistry* terms and conditions: (<http://www.beilstein-journals.org/bjoc>)

The definitive version of this article is the electronic one which can be found at: [doi:10.3762/bjoc.12.182](http://doi:10.3762/bjoc.12.182)



# Comparing blends and blocks: Synthesis of partially fluorinated diblock polythiophene copolymers to investigate the thermal stability of optical and morphological properties

Pierre Boufflet<sup>1</sup>, Sebastian Wood<sup>2</sup>, Jessica Wade<sup>2</sup>, Zhuping Fei<sup>1</sup>, Ji-Seon Kim<sup>2</sup>  
and Martin Heeney<sup>\*1</sup>

## Full Research Paper

Open Access

Address:

<sup>1</sup>Department of Chemistry and Centre for Plastic Electronics, Imperial College London, Exhibition Rd, London, SW7 2AZ, UK and

<sup>2</sup>Department of Physics and Centre for Plastic Electronics, Imperial College London, London, SW7 2AZ, UK

Email:

Martin Heeney<sup>\*</sup> - m.heeney@imperial.ac.uk

\* Corresponding author

Keywords:

conjugated block-copolymer synthesis; fluorination; microphase stabilization; polythiophene; temperature-dependent Raman spectroscopy

*Beilstein J. Org. Chem.* **2016**, *12*, 2150–2163.

doi:10.3762/bjoc.12.205

Received: 19 July 2016

Accepted: 16 September 2016

Published: 10 October 2016

This article is part of the Thematic Series "Organic photovoltaics".

Guest Editor: D. J. Jones

© 2016 Boufflet et al.; licensee Beilstein-Institut.

License and terms: see end of document.

## Abstract

The microstructure of the active blend layer has been shown to be a critically important factor in the performance of organic solar devices. Block copolymers provide a potentially interesting avenue for controlling this active layer microstructure in solar cell blends. Here we explore the impact of backbone fluorination in block copolymers of poly(3-octyl-4-fluorothiophene)s and poly(3-octylthiophene) (F-P3OT-b-P3OT). Two block co-polymers with varying block lengths were prepared via sequential monomer addition under Kumada catalyst transfer polymerisation (KCTP) conditions. We compare the behavior of the block copolymer to that of the corresponding homopolymer blends. In both types of system, we find the fluorinated segments tend to dominate the UV-visible absorption and molecular vibrational spectral features, as well as the thermal behavior. In the block copolymer case, non-fluorinated segments appear to slightly frustrate the aggregation of the more fluorinated block. However, in situ temperature dependent Raman spectroscopy shows that the intramolecular order is more thermally stable in the block copolymer than in the corresponding blend, suggesting that such materials may be interesting for enhanced thermal stability of organic photovoltaic active layers based on similar systems.

## Introduction

With thin-film microstructure playing such a key role in the optoelectronic and charge transport properties of conjugated polymers, block copolymers naturally appear as useful tools for tailoring the thin-film morphology [1–5]. The propensity of some block copolymers to phase segregate at the nano-scale is

of particular interest in the field of organic photovoltaics (OPV), where separation of the electron donor and acceptor domains on the order of the exciton diffusion length (5–10 nm) is required [1,6–9]. Many approaches have been reported to tether two or more light-absorbing polymers to form a block

copolymer [1,10–15], with some attempts focusing on one block being the donor and the other the acceptor [16–18]. The main objective is that the blocks spontaneously “phase-separate” on the necessary length scales for efficient charge separation, transport and collection. With the thermal stability of all-polymer and polymer–fullerene blend microstructures being particularly problematic [19], block copolymers present a potential solution. Indeed, it has been shown that when block copolymers are used as additives in bulk heterojunction donor–acceptor blend layers, the morphology of the resulting ternary blend film can be more stable over long periods of time, even under thermal annealing [14,20,21].

However, the synthesis of block copolymers can be difficult to control, particularly in the case of step-growth polymerizations that are often used to synthesize conjugated polymers. In these polymerizations, such as Stille or Suzuki polycondensations, one approach to the block copolymer synthesis is the addition of a well-defined polymeric end-capper, commonly bromine terminated poly(3-hexylthiophene). An issue with this approach can be the formation of a mixture of di- and triblock copolymers, which adds to the complexity of the system and makes batch-to-batch reproducibility difficult [1,2]. Particularly problematic is the lack of control over the block lengths and molecular weight for the step-growth polymerization. Indeed, the relative block lengths play a key role in the morphology control and the self-assembly behavior of these polymers [7,22,23]. The Grignard Metathesis (GRIM) polymerization, also known as the Kumada catalyst transfer polymerisation (KCTP), is a popular method to synthesize conjugated block copolymers because its chain growth behavior avoids any issues of triblock copolymers, and also provides good control over the molecular weight and relative block lengths [24–31]. In addition to enabling the formation of a diblock copolymer via sequential monomer addition, the KCTP can lead to controlled end-functionalization [1,28,32]. This has been used as a handle for further applications such as macroinitiation [7,10,21,31,33], endcapping [34], and grafting [35–39]. Despite the KCTP having somewhat limited scope and functional group tolerance, its advantages in terms of synthetic control mean that it is one of the most common methods for synthesizing fully conjugated block copolymers.

Since the backbone flexibility of each block has a crucial impact on the self-assembly of a block copolymer [7,40], the properties of polythiophene-based block copolymers can potentially be tuned by backbone fluorination which increases backbone rigidity [41,42]. As an initial exploration, this contribution presents the synthesis and purification of two block copolymers of poly(3-octylthiophene) (P3OT) and poly(3-fluoro-4-octylthiophene) (F-P3OT) with different relative block lengths.

The thermal behavior of the polymers’ UV–visible absorption and Raman scattering spectra are compared with those of the corresponding blends of P3OT and F-P3OT, as well as the homopolymers. The results of this study suggest that the tethering of P3OT and F-P3OT blocks may not lead to spontaneous large-scale phase separation behavior, but critically increases the thermal stability of intramolecular order, as observed by temperature dependent Raman spectroscopy studies.

## Results and Discussion

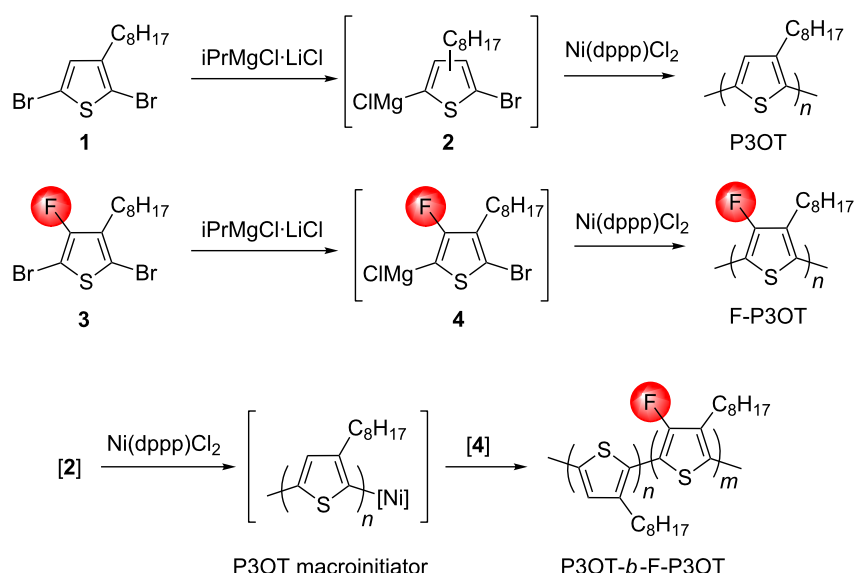
### Synthesis

The monomers and homopolymers P3OT and F-P3OT were synthesized via KCTP from the activated monomers **2** and **4**, as reported in our previous work (Scheme 1) [42]. The precipitated polymers were purified by Soxhlet extraction, washing sequentially with methanol, acetone and hexane (and chloroform for F-P3OT). P3OT was then extracted using chloroform, and F-P3OT with chlorobenzene.

The P3OT-*b*-F-P3OT copolymers were also synthesized by KCTP using a method analogous to that used for thiophene–selenophene block copolymers [26]. Due to the much lower solubility of F-P3OT compared to P3OT, the more soluble P3OT block was grown first from the activated monomer **2**, followed by the addition of **4** to the P3OT macroinitiator. Relative block lengths were controlled by varying the relative feed ratios of **2** to **4**. In order to probe the effect of block lengths on the polymer properties, 1:3 and 3:1 feed ratios of **2** to **4** were used, respectively. True block-lengths as determined by <sup>1</sup>H NMR (vide infra) were found to be 1:4 and 2:1, and the polymers will be referred to as such hereafter.

The block copolymers were initially purified by Soxhlet extraction, washing sequentially with methanol, acetone and hexane. In order to remove any P3OT homopolymer that may have been produced through chain termination prior to the addition of **4**, the P3OT-*b*-F-P3OT polymers were washed with a solvent that could selectively dissolve P3OT, but not dissolve the block-copolymers. Since the F-P3OT block decreases the overall solubility of the polymers, this was easily achieved in the case of the polymer resulting from a 1:3 feed. Indeed, this diblock polymer being insoluble in chloroform and P3OT exhibiting excellent solubility in this solvent, the P3OT homopolymer was simply removed by Soxhlet extraction with chloroform.

On the other hand, the comparatively smaller difference in solubility between P3OT and the P3OT-*b*-F-P3OT resulting from a 3:1 feed meant that this approach was not feasible. In that case, washing with dichloromethane resulted in a demonstrable removal of P3OT homopolymer, as indicated by the differential scanning calorimetry (DSC) thermogram (see Figure 1). Indeed,



**Scheme 1:** Grignard metathesis polymerization method of synthesizing the diblock copolymer. Relative block lengths are modified by changing the feed ratio of **2** to **4**.

the melting peak around 190 °C, apparent in the crude block copolymer and attributable to free P3OT, is clearly reduced upon washing. It is worth noting that shallow thermal transitions in the regions expected for P3OT are still present in this block copolymer, and this may be due to a small fraction of higher molecular weight P3OT that could not be fully removed by dichloromethane washing.

intensities of the signals assigned to the methylene protons adjacent to the thiophene ring (Figure 2). Due to the reduced solubility of the polymers, the spectra were recorded in 1,1,2,2-tetrachloroethane-*d*<sub>2</sub> at 403 K. The chemical shifts of the methylene protons for the fluorinated and non-fluorinated polymers are distinct, with the fluorinated block apparent as a triplet at 2.82 ppm, in very close agreement to the signal observed for the pure F-P3OT. In comparison, the non-fluorinated block occurs as a distinct triplet at 2.89 ppm, demonstrating the shielding effect of the *ortho*-fluorine. The <sup>19</sup>F NMR (see Supporting Information File 1, Figures S1 and S2) shows a single peak in both cases, demonstrating that these polymers are indeed regioregular block copolymers with little mixed region within a polymer chain. Integration of the methylene regions in the <sup>1</sup>H NMR indicates that the ratio of the two blocks deviates from the feed ratio, with a ratio P3OT-*b*-F-P3OT 2:1 and P3OT-*b*-F-P3OT 1:4 found (cf., 3:1 and 1:3 feed ratios, respectively).

We note that the peaks around 2.65 ppm are likely related to regiochemical defects such as head-to-head or tail-to-tail couplings in the backbone [43], as well as the methylene region from the chain end [44]. Integration of this region with respect to the overall methylene region gives approximate regioregularities of 92 and 97% for P3OT-*b*-F-P3OT 2:1 and P3OT-*b*-F-P3OT 1:4, respectively. The higher regioregularity for the dominant F-P3OT block polymer may result from the fact that a single isomer is formed during the Grignard metathesis reaction for 2,5-dibromo-4-fluoro-3-octylthiophene [42], whereas the equivalent non-fluorinated monomer gives an approximate 4:1 mixture of regioisomers [45,46]. Although this mixture of

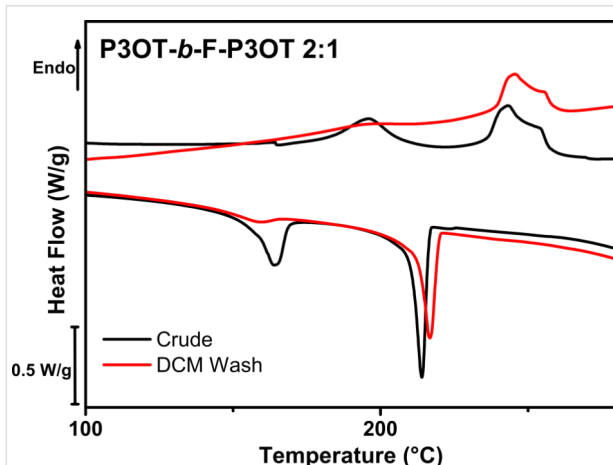


**Figure 1:** Differential scanning calorimetry thermogram (second cycle, 10 K/min) of P3OT-*b*-F-P3OT 2:1 before (black) and after (red) washing with dichloromethane. The reduction in the thermal transitions occurring below 200 °C, attributed to P3OT, indicate that a substantial amount of P3OT homopolymer was present in the crude polymer, but was removed by extraction.

The true relative block lengths were calculated from the <sup>1</sup>H NMR spectra of the purified polymers, based on the relative

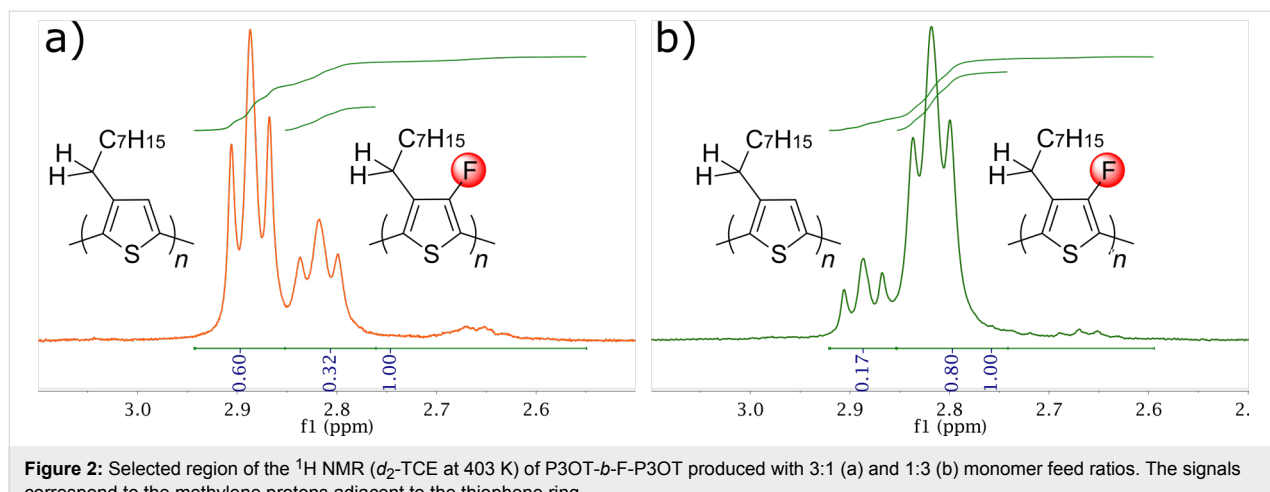


**Figure 2:** Selected region of the  $^1\text{H}$  NMR ( $d_2$ -TCE at 403 K) of P3OT-*b*-F-P3OT produced with 3:1 (a) and 1:3 (b) monomer feed ratios. The signals correspond to the methylene protons adjacent to the thiophene ring.

isomers can afford good regularity under certain conditions, it can be expected to have a detrimental effect on regioregularity [47]. For this reason most block co-polymers utilize a regiochemically pure organomagnesium reagent prepared from 2-bromo-5-iodo-3-alkylthiophene [28].

The reason for the large discrepancy between the feed ratio and the true block lengths in P3OT-*b*-F-P3OT 2:1 may be attributed to unexpected chain termination during the growth of the P3OT block. This theory is consistent with the large amount of P3OT homopolymer that was removed from the crude product upon Soxhlet extraction, as indicated by DSC. In the case of P3OT-*b*-F-P3OT 1:4, the discrepancy likely arises from the fact that the activated M–H monomer is intrinsically comprised of ca. 20% of a regioisomer which is relatively unreactive towards KCTP when using 1,2-bis(diphenylphosphino)propane as ligand [32,46,48,49]. This results in a reduced effective concentration of **2** relative to **4**, since in the case of **4** the regioselectivity of the monomer activation is over 95% [42].

Gel-permeation chromatography (GPC) measurements in hot (80 °C) chlorobenzene gave the number average molecular weight ( $M_n$ ) of P3OT-*b*-F-P3OT 2:1 as 55 kg/mol against polystyrene standards. Although this is higher than the theoretical  $M_n$  (ca. 39 kg/mol for a monomer:catalyst ratio of 200:1), it is likely due to the removal of lower molecular weight oligomers during Soxhlet extraction as well as the known overestimation of molecular weight for polythiophenes when measured by GPC against polystyrene standards [50,51]. Accounting for the purification, the  $M_n$  of P3OT-*b*-F-P3OT 2:1 is in reasonable agreement with the ratio of H and F blocks as determined by  $^1\text{H}$  NMR, and the molecular weight of a crude sample taken prior to the addition of **4**, which showed an  $M_n$  of 31 kg/mol (theoretical  $M_n$  29 kg/mol, Supporting Information File 1, Figure S3).

Despite having slightly better solubility than the homopolymer of F-P3OT, the solubility of P3OT-*b*-F-P3OT 1:4 in chlorobenzene was nevertheless too low to allow the molecular weight to be measured on our GPC instrument. A sample taken prior to the addition of **4** gave the molecular weight of the P3OT block as  $M_n$  15 kg/mol (theoretical  $M_n$  10 kg/mol), which would afford a final  $M_n$  at ca. 75 kg/mol when accounting for the  $^1\text{H}$  NMR ratios of H to F blocks.

## Optoelectronic properties

Our previous study on fluorinated poly(3-alkylthiophene) demonstrated that backbone fluorination leads to a ca. 0.3 eV increase in the ionisation potential (IP) compared to the non-fluorinated polymer [42]. In order to probe this effect in block copolymers, the IPs of P3OT-*b*-F-P3OT 2:1 and P3OT-*b*-F-P3OT 1:4 were measured by photoelectron spectroscopy in air (PESA). The results suggest that the IP in this system is mostly defined by the most abundant block. Indeed, the 2:1 block copolymer has an IP of 4.83 eV, slightly higher than that of P3OT (4.70 eV) measured by the same technique [42], while the 1:4 copolymer had an IP of 5.03 eV, which is within experimental error ( $\pm 0.05$  eV) of the IP of F-P3OT (4.99 eV) [42].

To investigate the influence of the block compositions on the optical properties, the UV–visible absorption spectra of thin films spin-cast from hot 1,2,4-trichlorobenzene were measured. The thin film UV–visible absorption of polythiophene derivatives can provide some information about the molecular order of the polymer chains, via the interpretation of the vibronic shoulders [52–55]. In the case of mixtures and block copolymers this is somewhat complicated by the different overlapping absorption profiles of the components. The absorption spectrum of a polymer blend typically corresponds to the sum of the absorptions of the component polymers (assuming complete phase separation occurs). Making use of complementary

absorption profiles for optimized harvesting of the solar spectrum is thus one of the main advantages of all-polymer photovoltaic devices [19,56–58]. The absorption spectra of block copolymers vary according to the system studied and processing conditions, since spontaneous phase separation is more difficult than in the case of polymer blends due to the chromophores being tethered. For example, in a polythiophene-polyselenophene block copolymer, isothermal recrystallization of the film results in an absorption profile that perfectly matches the linear combination of the homopolymers [26]. On the other hand, the absorption spectra of as spun block copolymers of P3HT with an analogue containing a ketone-functionalized side chain do not seem to linearly correlate to the composition ratio [59,60].

Figure 3 shows the absorption spectra of P3OT-*b*-F-P3OT in 2:1 and 1:4 ratios, as spun (see Figure 4 for overlay of both block copolymers and their corresponding blends). Also presented in Figure 3 are the absorption profiles of spin coated blends of P3OT and F-P3OT in the same ratios, as well as the weighted linear combination of the as spun absorption spectra of pure P3OT and F-P3OT polymers. All films were spin cast from hot 1,2,4-trichlorobenzene for comparison purposes. In the 2:1 ratio, all absorption profiles appear subtly different, both in terms of the peak positions and the vibronic structure. The block and blend films exhibit a slightly blue-shifted absorption maxima compared to the linear combination of homopolymers, as well as a more pronounced vibronic structure. Since F-P3OT homopolymer has a blue-shifted absorption with more vibronic structure than P3OT (vide infra), it can be deduced that the absorption profile of the block and blends are dominated by

F-P3OT sections of the mixture, despite it having a lower concentration. Unsurprisingly therefore, the films in 1:4 ratios have approximately the same absorption profile, with the peak positions being nearly identical to the F-P3OT homopolymer. Although the multicomponent nature of the systems likely complicates the interpretation of the vibronic structure in relation to the order in the thin film, it is worth noting that the vibronic structure of the block copolymers in both cases is less pronounced than for the corresponding blend. Considering the aforementioned link between the vibronic structure and aggregation, this likely indicates less inter- and intrachain coupling, and possibly a frustration of the crystallization and phase separation in the case of these block copolymers.

## Thermal behavior

### Differential scanning calorimetry

Fluorination of P3OT has previously been shown to result in a 50–60 °C increase in the melting and crystallization temperatures, an effect that was predominantly attributed to the increased backbone planarity and rigidity in combination with the increased aggregation it engenders [42]. In order to probe the crystallization behavior of the block copolymers and blends in thin films, DSC was therefore performed. Rather than investigating the melting transitions of bulk polymer powders, which are not always representative of films cast from solution, films were cast and then scraped off the substrate to be measured. Due to the poor solubility of the polymers with high fluorine content, the film thicknesses achievable when spin coating were low, and dropcasting onto a hot substrate was therefore used. The DSC thermograms of the resulting films are shown in Figure 4b.

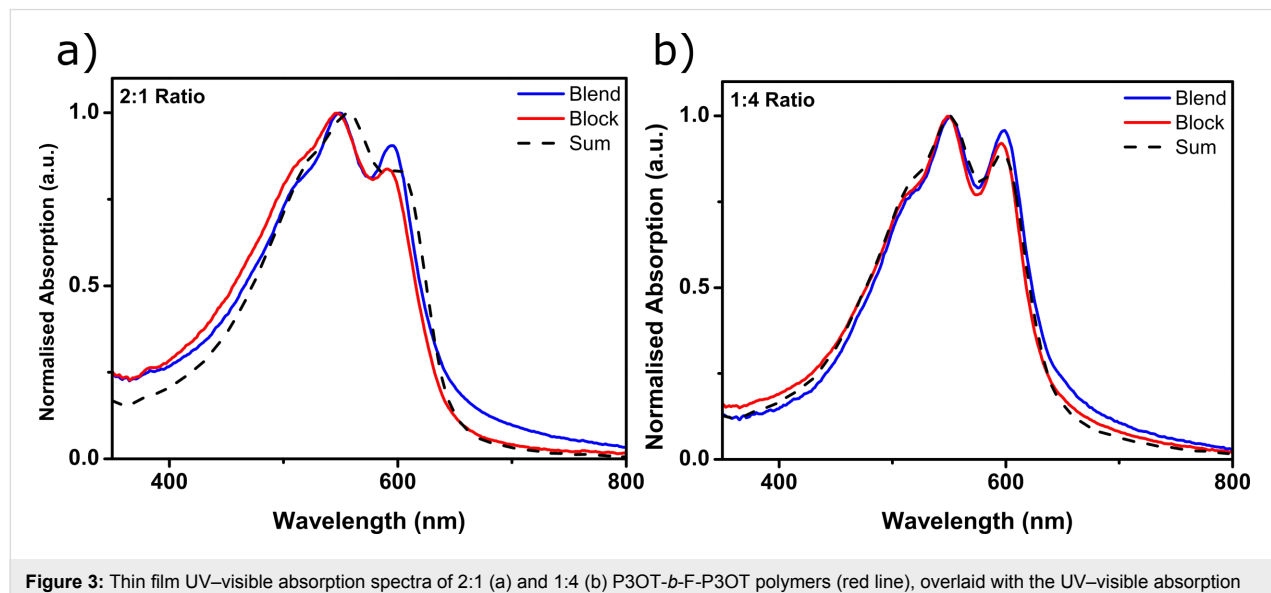


**Figure 3:** Thin film UV–visible absorption spectra of 2:1 (a) and 1:4 (b) P3OT-*b*-F-P3OT polymers (red line), overlaid with the UV–visible absorption spectra of a blend of P3OT and F-P3OT in the same ratio (blue line). The dotted line indicates the corresponding sum of the UV–visible absorption of P3OT and F-P3OT, weighted according to the composition. Thin films were spin cast from hot 1,2,4-trichlorobenzene.

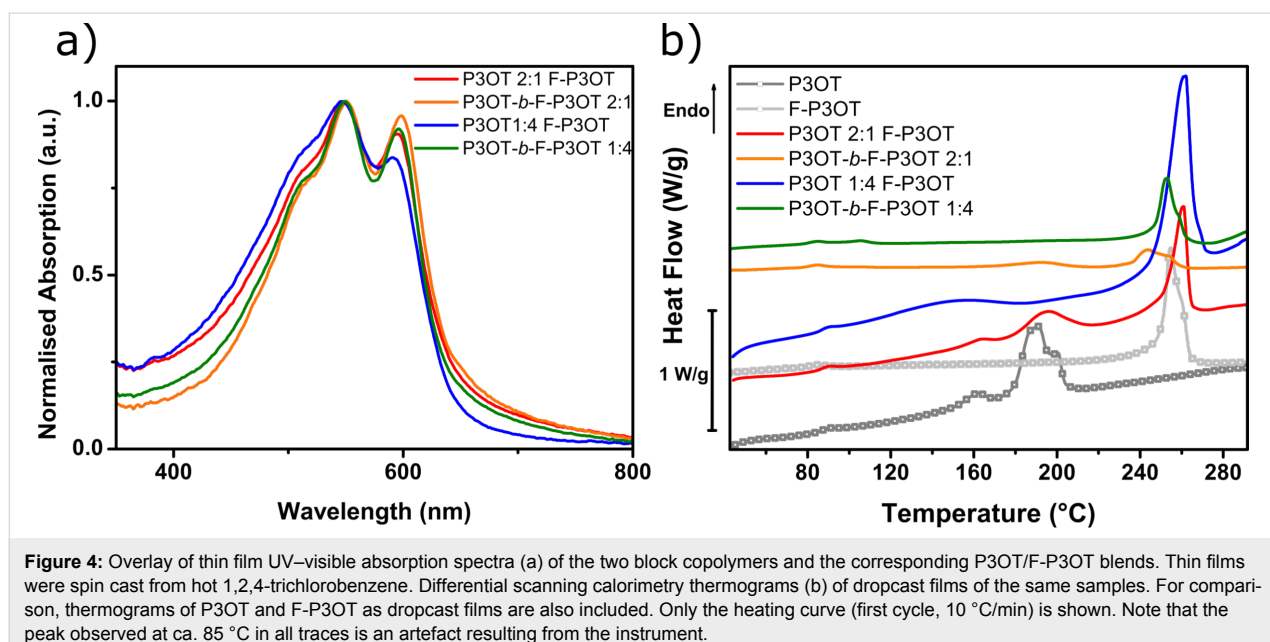


**Figure 4:** Overlay of thin film UV–visible absorption spectra (a) of the two block copolymers and the corresponding P3OT/F-P3OT blends. Thin films were spin cast from hot 1,2,4-trichlorobenzene. Differential scanning calorimetry thermograms (b) of dropcast films of the same samples. For comparison, thermograms of P3OT and F-P3OT as dropcast films are also included. Only the heating curve (first cycle, 10 °C/min) is shown. Note that the peak observed at ca. 85 °C in all traces is an artefact resulting from the instrument.

Immediately obvious from these thermograms is the prominence of a high-temperature (>240 °C) melting transition, in all cases except pure P3OT (ca. 180 °C). This transition can reasonably be attributed to the fluorinated block/polymer portion, due to its close proximity with the melting point of the F-P3OT homopolymer. As in the UV–visible absorption spectra, the domination of F-P3OT features is evident, particularly in the 2:1 blend which, despite containing twice the amount of P3OT than F-P3OT, still shows a much sharper and evident higher temperature melting transition characteristic of F-P3OT. The fact that the 2:1 blend undergoes two melts closely corresponding to each component polymer suggests that it has sufficient phase separation to allow both polymers to crystallize in discrete domains. On the other hand, in the 1:4 blend the melting transition of P3OT is absent. These observations may be explained by the greater melting enthalpy of the crystalline phase of F-P3OT compared to P3OT (28 and 17 J/g, respectively [42]), which could result in a masking of the P3OT melt in the baseline. However, the apparent suppression of the P3OT melt could also be explained by some degree of frustration of the P3OT crystallization, likely due to the earlier precipitation of the less soluble F-P3OT during the film formation.

P3OT-*b*-F-P3OT in a 1:4 ratio displays much the same melting behavior as the corresponding blend, although the onset of melting is slightly lower. This may be explained by the short P3OT segments, which although they may be too short to cause phase separation and crystallize themselves, likely cause some disruption to the crystallization of the F-P3OT segment [59,61]. In the case of P3OT-*b*-F-P3OT 2:1, there are two distinct

melting transitions which match those of P3OT and F-P3OT. Since it cannot be said with full confidence that all P3OT homopolymer was removed during purification, it is unclear whether these two transitions indicate phase separation and therefore separate melting transitions for each block, or are simply due to the residual P3OT impurity. However, the low melting enthalpies of both peaks and the lower melt onset of the F-P3OT block suggests that crystallization is frustrated even for the fluorinated block.

#### Influence of annealing temperature on UV–visible absorption

The influence of annealing temperature on the optical absorption spectra of the polymers was also investigated. Here films were annealed at the specified temperature for 20 minutes on a hotplate under argon before rapid quench cooling. The evolution of the thin film UV–visible absorption spectra with increasing annealing temperature (see Figure 5) partly reflects the thermal behavior of the samples as observed by DSC. In all cases, the low energy shoulder decreases in intensity with increasing annealing temperature, until a critical point when the absorption profile dramatically blue shifts and loses all or most of its vibronic structures. The broad absorption exhibited by the samples beyond this critical point is reminiscent of the absorption of fully solvated polythiophene derivatives, and therefore suggests that beyond this point the polymers have essentially been quenched in the melt state with disordered backbones and little inter- and intrachain coupling. This is further supported by the fact that these critical temperatures are in good agreement with the melt temperatures exhibited by the dropcast samples (see Table 1).

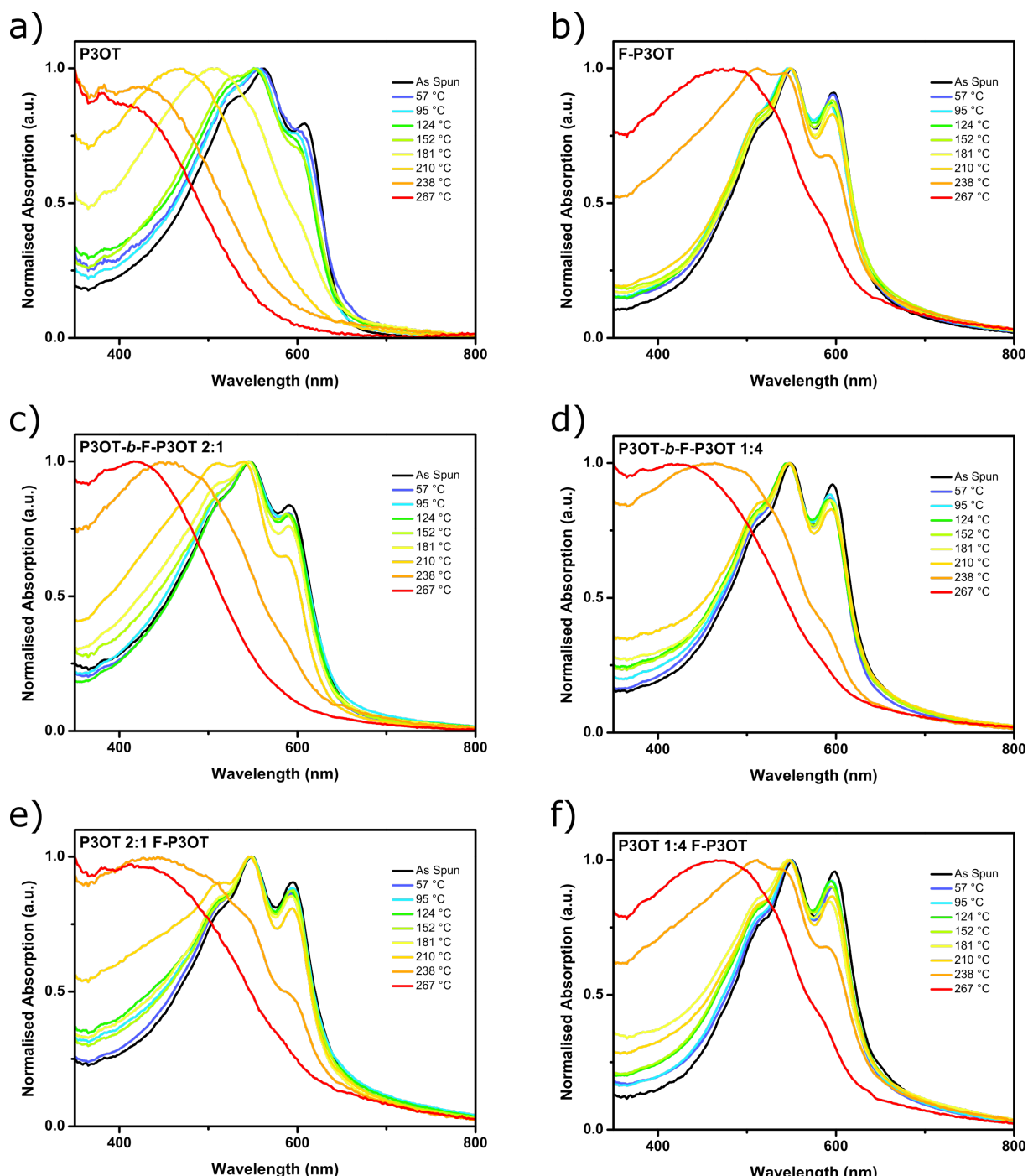


**Figure 5:** Thin-film UV–visible absorption spectra of a) P3OT, b) F-P3OT, c) P3OT-*b*-F-P3OT 2:1, d) P3OT-*b*-F-P3OT 4:1, e) P3OT/F-P3OT blend in a 2:1 ratio, and f) P3OT/F-P3OT blend in a 4:1 ratio. Films were annealed at the temperatures indicated for 20 min, then quench cooled and the UV–visible absorption spectrum measured. The same films were used for subsequent annealing at higher temperatures. Thin films were spin cast from hot 1,2,4-trichlorobenzene.

The critical temperature in the case of P3OT is near 181 °C, which is above the onset of melting transition, and all the vibronic structure is lost from the absorption when annealed well above the melt at 210 °C. Higher temperature annealing simply shifts the absorption to higher energy, consistent with

more disordered backbones as is observed in heated solutions of polythiophenes [42]. In the case of F-P3OT, annealing just under the melting onset (238 °C) leads to a significant shift in the vibronic structure. The large increase in the intensity of the high-energy part of the spectrum suggests an increase in the

**Table 1:** Melting point of dropcast films taken as the maximum (onset in parentheses), and critical annealing temperature of spin cast films at which vibronic structure is mostly lost from the UV-visible absorption.

	P3OT	F-P3OT	P3OT- <i>b</i> -F-P3OT		P3OT blend with F-P3OT	
			2:1	1:4	2:1	1:4
Melting point (°C)	190 (177)	254 (242)	193 (178) / 243 (235)	253 (243)	194 (180) / 261 (240)	261 (241)
Critical annealing temperature (°C)	181	267	238	238	238	267

proportion of disordered polymer [55,62], as expected at the onset of a melt, while the decreased intensity of the 0–0 shoulder may be indicative of a greater degree of interchain coupling and therefore the formation of H-aggregates [63]. Annealing at temperatures higher than the melt disrupts these aggregates, and although minor vibronic shoulders are still present, these are likely due to some degree of aggregation during the cooling prior to the measurement of the spectrum.

The blend and block copolymers behave in a similar manner to each other, with dramatic shifts in the vibronic structure near the onset of the melting transition and then a blue shift and loss in the vibronic structure when annealed beyond the highest temperature melt. In the 2:1 ratio samples, phase separation is suggested by the additional small changes in the vibronic structure seen when annealing is performed at 210 °C, beyond the low temperature transitions associated with P3OT domains melting, but below the onset of the F-P3OT melt. In the 1:4 ratio samples, the dominance of F-P3OT in the absorption profile means such small changes are not obvious. The only suggestion of P3OT chains melting is the small increase in absorption that is seen in the high-energy (ca. 400 nm) region of the spectra. The fact that this progression is more pronounced than in the case of pure F-P3OT may indicate phase separation since pure P3OT domains would be fully melted and disordered at such temperatures, and thus result in increased absorption in the high-energy region.

It is interesting to note that the vibronic structure is more resistant to higher annealing temperatures in the blends, perhaps indicating that in the block copolymers the disorder of the melted P3OT sections help break up the F-P3OT rich aggregates, or that these polymers do not phase separate as much, and may even produce co-crystals with lower melt onsets.

### Temperature dependent Raman spectroscopy

Having probed the effect of temperature on the intermolecular interactions of the samples using DSC and UV-visible absorption spectroscopy, we performed *in situ* Raman spectroscopy measurements, similar to those previously carried out on P3OT and F-P3OT [42] in order to observe the evolution of intramo-

lecular order with temperature, and compare the block copolymers with the polymer blends. The room temperature Raman spectra (see Supporting Information File 1, Figures S4–S6) show four strong peaks in the range 1300 cm<sup>−1</sup> to 1700 cm<sup>−1</sup>, associated with stretching modes of the conjugated polymer backbone. These peaks can be readily assigned to the P3OT and F-P3OT blocks of the polymer chain by comparison with the homopolymer spectra. We identify the 1381 cm<sup>−1</sup> and 1446 cm<sup>−1</sup> peaks as the stretching modes of the P3OT block, corresponding with symmetric C–C and C=C collective bond stretches. In the F-P3OT block, a similar pair of modes is observed with peaks at 1416 cm<sup>−1</sup> and 1491 cm<sup>−1</sup>, whose natures appear to be comparable to the non-fluorinated case and so can also be described as C–C and C=C collective stretches, respectively [42].

The Raman spectra of both the 2:1 diblock and blend films resemble a linear combination of the spectra for the neat homopolymers, where the peak positions are the same as for the homopolymers, but the intensities of the F-P3OT modes are stronger than those of the P3OT modes, contrary to what is expected from the molar ratio. This indicates that the Raman scattering cross-sections for these modes in the F-P3OT polymer are greater than for the corresponding modes in P3OT (by a factor of  $\approx 2$ ). As a result, the Raman spectra for both the 1:4 diblock and blend samples are dominated by the F-P3OT peaks, with minimal distinct contributions from the P3OT modes.

The temperature dependent Raman spectra of the pure homopolymers have been reported previously, and the blend and diblock samples display similar trends [42]. Specifically, as the temperature increases, all four main peaks move towards lower Raman shifts; the overall scattering Raman scattering intensity gradually reduces; and the intensities of the C–C modes (1381 cm<sup>−1</sup> and 1416 cm<sup>−1</sup>) reduce with respect to the corresponding C=C modes (1446 cm<sup>−1</sup> and 1491 cm<sup>−1</sup>, respectively). A distinct transition is observed in the Raman spectra at around 260–270 °C for P3OT and at 300–310 °C for F-P3OT, where the Raman scattering intensity reduces dramatically and the C=C peaks move towards higher Raman shifts (1469 cm<sup>−1</sup> for P3OT and 1505 cm<sup>−1</sup> for F-P3OT). These effects are found to

be largely reversible upon cooling (see Supporting Information File 1, Figure S7).

Below the transition, the observed reduction in Raman scattering intensity is consistent with a thermally-induced reduction in the ground vibrational state population, and the shifts in Raman peak position are associated with a combination of anharmonic ‘softening’ of the vibrational modes as well as conformational planarization of the polymer backbone [64,65]. The observed transition at 260–310 °C was previously assigned to overcoming the energetic barrier to rotation around the inter-ring C–C bond, resulting in a loss of effective  $\pi$ -conjugation as well as the Raman peaks associated with highly ordered polymer phases (in particular the lower energy contribution to the main C=C peak) [42].

The temperature dependent Raman spectra of the diblock and blend films presented in Figure 6, show broadly the same features and trends as their component homopolymers: all four

main peaks move towards lower Raman shifts with increasing temperature and the intensity of the C–C peaks also decrease with respect to the C=C peaks. The same transition is also observed in the range of 270–290 °C, for all of the samples, except for the 4:1 blend film. Since the Raman scattering from all of these samples is dominated by the F-P3OT component, the P3OT thermal transition temperature range is not distinct, however, it is striking that the F-P3OT transition is observed at a lower temperature for both diblocks and the 1:2 blend samples than for neat F-P3OT. In fact, the observed temperature range of the transition is comparable with that of the neat P3OT homopolymer ( $\approx$ 260 °C), which suggests that the event occurring within the P3OT chains promotes a similar event in the F-P3OT sections. In the block copolymers, where the F-P3OT and P3OT segments are tethered and electronically conjugated this is perhaps less surprising. However the 2:1 blend, which shows evidence of phase separation from the DSC measurements, also exhibits a 20–40 °C depression in the temperature of the Raman transition of the F-P3OT signals. The conclusion

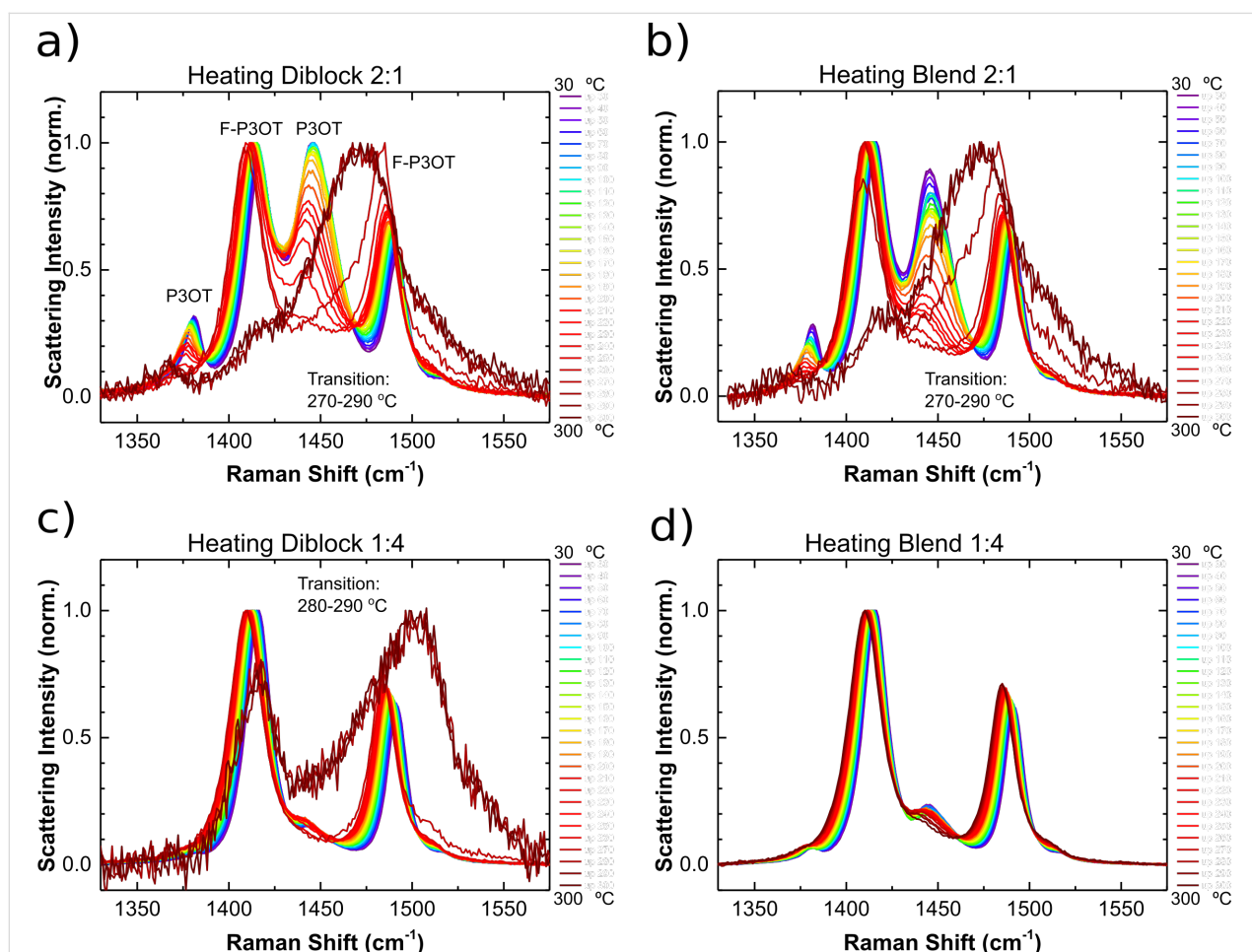


**Figure 6:** Temperature dependent Raman spectra measured during heating showing the main C–C and C=C stretches of a) P3OT-*b*-F-P3OT 2:1, b) P3OT/F-P3OT blend in a 2:1 ratio, c) P3OT-*b*-F-P3OT 4:1, and d) P3OT/F-P3OT blend in a 4:1 ratio. The main peaks are assigned to the fluorinated (F-P3OT) and nonfluorinated (P3OT) segments in a) based on the homopolymer spectra [42].

from this observation is that the structural event that leads to the Raman transition may be somewhat cooperative, even between polymer domains.

With previous reports of block copolymers stabilizing morphology (see Introduction), it is interesting to note that the P3OT-*b*-F-P3OT 2:1 exhibits greater thermal stability than the corresponding blend, when probed using the temperature dependent Raman spectrum. In this case, we consider the intensities of the strongest peaks measured for the P3OT ( $1446\text{ cm}^{-1}$ ) and F-P3OT chains ( $1416\text{ cm}^{-1}$ ). Since the intensities of these peaks correspond with the degree of conjugated backbone planarity for their respective chain segments, the ratio  $I_{1446}/I_{1416}$  gives an indication of the relative planarity of the P3OT part compared with the F-P3OT. This ratio is plotted as a function of temperature for both the 2:1 blend and diblock films in Figure 7. We find that this ratio drops consistently with temperature for the 2:1 blend film up to ca.  $175\text{ }^{\circ}\text{C}$ , where a more dramatic decrease is observed. In contrast, for the diblock copolymer, the ratio remains almost constant up to a similar temperature (ca.  $175\text{ }^{\circ}\text{C}$ ) before decreasingly more sharply. At temperatures above  $\approx 250\text{ }^{\circ}\text{C}$  the intensity ratios for both films are similar. It is noteworthy, that the onset of the change in decay rate of this ratio at around  $175\text{ }^{\circ}\text{C}$  occurs at a similar temperature to the onset of the P3OT melting transition in the DSC thermogram. The increased thermal stability of the diblock over the blend sample in this case does not appear to affect the melting temperature significantly, rather the stabilization relates to the molecular conformational order and particularly the planarity of the conjugated polymer backbone. This result indicates that the diblock copolymer is able to maintain ordered P3OT domains to a higher temperature than the equivalent blend film, and suggests that this is a viable strategy for enhancing morphological stability at elevated temperatures.

## Conclusion

In order to investigate the effects of partial planarization of the polymer backbone through fluorination on the physical and optoelectronic properties of the P3OT system, two block copolymers were synthesized via sequential monomer addition under by Kumada catalyst transfer polymerisation (KCTP) conditions. Diblock polymers with a large and small F-P3OT block were therefore synthesized. The P3OT-*b*-F-P3OT polymers were compared to their analogous blends of the corresponding homopolymers.

The F-P3OT block dominates the UV-visible absorption spectra, thermal behavior and Raman spectra, both in block copolymers and blends. The crystallization in the block copolymers appears to be slightly impeded, as suggested by the depressed melting point and reduced vibronic structure in the UV-visible

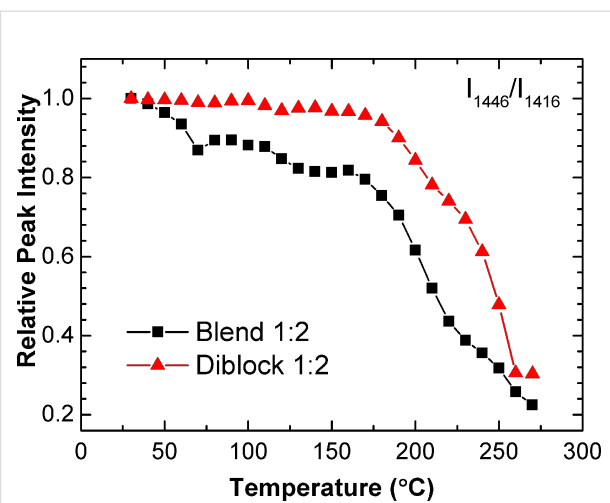


**Figure 7:** Influence of temperature on the relative Raman scattering intensities of the P3OT ( $1446\text{ cm}^{-1}$ ) and F-P3OT ( $1416\text{ cm}^{-1}$ ) C=C bond stretching modes. The block copolymer appears to have a constant relative intensity until ca.  $175\text{ }^{\circ}\text{C}$ , while the blend appears less stable, showing decay almost immediately upon heating.

absorption spectrum. The highest melting transition temperatures for each polymer or blend matches well with the critical annealing temperature at which the thin-film UV-visible absorption spectra exhibit a dramatic blue-shift in the absorption, and a loss in vibronic structure. The block copolymers have marginally lower critical temperatures than their blend analogues, perhaps further signifying impeded crystallization due to the P3OT segments disrupting the F-P3OT domains.

This is further corroborated by the fact that a thermal event, evident in the Raman spectra, attributed to a significant change in intramolecular order occurs in 3 of the 4 mixed systems at the same temperature as for pure P3OT (ca.  $260\text{--}270\text{ }^{\circ}\text{C}$ ), even for F-P3OT segments ( $310\text{ }^{\circ}\text{C}$  for pure polymer). Only in the 1:4 P3OT/F-P3OT blended film are the temperature dependent Raman spectra unaffected by the presence of P3OT, as is the case in the behavior measured using UV-visible absorption spectroscopy and DSC.

In the case of the 2:1 block copolymer, the temperature dependence of the Raman signals attributed to P3OT-rich polymer chains is found to be substantially different to the corresponding blend at temperatures below the thermal transition. While the intensity of the thiophene C=C stretching mode steadily decreases with increasing temperature in the case of the blend, it remains constant in the block copolymer until temperatures approaching the melting point of P3OT.

All the experimental data collected suggests that the increased propensity of F-P3OT to aggregate translates to a domination of

the optoelectronic and temperature dependent properties of the thin film, even as a minority component. P3OT and F-P3OT blends are also found to behave like a mostly phase-separated system, while the block copolymers exhibit signs of frustrated crystallization and self-assembly. It is likely that optimizations in the processing techniques, thermal annealing and solution self-assembly may help to improve this self-assembly.

## Experimental

### General

Reagents and chemicals were purchased from commercial sources such as Aldrich and Acros etc. unless otherwise noted. P3OT and F-P3OT and the corresponding monomers were synthesized according to our previous work [42]. The batch of P3OT used in this study had  $M_n$  26 kg/mol,  $M_w$  33 kg/mol (as measured by GPC in chlorobenzene at 80 °C), while the F-P3OT used  $M_n$  53 kg/mol,  $M_w$  98 kg/mol (as measured by HT-GPC in 1,2,4-trichlorobenzene at 130 °C).

All reactions were carried out under argon using solvents and reagents as commercially supplied, unless otherwise stated.  $^1\text{H}$  and  $^{19}\text{F}$  NMR spectra were recorded on a Bruker AV-400 (400 MHz), using the residual solvent resonance of  $\text{CDCl}_3$  or  $d_2$ -1,1,2,2-tetrachloroethane and are given in ppm. Number-average ( $M_n$ ) and weight-average ( $M_w$ ) were determined by Agilent Technologies 1200 series GPC running in chlorobenzene at 80 °C, using two PL mixed B columns in series, and calibrated against narrow polydispersity polystyrene standards.

Films for PESA, UV-visible absorption and Raman spectroscopy, were prepared by spin-coating from hot (ca. 150 °C) solution in 1,2,4-trichlorobenzene (5 mg/mL) at 3000 rpm for 2 minutes. Dropcast films for DSC measurements were prepared by dropcasting a hot (ca. 150 °C) 5 mg/mL solution in 1,2,4-trichlorobenzene onto hot glass substrates (ca. 120 °C) and letting the solvent evaporate. The film was then scraped off using a knife and the powder used for DSC analysis.

UV-visible absorption spectra were recorded on a UV-1601 Shimadzu UV-vis spectrometer. Each film was annealed (under flow of Ar) for 20 min at the lowest temperature, then cooled on a surface at room temperature before measuring the UV-visible absorption spectrum. The same film was then annealed and spectrum measured in a similar way for each subsequent temperature.

Photo electron spectroscopy in air (PESA) measurements were recorded with a Riken Keiki AC-2 PESA spectrometer with a power setting of 5 nW and a power number of 0.5. Samples for PESA were prepared on glass substrates by spin-coating.

Differential scanning calorimetry (DSC) measurements:  $\approx$ 2 mg material was used for the DSC experiments, which was conducted under nitrogen at a scan rate of 10 °C/min with a TA DSC-Q20 instrument.

Raman spectra were measured using a Renishaw inVia Raman spectrometer with 785 nm diode laser excitation. Laser power at the sample was 130 mW focussed to a 40  $\mu\text{m}^2$  area. The photoluminescence background was subtracted from the spectra using a polynomial baseline and then the spectra were normalized to the main peak. A Linkam THMS600 hot-cold cell purged with nitrogen was used to prevent polymer degradation as well as to control the temperature of the sample. For room temperature measurements the total laser exposure time was 25 s, the exposure time for temperature dependent spectra was 10 s. Starting from room temperature, the sample was heated at 10 °C/min to 300 °C, then cooled at the same rate. The temperature was held for 1 minute at every 10 °C interval in order to measure spectra.

### Typical procedure for the synthesis of Grignard monomer

To a solution of 2,5-dibromo-3-octylthiophene (361.2 mg, 1.02 mmol) in dry THF (2.86 mL) at room temperature was added isopropylmagnesium chloride lithium chloride complex (0.78 mL, 1.3 M in THF) dropwise. After 30 min, the resulting Grignard monomer solution (0.28 M in THF) was ready for use as indicated by the near total consumption of starting material (<3% remaining by quenching a sample with methanol and analysing by GC-MS).

### Synthesis of P3OT-*b*-F-P3OT 2:1

In a sealed dry 2–5 mL microwave vial charged with dichloro(1,3-bis(diphenylphosphino)propane)nickel (2.27 mg, 0.5 mol %) was added Grignard solution freshly prepared from 2,5-dibromo-3-octylthiophene (2.25 mL, 0.28 M in THF), and the reaction mixture was stirred at 40 °C for 1 h. GPC analysis of an aliquot quenched with methanol/HCl indicated  $M_n$  31 kg/mol,  $M_w$  43 kg/mol. A Grignard solution freshly prepared from 2,5-dibromo-3-fluoro-4-octylthiophene (0.75 mL, 0.28 M) was added to the reaction mixture, and the reaction heated to 70 °C for 2 h before being poured into methanol (200 mL) acidified with a few drops of conc. HCl. The precipitate was filtered through a cellulose thimble, and the solid purified by Soxhlet extraction with methanol, acetone, and hexane. In order to determine if substantial amounts of P3OT homopolymer still remaining in the sample, a DSC was run on a sample, and after confirmation that this was indeed the case, the solid was further washed with dichloromethane and finally extracted with chloroform, before precipitation into methanol and filtration. The resulting solid was dried under vacuum to

give P3OT-*b*-F-P3OT 2:1 (50 mg, 25%).  $M_n$  55 kg/mol,  $M_w$  60 kg/mol;  $^1\text{H}$  NMR (400 MHz, TCE-*d*<sub>2</sub>, 403 K,  $\delta$ ) 7.05 (s, 1H), 2.94–2.85 (m, 1.8H), 2.85–2.77 (m, 0.9H), 1.90–1.66 (m, 3H), 1.56–1.35 (m, 15H), 1.03–0.90 (m, 4.2H);  $^{19}\text{F}$  NMR (376 MHz, TCE-*d*<sub>2</sub>, 403 K,  $\delta$ ) –122.94 (s).

### Synthesis of P3OT-*b*-F-P3OT 1:4

In a sealed dry 2–5 mL microwave vial charged with dichloro(1,3-bis(diphenylphosphino)propane)nickel (2.27 mg, 0.5 mol %) was added Grignard solution freshly prepared from 2,5-dibromo-3-octylthiophene (0.75 mL, 0.28M in THF), and the reaction mixture was stirred at 40 °C for 1 h. GPC analysis of an aliquot quenched with methanol/HCl indicated  $M_n$ : 15 kg/mol,  $M_w$ : 18 kg/mol. A Grignard solution freshly prepared from 2,5-dibromo-3-fluoro-4-octylthiophene (2.25 mL, 0.28 M) was added, and the reaction heated to 70 °C for 2 h before being poured into methanol (200 mL) acidified with a few drops of conc. HCl. The precipitate was filtered through a cellulose thimble, and the solid purified by Soxhlet extraction with methanol, acetone, hexane and chloroform. The solid was dried and reprecipitated from 1,2,4-trichlorobenzene into methanol and filtered. The solid was dried under vacuum to give P3OT-*b*-F-P3OT 1:4 (104 mg, 64%). Molecular weight could not be measured due to lack of solubility.  $^1\text{H}$  NMR (400 MHz, TCE-*d*<sub>2</sub>, 403 K,  $\delta$ ) 7.05 (s, 1H), 2.93–2.86 (m, 1.8H), 2.85–2.76 (m, 8.3H), 1.91–1.64 (m, 10.9H), 1.58–1.27 (m, 56.9H), 1.06–0.89 (m, 15.1H);  $^{19}\text{F}$  NMR (376 MHz, TCE-*d*<sub>2</sub>, 403 K,  $\delta$ ) –122.94 (s).

### Supporting Information

$^1\text{H}$  and  $^{19}\text{F}$  NMR of P3OT-*b*-F-P3OT 2:1 and P3OT-*b*-F-P3OT 4:1, gel permeation chromatography trace for P3OT-*b*-F-P3OT 2:1, room temperature Raman spectra of P3OT and F-P3OT, room temperature Raman spectra of P3OT-*b*-F-P3OT 2:1 and P3OT-*b*-F-P3OT 1:4, room temperature Raman spectra of blends of P3OT and F-P3OT in 2:1 and 1:4 ratios, and temperature dependent Raman spectra measured during cooling.

### Supporting Information File 1

Additional spectra.

[<http://www.beilstein-journals.org/bjoc/content/supplementary/1860-5397-12-205-S1.pdf>]

### References

- Robb, M. J.; Ku, S.-Y.; Hawker, C. J. *Adv. Mater.* **2013**, *25*, 5686–5700. doi:10.1002/adma.201302677
- Lee, Y.; Gomez, E. D. *Macromolecules* **2015**, *48*, 7385–7395. doi:10.1021/acs.macromol.5b00112
- Yassar, A.; Miozzo, L.; Gironda, R.; Horowitz, G. *Prog. Polym. Sci.* **2013**, *38*, 791–844. doi:10.1016/j.progpolymsci.2012.10.001
- Darling, S. B. *Energy Environ. Sci.* **2009**, *2*, 1266–1273. doi:10.1039/b912086f
- Verswyvel, M.; Steverlynck, J.; Hadj Mohamed, S.; Trabelsi, M.; Champagne, B.; Koeckelberghs, G. *Macromolecules* **2014**, *47*, 4668–4675. doi:10.1021/ma500610p
- Segalman, R. A.; McCulloch, B.; Kirmayer, S.; Urban, J. J. *Macromolecules* **2009**, *42*, 9205–9216. doi:10.1021/ma901350w
- He, M.; Qiu, F.; Lin, Z. *J. Mater. Chem.* **2011**, *21*, 17039–17048. doi:10.1039/c1jm11518a
- Proctor, C. M.; Kuik, M.; Nguyen, T.-Q. *Prog. Polym. Sci.* **2013**, *38*, 1941–1960. doi:10.1016/j.progpolymsci.2013.08.008
- Shaw, P. E.; Ruseckas, A.; Samuel, I. D. W. *Adv. Mater.* **2008**, *20*, 3516–3520. doi:10.1002/adma.200800982
- Ku, S.-Y.; Brady, M. A.; Treat, N. D.; Cochran, J. E.; Robb, M. J.; Kramer, E. J.; Chabinyc, M. L.; Hawker, C. J. *J. Am. Chem. Soc.* **2012**, *134*, 16040–16046. doi:10.1021/ja307431k
- Yamada, I.; Takagi, K.; Hayashi, Y.; Soga, T.; Shibata, N.; Toru, T. *Int. J. Mol. Sci.* **2010**, *11*, 5027–5039. doi:10.3390/ijms11125027
- Suspène, C.; Miozzo, L.; Choi, J.; Gironda, R.; Geffroy, B.; Tondelier, D.; Bonnassieux, Y.; Horowitz, G.; Yassar, A. *J. Mater. Chem.* **2012**, *22*, 4511–4518. doi:10.1039/c2jm14960e
- Mulherin, R. C.; Jung, S.; Huetter, S.; Johnson, K.; Kohn, P.; Sommer, M.; Allard, S.; Scherf, U.; Greenham, N. C. *Nano Lett.* **2011**, *11*, 4846–4851. doi:10.1021/nl202691n
- Gao, D.; Hollinger, J.; Seferos, D. S. *ACS Nano* **2012**, *6*, 7114–7121. doi:10.1021/nn3021844
- Lai, Y.-C.; Ohshimizu, K.; Takahashi, A.; Hsu, J.-C.; Higashihara, T.; Ueda, M.; Chen, W.-C. *J. Polym. Sci., Part A: Polym. Chem.* **2011**, *49*, 2577–2587. doi:10.1002/pola.24689
- Zhang, Q.; Cirpan, A.; Russell, T. P.; Emrick, T. *Macromolecules* **2009**, *42*, 1079–1082. doi:10.1021/ma801504e
- Nakabayashi, K.; Mori, H. *Macromolecules* **2012**, *45*, 9618–9625. doi:10.1021/ma302170e
- Guo, C.; Lin, Y.-H.; Witman, M. D.; Smith, K. A.; Wang, C.; Hexemer, A.; Strzalka, J.; Gomez, E. D.; Verduzco, R. *Nano Lett.* **2013**, *13*, 2957–2963. doi:10.1021/nl401420s
- McNeill, C. R. *Energy Environ. Sci.* **2012**, *5*, 5653–5667. doi:10.1039/c2ee03071c
- Sivula, K.; Ball, Z. T.; Watanabe, N.; Fréchet, J. M. J. *Adv. Mater.* **2006**, *18*, 206–210. doi:10.1002/adma.200501787
- Renaud, C.; Mognier, S.-J.; Pavlopoulou, E.; Brochon, C.; Fleury, G.; Deribew, D.; Portale, G.; Cloutet, E.; Chambon, S.; Vignau, L.; Hadzioannou, G. *Adv. Mater.* **2012**, *24*, 2196–2201. doi:10.1002/adma.201104461
- Segalman, R. A. *Mater. Sci. Eng., R* **2005**, *48*, 191–226. doi:10.1016/j.mser.2004.12.003
- Bates, F. S.; Fredrickson, G. H. *Phys. Today* **1999**, *52*, 32–38. doi:10.1063/1.882522
- Locke, J. R.; McNeil, A. J. *Macromolecules* **2010**, *43*, 8709–8710. doi:10.1021/ma102218y
- Hollinger, J.; DiCarmine, P. M.; Karl, D.; Seferos, D. S. *Macromolecules* **2012**, *45*, 3772–3778. doi:10.1021/ma300394u

### Acknowledgements

We gratefully acknowledge Peter Haycock for running the high-temperature NMR experiments, and Dr. Scott E. Watkins (CSIRO Melbourne) for the PESA measurements.

26. Palermo, E. F.; McNeil, A. J. *Macromolecules* **2012**, *45*, 5948–5955. doi:10.1021/ma301135n

27. Iovu, M. C.; Sheina, E. E.; Gil, R. R.; McCullough, R. D. *Macromolecules* **2005**, *38*, 8649–8656. doi:10.1021/ma051122k

28. Bryan, Z. J.; McNeil, A. J. *Macromolecules* **2013**, *46*, 8395–8405. doi:10.1021/ma401314x

29. Hollinger, J.; Jahnke, A. A.; Coombs, N.; Seferos, D. S. *J. Am. Chem. Soc.* **2010**, *132*, 8546–8547. doi:10.1021/ja103191u

30. Kozyycz, L. M.; Gao, D.; Hollinger, J.; Seferos, D. S. *Macromolecules* **2012**, *45*, 5823–5832. doi:10.1021/ma3009349

31. Stefan, M. C.; Bhatt, M. P.; Sista, P.; Magurudeniya, H. D. *Polym. Chem.* **2012**, *3*, 1693–1701. doi:10.1039/C1PY00453K

32. Kiriy, A.; Senkovskyy, V.; Sommer, M. *Macromol. Rapid Commun.* **2011**, *32*, 1503–1517. doi:10.1002/marc.201100316

33. Kim, Y.-J.; Cho, C.-H.; Paek, K.; Jo, M.; Park, M.-k.; Lee, N.-E.; Kim, Y.-j.; Kim, B. J.; Lee, E. *J. Am. Chem. Soc.* **2014**, *136*, 2767–2774. doi:10.1021/ja410165f

34. Sommer, M.; Komber, H.; Huetter, S.; Mulherin, R.; Kohn, P.; Greenham, N. C.; Huck, W. T. S. *Macromolecules* **2012**, *45*, 4142–4151. doi:10.1021/ma300533k

35. Senkovskyy, V.; Tkachov, R.; Beryozkina, T.; Komber, H.; Oertel, U.; Horecha, M.; Bocharova, V.; Stamm, M.; Gevorgyan, S. A.; Krebs, F. C.; Kiriy, A. *J. Am. Chem. Soc.* **2009**, *131*, 16445–16453. doi:10.1021/ja904885w

36. Paoprasert, P.; Spalenka, J. W.; Peterson, D. L.; Ruther, R. E.; Hamers, R. J.; Evans, P. G.; Gopalan, P. *J. Mater. Chem.* **2010**, *20*, 2651–2658. doi:10.1039/B920233A

37. Awada, H.; Medlej, H.; Blanc, S.; Delville, M.-H.; Hiorns, R. C.; Bousquet, A.; Dagron-Lartigau, C.; Billon, L. *J. Polym. Sci., Part A: Polym. Chem.* **2014**, *52*, 30–38. doi:10.1002/pola.26964

38. Awada, H.; Mezzasalma, L.; Blanc, S.; Flahaut, D.; Dagron-Lartigau, C.; Lyskawa, J.; Woisel, P.; Bousquet, A.; Billon, L. *Macromol. Rapid Commun.* **2015**, *36*, 1486–1491. doi:10.1002/marc.201500184

39. Okamoto, K.; Luscombe, C. K. *Polym. Chem.* **2011**, *2*, 2424–2434. doi:10.1039/c1py00171j

40. Olsen, B. D.; Segalman, R. A. *Mater. Sci. Eng., R* **2008**, *62*, 37–66. doi:10.1016/j.mser.2008.04.001

41. Boufflet, P.; Han, Y.; Fei, Z.; Treat, N. D.; Li, R.; Smilgies, D.-M.; Stingelin, N.; Anthopoulos, T. D.; Heeney, M. *Adv. Funct. Mater.* **2015**, *25*, 7038–7048. doi:10.1002/adfm.201502826

42. Fei, Z.; Boufflet, P.; Wood, S.; Wade, J.; Moriarty, J.; Gann, E.; Ratcliff, E. L.; McNeill, C. R.; Sirringhaus, H.; Kim, J.-S.; Heeney, M. *J. Am. Chem. Soc.* **2015**, *137*, 6866–6879. doi:10.1021/jacs.5b02785

43. Chen, T.-A.; Wu, X.; Rieke, R. D. *J. Am. Chem. Soc.* **1995**, *117*, 233–244. doi:10.1021/ja00106a027

44. Koch, F. P. V.; Smith, P.; Heeney, M. *J. Am. Chem. Soc.* **2013**, *135*, 13695–13698. doi:10.1021/ja4057932

45. Loewe, R. S.; Khersonsky, S. M.; McCullough, R. D. *Adv. Mater.* **1999**, *11*, 250–253. doi:10.1002/(SICI)1521-4095(199903)11:3<250::AID-ADMA250>3.0.C O;2-J

46. Loewe, R. S.; Ewbank, P. C.; Liu, J.; Zhai, L.; McCullough, R. D. *Macromolecules* **2001**, *34*, 4324–4333. doi:10.1021/ma001677+

47. Lohwasser, R. H.; Thelakkat, M. *Macromolecules* **2011**, *44*, 3388–3397. doi:10.1021/ma200119s

48. Tkachov, R.; Senkovskyy, V.; Komber, H.; Kiriy, A. *Macromolecules* **2011**, *44*, 2006–2015. doi:10.1021/ma102724y

49. Boyd, S. D.; Jen, A. K.-Y.; Luscombe, C. K. *Macromolecules* **2009**, *42*, 9387–9389. doi:10.1021/ma902190p

50. Liu, J.; Loewe, R. S.; McCullough, R. D. *Macromolecules* **1999**, *32*, 5777–5785. doi:10.1021/ma9905324

51. Wong, M.; Hollinger, J.; Kozyycz, L. M.; McCormick, T. M.; Lu, Y.; Burns, D. C.; Seferos, D. S. *ACS Macro Lett.* **2012**, *1*, 1266–1269. doi:10.1021/mz300333f

52. Clark, J.; Silva, C.; Friend, R. H.; Spano, F. C. *Phys. Rev. Lett.* **2007**, *98*, No. 206406. doi:10.1103/physrevlett.98.206406

53. Yamagata, H.; Pochas, C. M.; Spano, F. C. *J. Phys. Chem. B* **2012**, *116*, 14494–14503. doi:10.1021/jp309407r

54. Martin, T. P.; Wise, A. J.; Busby, E.; Gao, J.; Roehling, J. D.; Ford, M. J.; Larsen, D. S.; Moulé, A. J.; Grey, J. K. *J. Phys. Chem. B* **2013**, *117*, 4478–4487. doi:10.1021/jp308586k

55. Baghgar, M.; Labastide, J. A.; Bokel, F.; Hayward, R. C.; Barnes, M. D. *J. Phys. Chem. C* **2014**, *118*, 2229–2235. doi:10.1021/jp411668g

56. Schubert, M.; Dolfen, D.; Frisch, J.; Roland, S.; Steyrlleuthner, R.; Stiller, B.; Chen, Z.; Scherf, U.; Koch, N.; Facchetti, A.; Neher, D. *Adv. Energy Mater.* **2012**, *2*, 369–380. doi:10.1002/aenm.201100601

57. Fabiano, S.; Chen, Z.; Vahedi, S.; Facchetti, A.; Pignataro, B.; Loi, M. A. *J. Mater. Chem.* **2011**, *21*, 5891–5896. doi:10.1039/c0jm03405c

58. Mori, D.; Benten, H.; Kosaka, J.; Ohkita, H.; Ito, S.; Miyake, K. *ACS Appl. Mater. Interfaces* **2011**, *3*, 2924–2927. doi:10.1021/am200624s

59. Ho, C.-C.; Liu, Y.-C.; Lin, S.-H.; Su, W.-F. *Macromolecules* **2012**, *45*, 813–820. doi:10.1021/ma202164d

60. Campo, B. J.; Bevk, D.; Kesters, J.; Gilot, J.; Bolink, H. J.; Zhao, J.; Bolsée, J.-C.; Oosterbaan, W. D.; Bertho, S.; D'Haen, J.; Manca, J.; Lutsen, L.; Van Assche, G.; Maes, W.; Janssen, R. A. J.; Vanderzande, D. *Org. Electron.* **2013**, *14*, 523–534. doi:10.1016/j.orgel.2012.11.021

61. Zhang, Y.; Tajima, K.; Hirota, K.; Hashimoto, K. *J. Am. Chem. Soc.* **2008**, *130*, 7812–7813. doi:10.1021/ja8023516

62. Noriega, R.; Rivnay, J.; Vandewal, K.; Koch, F. P. V.; Stingelin, N.; Smith, P.; Toney, M. F.; Salleo, A. *Nat. Mater.* **2013**, *12*, 1038–1044. doi:10.1038/nmat3722

63. Spano, F. C. *Acc. Chem. Res.* **2010**, *43*, 429–439. doi:10.1021/ar900233v

64. Wood, S.; Garnett, O.; Tokmoldin, N.; Tsoi, W. C.; Haque, S. A.; Kim, J.-S. *Faraday Discuss.* **2014**, 267–279. doi:10.1039/C4FD00141A

65. Tsoi, W. C.; James, D. T.; Kim, J. S.; Nicholson, P. G.; Murphy, C. E.; Bradley, D. D. C.; Nelson, J.; Kim, J.-S. *J. Am. Chem. Soc.* **2011**, *133*, 9834–9843. doi:10.1021/ja2013104

## License and Terms

This is an Open Access article under the terms of the Creative Commons Attribution License (<http://creativecommons.org/licenses/by/4.0>), which permits unrestricted use, distribution, and reproduction in any medium, provided the original work is properly cited.

The license is subject to the *Beilstein Journal of Organic Chemistry* terms and conditions: (<http://www.beilstein-journals.org/bjoc>)

The definitive version of this article is the electronic one which can be found at:  
[doi:10.3762/bjoc.12.205](https://doi.org/10.3762/bjoc.12.205)



# High performance p-type molecular electron donors for OPV applications via alkylthiophene catenation chromophore extension

Paul B. Geraghty<sup>1</sup>, Calvin Lee<sup>1</sup>, Jegadesan Subbiah<sup>1</sup>, Wallace W. H. Wong<sup>1</sup>, James L. Banal<sup>1</sup>, Mohammed A. Jameel<sup>2</sup>, Trevor A. Smith<sup>2</sup> and David J. Jones<sup>\*1</sup>

## Full Research Paper

Open Access

Address:

<sup>1</sup>School of Chemistry, Bio21 Institute, University of Melbourne, Parkville Vic 3010, Melbourne, Australia and <sup>2</sup>School of Chemistry, University of Melbourne, Parkville Vic 3010, Melbourne, Australia

Email:

David J. Jones<sup>\*</sup> - [djjones@unimelb.edu.au](mailto:djjones@unimelb.edu.au)

\* Corresponding author

Keywords:

molecular materials; nematic liquid crystal; organic solar cells; organic synthesis; p-type organic semiconductors; small molecule

*Beilstein J. Org. Chem.* **2016**, *12*, 2298–2314.

doi:10.3762/bjoc.12.223

Received: 30 May 2016

Accepted: 12 October 2016

Published: 02 November 2016

This article is part of the Thematic Series "Organic photovoltaics".

Associate Editor: P. J. Skabara

© 2016 Geraghty et al.; licensee Beilstein-Institut.

License and terms: see end of document.

## Abstract

The synthesis of key 4-alkyl-substituted 5-(trimethylsilyl)thiophene-2-boronic acid pinacol esters **3** allowed a simplified alkylthiophene catenation process to access bis-, ter-, quater-, and quinquethiophene  $\pi$ -bridges for the synthesis of acceptor- $\pi$ -bridge-donor- $\pi$ -bridge-acceptor (A- $\pi$ -D- $\pi$ -A) electron donor molecules. Based on the known benzodithiophene-terthiophene-rhodanine (**BTR**) material, the **BXR** series of materials, **BMR** (X = M, monothiophene), **BBR** (X = B, bithiophene), known **BTR** (X = T, terthiophene), **BQR** (X = Q, quaterthiophene), and **BPR** (X = P(penta), quinquethiophene) were synthesised to examine the influence of chromophore extension on the device performance and stability for OPV applications. The **BT<sup>x</sup>R** (x = 4, butyl, and x = 8, octyl) series of materials were synthesised by varying the oligothiophene  $\pi$ -bridge alkyl substituent to examine structure–property relationships in OPV device performance. The devices assembled using electron donors with an extended chromophore (**BQR** and **BPR**) are shown to be more thermally stable than the **BTR** containing devices, with un-optimized efficiencies up to 9.0% PCE. **BQR** has been incorporated as a secondary donor in ternary blend devices with **PTB7-Th** resulting in high-performance OPV devices with up to 10.7% PCE.

## Introduction

Bulk heterojunction (BHJ) organic solar cells (OSC), a blend of p-type and n-type conjugated polymers or molecular materials (MM), have attracted significant attention as alternative solar cell technologies as they are light-weight, low-cost and offer the

opportunity of cheaper manufacturing employing roll-to-roll printing processes [1–3]. Recent advances in materials synthesis and device architecture has pushed OSC power conversion efficiencies (PCEs) to 11.5% [4,5]. Further materials design and

device optimizations have been proposed to deliver OSCs with PCEs up to 15% [6,7]. Although the field has been dominated by polymeric conjugated organic semiconductors, there has been a rapid advance in the development of MMs with PCEs over 10% now reported [8,9]. The switch to MMs has in part been due to their discrete structure and relative ease of purification, which offers significant advantages, especially reduced batch-to-batch variation [10-12].

We recently used side-chain engineering, through regioregular placement of hexyl side chains on a thiophene  $\pi$ -bridge [13], to generate a MM with a planar core structure and enhanced device performance, up to 9.3% power conversion efficiency (PCE) [14]. This material, built from three key building blocks benzodithiophene-terthiophene-rhodanine (**BTR**), has been shown to have intriguing materials behaviour and excellent device performance when combined with [6,6]-phenyl C<sub>71</sub> butyric acid methyl ester (**PC<sub>71</sub>BM**). Maximum PCEs of 9.3% for OSCs containing **BTR** are achieved after solvent vapor annealing, for devices with an active layer up to 310 nm thick. In this case fill-factors (FF) remain above 70%. However, OSC devices containing **BTR** are not stable to thermal annealing, a requirement for scale up using common printing processes, where temperatures >80 °C are required for drying or annealing of printed layers [15]. **BTR** has extremely interesting properties worth further study and leads to three key questions;

1. Synthesis: Can we simplify the synthesis of **BTR** removing some chromatographic purification steps and use of toxic tin containing Stille condensation reactions?
2. Scale-up: Can we develop a multi-gram synthesis route to facilitate translation to printing programs?

3. Structure–property relationships: Can we modify the **BTR** chromophore length or alkyl side-chain length thereby improving device thermal stability and device performance?

We report here a simplified synthetic route to a series of **BTR** analogues (Figure 1), where we have varied the chromophore length through the **BXR** series, where X = mono thiophene (M), bithiophene (B), the known terthiophene (T), quaterthiophene (Q), and quinquetiophene (P), respectively and allowing isolation of products on the multigram scale. The simplified synthesis was translated to a second series of products where the oligothiophene sidechain length for the parent (**BTR**) was systematically varied, i.e. **BT<sup>x</sup>R**, where x = 4 (butyl), or 8 (octyl). Incorporation of the **BXR** series in devices with **PC<sub>71</sub>BM** has demonstrated that with increasing chromophore length, the thermal stability of the OSC devices increases giving a PCE of 8.9% for **BQR** after thermal annealing at 120 °C for 10 minutes. We also report an initial result of PCE of 10.7% for ternary blends of **BQR** with the commercially available **PTB7-Th** as the donor and **PC<sub>71</sub>BM** as the acceptor.

## Results and Discussion

**Synthesis:** Our modified synthesis of **BTR** and its analogues starts with the lithiation of 3-alkylthiophene **1a–c** by lithium diisopropylamide formed in situ from the reaction of *n*-butyllithium with diisopropylamine (DIA) in the presence of the alkylthiophene, followed by quenching with trimethylsilyl chloride to generate the previously unreported 4-alkyl-2-(trimethylsilyl)thiophenes **2a–c**, which could be purified by distillation to ensure removal of unreacted 3-alkylthiophene, Scheme 1. Deprotonation of **2** with *n*-butyllithium and reaction with 2-isopropoxy-4,4,5,5-tetramethyl-1,3,2-dioxaborolane

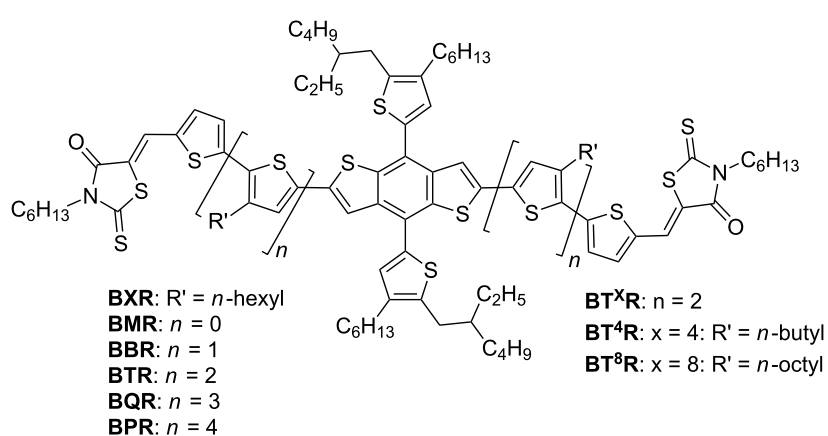
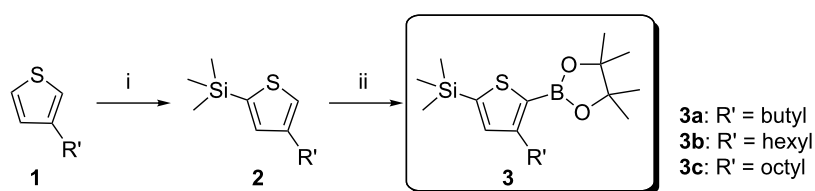


**Figure 1:** Chemical structures of molecular materials with the following variations; **BT<sup>x</sup>R**, alkyl side chains of the terthiophene bridging arm and **BXR**, oligothiophene bridging arm.

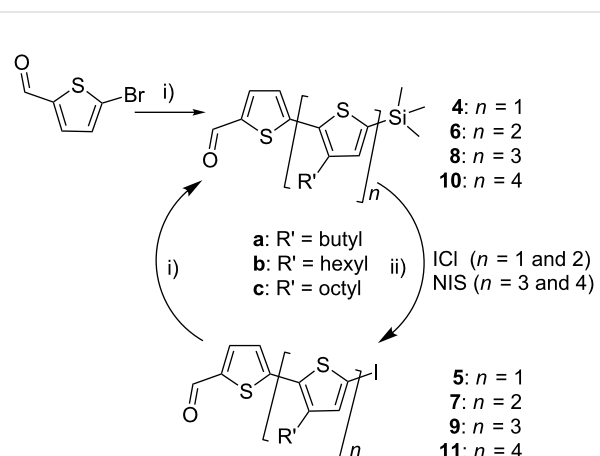


**Scheme 1:** Synthesis of the key intermediates TMS-T<sub>x</sub>-BPin (3), i) diisopropylamine (DIA), THF, *n*-BuLi,  $-78^{\circ}\text{C}$  TMS-Cl, ii) *n*-BuLi, iPrOBPin, THF,  $-78^{\circ}\text{C}$ .

(iPrOBPin) resulted in formation of the key intermediates **3a–c**, after distillation, in high yield of 60–70% (see refs [16–18] for recent similar chemistry). Intermediate **3b** has been scaled to the mole scale with no issues noted.

With **3a–c** in hand, synthesis of the required series of alkyl substituted oligothiophene  $\pi$ -bridges by simple Suzuki–Miyaura cross-coupling reactions could be completed. Starting with commercially available 5-bromothiophene-2-carboxaldehyde and then reaction with **3a–c** to generate the required bithiophenes, then terthiophenes, while further catenation with **3b** resulted in synthesis of the hexyl-substituted quater- and quinque thiophenes **8b** and **10b**, Scheme 2. Conversion of the intermediate TMS-protected oligothiophenes to the iodo-oligothiophenes ( $n=1$  and 2) was achieved using iodine monochloride (ICl), however for  $n=3$  and 4 a number of side reactions leading to unidentified side products significantly reduced the yield. For the quater- and quinque thiophenes *N*-iodosuccinimide (NIS) was used to give a clean product.

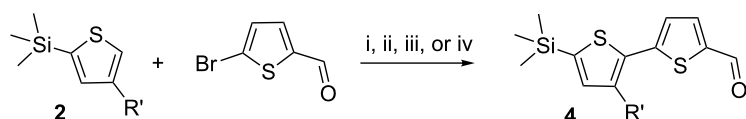
Ideally, the synthesis could be further simplified by direct palladium-catalyzed CH-activation, arylation of **2** followed by reaction with the commercially available 5-bromothiophene-2-carboxaldehyde to generate the bithiophene **4**, Scheme 3. It has previously been reported that direct coupling of 2-(trimethylsilyl)thiophene with aryl halides proceeds in good yield with protodesilylation being the major side reaction under the reaction conditions, even at short reaction times [19]. An initial reaction screening, investigating ligand, base and solvent variation, showed positive results with up to 32% yield of the required bithiophene **4**. We are currently examining catalyst opti-



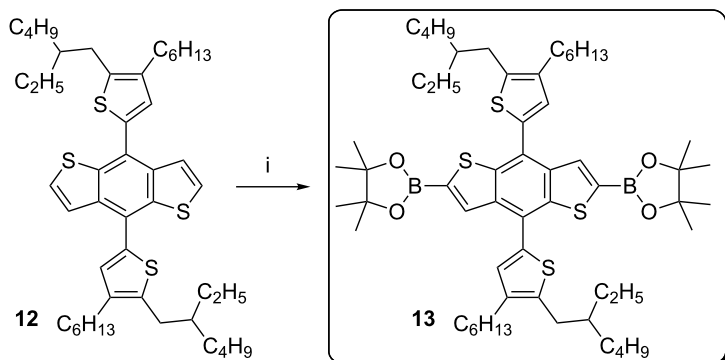
**Scheme 2:** Oligothiophenes **4–11** synthesised through reaction of the commercially available 5-bromo-2-thiophenecarboxaldehyde with **3a–c**, i) 3, cat.  $\text{Pd}_2\text{dba}_3\cdot 4[t\text{-Bu}_3\text{PH}] \text{BF}_4$ , THF,  $\text{K}_3\text{PO}_4$  (2 M),  $80^{\circ}\text{C}$ , 16 h, ii) ICl, DCM,  $0^{\circ}\text{C}$  or NIS, 50:50  $\text{CHCl}_3/\text{CH}_3\text{CO}_2\text{H}$ , rt, 2 h.

mization to improve the yields of this simplified route to the required oligothiophenes.

To avoid large scale use of tin reagents we required the key bis-borylated benzodithiophene (BDT) core **13**, which was synthesised from the known BDT core **12** using iridium catalyzed borylation via CH-activation. The bis-borylated product was isolated by precipitation on addition of isopropanol (IPA), and an analytically pure material isolated by filtration in excellent yields >90%, Scheme 4. This simplified purification is in direct contrast with reported procedures for the bis-iodinated or bis-stannylated analogues [20,21].



**Scheme 3:** Synthesis of the bithiophene through palladium catalyzed direct arylation, a) i)  $\text{Pd}(\text{OAc})_2$ ,  $\text{PCy}_3$ ,  $\text{PivOH}$ ,  $\text{K}_2\text{CO}_3$ , toluene  $100^{\circ}\text{C}$ , 4 h, 1%, ii)  $\text{Pd}(\text{OAc})_2$ ,  $\text{PPh}_3$ ,  $\text{K}_2\text{CO}_3$ , DMF  $120^{\circ}\text{C}$ , 6 h, 10%, iii)  $\text{Pd}(\text{OAc})_2$ , dppp,  $\text{KOAc}$ , DMAc  $120^{\circ}\text{C}$ , 5 h, 32%, iv)  $\text{Pd}(\text{OAc})_2$ , dppb,  $\text{KOAc}$ , DMAc  $120^{\circ}\text{C}$ , 5 h, 32%.



**Scheme 4:** Synthesis of the key bis-borylated BDT core **13**, i) 1.5 equiv  $\text{B}_2\text{Pin}_2$ , 0.025 equiv  $[\text{Ir}(\text{COD})\text{OMe}]_2$ , 0.05 equiv  $t\text{-Bu}_2\text{bipy}$ , DME,  $80\text{ }^\circ\text{C}$ , 2 h.

A simple Suzuki–Miyaura cross coupling of **5**, **7**, **9** or **11** with **13** gave the required  $\text{BX}^x$ -dialdehydes **14**, Scheme 5, which were purified by a combination of silica chromatography and size exclusion chromatography (SEC). A final Knoevenagel condensation coupling the  $\text{BX}^x$ -dialdehydes with *N*-hexylrhodanine resulted in the required series of products, both **BXR** and **BT<sup>x</sup>R**. The new materials have been fully characterized by NMR, IR, UV–vis, TGA, DSC, electrochemistry, photoelectron spectroscopy in air (PESA), and have satisfactory mass spectra and microanalysis results. Full experimental details are described in Supporting Information File 1.

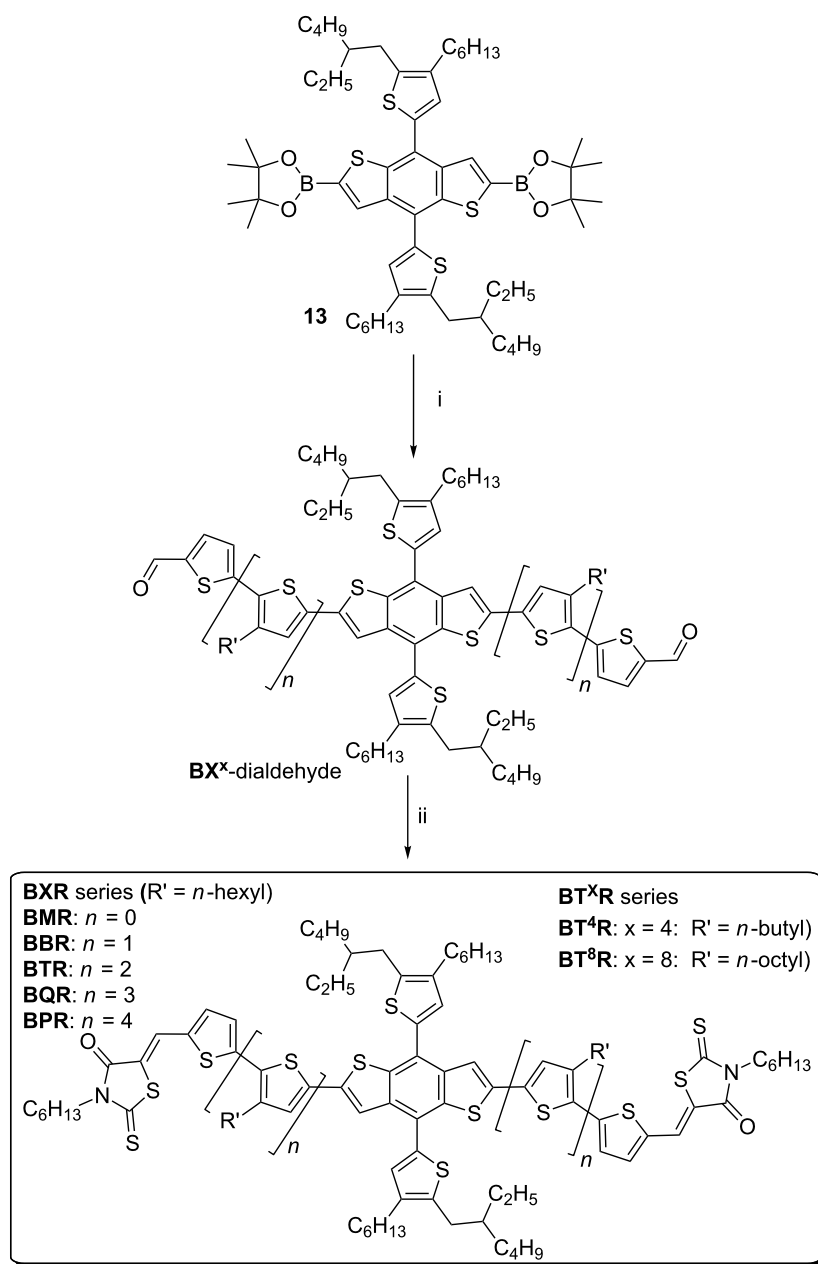
**Thermal behaviour: TGA and DSC.** The thermal behaviour of the **BXR** and **BT<sup>x</sup>R** series has been studied by TGA and DSC. All of the materials show good thermal stability with <5% weight loss below  $390\text{ }^\circ\text{C}$ , see Supporting Information File 1, Figure S5.1. The phase behaviour was examined by DSC (see Supporting Information File 1, Figure S6.1 for full details) with a single melt temperature recorded for **BMR**, **BBR** and **BPR** at  $179\text{ }^\circ\text{C}$ ,  $215\text{ }^\circ\text{C}$  and  $196\text{ }^\circ\text{C}$ , respectively. Subsequent crystallization was observed at  $154\text{ }^\circ\text{C}$ ,  $175\text{ }^\circ\text{C}$  and  $174\text{ }^\circ\text{C}$  for **BMR**, **BBR** and **BPR**, respectively. The phase behaviour for **BTR** has been previously reported and shows three phase transitions on heating and cooling with the formation of a high-temperature nematic liquid crystalline (NLC) phase change at  $186\text{ }^\circ\text{C}$ , with a change to the isotropic phase at  $196\text{ }^\circ\text{C}$  [14]. **BQR** can then be compared to **BTR** where, surprisingly, a single phase change is seen on heating, while three phase changes are observed on cooling, Figure 2a. Even on slowing the heating rate to  $0.1\text{ }^\circ\text{C}$  per minute no change in the single phase change on heating was observed. The three phase changes at  $190\text{ }^\circ\text{C}$ ,  $180\text{ }^\circ\text{C}$ , and  $164\text{ }^\circ\text{C}$  on cooling appear to be analogous to that seen in **BTR**.

Modification of the **BTR** oligothiophene alkyl chain lengths in the **BT<sup>x</sup>R** series results in an intuitive change in the temperatures of the relevant phase transitions, with an inverse corre-

lation observed between alkyl chain length and the specific phase change temperatures. Interestingly, as with **BQR** the DSC traces of the **BT<sup>x</sup>R** analogues reveal markedly different phase behaviour relative to that of **BTR**. **BT<sup>4</sup>R** has a single endothermic ( $206\text{ }^\circ\text{C}$ ) and a single exothermic peak ( $199\text{ }^\circ\text{C}$ ) that are higher than the phase transitions in **BTR**. Two exothermic peaks at  $148\text{ }^\circ\text{C}$  and  $182\text{ }^\circ\text{C}$  are observed in **BT<sup>8</sup>R**, and two endothermic peaks are recorded at  $100\text{ }^\circ\text{C}$  and  $166\text{ }^\circ\text{C}$ . As can be observed, even these small changes in alkyl chain length result in a significant impact on the phase change behaviour. However, unfortunately no correlation can be made at this stage between subsequent thermal stability of OPV devices and the phase transition of the **BXR** and **BT<sup>x</sup>R** materials.

**Polarized optical microscopy (POM).** POM was utilized in conjunction with a heating platform to directly observe these phase transitions and elucidate thin film structure. On heating at  $10\text{ }^\circ\text{C}\cdot\text{min}^{-1}$  **BQR** shows a single phase transition to the isotropic melt at  $202\text{ }^\circ\text{C}$ , while on cooling we have identified an initial transition to a high-temperature NLC phase at  $190\text{ }^\circ\text{C}$ , and then a crystallisation at  $180\text{ }^\circ\text{C}$ . On further cooling a thermochromic phase change is observed at  $164\text{ }^\circ\text{C}$ , see Figure 2 (and UV–vis discussion below). Even with the much slower cooling rates used for POM studies we did not observe more than the single phase change on heating the **BQR** sample. We have repeated POM studies on the new batches of **BTR** and they are identical to those reported; see Supporting Information File 1, Figure S8.2 [14].

Upon examination of **BT<sup>4</sup>R** with POM a single phase change on heating was observed, with a highly crystalline state below  $205\text{ }^\circ\text{C}$  giving way to an isotropic melt at  $206\text{ }^\circ\text{C}$ . Surprisingly, when the sample was cooled a characteristic NLC was observed at  $199\text{ }^\circ\text{C}$ , with a change to its crystalline state at  $193\text{ }^\circ\text{C}$ , Figure 3. This NLC transition was not observed in the DSC, even with a slowed cooling rate.



**Scheme 5:** Synthesis of the **BXR** and **BT<sup>x</sup>R** series of materials, i) 5-bromothiophene carboxaldehyde, **5b**, **7a–c**, **9b**, or **11b**, cat.  $\text{Pd}_2\text{dba}_3\cdot 4t\text{-Bu}_3\text{P}[\text{HBF}_4]$ , THF,  $\text{K}_3\text{PO}_4$  (2M),  $80\text{ }^\circ\text{C}$ , 16 h, and ii) *N*-hexylrhodanine (10 equiv),  $\text{CHCl}_3$ , cat DBU.

The thermal transitions in **BT<sup>8</sup>R** are not as defined as in the other cases with two broad endothermic ( $148\text{ }^\circ\text{C}$  and  $182\text{ }^\circ\text{C}$ ) and exothermic transitions ( $166\text{ }^\circ\text{C}$  and  $100\text{ }^\circ\text{C}$ ) (Supporting Information File 1, Figure S8.5). No high temperature NLC phase was observed when examined under POM.

The dramatic changes in the thermal behaviour and phase change properties for the **BXR** series materials are induced by either changes to the chromophore length, or by altering the side chain length on the oligothiophene. These changes have a

dramatic impact on the presence or absence of a NLC phase in these materials. All, however, show the appearance of long needle like crystal forms in the POM images obtained.

**UV-vis and fluorescence spectroscopy.** Solution and thin film UV-vis absorption profiles of the **BXR** are shown in Figure 4 and Figure 5, respectively, with selected data collected in Table 1 (all spectra can be found in the Supporting Information File 1). The members of the series all exhibit absorption maxima between  $450\text{--}600\text{ nm}$  in chloroform. In solution it is

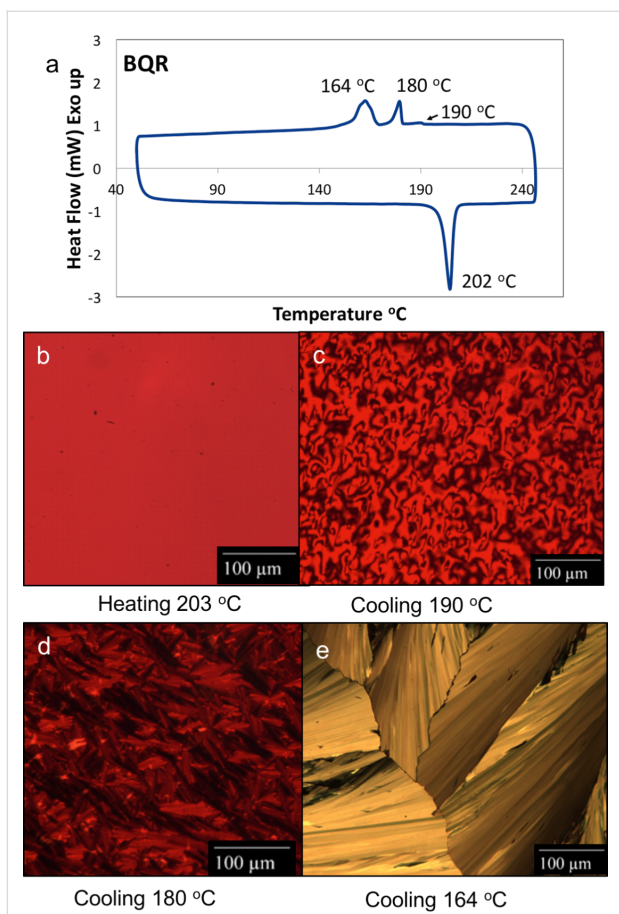


**Figure 2:** BQR thermal and POM properties. a) DSC thermogram of **BQR** under nitrogen at a ramp rate of  $10\text{ }^{\circ}\text{C min}^{-1}$ . b) **BQR** thin film sandwiched between two glass slides observed under a polarized optical microscope (POM) at  $203\text{ }^{\circ}\text{C}$  after heating. c) POM image of the same film when the stage temperature is lowered to  $190\text{ }^{\circ}\text{C}$  with distinct Schlieren texture for a NLC, d) POM image when the stage temperature is lowered to  $180\text{ }^{\circ}\text{C}$ , and e) POM image when the stage temperature is lowered to  $164\text{ }^{\circ}\text{C}$  where a distinct transmitted colour change is observed.

evident that, although all the materials have a similar onset of absorption at around  $600\text{ nm}$ , the peak maxima progress in the reverse order to that expected with **BPR** having a maximum absorption at  $490\text{ nm}$ , while **BMR** has a maximum absorbance at  $541\text{ nm}$ , Table 1. While the **BPR** and **BQR** spectra show broad featureless peaks, the spectra for **BMR** (and **BBR**) show more complicated structure indicating possible association in solution with the development of strong aggregates.

The UV-vis spectra for thin films of the **BX<sup>x</sup>R** series, cast from chloroform and subject to both solvent vapour annealing (SVA, THF 20 s) or thermal annealing (TA,  $120\text{ }^{\circ}\text{C}$  10 min,  $\text{N}_2$ ), are shown in Figure 5. On increasing the conjugation length from **BMR** to **BPR** the expected red-shift in the absorption peaks is now evident (Figure 5a). However,  $\lambda_{\text{max}}$  is dependent on the degree of formation of  $\pi$ - $\pi$  stacking and development of the

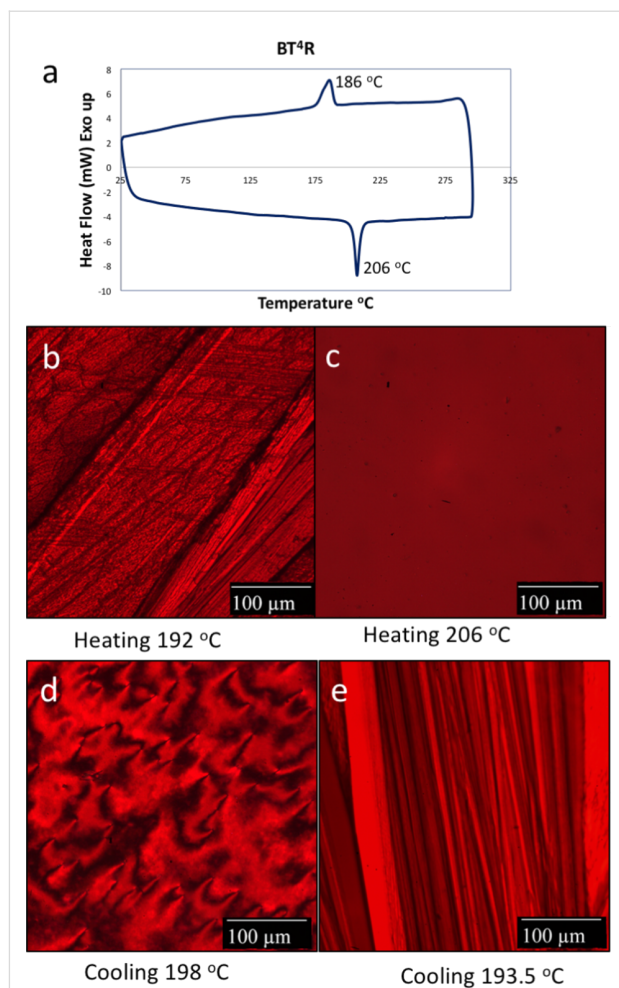


**Figure 3:** **BT<sup>4</sup>R** thermal and POM images. a) DSC thermogram of **BT<sup>4</sup>R** under nitrogen at a ramp rate of  $10\text{ }^{\circ}\text{C min}^{-1}$ . b) **BT<sup>4</sup>R** thin film sandwiched between two glass slides observed under a POM at  $192\text{ }^{\circ}\text{C}$  on heating. c) POM image of the same film when the stage temperature is at  $206\text{ }^{\circ}\text{C}$ , d) POM image when the stage temperature is lowered to  $198\text{ }^{\circ}\text{C}$  with distinct Schlieren texture for a NLC, and e) POM image when the stage temperature is lowered to  $193.5\text{ }^{\circ}\text{C}$ .

lowest energy transition with two clear sharp peaks at  $552\text{ nm}$  and  $590\text{ nm}$  ( $\lambda_{\text{max}}$ ) for **BMR**, while for **BPR**  $\lambda_{\text{max}}$  is at  $594\text{ nm}$  with a shoulder at around  $630\text{ nm}$  indicating poor formation of the aggregates (Figure 5d). Side-chain modification from butyl to octyl in the **BT<sup>4</sup>R**, **BTR** and **BT<sup>8</sup>R** series also impacts on the thin film formation as seen in as-cast films with poor development of the crystalline order in **BT<sup>4</sup>R** and **BT<sup>8</sup>R**, as well as a  $\lambda_{\text{max}}$  blue-shift of both **BT<sup>X</sup>R** analogues, when compared to **BTR**, Figure 5a and d.

Crystalline order develops for all films after SVA or TA, (Figure 5b and c). While after annealing  $\lambda_{\text{max}}$  corresponds to the lowest energy band for most of the thin films, or the two peaks are close in intensity, **BPR** is the exception where the long wavelength absorption is a shoulder that is not well resolved

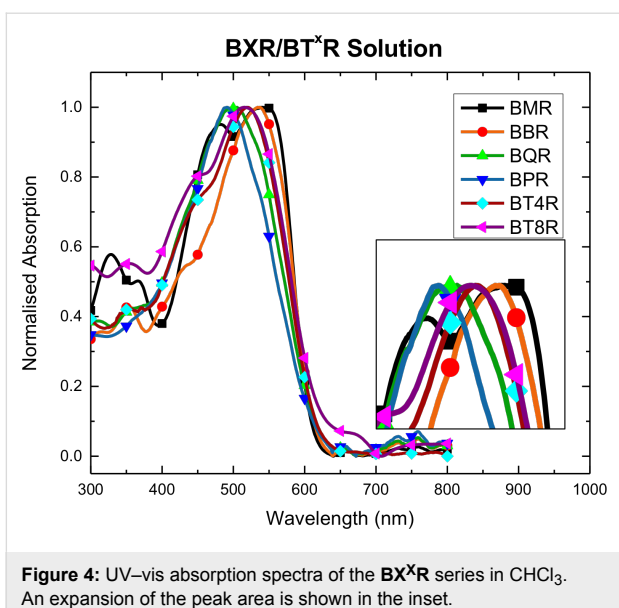
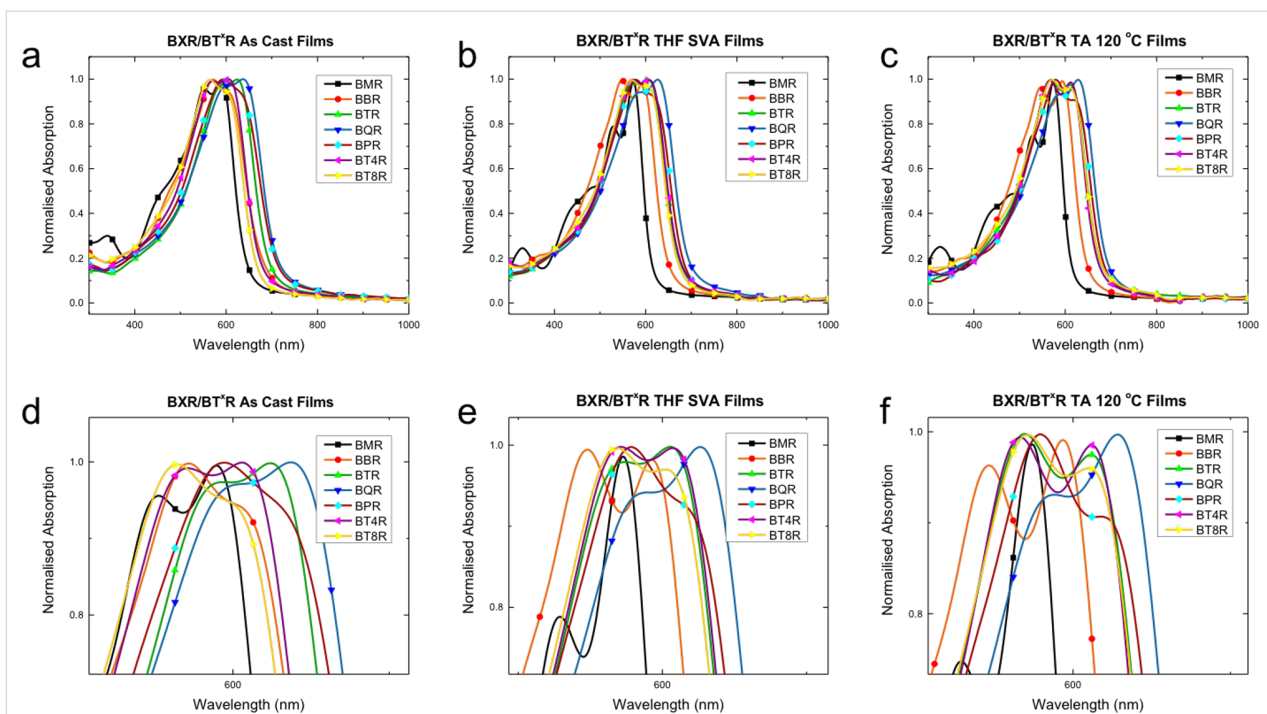


**Figure 4:** UV-vis absorption spectra of the **BX<sup>x</sup>R** series in  $\text{CHCl}_3$ . An expansion of the peak area is shown in the inset.

and  $\lambda_{\text{max}}$  corresponds to the higher energy band. In both cases **BQR** shows well-ordered films with the largest red shift and a  $\lambda_{\text{max}}$  at 625–630 nm. After annealing the absorption profiles of **BT<sup>4</sup>R**, **BTR** and **BT<sup>8</sup>R** are almost identical with only a small change in the intensity of the peak at around 570 nm, therefore indicating that the underlying packing structures are not significantly altered through side-chain substitution.

To better understand the annealing process UV-vis spectra have been replotted for each material, see Figure 6 (and Supporting Information File 1, Figures S9.1 and 2). As each material is annealed a small blue shift, 10–20 nm, is seen in most spectra with a concomitant increase in the prominence of the low energy peak. The shift is smallest in **BPR** (Figure 6c), and no significant change is seen for **BT<sup>4</sup>R** (Supporting Information File 1, Figure S9.2f). It is evident that subtle changes in molecular orientation and packing, with a tendency to H-aggregate formation, are present, however, further work is being undertaken to better understand the underlying processes leading to these changes.

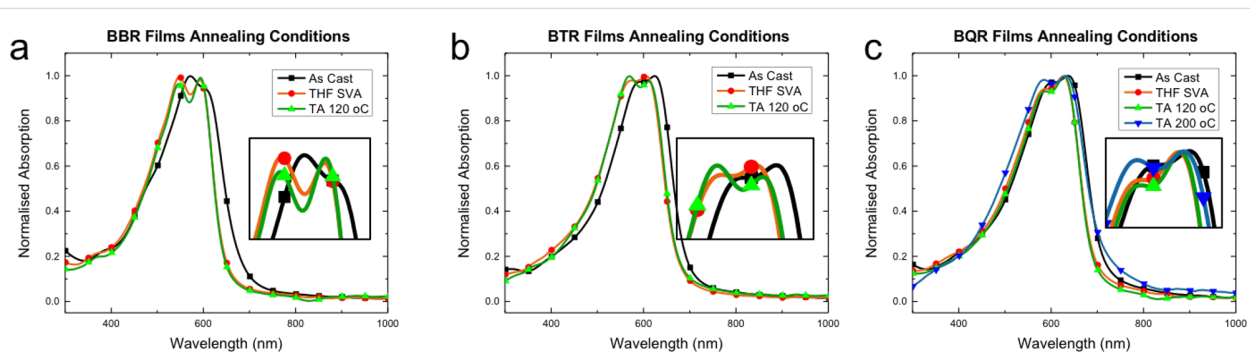
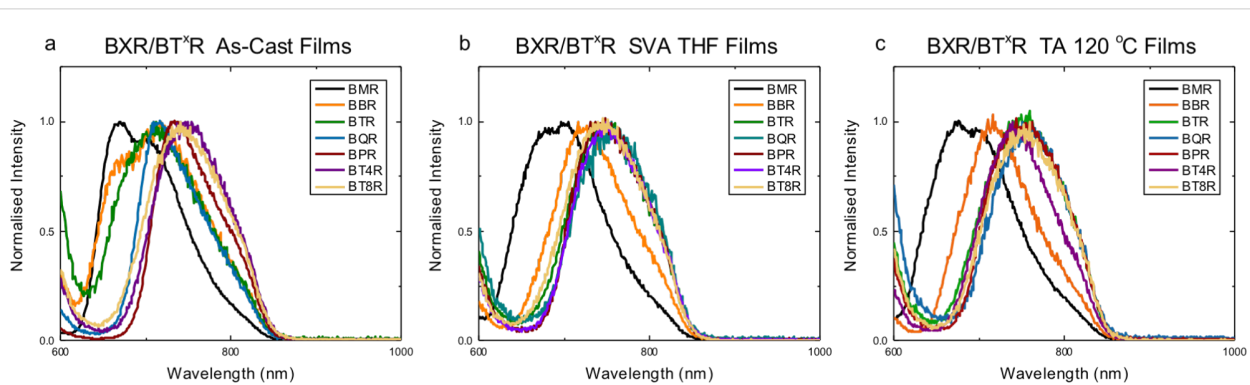
Fluorescence emission spectra were collected using the same films as those used to collect the UV-vis spectra above, with selected graphs shown in Figure 7, and extracted data in Table 2. The full spectra are presented in Supporting Information File 1, Figure S9.3. The as-cast films do not contain simple symmetric emission bands, indicating a significant level of structural complexity in the as-cast thin films. **BMR** shows two emission peaks at 670 nm and 704 nm with a long tail at around 800 nm. A number of absorption peaks are evident for **BMR**, Figure 5a and d, and these may represent the multiple environments for emission. **BBR**, **BTR** and **BQR** show surprisingly asymmetric peaks with long linear tails from a peak maximum located at around 715 nm. Following SVA a broad, more sym-



**Figure 5:** Normalised thin film UV-vis absorption profiles for the **BX<sup>x</sup>R** series for, a) as-cast films (from  $\text{CDCl}_3$ ), b) after solvent vapor annealing (SVA) with THF for 10 seconds, and c) thermally annealed (TA) at 120 °C for 10 minutes. Expansions of the peak areas in a), b), and c) are shown in d), e), and f).

**Table 1:** Extracted UV–vis absorption peak positions for the **BX<sup>x</sup>R** series. ( $\lambda_{\text{max}}$  in bold).

Solution		$\epsilon$	As cast		SVA		TA 120 °C	TA 200 °C	TA 220 °C
	$\lambda$ (nm)	(M <sup>-1</sup> cm <sup>-1</sup> )	$\lambda$ (nm)		$\lambda$ (nm)		$\lambda$ (nm)	$\lambda$ (nm)	$\lambda$ (nm)
<b>BMR</b>	480	<b>541</b>	95,500	552	<b>590</b>	528	<b>572</b>	529	<b>574</b>
<b>BBR</b>		<b>535</b>	62,500	<b>571</b>	602	<b>548</b>	593	545	<b>594</b>
<b>BTR</b>		<b>523</b>	110,000 <sup>a</sup>	<b>592</b>	624	573	<b>605</b>	<b>569</b>	610
<b>BQR</b>		<b>500</b>	92,500	600	<b>634</b>	587	<b>626</b>	588	<b>628</b>
<b>BPR</b>		<b>490</b>	104,000	<b>594</b>	630	<b>578</b>	612	<b>579</b>	618
<b>BT<sup>4</sup>R</b>		<b>520</b>	88,500	571	<b>605</b>	<b>570</b>	607	<b>566</b>	612
<b>BT<sup>8</sup>R</b>		<b>516</b>	69,100	<b>564</b>	595	<b>568</b>	602	<b>570</b>	610

<sup>a</sup>Taken from ref. [14].**Figure 6:** Normalised thin film UV–vis absorption profiles for a) **BBR**, b) **BTR** and c) **BQR** showing as-cast (black, square), SVA with THF for 10 s (orange, circle) and thermally annealed (TA) at 120 °C for 10 minutes (green, triangle). Insets show expansion of the main peak area.**Figure 7:** Normalised thin film fluorescence emission profiles for **BX<sup>x</sup>R** series after excitation at 580 nm, a) as-cast films (from CDCl<sub>3</sub>), b) after solvent vapor annealing (SVA with THF for 10 seconds), and c) thermally annealed (TA) at 120 °C for 10 minutes.

metric emission band is seen for all materials, except **BMR** and **BBR**, located at around 750 nm with a broad shoulder indicating a secondary emission located at around 810–825 nm. For TA films, there is little change in the emission from that seen for SVA films indicating that under these conditions a similar underlying structure is formed after solvent vapour or thermal annealing.

**Variable temperature UV–vis and fluorescence measurements.** POM measurements of **BQR** indicated a change in the transmitted spectrum during the phase change recorded at 164 °C, Figure 2, suggestive of significant structural rearrangements occurring during crystallization. The POM/heating stage apparatus was coupled to a fibre-optic based spectrometer to enable collection of variable temperature UV–vis and fluores-

**Table 2:** Extracted fluorescence emission peak positions for the **BX<sup>x</sup>R** materials ( $\lambda_{\text{excit}}$  580 nm).

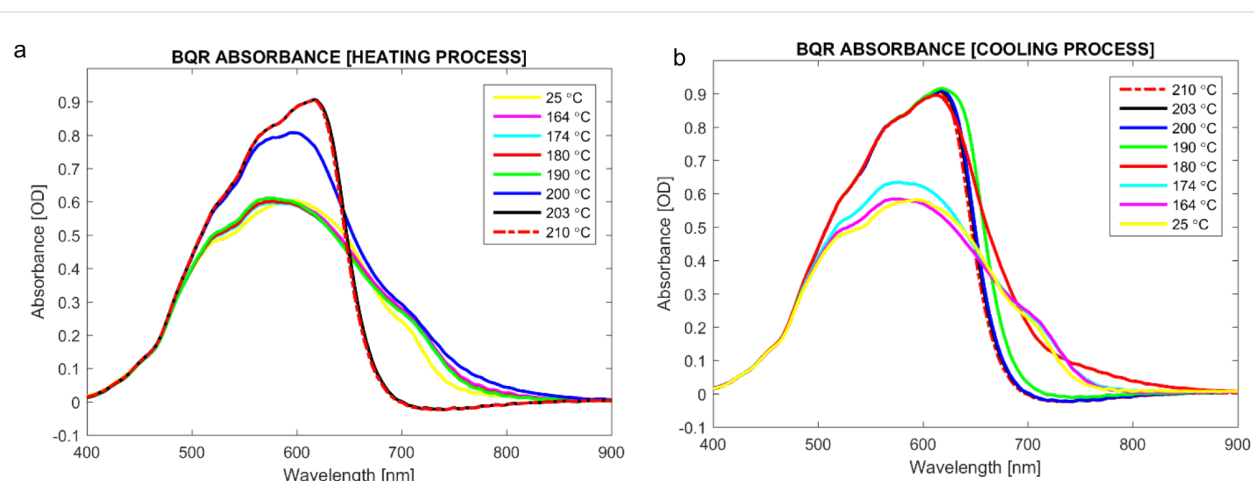
	As cast		SVA	TA 120 °C	TA 200 °C	TA 220 °C (fast cool)	TA 220 °C (slow cool)
		$\lambda$ (nm)		$\lambda$ (nm)		$\lambda$ (nm)	$\lambda$ (nm)
<b>BMR</b>	669	697	705	677			
<b>BBR</b>	678	718	716	719			
<b>BTR</b>		712	752	735			
<b>BQR</b>		716	756	763	760	730	709
<b>BPR</b>		732	736	762			
<b>BT<sup>4</sup>R</b>		746	749	739			
<b>BT<sup>8</sup>R</b>		741	740	759			

cence spectral data from **BTR** and **BQR**. The absorption spectra recorded for **BQR** are shown in Figure 8, while the those for **BTR** are included in the supplementary material (Figure S8.1). The absorption spectrum of **BQR** collected on the POM heated stage shows an extra shoulder located at around 730 nm that was not present in the as-cast films of **BQR** or the thermally annealed films (measured at room temperature). The **BQR** thin films were annealed up to 220 °C to probe the effect on the UV–vis spectrum (spectrum collected at room temperature after cooling) of cycling the **BQR** thin film up to the NLC phase change temperatures (Figure 10) but there is no appearance of the new shoulder, however as the films are rapidly cooled there may be a kinetic effect (see below).

Variable temperature fluorescence emission spectra were recorded on **BTR** and **BQR** (Figure 9) using a similar setup as for the UV–vis measurements (Figure 8), but employing the Hg fluorescence excitation lamp of the microscope. However, the

lamp used introduced a significant thermal load on the sample (approx. 18 °C) and therefore the apparent phase change temperatures are offset relative to the absorption data for this experiment. The data for **BQR** are shown below, while the data for **BTR** are included in Supporting Information File 1. At room temperature (after cycling once) **BQR** has two emission peaks at around 750 nm and 690 nm. On heating the low energy peak reduces in intensity with a concomitant increase in the peak at 690 nm and a blue shift to 655 nm at the sample melting point to the isotropic phase (Figure 9a). A similar shift is observed on cooling the sample, Figure 9b. The emission peaks appear to reflect the two absorption peaks observed in the variable temperature UV–vis absorption spectra, however the underlying structural changes remain unclear and are the subject of further structural studies on **BTR** and **BQR** thin films.

The appearance of the second fluorescence emission peak in variable temperature spectra on the POM stage, again not seen

**Figure 8:** Variable temperature thin film UV–vis absorption profiles for **BQR**, collected using the transmission lamp of the POM and fibre-optic spectrometer.

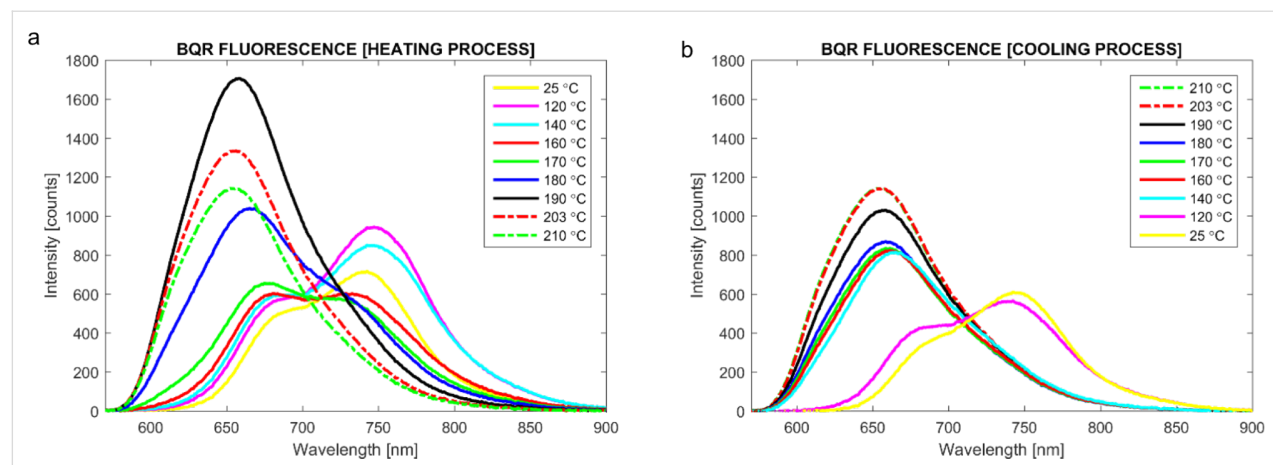


**Figure 9:** Variable temperature thin-film fluorescence emission profiles for **BQR**, a) heating and b) cooling, collected using the same apparatus as Figure 8 but with an Hg lamp as the excitation source.

on the thin films (Figure 7c), has been examined in more detail. The thin films used to obtain the UV–vis spectra, were heated to above the NLC phase change temperature, and collected fluorescence emission spectra are shown in Figure 10. It is clear that when the thin films are heated to 220 °C, i.e., above the NLC phase change temperature, a second blue shifted peak appears at 730 nm, however this is not at the same position recorded on films heated on the POM stage (690 nm). The thin films for these tests were heated to the annealing temperature and after the set time the microscope slide was removed, causing rapid cooling (220 °C fast in Figure 10). It is possible that the rate of heating/cooling impacts on the crystallization of the thin films, with the slower rates used for the fully enclosed, temperature ramped POM stage, leading to equilibrium phases, while rapid thermal quenching of isolated thin films on glass slides gives different results. To further probe this effect, the cooling rate for the thin film heated to 220 °C was modified by turning off the hotplate and allowing the thin film to cool slowly (220 °C slow in Figure 10). When the film is left to cool at a slow rate (220 °C to room temperature over 45 min) the emission spectrum is an almost perfect replica as for the as-cast film emission. Detailed variable temperature X-ray analysis of **BQR** thin films is currently underway to better understand these changes.

**CV and PESA:** The electrochemical properties of the **BXR** series of materials have been examined by cyclic voltammetry (CV), photoelectron spectroscopy in air (PESA), and UV–vis to determine approximate energy HOMO–LUMO energy levels, and the data are summarized in Table 3. From the UV–vis absorption onsets, determined from the as-cast thin films, we determined the  $E_{g(\text{opt})}$  levels, which demonstrate a clear trend in the reduction of  $E_{g(\text{opt})}$  on increasing the conjugation length in the **BXR** series dropping from 1.92 eV to 1.74 eV. Pseudo reversible oxidation potentials in the CVs have been recorded on

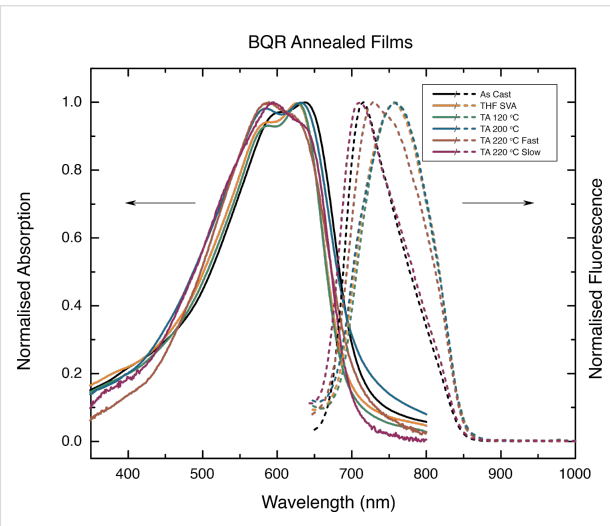


**Figure 10:** **BQR** thin film UV–vis (solid lines) and fluorescence emission spectra (dashed lines) collected at rt, after SVA and thermal annealing at 120 °C, 200 °C, and 220 °C (above the NLC phase change temperature). Films heated to 220 °C were either removed from the hotplate and cooled (fast) or left on the hotplate to cool (slow).

thin films for each of the materials and the data are listed in Table 3, (see Figure S7.1 Supporting Information File 1 for the cyclic voltammograms). The CV data show the expected gradual increase in HOMO levels as we increase the conjugation length and the expected general downward trend in energy gap from 2.40 eV to 1.77 eV for the **BXR** series. The first reduction potential could also be measured allowing an estimation of the LUMO levels for the **BXR** series and therefore an electrochemical energy gap ( $E_{g(\text{CV})}$ ), and these match well to the  $E_{g(\text{opt})}$  values reported above and listed in Table 3.

Ionisation potentials have also been measured by photoelectron spectroscopy in air (PESA), and give a direct measure of the

**Table 3:** Extracted UV–vis absorption peak position for **BX<sup>x</sup>R**.

<b>BX<sup>x</sup>R</b>	$E_{g(opt)}$ (eV)	UV-vis		Cyclic voltammetry		PESA	DFT Calculations		
		HOMO (eV)	LUMO (eV)	$E_{g(CV)}$ (eV)	HOMO (eV)		HOMO (eV)	LUMO (eV)	$E_{g(Theory)}$ (eV)
<b>BMR</b>	1.92	−5.79	−3.39	2.40	−5.51	−5.67	−3.14	2.53	
<b>BBR</b>	1.83	−5.55	−3.45	2.10	−5.39	−5.50	−3.01	2.49	
<b>BTR</b>	1.80	−5.43	−3.46	1.97	−5.20	−5.36	−2.93	2.43	
<b>BQR</b>	1.74	−5.33	−3.53	1.80	−5.09	−5.26	−2.88	2.38	
<b>BPR</b>	1.73	−5.29	−3.52	1.77	−5.02	−5.19	−2.85	2.34	
<b>BT<sup>4</sup>R</b>	1.73	−5.44	−3.46	1.98	−5.21	−	−	−	
<b>BT<sup>8</sup>R</b>	1.72	−5.49	−3.48	2.01	−5.14	−	−	−	

HOMO level which rises from −5.51 eV for **BMR** through to −5.02 eV for **BPR** (see Figures S10.1–S10.5). There is a good correlation between the HOMO energy levels measured by CV and PESA.

**DFT calculations.** To further understand the impact on varying the conjugation length of the oligothiophene bridging arm on the distribution of the HOMO/LUMO energy levels and overlap, density functional theory (DFT) calculations were performed. Geometry optimization and molecular orbital surfaces were determined and are shown in Figure 11. Geometries of the **BX<sup>x</sup>R** series were obtained at the D2 dispersion corrected B3LYP/6-311G(d,p) level of theory. Subsequent time-dependent DFT (TD-DFT) calculations were carried out on the optimized structures with PBE0/def2-TZVP level of theory based on our benchmark calculations (Supporting Information File 1, chapter S11). It is apparent in Figure 11 that as the **BX<sup>x</sup>R** molecular materials increase in size the overlap of the HOMO and LUMO decreases. The HOMO of the **BX<sup>x</sup>R** series extends as the number of the thiophene rings increases. In contrast, the LUMO becomes more localized towards the *N*-hexylrhodamine acceptor moiety as the conjugation length increases. The calculated HOMO values and HOMO–LUMO energy difference follows the same trend as the observed values determined by CV and PESA.

**Photovoltaic performances.** The **BX<sup>x</sup>R** series of materials were incorporated into bulk heterojunction devices with a conventional architecture, i.e. ITO/PEDOT:PSS/active layer/Ca/Al (Figure 12a). The active layer composition was held at 1:1 **BX<sup>x</sup>R:PC<sub>71</sub>BM** (by weight) and deposited from CHCl<sub>3</sub>. The active layer was ≈250 nm thick and Ca/Al was used as the back cathode.

We report here preliminary BHJ device data to indicate the impact of small structural variations on the device performance. Further device optimization is currently being completed and

will be reported at a later date. Devices assembled with as-cast films (Table 4, entries 1–5 and *J*–*V* curves Figure 12b) show acceptable device performance without annealing, with **BQR** delivering the best device performance at 5.3%. All devices show high open circuit voltages (*V*<sub>oc</sub>) above 0.90 V, but low fill factors (FF) <45%.

Using previously optimized SVA conditions for **BTR**, THF for 10 seconds, devices based on the **BX<sup>x</sup>R** series were fabricated and device data collected, see Table 4 (entries 6–10) and *J*–*V* curves in Figure 12c. The *V*<sub>oc</sub> decreases from 1.04 V for **BMR** to 0.82 V for **BPR** as the conjugation length increases. The *V*<sub>oc</sub> drop reflects the measured increase in the HOMO level across the series from −5.51 eV for **BMR** to −5.02 for **BPR**. The measured device data for **BTR** with *J*<sub>sc</sub> = 13.9 mA cm<sup>−2</sup>, *V*<sub>oc</sub> = 0.92 V, FF of 72% and PCE of 9.3% are almost identical to those previously reported at *J*<sub>sc</sub> = 13.9 mA cm<sup>−2</sup>, *V*<sub>oc</sub> = 0.90 V, FF 74.1% and PCE of 9.3% [14], showing the batch to batch reproducibility in device data for molecular materials.

Except for **BMR**, the FFs for SVA devices lie above 70%, indicating excellent morphology development. The best device contains **BQR** with a PCE of 9.4% and a *J*<sub>sc</sub> = 15.3 mA cm<sup>−2</sup>. **BPR** shows promise with a high FF (74%), however a lower *V*<sub>oc</sub> (0.82 V) and a reduced *J*<sub>sc</sub> (14.3 mA cm<sup>−2</sup>) reduce the PCE to 8.7%. UV–vis data indicate that under these SVA conditions the π–π stacking is not fully developed indicating that optimizing SVA conditions may lead to improved light harvesting.

It is important for commercialization of printed BHJ devices that any active layer can withstand the requirements of a printing process, which normally requires a drying or curing step for printed electrodes of >80 °C. To evaluate our new materials for possible translation to a printing process devices incorporating the **BX<sup>x</sup>R** series of donors were assembled and the active layer thermally annealed at 120 °C for 10 minutes before

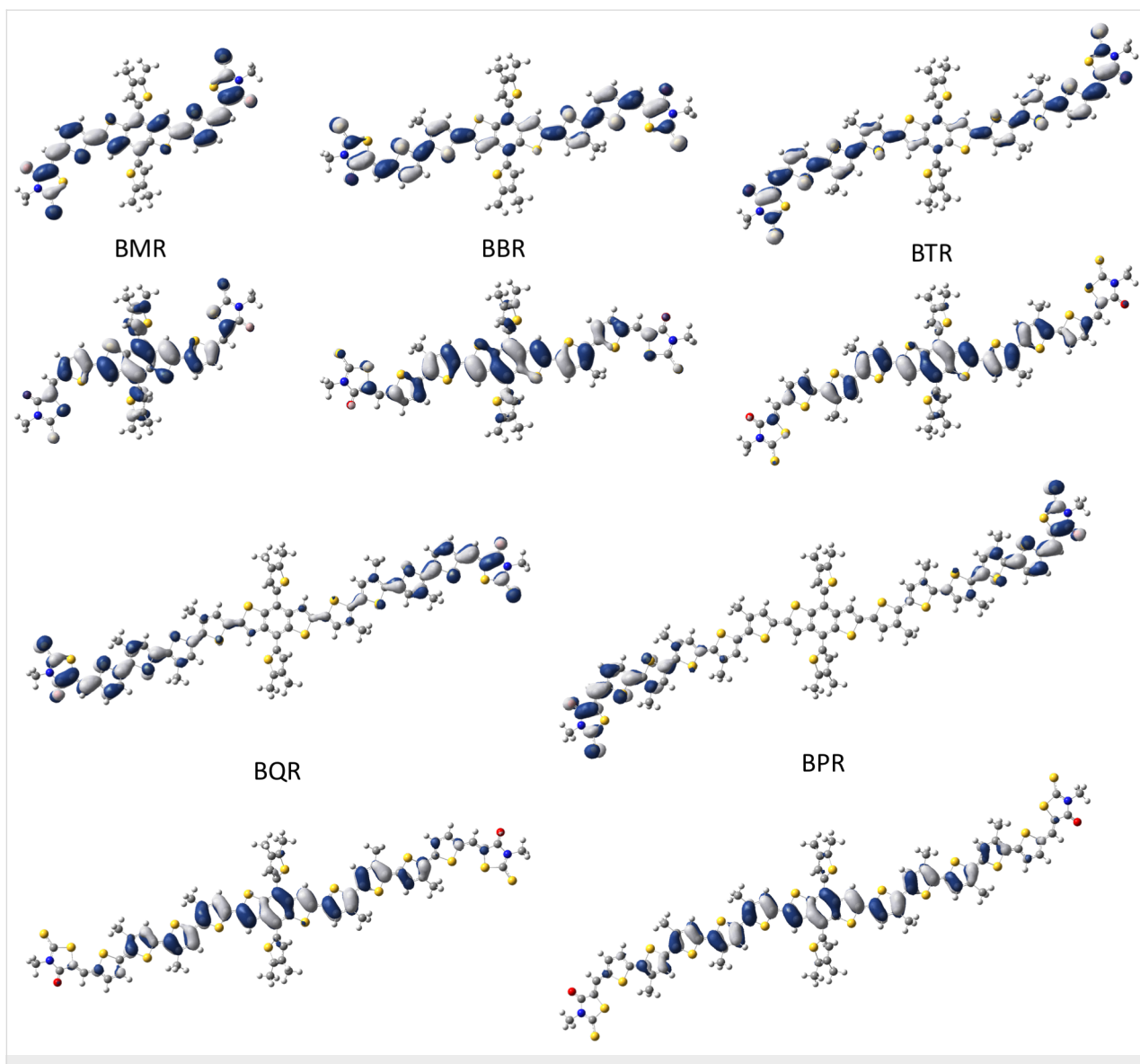


**Figure 11:** Optimized geometry and molecular orbital surfaces of HOMO (bottom) and LUMO (top) for the **BXR** series. Calculated at the B3LYP-D2/6-311G(d,p)//PBE0/def2-TZVP level. Alkyl chains have been substituted by methyl groups.

electrode deposition, data collected from the devices are listed in Table 4 (entries 11–15) and  $J$ – $V$  curves are shown in Figure 12d. The thermally annealed devices do not show as

clear a trend as seen for SVA annealed devices with, e.g., no clear systematic decrease in the  $V_{oc}$ s on going from **BMR** through to **BPR**. Also, apart from **BPR**, device FFs remain

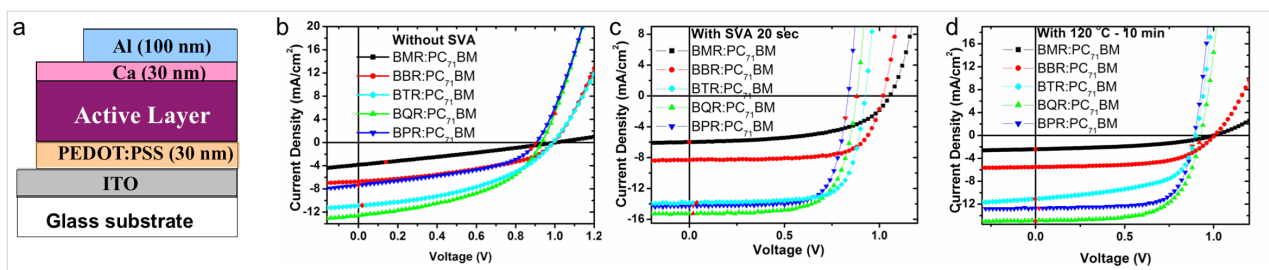


**Figure 12:**  $J$ – $V$  characteristics of **BXR:PC<sub>71</sub>BM** BHJ solar cells. (a) device structure, (b)  $J$ – $V$  curves for as-cast, (c)  $J$ – $V$  curves for SVA with THF, (d) and  $J$ – $V$  curves for TA at 120 °C for 10 min.

**Table 4:** Photovoltaic performances of **BXR:PC<sub>71</sub>BM** BHJ solar cells fabricated under different annealing conditions.

	Active layer	Annealing conditions	$J_{sc}$ (mA/cm <sup>2</sup> )	$V_{oc}$ (V)	FF (%)	PCE (%)
1	<b>BMR:PC<sub>71</sub>BM</b>	as cast	3.9	1.00	26	1.0
2	<b>BBR:PC<sub>71</sub>BM</b>	as cast	6.7	0.98	43	2.8
3	<b>BTR:PC<sub>71</sub>BM</b>	as cast	10.8	0.98	43	4.6
4	<b>BQR:PC<sub>71</sub>BM</b>	<b>as cast</b>	<b>12.6</b>	<b>0.94</b>	<b>45</b>	<b>5.3</b>
5	<b>BPR:PC<sub>71</sub>BM</b>	as cast	7.5	0.90	45	3.0
6	<b>BMR:PC<sub>71</sub>BM</b>	SVA 20 s	6.0	1.04	56	3.5
7	<b>BBR:PC<sub>71</sub>BM</b>	SVA 20 s	8.4	1.00	71	6.0
8	<b>BTR:PC<sub>71</sub>BM</b>	SVA 20 s	13.9	0.92	72	9.3
9	<b>BQR:PC<sub>71</sub>BM</b>	<b>SVA 20 s</b>	<b>15.3</b>	<b>0.88</b>	<b>70</b>	<b>9.4</b>
10	<b>BPR:PC<sub>71</sub>BM</b>	SVA 20 s	14.3	0.82	74	8.7
11	<b>BMR:PC<sub>71</sub>BM</b>	TA 120 °C, 10 min	2.5	1.00	44	1.1
12	<b>BBR:PC<sub>71</sub>BM</b>	TA 120 °C, 10 min	5.5	1.00	60	3.3
13	<b>BTR:PC<sub>71</sub>BM</b>	TA 120 °C, 10 min	11.0	0.88	58	5.7
14	<b>BQR:PC<sub>71</sub>BM</b>	<b>TA 120 °C, 10 min</b>	<b>14.9</b>	<b>0.92</b>	<b>65</b>	<b>8.9</b>
15	<b>BPR:PC<sub>71</sub>BM</b>	TA 120 °C, 10 min	12.8	0.88	71	8.1

below 70%. This suggests that further device optimization is required. The device performances of **BMR** (PCE 1.1%), **BBR** (PCE 3.3%), and **BTR** (PCE 5.7%) are significantly lower than the SVA devices, primarily due to lower FFs and  $J_{sc}$  values.

Both **BQR** (PCE 8.9%) and **BPR** (PCE 8.1%) do not show significant performance loss after thermal annealing, maintaining good FF's,  $J_{sc}$  values and  $V_{oc}$ 's. The drop in performance compared to the SVA devices indicates that further optimization may be required.

It is evident that modification of the chromophore length has a large impact on the device stability and performance. **BQR** as a molecular electron donor is the stand-out performer with the best initial results under all device assembly conditions, and shows thermal stability compatible with printing processes.

The influence on the oligo-thiophene alkyl chain length on molecular packing, and thereby device performance, was examined in the **BT<sup>x</sup>R** series. BHJ devices using **BT<sup>4</sup>R** and **BT<sup>8</sup>R** were assembled using the same device architecture described above. The collected device data are summarized in Table 5, and the  $J$ – $V$  curves are shown in Figure 13. Examination of the **BT<sup>x</sup>R** UV–vis data for as-cast films (Figure 5d) indicates that **BT<sup>8</sup>R** does not have a well-developed  $\pi$ – $\pi$  stacking peak in as-cast films, unlike **BTR**. Also, both **BT<sup>4</sup>R** and **BT<sup>8</sup>R** are blue-shifted in comparison to **BTR**, by 18 nm and 26 nm respectively for **BT<sup>4</sup>R** and **BT<sup>8</sup>R**. As it is not expected that modifications of the oligothiophene bridge side-chain length should significantly impact the chromophore energy levels, variations

in measured properties will be due to impacts of side-chain variation on intra-/intermolecular interactions. The differences are reflected in the performance of **BT<sup>4</sup>R** and **BT<sup>8</sup>R** containing devices, Table 5, entries 1–3 and the  $J$ – $V$  curves reproduced in Figure 13b, where the device efficiency for **BTR** at 4.6% PCE remains above that for **BT<sup>4</sup>R** (3.8% PCE) and **BT<sup>8</sup>R** (2.4% PCE). The major change is a significant drop in short circuit current for **BT<sup>8</sup>R** down to 5.7 mA cm<sup>−2</sup>, from over 10.3 mA cm<sup>−2</sup> for **BTR** and **BT<sup>4</sup>R**. The open circuit voltage is also lower for both **BT<sup>4</sup>R** and **BT<sup>8</sup>R** in comparison to **BTR**, however there is no obvious trend.

After SVA the UV–vis spectra for **BT<sup>4</sup>R** and **BT<sup>8</sup>R** match more closely that for **BTR**, however the  $\pi$ – $\pi$  stacking peak remains poorly resolved for **BT<sup>8</sup>R**. Again this is reflected in the lower device performance for **BT<sup>8</sup>R** (5.2% PCE) in comparison to **BTR** (9.3% PCE) and **BT<sup>4</sup>R** (9.0% PCE). In fact, the device parameters for **BT<sup>4</sup>R** are almost identical to those for **BTR**, except for a significant drop in  $V_{oc}$  to 0.88 V from 0.92 V. One can only speculate on the cause of the  $V_{oc}$  drop until further structural characterisation of the thin films is completed. The poor  $J_{sc}$  and FF for the **BT<sup>8</sup>R** devices indicates a poor development of morphology and indicates that devices optimization is still required.

The performance of **BQR** as a molecular electron donor and the stability of **BQR** containing BHJ devices encouraged the examination of **BQR** in ternary BHJ devices. It has been reported that addition of a small percentage of a molecular electron donor to polymer:fullerene BHJ devices leads to an improve-

**Table 5:** Photovoltaic performances of **BT<sup>x</sup>R:PC<sub>71</sub>BM** BHJ solar cells fabricated under different annealing conditions.

	Active layer	Annealing conditions	$J_{sc}$ (mA/cm <sup>2</sup> )	$V_{oc}$ (V)	FF (%)	PCE (%)
1	<b>BT<sup>4</sup>R:PC<sub>71</sub>BM</b>	as cast	10.3	0.94	39	3.8
2 <sup>a</sup>	<b>BTR:PC<sub>71</sub>BM</b>	as cast	10.8	0.98	43	4.6
3	<b>BT<sup>8</sup>R:PC<sub>71</sub>BM</b>	as cast	5.7	0.92	46	2.4
4	<b>BT<sup>4</sup>R:PC<sub>71</sub>BM</b>	SVA 20 s	14.0	0.88	73	9.0
5 <sup>a</sup>	<b>BTR:PC<sub>71</sub>BM</b>	SVA 20 s	13.9	0.92	72	9.3
6	<b>BT<sup>8</sup>R:PC<sub>71</sub>BM</b>	SVA 20 s	9.6	0.88	62	5.2

<sup>a</sup>BTR data from Table 4 has been reproduced to aid in data interpretation.

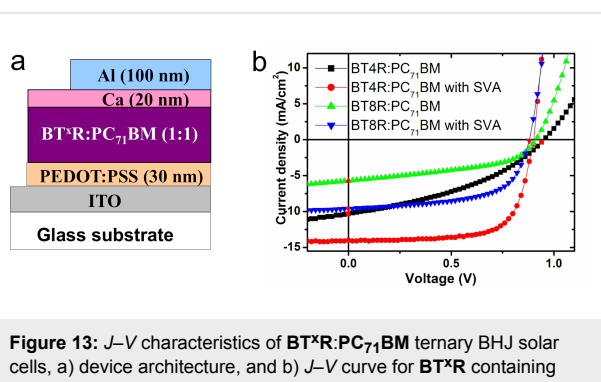


**Figure 13:**  $J$ – $V$  characteristics of **BT<sup>x</sup>R:PC<sub>71</sub>BM** ternary BHJ solar cells, a) device architecture, and b)  $J$ – $V$  curve for **BT<sup>x</sup>R** containing devices.

ment in overall device performance [22]. The underlying reason for the improved performance in these ternary devices is not yet clear with a combination of favourable morphology, energy level cascading and recombination in the ternary blend being suggested [23,24], however the performance enhancement is real and reproducible. Ternary blend devices containing **BQR** have been assembled using poly[4,8-bis(5-(2-ethylhexyl)thiophen-2-yl)benzo[1,2-*b*:4,5-*b*']dithiophene-*alt*-3-fluorothieno[3,4-*b*]thiophene-2-carboxylate] (**PTB7-Th**) as the polymeric electron donor, Figure 14a, as we expected the similarities of the BDT cores to allow better interaction between

**BQR** and **PTB7-Th**, if this is important. Inverted devices with a structure ITO/ZnO/PTB7-Th:BQR:PC<sub>71</sub>BM/MoO<sub>3</sub>/Ag were assembled, and device data are collected in Table 6 and  $J$ – $V$  curves are shown in Figure 14c. Devices were spun cast from chlorobenzene containing 3% diiodooctane as a processing additive. When **PTB7-Th** was as the polymeric donor with our standard inverted device architecture and processing conditions, we were able to assemble BHJ devices with a PCE of 9.6%. For these **PTB7-Th** only devices we achieved a good  $J_{sc} = 17.2$  mA cm<sup>-2</sup> and a FF of 69% with the expected  $V_{oc}$  of 0.80 V for devices containing **PTB7-Th** (Table 6, entry 1). These results compare very well with previously reported devices containing **PTB7-Th:PC<sub>71</sub>BM** as the active layer, with a similar simple device architecture (see for example ref [25],  $J_{sc} = 17.23$  mA cm<sup>-2</sup>, FF 63.42%,  $V_{oc}$  of 0.793 V, and a PCE 8.81%, 1:1.5 **PTB7-Th:PC<sub>71</sub>BM**).

Inclusion of 15 wt % of **BQR** in the donor phase resulted in a significantly enhanced efficiency from 9.6% to 10.7% PCE, with increase in the device  $J_{sc}$  to 19.8 mA cm<sup>-2</sup>, while the  $V_{oc}$  and FF remain effectively unchanged. To investigate the enhanced performance due to addition of **BQR**, we have studied the absorption spectra (Figure 14d) of the ternary and binary blend films. The normalized absorption intensity of

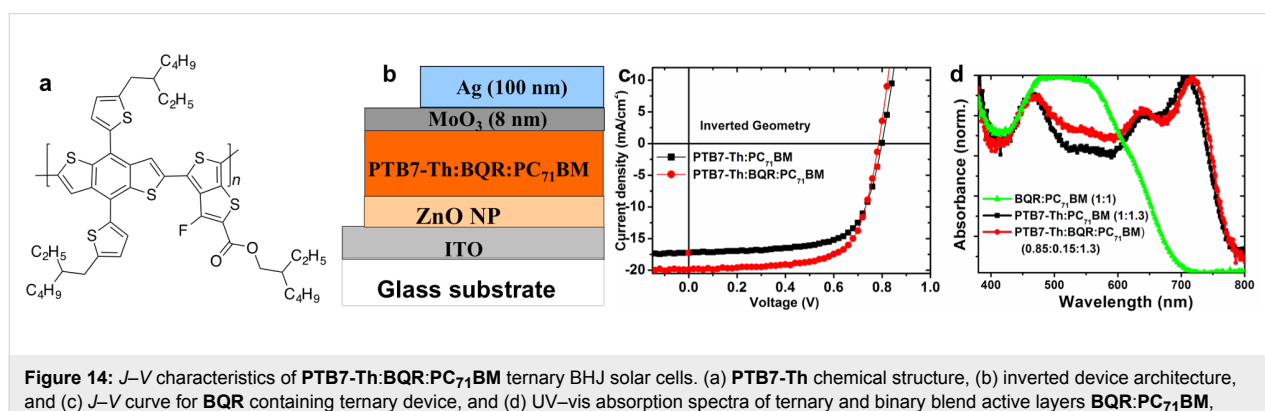


**Figure 14:**  $J$ – $V$  characteristics of **PTB7-Th:BQR:PC<sub>71</sub>BM** ternary BHJ solar cells. (a) **PTB7-Th** chemical structure, (b) inverted device architecture, and (c)  $J$ – $V$  curve for **BQR** containing ternary device, and (d) UV–vis absorption spectra of ternary and binary blend active layers **BQR:PC<sub>71</sub>BM**, **PTB7-Th:PC<sub>71</sub>BM** and **PTB7-Th:BQR:PC<sub>71</sub>BM**.

**Table 6:** Photovoltaic Performances of **PTB7-Th:BQR:PC<sub>71</sub>BM** ternary BHJ solar cells.

Active layer	Ratio	$J_{sc}$ (mA cm <sup>-2</sup> )	$V_{oc}$ (V)	FF (%)	PCE (%)
1 <b>PTB7-Th:PC<sub>71</sub>BM</b>	1:1.3	17.2	0.80	69	9.6
2 <b>PTB7-Th:BQR:PC<sub>71</sub>BM</b>	0.85:0.15:1.3	19.8	0.80	68	10.7

ternary blend (**PTB7-Th:BQR:PC<sub>71</sub>BM**) active layer shows the enhanced absorption intensities in the wavelength range between 500–600 nm comparing to the binary blend (**PTB7-Th:PC<sub>71</sub>BM**). This enhanced absorption in the ternary blend is due to the inclusion of **BQR** as confirmed from the absorption spectrum of **BQR: PC<sub>71</sub>BM**, which shows the absorption maximum in the wavelength range 500–600 nm. Further device optimization and active layer morphology investigation for enhanced performance of ternary blend OPV devices are being explored currently and the results will be communicated elsewhere.

## Conclusion

We have reported a simplified synthesis of alkylsubstituted oligothiophenes used as  $\pi$ -bridges in A– $\pi$ -D– $\pi$ -A molecular electron donors via chain extension catenation of alkylthiophenes. We have used commercially available 3-butyl-, 3-hexyl- and 3-octylthiophene to form the key intermediate TMS-alkylthiophene boronic acid pinacol esters (**3**) in high yield on a large scale and in high purity as they can be purified by distillation. Access to the mono-, bis-, ter-, quater-, and quinquethiophene  $\pi$ -bridge oligothiophenes by alkylthiophene catenation has allowed the synthesis of chromophore extended versions of the previously reported **BTR**, the **BXR** series of materials, that is **BMR** (X = M, monothiophene), **BBR** (X = B, bithiophene), the known **BTR** (X = T, terthiophene), **BQR** (X = Q, quaterthiophene), and the **BPR** (X = P, quinquethiophene). The impact of the oligothiophene alkyl side-chain on OPV device performance was studied using the 3-butyl and 3-octylthiophene starting materials to generate the **BT<sup>X</sup>R** analogues with butyl- and octyl-substituted oligothiophene  $\pi$ -bridges, the **BT<sup>X</sup>R** series of materials, where x = 4 (butyl) and x = 8 (octyl). Thin films of the pure materials have been analysed by UV–vis absorption spectroscopy which indicated that extension of the **BXR** chromophore through oligothiophene extension and side-chain variation impacts significantly on the development of highly  $\pi$ – $\pi$  stacked materials. Shorter chromophore length leads to good stacking in thin films with dominant absorption transitions even in as-cast films for **BMR**, **BTR** and **BQR**. Molecular organization is improved in all films with SVA, except for the longest chromophore (**BPR**), where good  $\pi$ – $\pi$  stacking is not observed, even on extended thermal annealing.

Small changes in the molecular structures lead to larger impacts on the thermal behaviour of the materials. DSC thermograms for materials indicate that short and long chromophores (**BMR**, **BBR**, and **BPR**) show single phase changes, while **BTR** and **BQR** show a number of phase changes and high temperature NLC phases. Surprisingly when **BT<sup>4</sup>R** was examined using DSC a single exothermic and endothermic peak were recorded, however when the materials were examined by POM a high temperature NLC phase was observed indicating a rich and more complicated phase space than indicated by simple thermal analysis. For **BQR**, variable temperature UV–vis spectroscopy mapped the transmitted light variations that accompany the phase change noted in the POM studies of **BQR**. We are currently studying the structural changes occurring in thin films of our **B<sup>X</sup>R** materials to better understand the changes observed and these will be reported in due course.

All the new materials have been tested as electron donors in OPV devices with **PC<sub>71</sub>BM** as the acceptor with thick active layers (approx. 250 nm). The preliminary results show interesting patterns with good OPV device performance for both solvent vapour and thermally annealed devices, up to 9.4% PCE. Device performance improved with chromophore extension in SVA devices increasing from 3.5% PCE for **BMR** containing devices through to 9.4% PCE for **BQR**. The results indicated an improved performance for **BQR** over that for **BTR** previously reported, 9.3% PCE, also reproduced for materials made in this study with our modified procedure. Further extension of the chromophore length in these preliminary studies, for **BPR**, results in a lower PCE of 8.7%, mainly due to a lower  $J_{sc}$  and  $V_{oc}$ . However, again with a FF of 74% there is scope for device improvements through more optimization.

Device performance improved with chromophore extension in TA devices, increasing from 1.1% PCE for **BMR** through to 8.9% PCE for **BQR**. The results indicated an improved thermal stability for OPV devices containing **BQR** over that for **BTR** previously reported. Incorporating **BPR** in OPV devices, with the longest chromophore length in this study, also resulted in thermally stable devices, but with a lower PCE of 8.1%, mainly due to a lower  $J_{sc}$  and  $V_{oc}$ . However, with a FF of 71%, the highest in this thermally annealed series, there is again scope for device improvements through more optimization.

In an extension of these studies, we have used the best material (**BQR**) as a secondary donor in ternary blend devices with commercially available **PTB7-Th** as the main polymeric donor. In initial studies using these ternary blends we have recorded OPV device efficiencies of up to 10.7% PCE. The improved efficiency in these devices is a result of a significantly higher  $J_{sc}$ , rising from 17.2 to 19.8 mA cm<sup>-2</sup>, with no significant change in  $V_{oc}$  or FF.

Therefore, we have shown using a simplified synthesis that chain extended chromophores can be accessed, and thereby the thermal stability of OPV devices containing these new materials can be improved. We are currently examining **BQR** in printed solar cells.

In all cases in our structure–property relationship studies, devices incorporating materials that exhibited a high temperature NLC phase gave the best results. The role of the high temperature NLC behaviour in device performance remains unclear, and as we do not anneal to temperatures where the NLC phase change temperature is reached, its presence is unlikely. However, it may be that structural properties leading to a high temperature NLC phase may help to pre-organise the donor material into a morphology best suited for OPV devices. We are currently probing the structure of these materials in thin films, and these results will be published in the near future, along with device optimization studies and translation to large area devices.

In summary, we have developed a simplified synthetic route to afford a range of MMs analogues of **BTR**. This simplified route has allowed large-scale synthesis of intermediate building blocks and of a multi-gram synthesis of the required MMs. Detailed structure–property studies have identified **BQR** and **BPR** as excellent materials for further optimization with an improved performance over **BTR**. OPV devices containing **BQR** or **BPR** show a good thermal stability at 120 °C for 10 min, maintaining a high PCE (**BQR**, 8.9% and **BPR**, 8.1%) and FF (**BQR**, 65% and **BPR**, 71%). These are promising results for high performance OPV devices and the translation to large area and printed OPV devices.

## Supporting Information

### Supporting Information File 1

Synthetic procedures, NMR spectra, MALDI, TGA, DSC, CVs, POM methods and images, UV–vis, fluorescence, and DFT cartesian coordinates.

[<http://www.beilstein-journals.org/bjoc/content/supplementary/1860-5397-12-223-S1.pdf>]

## Acknowledgements

This work was made possible by support from the Australian Renewable Energy Agency which funds the project grants within the Australian Centre for Advanced Photovoltaics. Responsibility for the views, information or advice expressed herein is not accepted by the Australian Government. We thank CSIRO for access to the PESA and glovebox equipment. This work was performed in part at the Melbourne Centre for Nanofabrication (MCN) in the Victorian Node of the Australian National Fabrication Facility (ANFF).

## References

1. Li, Y. *Acc. Chem. Res.* **2012**, *45*, 723–733. doi:10.1021/ar2002446
2. Cheng, Y.-J.; Yang, S.-H.; Hsu, C.-S. *Chem. Rev.* **2009**, *109*, 5868–5923. doi:10.1021/cr900182s
3. Eggenhuisen, T. M.; Galagan, Y.; Coenen, E. W. C.; Voorthuizen, W. P.; Slaats, M. W. L.; Kommeren, S. A.; Shanmuganam, S.; Coenen, M. J. J.; Andriessen, R.; Groen, W. A. *Sol. Energy Mater. Sol. Cells* **2015**, *134*, 364–372. doi:10.1016/j.solmat.2014.12.014
4. Chen, C.-C.; Chang, W.-H.; Yoshimura, K.; Ohya, K.; You, J.; Gao, J.; Hong, Z.; Yang, Y. *Adv. Mater.* **2014**, *26*, 5670–5677. doi:10.1002/adma.201402072
5. Zhao, J.; Li, Y.; Yang, G.; Jiang, K.; Lin, H.; Ade, H.; Ma, W.; Yan, H. *Nat. Energy* **2016**, *1*, No. 15027. doi:10.1038/nenergy.2015.27
6. Li, N.; Baran, D.; Forberich, K.; Machui, F.; Ameri, T.; Turbiez, M.; Carrasco-Orozco, M.; Drees, M.; Facchetti, A.; Krebs, F. C.; Brabec, C. J. *Energy Environ. Sci.* **2013**, *6*, 3407–3413. doi:10.1039/C3EE42307G
7. Bartelt, J. A.; Lam, D.; Burke, T. M.; Sweetnam, S. M.; McGehee, M. D. *Adv. Energy Mater.* **2015**, *5*, No. 1500577. doi:10.1002/aenm.201500577
8. Kan, B.; Li, M.; Zhang, Q.; Liu, F.; Wan, X.; Wang, Y.; Ni, W.; Long, G.; Yang, X.; Feng, H.; Zuo, Y.; Zhang, M.; Huang, F.; Cao, Y.; Russell, T. P.; Chen, Y. *J. Am. Chem. Soc.* **2015**, *137*, 3886–3893. doi:10.1021/jacs.5b00305
9. Liu, Y.; Chen, C.-C.; Hong, Z.; Gao, J.; Yang, Y.; Zhou, H.; Dou, L.; Li, G.; Yang, Y. *Sci. Rep.* **2013**, *3*, No. 3356. doi:10.1038/srep03356
10. Lin, Y.; Li, Y.; Zhan, X. *Chem. Soc. Rev.* **2012**, *41*, 4245–4272. doi:10.1039/C2CS15313K
11. Mishra, A.; Bäuerle, P. *Angew. Chem., Int. Ed.* **2012**, *51*, 2020–2067. doi:10.1002/anie.201102326
12. Lin, Y.; Ma, L.; Li, Y.; Liu, Y.; Zhu, D.; Zhan, X. *Adv. Energy Mater.* **2013**, *3*, 1166–1170. doi:10.1002/aenm.201300181
13. Kim, Y. J.; Baek, J. Y.; Ha, J.-J.; Chung, D. S.; Kwon, S.-K.; Park, C. E.; Kim, Y.-H. *J. Mater. Chem. C* **2014**, *2*, 4937–4946. doi:10.1039/C4TC00187G
14. Sun, K.; Xiao, Z.; Lu, S.; Zajaczkowski, W.; Pisula, W.; Hanssen, E.; White, J. M.; Williamson, R. M.; Subbiah, J.; Ouyang, J.; Holmes, A. B.; Wong, W. W. H.; Jones, D. J. *Nat. Commun.* **2015**, *6*, No. 6013. doi:10.1038/ncomms7013
15. Carlé, J. E.; Helgesen, M.; Madsen, M. V.; Bundgaard, E.; Krebs, F. C. *J. Mater. Chem. C* **2014**, *2*, 1290–1297. doi:10.1039/c3tc31859a
16. Spivey, A. C.; Turner, D. J.; Turner, M. L.; Yeates, S. *Org. Lett.* **2002**, *4*, 1899–1902. doi:10.1021/o1025879x
17. Turner, D. J.; Anémian, R.; Mackie, P. R.; Cupertino, D. C.; Yeates, S. G.; Turner, M. L.; Spivey, A. C. *Org. Biomol. Chem.* **2007**, *5*, 1752–1763. doi:10.1039/b703022c

18. Yin, N.; Wang, L.; Lin, Y.; Yi, J.; Yan, L.; Dou, J.; Yang, H.-B.; Zhao, X.; Ma, C.-Q. *Beilstein J. Org. Chem.* **2016**, *12*, 1788–1797.  
doi:10.3762/bjoc.12.169
19. Chen, L.; Roger, J.; Bruneau, C.; Dixneuf, P. H.; Doucet, H. *Chem. Commun.* **2011**, *47*, 1872–1874. doi:10.1039/C0CC04302H
20. Subbiah, J.; Purushothaman, B.; Chen, M.; Qin, T.; Gao, M.; Vak, D.; Scholes, F. H.; Chen, X.; Watkins, S. E.; Wilson, G. J.; Holmes, A. B.; Wong, W. W. H.; Jones, D. J. *Adv. Mater.* **2015**, *27*, 702–705.  
doi:10.1002/adma.201403080
21. Gao, M.; Subbiah, J.; Geraghty, P. B.; Chen, M.; Purushothaman, B.; Chen, X.; Qin, T.; Vak, D.; Scholes, F. H.; Watkins, S. E.; Skidmore, M.; Wilson, G. J.; Holmes, A. B.; Jones, D. J.; Wong, W. W. H. *Chem. Mater.* **2016**, *28*, 3481–3487.  
doi:10.1021/acs.chemmater.6b01194
22. Zhang, J.; Zhang, Y.; Fang, J.; Lu, K.; Wang, Z.; Ma, W.; Wei, Z. *J. Am. Chem. Soc.* **2015**, *137*, 8176–8183. doi:10.1021/jacs.5b03449
23. Lu, L.; Xu, T.; Chen, W.; Landry, E. S.; Yu, L. *Nat. Photonics* **2014**, *8*, 716–722. doi:10.1038/NPHOTON.2014.172
24. Savoie, B. M.; Dunaisky, S.; Marks, T. J.; Ratner, M. A. *Adv. Energy Mater.* **2015**, *5*, No. 1400891.  
doi:10.1002/Aenm.201400891
25. Nam, S.; Seo, J.; Woo, S.; Kim, W. H.; Kim, H.; Bradley, D. D. C.; Kim, Y. *Nat. Commun.* **2015**, *6*, No. 8929. doi:10.1038/ncomms9929

## License and Terms

This is an Open Access article under the terms of the Creative Commons Attribution License (<http://creativecommons.org/licenses/by/4.0>), which permits unrestricted use, distribution, and reproduction in any medium, provided the original work is properly cited.

The license is subject to the *Beilstein Journal of Organic Chemistry* terms and conditions:  
(<http://www.beilstein-journals.org/bjoc>)

The definitive version of this article is the electronic one which can be found at:  
doi:10.3762/bjoc.12.223



## Effects of solvent additive on “s-shaped” curves in solution-processed small molecule solar cells

John A. Love<sup>\*1,2</sup>, Shu-Hua Chou<sup>1,3</sup>, Ye Huang<sup>1</sup>, Guillermo C. Bazan<sup>\*1</sup>  
and Thuc-Quyen Nguyen<sup>\*1</sup>

### Full Research Paper

Open Access

Address:

<sup>1</sup>Center for Polymers and Organic Solids, University of California, Santa Barbara, California 93106, United States, <sup>2</sup>Institute of Physics and Astronomy, University of Potsdam, Potsdam-Golm 14476, Germany and <sup>3</sup>Department of Chemistry, National Taiwan University, Taipei, 10617, Taiwan

Email:

John A. Love<sup>\*</sup> - johnlove@uni-potsdam.de; Guillermo C. Bazan<sup>\*</sup> - bazan@chem.ucsb.edu; Thuc-Quyen Nguyen<sup>\*</sup> - quyen@chem.ucsb.edu

\* Corresponding author

Keywords:

current voltage analysis; morphology; organic solar cells

*Beilstein J. Org. Chem.* **2016**, *12*, 2543–2555.

doi:10.3762/bjoc.12.249

Received: 24 June 2016

Accepted: 04 November 2016

Published: 28 November 2016

This article is part of the Thematic Series "Organic photovoltaics".

Guest Editor: D. J. Jones

© 2016 Love et al.; licensee Beilstein-Institut.

License and terms: see end of document.

### Abstract

A novel molecular chromophore, p-SIDT(FBTThCA8)<sub>2</sub>, is introduced as an electron-donor material for bulk heterojunction (BHJ) solar cells with broad absorption and near ideal energy levels for the use in combination with common acceptor materials. It is found that films cast from chlorobenzene yield devices with strongly s-shaped current–voltage curves, drastically limiting performance. We find that addition of the common solvent additive diiodooctane, in addition to facilitating crystallization, leads to improved vertical phase separation. This yields much better performing devices, with improved curve shape, demonstrating the importance of morphology control in BHJ devices and improving the understanding of the role of solvent additives.

### Introduction

Tremendous multidisciplinary research efforts have led to consistent increases in the efficiency of organic solar cells, making the technology a bright prospect in the quest for alternative energy [1–4]. In particular the rapid development of solution-processed small molecule materials over the last several years has led to leaps in state-of-the-art efficiencies and improved understanding of structure–property relationships.

The well-defined molecular structures have inherent amenability to purification, batch-to-batch reproducibility and monodispersity, which make them an attractive alternative to their polymeric counterparts [5,6]. Also of import stands the fact that easily modified, modular structures lead to finely-tunable energy levels and optical properties through molecular design [7,8]. Most high-performing small molecule electron-

donor materials are configured such that the conjugated backbone consists of alternating electron-rich donor (D) and the electron-deficient acceptor (A) moieties so as to facilitate efficient photo-induced charge transfer and harvest a broad spectral response [9-11]. One such molecular architecture introduced by Bazan and co-workers can be described as a D<sub>1</sub>–A–D<sub>2</sub>–A–D<sub>1</sub> system [12], where D<sub>1</sub> is an electron-rich unit such as bithiophene, A is a benzothiadiazole derivative and D<sub>2</sub> can be different electron-rich planar cores such as dithienosilol or silanindacenothiophene. Utilizing this push–pull molecular approach, efficiencies up to 9.0% have been achieved [13] due to deep highest occupied molecular orbitals (HOMO) and the corresponding large open circuit voltages ( $V_{OC}$ ). There remains, however, room for improvement by further tuning the energetics of these materials so as to harvest photons from the widest possible spectral range while still maintaining high  $V_{OC}$ . Expressly, the optical bandgap must be further reduced by minimizing the energetic gap in the lowest occupied molecular orbitals (LUMO) between donor and acceptor [14].

One design approach towards this end involves adding electron-withdrawing end groups to existing central core chromophores. Chen and co-workers have successfully used cyanoacetate [15] and other electron-withdrawing end groups to create A–D–A type oligothiophene derivatives with tunable electronics, which are among the highest performing materials to date [16-19]. Starting with the previously reported molecule benzo[1,2-b:4,5-b]bis(4,4'-dihexyl-4H-silolo[3,2-b]thiophene-2,2'-diyl)bis(6-fluoro-4-(5'-hexyl-[2,2'-bithiophene]-5-yl)benzo[c][1,2,5]thia-

diazole, p-SIDT(FBTTh<sub>2</sub>)<sub>2</sub> (Figure 1), we have modified the conjugated backbone to include electron-withdrawing octyl cyanoacetate (CA8) end groups, essentially forming an “A<sub>1</sub>–D<sub>1</sub>–A<sub>2</sub>–D<sub>2</sub>–A<sub>2</sub>–D<sub>1</sub>–A<sub>1</sub>” molecular skeleton, benzo[1,2-b:4,5-b]bis(4,4'-dihexyl-4H-silolo[3,2-b]thiophene-2,2'-diyl)bis(6-fluoro-4-((E)-octyl-3-(5-thiophen-2-yl)-2-cyanoacrylate)-5-yl)benzo[c][1,2,5]thiadiazole, p-SIDT(FBTThCA8)<sub>2</sub>. We will show that this molecular substitution did indeed significantly reduce the bandgap while maintaining deep energy levels, as well as some of the other desirable properties of the parent material [20-22].

However, molecular design remains only the first step towards the development of high performance devices. Mismanagement of the organization and phase-separation processes or inappropriate device architecture choices can lead to non-ideal electronics at electrode interfaces and severely limit the performance of a materials system. In particular, the fill factor (FF), which is simply a metric describing the field dependence of current, can be particularly sensitive to changes in morphology or interfacial effects. At the extreme, a strong field dependence near open circuit conditions can result in current vs voltage ( $J$ – $V$ ) curves adopting an “s-shape.” Such curves have been observed experimentally in a number of diverse OPV systems, and have been ascribed to a host of morphological or interfacial issues. The s-shape arises from inefficient charge extraction of one charge carrier type at small electric fields. Mechanistically, a variety of underlying causes have been proposed, including large imbalances in charge carrier mobilities, energetic barriers

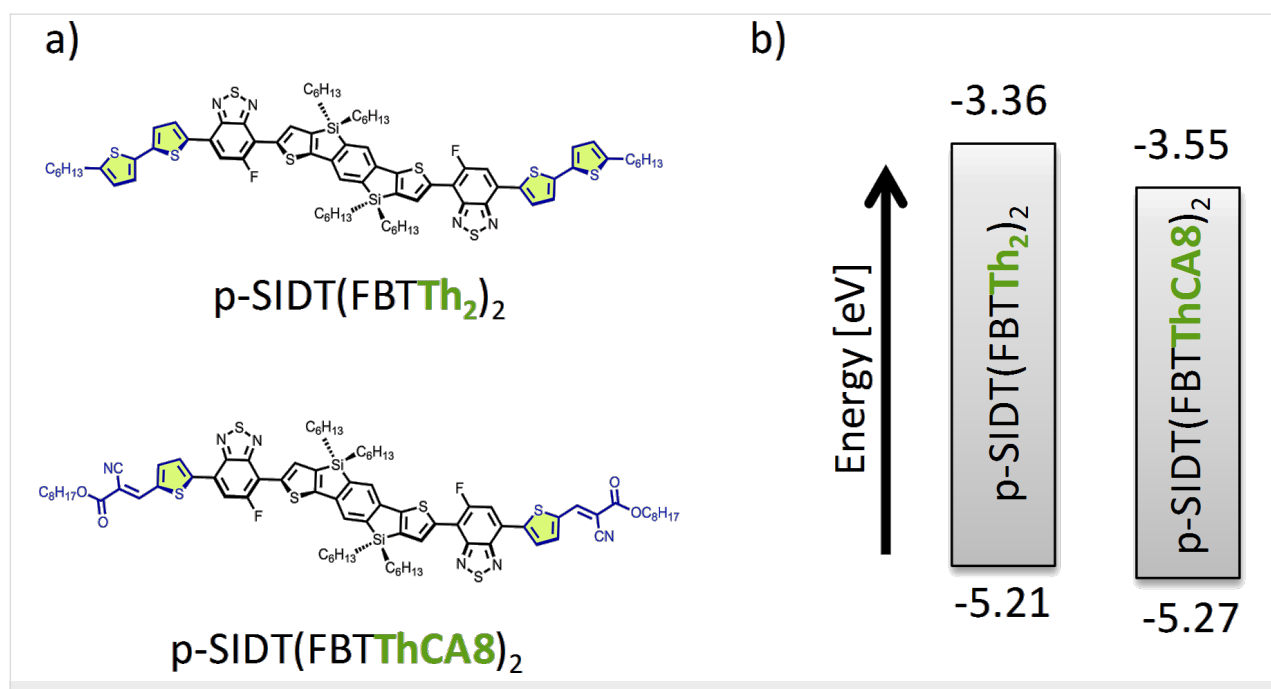


Figure 1: a) Molecular structures and b) energy levels of p-SIDT(FBTTh<sub>2</sub>)<sub>2</sub> and p-SIDT(FBTThCA8)<sub>2</sub> highlighting the modification of the end groups.

to charge extraction at electrode interfaces, reduced surface recombination, and interfacial defects leading to traps; device simulations have shown that all of these could indeed result in the s-shape behavior [23–30].

Herein we describe the development of a novel small molecule system with nearly ideal optoelectronic properties, which unfortunately results in s-shaped *J*–*V* curves and poor performance. We show that this is due to non-ideal phase separation, specifically a preferential migration of the electron acceptor to the bottom anode interface. This can, however, be mitigated through appropriate processing, using a small amount of the solvent additive 1,8-diiodooctane (DIO).

## Results and Discussion

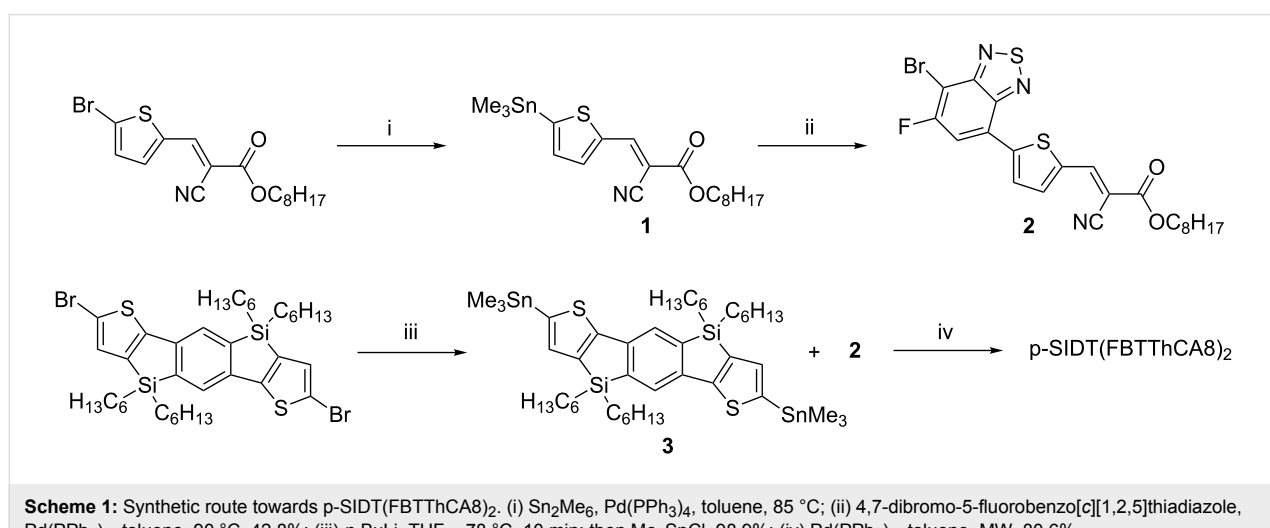
### Synthesis and characterization

Scheme 1 depicts the synthesis toward p-SIDT(FBTThCA8)<sub>2</sub>. As opposed to using bottom-up synthetic procedures as reported in the literature in which ketone derivatives are converted to octyl cyanoacetates in the final synthetic step via Knoevenagel condensation [15,31–35], we chose to begin with (*E*)-octyl 3-(5-bromothiophen-2-yl)-2-cyanoacrylate as the starting material to ensure good solubility. Intermediate **1** was prepared by palladium-mediated stannylation [36] and then subjected to regioselective Stille conditions [37] in an oil bath (90 °C) to generate **2**. (Complete synthetic details and characterization of all compounds are provided in Supporting Information File 1, Figure S1). Compound **3** was obtained through lithium–halogen exchange with *n*-BuLi followed by addition of trimethyltin chloride. Segments **2** and **3** were cross-coupled using a microwave-assisted Stille reaction to afford the target p-SIDT(FBTThCA8)<sub>2</sub>.

The thermal transitions of p-SIDT(FBTThCA8)<sub>2</sub> were evaluated by differential scanning calorimetry (DSC) and compared to its predecessor, p-SIDT(FBTTh<sub>2</sub>)<sub>2</sub>. A significant impact on thermal behaviors was observed upon substituting 2-hexylthiophene with octyl cyanoacetate (Supporting Information File 1, Figure S4 and Table S1). As compared to p-SIDT(FBTTh<sub>2</sub>)<sub>2</sub>, the melting (*T*<sub>m</sub>) and crystallization (*T*<sub>c</sub>) temperatures of p-SIDT(FBTThCA8)<sub>2</sub> are increased by 76.9 and 117.1 °C, respectively, which implies an enhancement of the intermolecular interaction in the solid state. This improved rigidity of p-SIDT(FBTThCA8)<sub>2</sub> is correlated to a noticeable decrease in solubility, which was measured to be 32 mg/mL for p-SIDT(FBTThCA8)<sub>2</sub> compared with over 50 mg/mL for p-SIDT(FBTTh<sub>2</sub>)<sub>2</sub> in chloroform at room temperature.

Frontier molecular energy levels were estimated by cyclic voltammograms (CV) in dichloromethane and calculated theoretically by density functional theory (DFT) (Supporting Information File 1, Figure S5 and Table S2). In the CV measurement, energy levels of HOMO and LUMO were calculated from the onsets of oxidation and reduction potentials. The HOMO level (*E*<sub>HOMO</sub>, CV: −5.27 eV, *E*<sub>HOMO</sub>, DFT: −5.43 eV) is quite deep, even compared to that of p-SIDT(FBTTh<sub>2</sub>)<sub>2</sub> (*E*<sub>HOMO</sub>, CV: −5.21 eV, *E*<sub>HOMO</sub>, DFT: −4.97 eV). We anticipate this should provide a high *V*<sub>OC</sub> when blended with PCBM. The band gap of p-SIDT(FBTThCA8)<sub>2</sub> is also reduced with respect to p-SIDT(FBTTh<sub>2</sub>)<sub>2</sub> as determined by CV (1.72 eV and 1.85 eV, respectively) and by DFT (1.90 eV and 2.01 eV, respectively) suggesting that substituting 2-hexylthiophene with octyl cyanoacetate on both wing-ends does noticeably reduce the bandgap while maintaining a deep HOMO level.

The normalized solid-state absorption profile of p-SIDT(FBTThCA8)<sub>2</sub> is shown as the dotted line in Figure 2a



and the data are also summarized in Table S1 (Supporting Information File 1). The film has strong absorption in the visible range, with an onset at 750 nm corresponding to an optical bandgap of 1.65 eV. This is consistent with the electrochemically determined bandgap. The primary absorption band shows vibronic progression, suggesting ordering in the solid state, with peak absorption at 650 nm. The red-shifted absorption of p-SIDT(FBTThCA8)<sub>2</sub> with respect to p-SIDT(FBTTh)<sub>2</sub>, whose absorption onset in the solid state occurs at 670 nm, is

further confirmation that the addition of electron-withdrawing endgroups reduces the bandgap of the chromophore. Importantly, the shift in absorption onset represents about a 25% increase in the number of photons in the AM 1.5 solar spectrum available for absorption. If p-SIDT(FBTThCA8)<sub>2</sub> maintains high internal quantum efficiencies and *FF* like its predecessor, and also achieves a high *V<sub>OC</sub>* as expected based on energy levels, the improved absorption imparts p-SIDT(FBTThCA8)<sub>2</sub> with great potential.

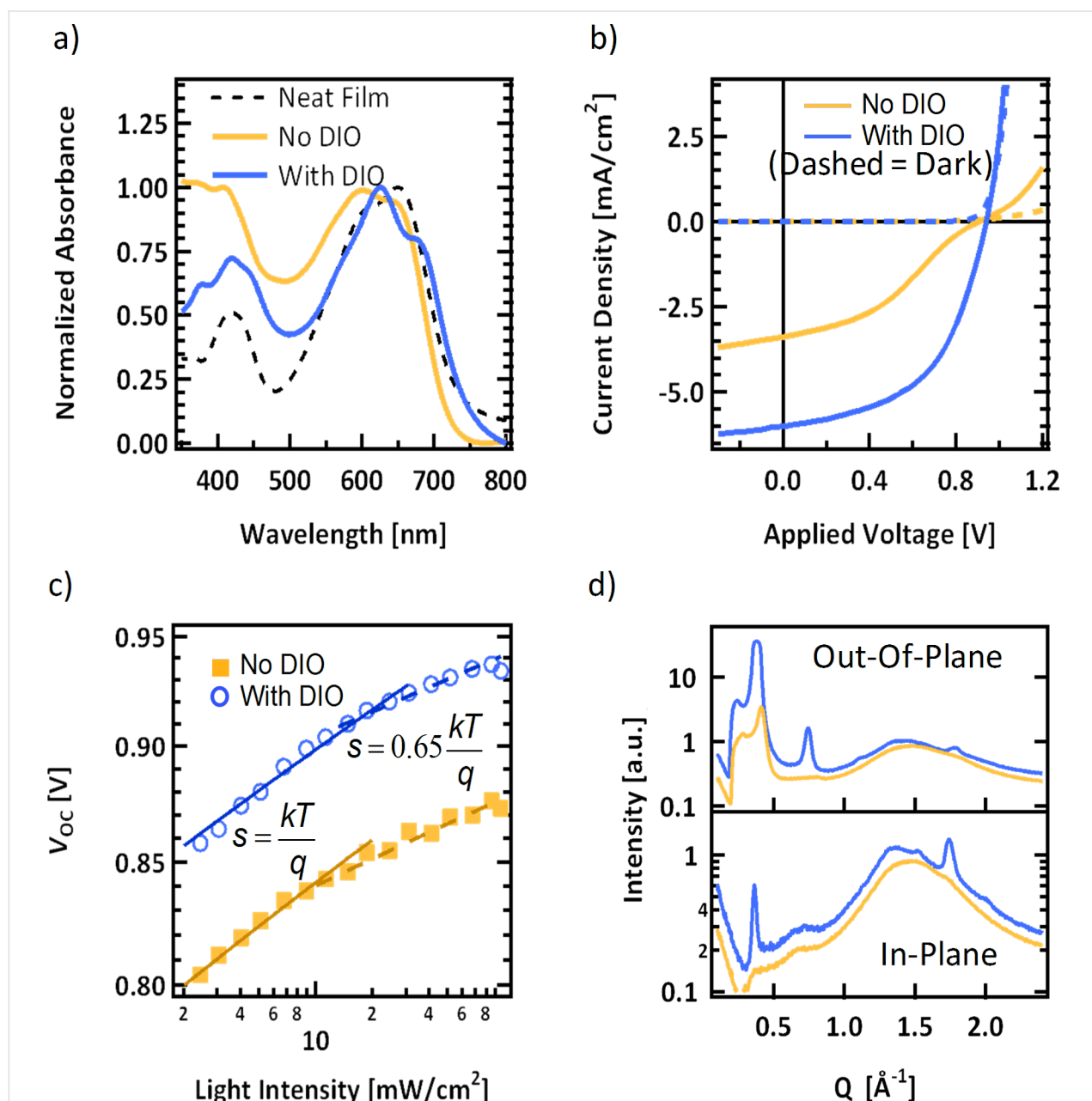


**Figure 2:** a) Solid-state absorption profiles of neat p-SIDT(FBTThCA8)<sub>2</sub> (dashed line) and p-SIDT(FBTThCA8)<sub>2</sub>:PC<sub>71</sub>BM blends cast from pure chlorobenzene (yellow) and with 1.5% DIO (blue). b) Photovoltaic performance of equivalent blend solar cells with c) corresponding light intensity open circuit voltage measurements where the empirically fit solid lines have a slope of  $kT/q$  and dashed lines indicate a slope of  $0.65 kT/q$ , d) blend film X-ray diffraction line cuts from crystallites oriented out-of-plane (top) and in-plane (bottom).

## Solar cell performance

For initial photovoltaic device fabrication, conditions were chosen according to previously reported protocols of structurally similar small molecule systems [38–40]. Specifically, p-SIDT(FBTThCA8)<sub>2</sub> was mixed with PC<sub>71</sub>BM and cast to form a bulk heterojunction (BHJ) atop poly(3,4-ethylenedioxythiophene) polystyrene sulfate (PEDOT) giving an architecture of ITO/PEDOT/p-SIDT(FBTThCA8)<sub>2</sub>:PC<sub>71</sub>BM/Ca/Al. The mass ratio of p-SIDT(FBTThCA8)<sub>2</sub>:PC<sub>71</sub>BM was held at 1:1 and cast from a chlorobenzene solution containing 40 mg/mL total solids, giving 120 nm thick active layers. Such devices show modest performance ( $J_{SC} = 3.4$  mA/cm<sup>2</sup>,  $V_{OC} = 0.91$  V,  $FF = 0.37$ ,  $PCE = 1.1\%$ ). Though the performance is low, the efficiency is similar compared to other systems cast from pure chlorobenzene. Furthermore, the high  $V_{OC}$  of 910 mV is encouraging, as it further confirms the advantage of the deep lying HOMO level of p-SIDT(FBTThCA8)<sub>2</sub>. However, an inflection point near  $V_{OC}$ , a clear kink in the  $J$ – $V$  curve gives the curve a dramatic “s-shape” (Figure 2b) limiting  $FF$  and  $PCE$ .

In the literature, it has been shown that incorporation of small amounts of the solvent additive DIO into the casting solvent can vastly improve small molecule device performance [38–43]. Accordingly, initial optimization required adjusting the concentration of DIO. It was found that at a concentration of 1.5% DIO (by volume) in chlorobenzene, the  $PCE$  was increased to 2.9% ( $J_{SC} = 6.0$  mA/cm<sup>2</sup>,  $V_{OC} = 0.94$  V,  $FF = 0.52$ ); device characteristics are shown in Table 1. Though, the improvements in device performance are relatively modest compared to what has been observed in other systems, incorporation of the DIO into the solution noticeably reduces the s-shape of the curve leading to a greatly enhanced  $FF$ . While the use of additives has been shown to have a number of consequences on film formation and device operation [38–44], to the best of our knowledge, such a dramatic change in curve shape has not been demonstrated previously using solvent additives. And while these additive-processed devices still have not nearly reached the full potential of this materials system, and other possible processing changes may also affect the nature of the  $J$ – $V$  curve, we have focused herein on understanding the mechanism leading to the change in curve shape to gain a better, fundamental understanding of the nature and operation of small-molecule solar cell devices and the role of solvent additives in film formation.

As a first insight into the difference in  $J$ – $V$  behavior with and without DIO we examined the light intensity dependence of the two devices. Varying the intensity of the incident light serves to proportionally change the number of absorbed photons and thus generation of free charges. Of particular interest is the effect of light intensity on  $V_{OC}$ , since at the open circuit voltage carriers

**Table 1:** Device characteristics when cast with and without DIO, before and after treatment with MeOH in a standard architecture as well as in an inverted cell.

		Solar cell characteristics			
Conditions		$J_{SC}$ (mA/cm <sup>2</sup> )	$V_{OC}$ (V)	$FF$	$PCE$ (%)
No DIO	standard	3.4	0.91	0.37	1.1
	w/MeOH	3.4	0.95	0.37	1.2
	inverted	4.5	1.09	0.51	2.5
	standard	6.0	0.94	0.52	2.9
With DIO	w/MeOH	6.1	1.02	0.52	3.2
	inverted	7.0	0.73	0.47	2.4

are created, but nearly none of the charges are extracted,  $J = 0$ ; all charges must therefore recombine [45]. Thus, the relation of  $V_{OC}$  with the incident light intensity for bimolecular (free charge) recombination has been shown to depend only on temperature and light intensity, given by

$$V_{OC} \propto \frac{kT}{q} \ln(I), \quad (1)$$

where  $I$  is light intensity,  $k$  is the Boltzman constant,  $T$  is temperature and  $q$  is the elementary charge. Thus, in a system dominated by bimolecular recombination, on a semi-log plot of  $V_{OC}$  vs  $I$  we expect a linear relationship with a slope of  $kT/q$  [45]. It is worth noting that proper analysis of low light intensity data requires sufficiently low dark current, such that it does not constitute a significant fraction of the device current in the voltage regime close to  $V_{OC}$ . In both the devices cast with and without additive, even at only 0.02 suns, the dark current remains at least two orders of magnitude lower than the device current (see Supporting Information File 1, Figure S6). The  $V_{OC}$  as a function of light intensity are shown in Figure 2c for devices without and with DIO.

It is immediately clear that the  $V_{OC}$  in devices without additive do not follow a single linear relationship across all light intensities. Instead it seems to follow a slope of  $kT/q$  closely at light intensities lower than 10 mW/cm<sup>2</sup>, but then has a shallower, seemingly linear dependence with a slope of  $\approx 0.65 kT/q$  at higher intensities. The slope of  $0.65 kT/q$  was fit empirically and does not fit the data unequivocally, but is displayed to show at the very least, that at higher light intensities the  $V_{OC}$  has a dependency that is less than the expected  $kT/q$ . The suggestion is that at high charge densities, the dominant recombination mechanism may change. The device cast with DIO shows similar behavior but to a much lesser extent. The  $V_{OC}$  only deviates from  $s = kT/q$  significantly at intensities close to 100 mW/cm<sup>2</sup>.

Thus, even devices processed with DIO may, to some extent, suffer from the same problems as those cast from pure chlorobenzene albeit to a much lesser extent. Light intensity studies are thus a powerful tool to look at more nuanced details of current voltage characteristics.

To further inspect the effects of light intensity on device operation, the photocurrent,  $J_{\text{Ph}}$ , defined as the current upon illumination with the dark current subtracted, was examined as a function effective voltage [46-49]. The effective voltage is the voltage difference between the applied voltage and the voltage

at which no photocurrent is generated,  $V_0 - V$ , and determines the strength of the electric field within the device, the driving force for charge extraction.  $J_{\text{Ph}}$  is shown as a function of light intensity for devices cast without and with DIO in Figure 3a and 3b, respectively.

At low effective voltages, ( $V_0 - V < \approx 0.1$  V) implying a small electric field, the photocurrent of both devices linearly increases with voltage. This is due to the competition between drift and diffusion of photogenerated charges to the contacts [49]. In the device processed with DIO, beyond  $V_0 - V = 0.2$  V

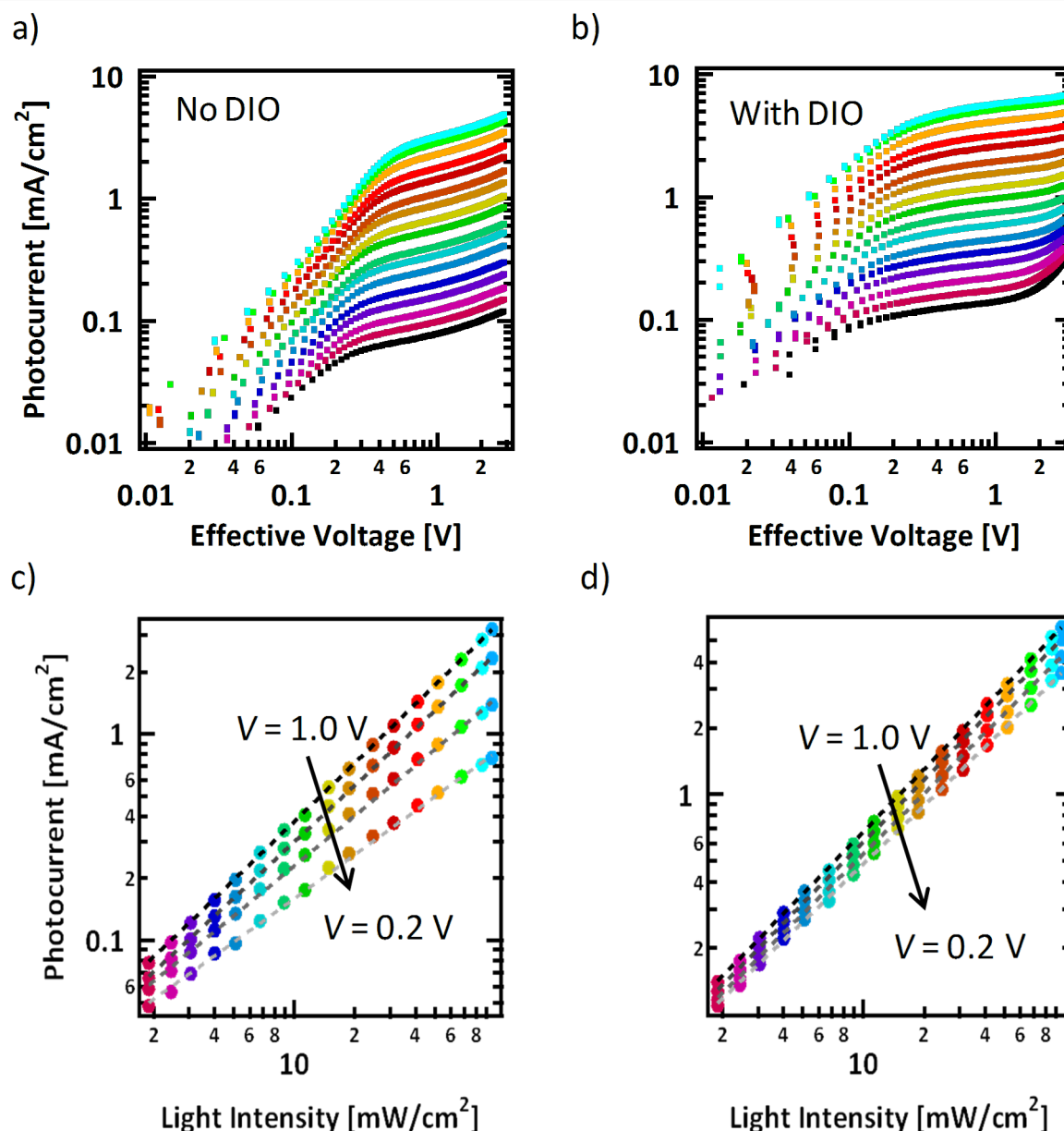


**Figure 3:** Light intensity dependence of photocurrent as a function of the effective voltage,  $V_0 - V$ , for devices cast a) without DIO and b) with DIO and the extracted photocurrent at effective voltages of 1.0, 0.5, 0.3, and 0.2 V (from black to grey, respectively) as detailed in Table 2 for devices cast c) without DIO and d) with DIO.

the  $J_{\text{Ph}}$  reaches a saturation regime, where it increases much less significantly with voltage. In this saturation regime, the larger electric field can effectively sweep out charges and bimolecular recombination does not play as significant a role. The voltage at which this rollover point occurs is independent of intensity. In these devices, there is not a true “saturation” as the photocurrent is always increasing, however, there is still a clear rollover point between two regimes. This increasing photocurrent could be due to field dependent charge generation [50-53].

As seen in Figure 3a,  $J_{\text{Ph}}$  has a much stronger dependence on voltage in devices processed without DIO. Even at high effective voltages, there remains a strong voltage effect and  $J_{\text{Ph}}$  continues to increase without saturating. There are two clear regimes with two different voltage dependencies, but in contrast to devices processed with DIO, in this case the rollover voltage at which  $J_{\text{Ph}}$  switches from one regime to the other does indeed depend on light intensity. At higher intensities, a higher voltage is required to reach the “saturation” regime. This has previously been associated with a build-up of space charge in the film [47].

It is expected that for devices not limited by charge extraction,  $J_{\text{Ph}}$  at each and every effective voltage, should scale linearly with intensity,  $J_{\text{Ph}} \propto I$ , while devices limited by space charge build-up have been shown to characteristically have a sub-linear dependence, where  $J_{\text{Ph}} \propto I^{0.75}$  [47]. At  $V_0 - V = 1.0$  V, close to short-circuit conditions, in devices processed with and without additive,  $J_{\text{Ph}}$  scales nearly linearly, following a power law where  $s = 0.95$ . This relation deviates from linearity when moving to lower fields particularly in the devices cast without DIO. As seen in Table 2, at an effective voltage of 0.3 V,  $s = 0.81$  and at 0.2 V,  $s = 0.71$ . This is quite close to 0.75, the value one would expect for a device limited by space charge.

**Table 2:** Power law dependences of photocurrent on light intensity at specific effective voltages for BHJ devices from Figure 3.

Conditions	Power law dependence			
	0.2 V	0.3 V	0.5 V	1.0 V
no DIO	0.71	0.81	0.91	0.95
with DIO	0.88	0.91	0.94	0.95

In Figure 3b, a pronounced uptick in photocurrent is seen at high reverse biases ( $>1.5$  V). This, however, is likely an artifact, as the “photocurrent” seems to follow the dark current which is not as low in the additive processed film as in the film without DIO. The dark current is plotted with the light intensity studies in Figure S6 (Supporting Information File 1). While in the

photocurrent the dark current is subtracted from, the illuminated it is likely that the linear leakage current may also change with light. This highlights the need for low levels of leakage current for reliable measurements at higher voltages.

At low fields, the device processed without DIO suffers from space charge build-up, while at higher fields, there is sufficient driving force to overcome these effects and extract the charges. A similar effect can be seen in the device processed with DIO, albeit to a lesser extent. At  $V_0 - V = 0.2$  V in the optimized device,  $s = 0.88$ . This suggests again that while the DIO does not completely remove problems associated with charge extraction, it significantly reduces the magnitude of the effects, removing the dramatic s-shape of the curve.

### Thin film X-ray diffraction

Changes in device performance upon addition of solvent additives are typically ascribed to improvements in the BHJ nanostructure by affecting the thermodynamics and kinetics of phase separation. In this class of small molecule systems, this is often attributed to asserting control over the crystallization and phase-separation processes within the blend; DIO helps induce crystallinity of the donor material [40-42,54-56]. Grazing incidence wide-angle X-ray scattering (GIWAXS) was used to probe the crystallization behavior of the blend system with and without additive. The full 2-dimensional GIWAXS spectra from a film of the neat p-SIDT(FBTThCA8)<sub>2</sub> and the two blends are shown in Figure S7 (Supporting Information File 1) while line cuts showing  $Q_z$  (“out-of-plane”) and  $Q_{x-y}$  (“in-plane”) of the two blends are shown in the top and bottom plots respectively of Figure 2d.

Looking first at the out-of-plane diffraction in the top panel of Figure 2d, the BHJ film cast with no DIO shows a prominent peak at  $0.37 \text{ \AA}^{-1}$ . This corresponds to a real-space distance of 1.7 nm. While attempts to grow single crystals of this material have thus far been unsuccessful and thus the peaks cannot be indexed precisely, by convention we attribute this spacing to an “alkyl stacking peak”, that is a spacing arising from molecules separated by alkyl chains analogous to the lamellae stacking in P3HT (i.e., (100) planes). In the film cast with DIO, this peak is more prominent suggesting a greater degree of crystallinity. There is also a peak at  $0.74 \text{ \AA}^{-1}$ , which corresponds to the second order reflection. There is even a small peak at  $1.11 \text{ \AA}^{-1}$ , which likely corresponds to a third-order reflection, suggesting a quite well-ordered film. Additionally, there is a small peak at  $1.79 \text{ \AA}^{-1}$ , corresponding to a spacing of 3.5 Å, which we attribute to  $\pi-\pi$  stacking. There is a broad feature centered at  $Q = 1.5 \text{ \AA}^{-1}$  which is seen in both films and at all orientations, which is the convolution of two peaks. In the neat p-SIDT(FBTThCA8)<sub>2</sub> there is a relatively weak, broad feature

at  $1.52 \text{ \AA}^{-1}$  which convolves with the isotropic scattering peak of PC<sub>71</sub>BM which is typically found at  $1.3\text{--}1.4 \text{ \AA}^{-1}$ . These two peaks are nearly resolvable in the in-plane scattering of the film cast with DIO but are completely overlapping in the blend without additive, leading to a very broad peak.

Looking next at the traces from the  $Q_{x-y}$  direction, that is, just from crystallites oriented in the plane of the substrate, there are no discernible features from p-SIDT(FBTThCA8)<sub>2</sub> in the BHJ film cast without DIO. In the film processed with DIO, the alkyl stacking peak is again though is less prominent in-plane, while the  $\pi$ -stacking peak is more prominent. Assuming the alkyl and  $\pi$ -stacking directions are perpendicular, this suggests the material primarily adopts an edge-on orientation. This is in contrast with the preferential “face-on” orientation adopted by p-SIDT(FBTTh<sub>2</sub>)<sub>2</sub> [40], demonstrating how sensitive molecular self-assembly can be to relatively small molecular design choices. However, consistent with previous reports of related molecules, DIO does seem to improve crystallinity.

Atomic force microscopy (AFM) topography images are shown in Figure S8 (Supporting Information File 1). The film cast without DIO has a relatively smooth featureless surface while the film cast with DIO has a rougher surface with relatively large ( $>100 \text{ nm}$  diameter) features. This is consistent with phase separation and the crystallinity seen by GIWAXS.

Despite the differences in crystallization, this does not give a clear indication as to the root cause of why devices processed without DIO show signs of space charge and an s-shaped  $J\text{--}V$  curve. One might expect that the increase in crystallinity has a profound effect on the hole mobility in the blends, and space charge may occur due to imbalanced carrier mobilities in the device processed without DIO. However, the hole mobilities for blends processed without DIO and with 1.5% DIO are  $5 \times 10^{-5}$  and  $9 \times 10^{-5} \text{ cm}^2/\text{Vs}$ , respectively, each slightly lower than the neat hole mobility of p-SIDT(FBTThCA8)<sub>2</sub>, which is found to be  $2 \times 10^{-4} \text{ cm}^2/\text{Vs}$  (Supporting Information File 1, Figure S8). Although the mobility indeed increases with DIO processing, a mobility increase by a factor of two is not particularly significant and should not lead to such drastic changes in curve shape [24,30,57]. These mobilities are, however, somewhat lower than in related high-performance systems, which may always limit the system to a relatively low  $FF$  [40,57,58]. Unfortunately attempts to measure electron mobilities in charge-selective diodes were unsuccessful due to poor film formation on aluminum bottom contacts.

### Origin of the s-shape in $J\text{--}V$ curves

Despite the relatively high  $V_{OC}$ , based on the CV data, one might expect to achieve voltages that are even higher compared

with p-SIDT(FBTTh<sub>2</sub>)<sub>2</sub>, as p-SIDT(FBTThCA8)<sub>2</sub> seems to have an even deeper HOMO level. However, a HOMO of  $-5.27 \text{ eV}$  is close to the work function of the PEDOT interfacial layer, and thus there may be non-ohmic contacts between the PEDOT and active layer, limiting the voltage [59]. Such an extraction barrier may also explain the build-up of space charge at one contact, and the s-shape to the  $J\text{--}V$  curve [25,30,60–62]. It has recently been shown by Tan and co-workers that in some cases, when PEDOT limits the voltage in solar cells, casting methanol on top of the layer will improve efficiency [63]. The methanol has been shown to effectively deepen the work function of the anode layer while not significantly disrupting the morphology. Specifically, this improves the extraction rate of holes at the anode interface. An enhanced hole extraction rate at the semiconductor/anode interface will reduce the accumulation of holes near the electrode, thereby preventing the screening of the internal field and suppressing recombination. The reduction of charge recombination and improved transport enables a higher photocurrent collection yield across the forward bias regime and improved  $V_{OC}$  [63]. We employed this processing method to improve the voltages in p-SIDT(FBTThCA8)<sub>2</sub>:PC<sub>71</sub>BM cells and look at the effects on curve shape (Figure 4).

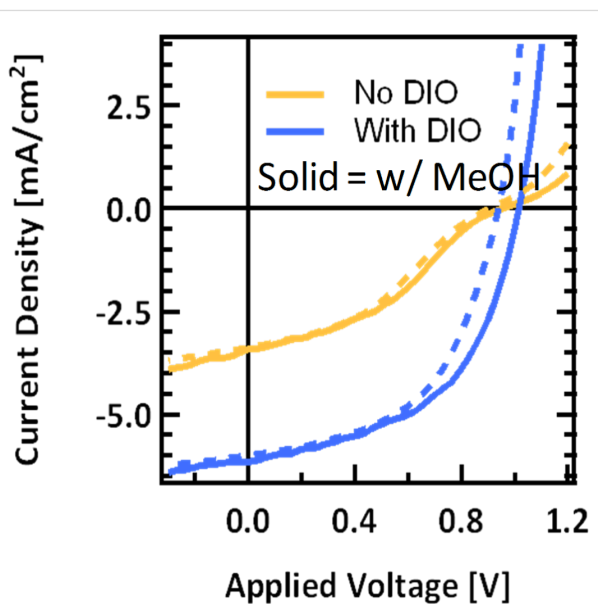


**Figure 4:** Current voltage curves for devices cast from pure chlorobenzene (yellow) and with 1.5% DIO (blue) with (solid) and without (dashed) methanol treatment.

After treatment with methanol, the  $V_{OC}$  of devices processed with DIO increases to  $1.01 \text{ V}$ . A similar improvement in  $V_{OC}$  is also seen for devices cast from chlorobenzene. The  $J\text{--}V$  characteristics are described in Table 1 and shown in Figure 4 along with the  $J\text{--}V$  curves replotted from Figure 2b for comparison.

Treatment with methanol has a little effect on  $J_{SC}$  or  $FF$ ; thus we suspect there is no significant change in morphology when methanol is cast. Rather, the treatments strictly improves electrical contact by deepening the work function as described previously [28,34,60–62]. Despite the improvement in  $V_{OC}$  in both devices, for devices processed without additive, the s-shaped kink in the  $J$ – $V$  curve near open circuit remains. Thus, a contact problem at the anode is ruled out as the underlying cause of the atypical curve shape.

Non-ideal vertical phase separation, that is to say, enrichment of donor material at the cathode or acceptor at the anode may also be a potential cause of s-kinks in  $J$ – $V$  curves. The acceptor material at the PEDOT interface, for instance, can act as a barrier to hole extraction, leading to ineffective sweep out and a build-up of holes [23,26,64]. To examine the vertical separation behavior of the two blends dynamic secondary ion mass spectrometry (DSIMS) was employed. In DSIMS, a sample is bombarded with ions, ablating ionized material, which is analyzed using a mass spectrometer [65]. The composition of the ablated material is monitored as the beam mills through the thin film, resulting in a depth profile. To improve contrast between the two materials, deuterated fullerene  $PC_61BM-d_5$  was used as a surrogate for  $PC_71BM$  to establish a unique mass signal for the fullerene component [12,66,67]. Thus detection of deuterium in the mass spectrum implicitly signifies  $PC_61BM-d_5$  in the film. The implicit assumption made here is that blends with the surrogate  $PC_61BM-d_5$  behave phenomologically like those made with  $PC_71BM$ , and thus the  $PC_61BM-d_5$  signal will be applied to analyze the  $PC_71BM$ -containing blend. The

amount of p-SIDT(FBTThCA8)<sub>2</sub> was monitored as the occurrence of nitrogen atoms in the mass spectrum. Unique signatures for each material help to make discerning relative concentrations simple and accurate. The DSIMS profiles of the two systems are shown in Figure 5.

As the DSIMS profile is collected, time corresponds to film depth, as the beam ablates material at a constant rate. Thus the x-axis has been scaled for film thickness, where the turn-on of the nitrogen and deuterium signals at  $x = 0$  nm corresponds to the top surface of the films, what would be the cathode interface in a complete device architecture. The turn-off of the signals thus corresponds to the BHJ/PEDOT interface. The absolute intensity of the two signals given by the instrument cannot be compared directly due to different instrumental sensitivity, thus each signal is scaled to an average composition of 50% based on the weight ratio used in the blend solutions. It is fair to monitor how the signals evolve relative to each other as the beam penetrates into the film.

Looking first at the BHJ processed without additive, when the signals first turn on, there is initially an enrichment of p-SIDT(FBTThCA8)<sub>2</sub> immediately followed by a depletion of donor and an enrichment of the  $PC_61BM-d_5$  signal. This corresponds to donor material preferentially accumulated on the top surface. Throughout the bulk of the trace, the concentration of the two materials remains nearly constant. At the PEDOT interface,  $x = 115$ – $120$  nm, the  $PC_61BM-d_5$  signal has a small peak while the p-SIDT(FBTThCA8)<sub>2</sub> signal begins to drop off. This suggests that in the device there is an enrichment of  $PC_71BM$  at

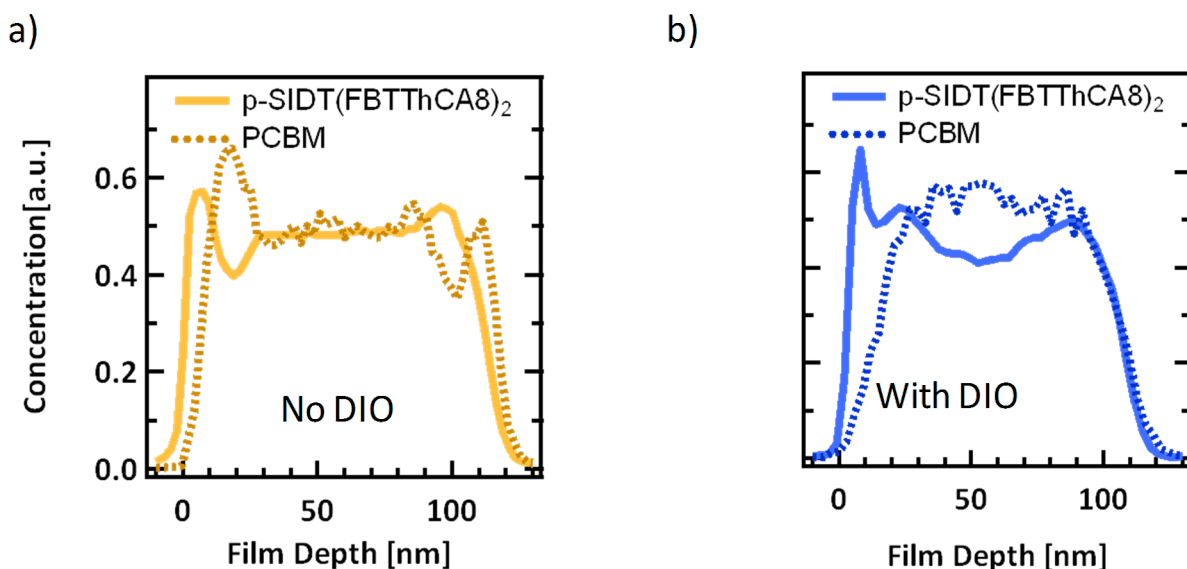


**Figure 5:** Dynamic secondary ion mass spectrometry (DSIMS) profile showing scaled nitrogen (solid) and deuterium (dashed) signals for films cast a) with no DIO and b) with 1.5% DIO.

the anode surface. Such an arrangement, with donor at the top surface and acceptor at the bottom, is non-ideal for the standard device architecture.

Processing with DIO has a significant effect on the vertical phase separation. At the top surface there is again an enrichment of the p-SIDT(FBTThCA8)<sub>2</sub>, evidenced by a faster turn on than the PC<sub>61</sub>BM-*d*<sub>6</sub> signal. There is then a slight depletion of the p-SIDT(FBTThCA8)<sub>2</sub> through the bulk of the device. At the bottom surface, however, unlike in the film cast without DIO, the two material signals overlap, suggesting an even distribution of p-SIDT(FBTThCA8)<sub>2</sub> and PC<sub>71</sub>BM in the better performing devices. The vertical phase separation is still not ideal in this additive processed film, as there remains an enrichment of p-SIDT(FBTThCA8)<sub>2</sub> at the cathode interface, however, DIO helps to overcome the problem of PC<sub>71</sub>BM concentrated at the anode interface.

A high concentration of PC<sub>71</sub>BM at the anode helps to explain the s-shape behavior of the *J*–*V* curve for the devices processed without additive. The low concentration of p-SIDT(FBTThCA8)<sub>2</sub> near that interface reduces the surface recombination velocity of holes within the device; reduced surface recombination results in a piling up of charges near the anode which creates a space charge effect in the device [64]. This helps to explain the anomalous *V*<sub>OC</sub> and *J*<sub>Ph</sub> light intensity data. The effect is most apparent at low fields and high carrier concentrations, i.e., near open circuit conditions and at high light intensities.

If the s-shape seen in devices cast from chlorobenzene is in fact due to an enrichment of PC<sub>71</sub>BM at the bottom interface, the use of an inverted device architecture should result in an improvement in curve shape. The inverted architecture has the cathode as the bottom contact and the anode on top; thus if the vertical separation in the BHJ remains, the PC<sub>71</sub>BM-rich phase will be at the cathode interface and p-SIDT(FBTThCA8)-rich phase at the anode interface [68]. However, it is not necessarily true that the phase separation observed in one architecture will occur in inverted devices, as fabrication requires casting atop different substrates with different surface energetics, which may play a role in determining film formation.

While the active layers were cast in the same way, for inverted devices we employed the architecture ITO/ZnO/PEIE/p-SIDT(FBTThCA8)<sub>2</sub>:PC<sub>71</sub>BM/MoO<sub>3</sub>/Al where PEIE refers to ethoxylated polyethylenimine. The cathode was cast from a sol-gel of zinc acetate, and thermally converted to ZnO in air as described in literature [69]. A thin (10 nm) layer of PEIE has been shown in the past to improve contact by reducing the work function of a ZnO surface, and was prepared as reported [70]. The *J*–*V* characteristics of the films cast with no DIO in the standard and inverted device architecture are shown in Figure 6.

Devices cast from pure chlorobenzene achieved much higher efficiency in the inverted architecture than in the standard architecture (*J*<sub>SC</sub> = 4.5 mA/cm<sup>2</sup>, *V*<sub>OC</sub> = 1.09 V, *FF* = 0.51, *PCE* = 2.5%). While the performance is still modest, there is a marked improvement in the shape of the *J*–*V* curve. The devices

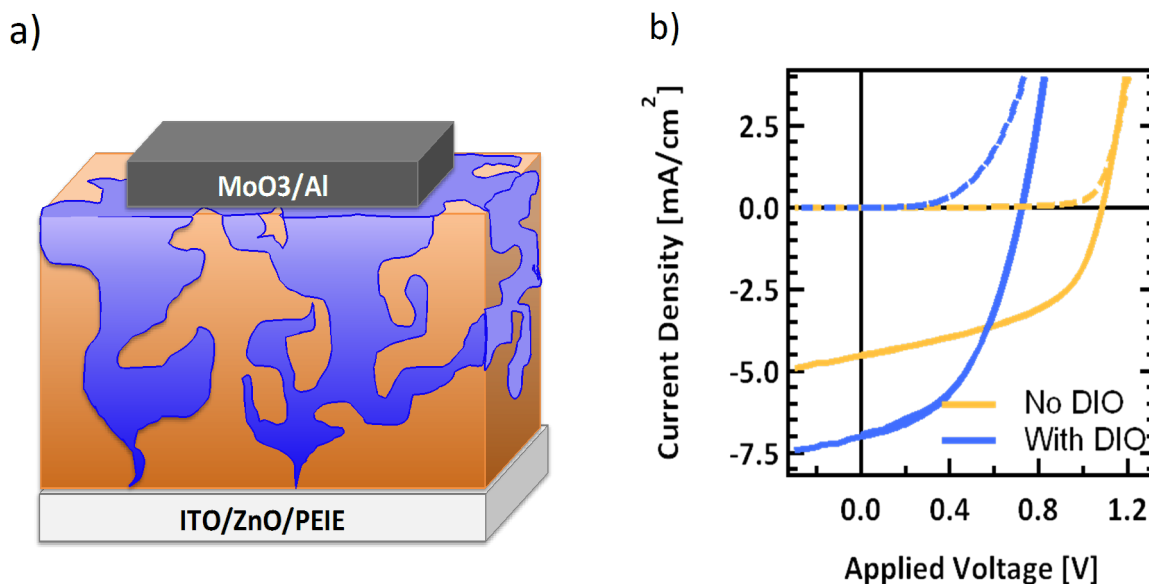


**Figure 6:** a) A schematic diagram of inverted architecture and b) *J*–*V* curves of device cast with no DIO in the standard (dashed) and inverted (solid) architecture.

achieve high open circuit voltage with no sign of space charge build-up. All device parameters improve. While we cannot be completely sure the morphology of this film is identical as when it is in a standard architecture, this is a strong indication that the primary cause for the s-shape is indeed non-ideal vertical phase separation. Further SIMS analysis of the inverted cells and optimization of the film casting process in the inverted architecture may be the focus of future work.

Unfortunately, when the optimized 1.5% DIO condition was used to make inverted devices, the efficiency was lower than in a standard architecture ( $J_{SC} = 7.0 \text{ mA/cm}^2$ ,  $V_{OC} = 0.73 \text{ V}$ ,  $FF = 0.47$ ,  $PCE = 2.4\%$ ). These devices showed very high dark (leakage) current (Supporting Information File 1, Figure S10), which is likely a result of a change in morphology when casting atop ZnO instead of PEDOT; the films show significantly rougher surfaces (Supporting Information File 1, Figure S11). It is possible that through further optimization using the inverted architecture, we may be able to improve the top efficiency, however, that is beyond the scope of this work. We were satisfied to demonstrate that changing architectures does indeed eradicate the s-shape of the curve for devices cast from pure chlorobenzene, helping to further prove the hypothesis that the root of s-shaped  $J$ – $V$  curves was indeed non-ideal vertical phase separation.

## Conclusion

A new molecular donor material, p-SIDT(FBTThCA8)<sub>2</sub>, was developed based on the inclusion of electron-withdrawing endcaps within a previously reported high-performance molecular framework. The structural modification had the desired effect of reducing the band gap for extended absorption in the visible spectrum while maintaining a low-lying HOMO level to achieve high  $V_{OC}$ . The energy levels are nearly ideal match for incorporation into BHJ devices with the acceptor PC<sub>71</sub>BM, maximizing voltage and spectral coverage. Despite the structural similarity to previously reported materials, however, blends of p-SIDT(FBTThCA8)<sub>2</sub> and PC<sub>71</sub>BM did not have device performance akin to its predecessors when processed in the same manner.

Specifically, when cast from chlorobenzene, the resulting  $J$ – $V$  curve gives rise to a significant s-shape, resulting in extremely low  $FF$  and  $PCE$ . Through light intensity studies, the s-shape in the curve was attributed to the build-up of space charge. The use of DIO as a solvent additive helped to remove the s-shape character from the  $J$ – $V$  curve and to improve the performance up to  $PCE = 3.2\%$ . Analogous to what has been reported in literature, DIO helps to induce crystallinity of the p-SIDT(FBTThCA8)<sub>2</sub> in the blend as evidenced by GIWAXS and a commensurate red shift in absorption. However, lack of

crystallinity is not typically associated with the s-shape in the  $J$ – $V$  curve seen when cast without additive.

Blends cast from chlorobenzene have reasonably high mobility, so a build-up of space charge simply due to an imbalance in carrier mobilities can likely be ruled out. Instead, the differences in curve shape are ascribed to changes in the vertical phase separation; when cast without additive there is an enrichment of PC<sub>71</sub>BM at the PEDOT:BHJ interface as evidenced by DSIMS. Subsequently, the low concentration of p-SIDT(FBTThCA8)<sub>2</sub> at the anode likely leads to reduced surface recombination, a build-up of space charge and ultimately, an s-kink in the  $J$ – $V$  curve. The inclusion of DIO helps to reduce the concentration of PC<sub>71</sub>BM at the anode improving surface recombination, and  $J$ – $V$  characteristics. This is further evidenced by the elimination of the s-kink upon moving to an inverted structure. In fact, in the inverted structure the blend device gives a  $V_{OC}$  of 1.09 V, which is quite remarkable, considering the absorption profile extends out to 730 nm (1.69 eV). Such a small voltage loss between absorption onset and  $V_{OC}$  demonstrates the tremendous potential of this blend system. Although without further device engineering the performance of this materials system is not yet on par with the state of the art, the drastic change in curve shape is important in understanding the nature of solvent additives and their effects on solution processed BHJ devices.

## Supporting Information

### Supporting Information File 1

Detailed experimental procedures with physical and chemical analysis of compounds and additional device characterization data.

[<http://www.beilstein-journals.org/bjoc/content/supplementary/1860-5397-12-249-S1.pdf>]

## Acknowledgements

The authors thank the Office of Naval Research (Award No. N000141410076) for support of this work. T.-Q.N. thanks the Camille Dreyfus Teacher Scholar Award. The authors acknowledge the support of Stanford Synchrotron Radiation Light source (SSRL), which is supported by the U.S. Department of Energy.

## References

1. Dou, L.; You, J.; Hong, Z.; Xu, Z.; Li, G.; Street, R. A.; Yang, Y. *Adv. Mater.* **2013**, *25*, 6642. doi:10.1002/adma.201302563
2. Liu, Y.; Zhao, J.; Li, Z.; Mu, C.; Ma, W.; Hu, H.; Jiang, K.; Lin, H.; Ade, H.; Yan, H. *Nat. Commun.* **2014**, *5*, No. 5293. doi:10.1038/ncomms6293

3. Li, W.; Furlan, A.; Hendriks, K. H.; Wienk, M. M.; Janssen, R. A. J. *J. Am. Chem. Soc.* **2013**, *135*, 5529. doi:10.1021/ja401434x
4. Service, R. F. *Science* **2011**, *332*, 293. doi:10.1126/science.332.6027.293
5. Walker, B.; Tomayo, A. B.; Dang, X.-D.; Zalar, P.; Seo, J. H.; Garcia, A.; Tantiwat, M.; Nguyen, T.-Q. *Adv. Funct. Mater.* **2009**, *19*, 3063. doi:10.1002/adfm.200900832
6. Tamayo, A. B.; Dang, X.-D.; Walker, B.; Seo, J.; Kent, T.; Nguyen, T.-Q. *Appl. Phys. Lett.* **2009**, *94*, 103301. doi:10.1063/1.3086897
7. Henson, Z. B.; Welch, G. C.; van der Poll, T.; Bazan, G. C. *J. Am. Chem. Soc.* **2012**, *134*, 3766. doi:10.1021/ja209331y
8. Coughlin, J. E.; Henson, Z. B.; Welch, G. C.; Bazan, G. C. *Acc. Chem. Res.* **2014**, *47*, 257. doi:10.1021/ar400136b
9. Wang, J.-L.; Wu, Z.; Miao, J.-S.; Liu, K.-K.; Chang, Z.-F.; Zhang, R.-B.; Wu, H.-B.; Cao, Y. *Chem. Mater.* **2015**, *27*, 4338. doi:10.1021/acs.chemmater.5b00848
10. Gao, K.; Li, L.; Lai, T.; Xiao, L.; Huang, Y.; Huang, F.; Peng, J.; Cao, Y.; Liu, F.; Russell, T. P.; Janssen, R. A. J.; Peng, X. *J. Am. Chem. Soc.* **2015**, *137*, 7282. doi:10.1021/jacs.5b03740
11. Wang, J.-L.; Xiao, F.; Yan, J.; Wu, Z.; Liu, K.-K.; Chang, Z.-F.; Zhang, R.-B.; Chen, H.; Wu, H.-B.; Cao, Y. *Adv. Funct. Mater.* **2016**, *26*, 1803. doi:10.1002/adfm.201505020
12. Welch, G. C.; Perez, L. A.; Hoven, C. V.; Zhang, Y.; Dang, X.-D.; Sharenko, A.; Toney, M. F.; Kramer, E. J.; Nguyen, T.-Q.; Bazan, G. C. *J. Mater. Chem.* **2011**, *21*, 12700. doi:10.1039/c1jm11963j
13. Gupta, V.; Kyaw, A. K. K.; Wang, D. H.; Chand, S.; Bazan, G. C.; Heeger, A. J. *Sci. Rep.* **2013**, *3*, No. 1965. doi:10.1038/srep01965
14. Scharber, M. C.; Mühlbacher, D.; Koppe, M.; Denk, P.; Waldauf, C.; Heeger, A. J.; Brabec, C. J. *Adv. Mater.* **2006**, *18*, 789. doi:10.1002/adma.200501717
15. Liu, Y.; Wan, X.; Wang, F.; Zhou, J.; Long, G.; Tian, J.; Chen, Y. *Adv. Mater.* **2011**, *23*, 5387. doi:10.1002/adma.201102790
16. Li, Z.; He, G.; Wan, X.; Liu, Y.; Zhou, J.; Long, G.; Zuo, Y.; Zhang, M.; Chen, Y. *Adv. Energy Mater.* **2012**, *2*, 74. doi:10.1002/aenm.201100572
17. Liu, Y.; Wan, X.; Yin, B.; Zhou, J.; Long, G.; Yin, S.; Chen, Y. *J. Mater. Chem.* **2010**, *20*, 2464. doi:10.1039/b925048d
18. He, G.; Li, Z.; Wan, X.; Liu, Y.; Zhou, J.; Long, G.; Zhang, M.; Chen, Y. *J. Mater. Chem.* **2012**, *22*, 9173. doi:10.1039/c2jm30194f
19. He, G.; Li, Z.; Wan, X.; Zhou, J.; Long, G.; Zhang, S.; Zhang, M.; Chen, Y. *J. Mater. Chem. A* **2013**, *1*, 1801. doi:10.1039/C2TA00496H
20. Ashraf, R. S.; Schroeder, B. C.; Bronstein, H. A.; Huang, Z.; Thomas, S.; Kline, R. J.; Brabec, C. J.; Rannou, P.; Anthopoulos, T. D.; Durrant, J. R.; McCulloch, I. *Adv. Mater.* **2013**, *25*, 2029. doi:10.1002/adma.201300027
21. McCulloch, I.; Ashraf, R. S.; Biniek, L.; Bronstein, H.; Combe, C.; Donaghey, J. E.; James, D. I.; Nielsen, C. B.; Schroeder, B. C.; Zhang, W. *Acc. Chem. Res.* **2012**, *45*, 714. doi:10.1021/ar200208g
22. Wang, J.-Y.; Hau, S. K.; Yip, H.-L.; Davies, J. A.; Chen, K.-S.; Zhang, Y.; Sun, Y.; Jen, A. K.-Y. *Chem. Mater.* **2011**, *23*, 765. doi:10.1021/cm1020228
23. Wagenpfahl, A.; Rauh, D.; Binder, M.; Deibel, C.; Dyakonov, V. *Phys. Rev. B* **2010**, *82*, 115306. doi:10.1103/PhysRevB.82.115306
24. Tress, W.; Petrich, A.; Hummert, M.; Hein, M.; Leo, K.; Riede, M. *Appl. Phys. Lett.* **2011**, *98*, 063301. doi:10.1063/1.3553764
25. Tress, W.; Leo, K.; Riede, M. *Adv. Funct. Mater.* **2011**, *21*, 2140. doi:10.1002/adfm.201002669
26. Wang, J. C.; Ren, X. C.; Shi, S. Q.; Leung, C. W.; Chan, P. K. L. *Org. Electron.* **2011**, *12*, 880. doi:10.1016/j.orgel.2011.02.016
27. Finck, B. Y.; Schwartz, B. *J. Appl. Phys. Lett.* **2013**, *103*, 053306. doi:10.1063/1.4817396
28. Tress, W. *Organic Solar Cells. Springer Series in Materials Science*; Springer International Publishing, 2014; pp 315–357.
29. Sandberg, O. J.; Nyman, M.; Österbacka, R. *Phys. Rev. Appl.* **2014**, *1*, No. 024003. doi:10.1103/PhysRevApplied.1.024003
30. Tress, W. *Organic Solar Cells. Springer Series in Materials Science*; Springer International Publishing, 2014; pp 359–376.
31. Patra, D.; Huang, T.-Y.; Chiang, C.-C.; Maturana, R. O. V.; Pao, C.-W.; Ho, K.-C.; Wei, K.-H.; Chu, C.-W. *ACS Appl. Mater. Interfaces* **2013**, *5*, 9494. doi:10.1021/am4021928
32. Zhou, J.; Wan, X.; Liu, Y.; Zuo, Y.; Li, Z.; He, G.; Long, G.; Ni, W.; Li, C.; Su, X.; Chen, Y. *J. Am. Chem. Soc.* **2012**, *134*, 16345. doi:10.1021/ja306865z
33. Cui, C.; Min, J.; Ho, C.-L.; Ameri, T.; Yang, P.; Zhao, J.; Brabec, C. J.; Wong, W.-Y. *Chem. Commun.* **2013**, *49*, 4409. doi:10.1039/c3cc38920k
34. Patra, D.; Chiang, C.-C.; Chen, W.-A.; Wei, K.-H.; Wu, M.-C.; Chu, C.-W. *J. Mater. Chem. A* **2013**, *1*, 7767. doi:10.1039/c3ta11544e
35. Zhou, J.; Wan, X.; Liu, Y.; Long, G.; Wang, F.; Li, Z.; Zuo, Y.; Li, C.; Chen, Y. *Chem. Mater.* **2011**, *23*, 4666. doi:10.1021/cm202588h
36. Benaglia, M.; Toyota, S.; Woods, C. R.; Siegel, J. S. *Tetrahedron Lett.* **1997**, *38*, 4737. doi:10.1016/S0040-4039(97)01025-3
37. Liu, X.; Sun, Y.; Hsu, B. B. Y.; Lorbach, A.; Qi, L.; Heeger, A. J.; Bazan, G. C. *J. Am. Chem. Soc.* **2014**, *136*, 5697. doi:10.1021/ja413144u
38. Sun, Y.; Welch, G. C.; Leong, W. L.; Takacs, C. J.; Bazan, G. C.; Heeger, A. J. *Nat. Mater.* **2012**, *11*, 44. doi:10.1038/nmat3160
39. van der Poll, T. S.; Love, J. A.; Nguyen, T.-Q.; Bazan, G. C. *Adv. Mater.* **2012**, *24*, 3646. doi:10.1002/adma.201201127
40. Love, J. A.; Nagao, I.; Huang, Y.; Kuik, M.; Gupta, V.; Takacs, C. J.; Coughlin, J. E.; Qi, L.; van der Poll, T. S.; Kramer, E. J.; Heeger, A. J.; Nguyen, T.-Q.; Bazan, G. C. *J. Am. Chem. Soc.* **2014**, *136*, 3597. doi:10.1021/ja412473p
41. Takacs, C. J.; Sun, Y.; Welch, G. C.; Perez, L. A.; Liu, X.; Wen, W.; Bazan, G. C.; Heeger, A. J. *J. Am. Chem. Soc.* **2012**, *134*, 16597. doi:10.1021/ja3050713
42. Love, J. A.; Proctor, C. M.; Liu, J.; Takacs, C. J.; Sharenko, A.; van der Poll, T. S.; Heeger, A. J.; Bazan, G. C.; Nguyen, T.-Q. *Adv. Funct. Mater.* **2013**, *23*, 5019. doi:10.1002/adfm.201300099
43. Love, J. A.; Collins, S. D.; Nagao, I.; Mukherjee, S.; Ade, H.; Bazan, G. C.; Nguyen, T.-Q. *Adv. Mater.* **2014**, *26*, 7308. doi:10.1002/adma.201402403
44. Amb, C. M.; Chen, S.; Graham, K. R.; Subbiah, J.; Small, C. E.; So, F.; Reynolds, J. R. *J. Am. Chem. Soc.* **2011**, *133*, 10062. doi:10.1021/ja204056m
45. Koster, L. J. A.; Mihailescu, V. D.; Ramaker, R.; Blom, P. W. M. *Appl. Phys. Lett.* **2005**, *86*, 123509. doi:10.1063/1.1889240
46. Mihailescu, V. D.; Koster, L. J. A.; Hummelen, J. C.; Blom, P. W. M. *Phys. Rev. Lett.* **2004**, *93*, 216601. doi:10.1103/PhysRevLett.93.216601
47. Mihailescu, V. D.; Wildeman, J.; Blom, P. W. M. *Phys. Rev. Lett.* **2005**, *94*, 126602. doi:10.1103/PhysRevLett.94.126602
48. Mihailescu, V. D.; Xie, H. X.; de Boer, B.; Koster, L. J. A.; Blom, P. W. M. *Adv. Funct. Mater.* **2006**, *16*, 699. doi:10.1002/adfm.200500420
49. Blom, P. W. M.; Mihailescu, V. D.; Koster, L. J. A.; Markov, D. E. *Adv. Mater.* **2007**, *19*, 1551. doi:10.1002/adma.200601093
50. Andersson, L. M.; Müller, C.; Badada, B. H.; Zhang, F.; Würfel, U.; Inganäs, O. *J. Appl. Phys.* **2011**, *110*, 024509. doi:10.1063/1.3609079

51. Albrecht, S.; Janietz, S.; Schindler, W.; Frisch, J.; Kurpiers, J.; Kniepert, J.; Inal, S.; Pingel, P.; Fostiropoulos, K.; Koch, N.; Neher, D. *J. Am. Chem. Soc.* **2012**, *134*, 14932. doi:10.1021/ja305039j

52. Tvingstedt, K.; Vandewal, K.; Zhang, F.; Inganäs, O. *J. Phys. Chem. C* **2010**, *114*, 21824. doi:10.1021/jp107587h

53. Credgington, D.; Jamieson, F. C.; Walker, B.; Nguyen, T.-Q.; Durrant, J. R. *Adv. Mater.* **2012**, *24*, 2135. doi:10.1002/adma.201104738

54. Perez, L. A.; Chou, K. W.; Love, J. A.; van der Poll, T. S.; Smilgies, D.-M.; Nguyen, T.-Q.; Kramer, E. J.; Amassian, A.; Bazan, G. C. *Adv. Mater.* **2013**, *25*, 6380. doi:10.1002/adma.201302389

55. Perez, L. A.; Rogers, J. T.; Brady, M. A.; Sun, Y.; Welch, G. C.; Schmidt, K.; Toney, M. F.; Jinnai, H.; Heeger, A. J.; Chabivny, M. L.; Bazan, G. C.; Kramer, E. J. *Chem. Mater.* **2014**, *26*, 6531. doi:10.1021/cm5031987

56. McDowell, C.; Abdelsamie, M.; Zhao, K.; Smilgies, D.-M.; Bazan, G. C.; Amassian, A. *Adv. Energy Mater.* **2015**, *5*, 1501121. doi:10.1002/aenm.201501121

57. Proctor, C. M.; Love, J. A.; Nguyen, T.-Q. *Adv. Mater.* **2014**, *26*, 5957. doi:10.1002/adma.201401725

58. Zalar, P.; Kuik, M.; Ran, N. A.; Love, J. A.; Nguyen, T.-Q. *Adv. Energy Mater.* **2014**, *4*, 1400438. doi:10.1002/aenm.201400438

59. Mihalek, V. D.; Blom, P. W. M.; Hummelen, J. C.; Rispens, M. T. *J. Appl. Phys.* **2003**, *94*, 6849. doi:10.1063/1.1620683

60. Schulze, K.; Uhrich, C.; Schüppel, R.; Leo, K.; Pfeiffer, M.; Brier, E.; Reinold, E.; Bäuerle, P. *Adv. Mater.* **2006**, *18*, 2872. doi:10.1002/adma.200600658

61. Jin, H.; Tuomikoski, M.; Hiltunen, J.; Kopola, P.; Maaninen, A.; Pino, F. *J. Phys. Chem. C* **2009**, *113*, 16807. doi:10.1021/jp906277k

62. Nelson, J.; Kirkpatrick, J.; Ravirajan, P. *Phys. Rev. B* **2004**, *69*, 035337. doi:10.1103/PhysRevB.69.035337

63. Tan, Z.-K.; Vaynzof, Y.; Credgington, D.; Li, C.; Casford, M. T. L.; Sepe, A.; Huettner, S.; Nikolla, M.; Paulus, F.; Yang, L.; Sirringhaus, H.; Greenham, N. C.; Friend, R. H. *Adv. Funct. Mater.* **2014**, *24*, 3051. doi:10.1002/adfm.201303426

64. Deibel, C.; Dyakonov, V. *Rep. Prog. Phys.* **2010**, *73*, 096401. doi:10.1088/0034-4885/73/9/096401

65. Magee, C. W. *Ultramicroscopy* **1984**, *14*, 55. doi:10.1016/0304-3991(84)90107-4

66. Treat, N. D.; Brady, M. A.; Smith, G.; Toney, M. F.; Kramer, E. J.; Hawker, C. J.; Chabivny, M. L. *Adv. Energy Mater.* **2011**, *1*, 82. doi:10.1002/aenm.201000023

67. van Duren, J. K. J.; Yang, X.; Loos, J.; Bulle-Lieuwma, C. W. T.; Sieval, A. B.; Hummelen, J. C.; Janssen, R. A. J. *Adv. Funct. Mater.* **2004**, *14*, 425. doi:10.1002/adfm.200305049

68. Subbiah, J.; Amb, C. M.; Reynolds, J. R.; So, F. *Sol. Energy Mater. Sol. Cells* **2012**, *97*, 97. doi:10.1016/j.solmat.2011.09.028

69. Sun, Y.; Seo, J. H.; Takacs, C. J.; Seifter, J.; Heeger, A. J. *Adv. Mater.* **2011**, *23*, 1679. doi:10.1002/adma.201004301

70. Zhou, Y.; Fuentes-Hernandez, C.; Shim, J.; Meyer, J.; Giordano, A. J.; Li, H.; Winget, P.; Papadopoulos, T.; Cheun, H.; Kim, J.; Fenoll, M.; Dindar, A.; Haske, W.; Najafabadi, E.; Khan, T. M.; Sojoudi, H.; Barlow, S.; Graham, S.; Brédas, J.-L.; Marder, S. R.; Kahn, A.; Kippelen, B. *Science* **2012**, *336*, 327. doi:10.1126/science.1218829

## License and Terms

This is an Open Access article under the terms of the Creative Commons Attribution License (<http://creativecommons.org/licenses/by/4.0>), which permits unrestricted use, distribution, and reproduction in any medium, provided the original work is properly cited.

The license is subject to the *Beilstein Journal of Organic Chemistry* terms and conditions: (<http://www.beilstein-journals.org/bjoc>)

The definitive version of this article is the electronic one which can be found at:

[doi:10.3762/bjoc.12.249](http://doi:10.3762/bjoc.12.249)